Semiconductors, Vol. 38, No. 4, 2004, pp. 369–375. Translated from Fizika i Tekhnika Poluprovodnikov, Vol. 38, No. 4, 2004, pp. 385–390.

ATOMIC STRUCTURE AND NONELECTRONIC PROPERTIES OF SEMICONDUCTORS

A Theory of the Effect of Impurities on the Yield Stress of Silicon Crystals

B. V. Petukhov

Shubnikov Institute of Crystallography, Russian Academy of Sciences, Leninskiĭ pr. 59, Moscow, 119333 Russia

e-mail: petukhov@ns.crys.ras.ru

Submitted June 25, 2003; accepted for publication September 22, 2003

Abstract—A theoretical model that attributes the effect of mobile neutral impurities on the special features of strain in semiconductor crystals to the phenomenon of dynamic aging of dislocations is suggested. Dependences of the upper yield stress on the concentration of impurity atoms, the strain rate, and other parameters are calculated. The results of calculations are consistent with experimental data for silicon. © *2004 MAIK "Nauka/Interperiodica".*

1. INTRODUCTION

It has been experimentally ascertained that neutral doping impurities exert a strengthening effect on mechanical properties of semiconducting materials. The motion and multiplication of dislocations become limited if the dislocations are pinned by impurity centers. This circumstance has important consequences for the production and operation of semiconductor devices in microelectronics [1, 2].

Strain in pure semiconductor crystals is described satisfactorily by the well-known Alexander–Haasen theory [3, 4], which makes it possible to explain the main mechanisms of the process. The most remarkable feature of the stress–strain curves (i.e., dependences of the stress τ on the strain ε at a constant strain rate $\dot{\varepsilon}$ = const) is the fact that they are nonmonotonic. As the strain increases, the strain-related stress first increases mainly owing to elastic deformation, attains a maximum referred to as the upper yield stress τ_u, and then rapidly decreases to the so-called lower yield stress τ_l. Finally, the strain-related stress increases relatively slowly again owing to strengthening by internal stresses caused, in particular, by the fields of generated dislocations. The Alexander–Haasen theory attributes the falloff of the strain-related stress to the onset of an intense multiplication of dislocations and describes the dependences of the upper and lower yield stresses on the initial dislocation density N_0, temperature T, strain rate $\dot{\varepsilon}$, and other parameters.

Despite the fact that doping is an extremely efficient method for controlling mechanical properties, the corresponding theory has been inadequately developed for extrinsic semiconductors. The study by Maroudas and Brown [5] is worth noting: in this study, the Alexander–Haasen model was supplemented by a numerical solution of the equation of oxygen-atom diffusion to mobile dislocations in silicon. In this paper, I report the results of studying another situation where the extended impurity cloud around a rapidly moving dislocation is not formed and direct contact interaction of impurities with dislocation cores plays the most important role. In this case, a drag of impurities occurs with the formation of an excess concentration of them in the dislocation core. The resulting decrease in the dislocation mobility is commonly referred to as the dynamic aging of dislocations. Certain special features of the effect of dynamic aging of dislocations on plastic strain in materials were studied previously using an alternative model [6]. In this study, I use the ideas developed in [6] about the dependence of effective internal stresses on the dislocation age in an ensemble of dislocations in order to generalize the original Alexander–Haasen model.

Let us first describe briefly the Alexander–Haasen model and then modify it taking into account the phenomenon of dynamic aging of dislocations. As a result, we will derive explicit analytical dependences of the upper yield stress on the numerous parameters that characterize the properties of the material, the type of impurities, and the conditions of deformation. In addition, an explanation for the following experimental facts will be given:

(i) The stress–strain curves of semiconductors that contain neutral interstitial impurities (oxygen, nitrogen, and such like) indicate a greater strengthening compared to the case of pure materials [1, 7–11]. At the same time, it is known from the results of in situ experiments [12] that, at high stresses corresponding to the upper yield point, these impurities do not affect the mobility of dislocations.

(ii) The effect of impurities is equivalent to a decrease in the initial dislocation density. It was reported [4, 7, 10] that in some cases the stress–strain curves for high-purity silicon grown by the float-zone method almost coincided within a large portion with those for silicon grown by the Czochralski method.

1063-7826/04/3804-0369$26.00

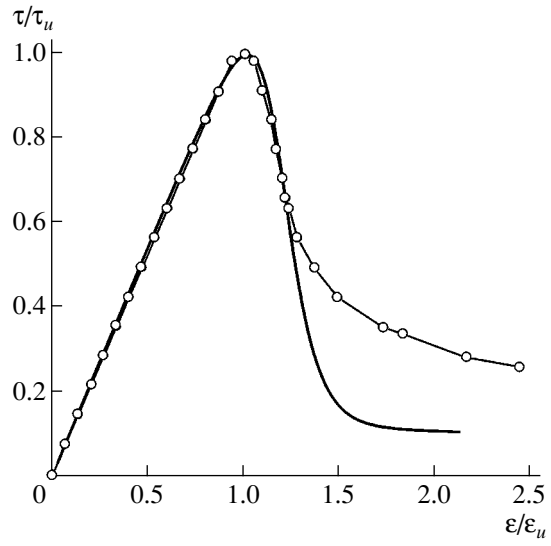

Fig. 1. Stress–strain curve in reduced coordinates. The solid line represents the theoretical dependence according to (5) and (6) for $\ln(N_*/N_0) = 5$. The line drawn through the circles represents experimental data for silicon [16] ($T = 800$°C, $\dot{\varepsilon} = 6.6 \times 10^{-5}$ s^{-1}).

This material contained 10^{18} cm^{-3} oxygen atoms and had an initial dislocation density that exceeded the dislocation density in float-zone silicon by two orders of magnitude.

2. DEFORMATION OF PURE CRYSTALS

A variation in the stress with time along a stress–strain curve is described by the following equation:

$$\dot{\varepsilon} = \dot{\varepsilon}_p + \dot{\tau}/S. \quad (1)$$

Here, ε is the total strain represented by the sum of the plastic ε_p and elastic τ/S strains, where τ is the applied stress and S is the combined elastic modulus of the sample and the testing setup; the Newtonian dot signifies the differentiation with respect to time.

Plastic strain is attained owing to the motion and multiplication of dislocations. The dislocation velocity in pure silicon crystals is described by the empirical equation

$$V = B(\tau - \tau_i), \quad (2)$$

where the factor B includes the temperature dependence [12–14] and quantities τ_i stand for internal stresses. The kinetic equation describing the evolution of the dislocation ensemble can be written in the following form in the model under investigation:

$$\frac{dN}{dt} = wV(\tau - \tau_i)N. \quad (3)$$

Here, w is the coefficient of self-multiplication of dislocations and N is the dislocation density (the initial value of this density is N_0). The rate of plastic strain in Eq. (1) is defined by the Orowan relation $\dot{\varepsilon}_p = NbV$, where b is the absolute value of the Burgers vector for dislocations.

In order to simplify the representation of the formulas, let us introduce the scaling factors for the stress τ_*, time t_*, and dislocation density N_*; i.e.,

$$\tau_* = \left(\frac{S\dot{\varepsilon}}{wB}\right)^{1/3}, \quad t_* = (wB)^{-1/3}(S\dot{\varepsilon})^{-2/3}, \quad N_* = \frac{1}{b}\left(\frac{\dot{\varepsilon}}{B}\right)^{2/3}\left(\frac{w}{S}\right)^{1/3}. \quad (4)$$

The dislocation density is still relatively low in the vicinity of the upper yield stress; as a result, the strain-related strengthening can be disregarded (i.e., it can be assumed that $\tau_i = 0$). An analytical formula for the shape of the peak in the stress–strain curve was derived previously [15]. In the case under consideration, this formula can be written as

$$\tau(N) = \tau_*\{[3\ln(N/N_0)]^{2/3} - 2N/N_*\}^{1/2}, \quad (5)$$

$$\varepsilon = \dot{\varepsilon}t \approx \dot{\varepsilon}t_*\left\{\left[3\ln\left(\frac{N}{N_0}\right)\right]^{1/3} - z_0\ln\left(1 - 2z_0\frac{N}{N_*}\right)\right\}. \quad (6)$$

Here, $z_0 \approx [3\ln(N_*/N_0) + 2\ln(\ln(N_*/N_0)) + 0.5855]^{-2/3}$.

Expression (5) indicates that there is a correlation between the strain-related stress and the dislocation density. Formula (6) describes the kinetics of the dislocation multiplication. By combining expressions (5) and (6), one can obtain the parametric representation for the shape of the yield-stress peak in the stress–strain curve, as is shown in Fig. 1 (solid line). The calculated curve is to be compared with the experimental data represented by circles [16].

The experimental data shown in Fig. 1 were obtained for silicon that contained a rather high concentration of oxygen impurity (8×10^{17} cm^{-3}). Therefore, one may question the correctness of comparing the observed shape of the yield-stress peak with that calculated for a pure crystal. However, as will be shown below, the shape of the yield-stress peak is universal to a great extent and, after appropriate normalization, is the same for both undoped and doped crystals. At the same time, the values of the yield stresses can differ significantly.

The upper yield stress of an undoped crystal is calculated as a maximum of the dependence $\tau(N)$ given by formula (5). The result of numerical solution, which satisfies the condition $d\tau/dN = 0$, of the nonlinear equation can be approximated by the formula

$$\tau \approx \tau_*[3\ln(0.1375N_*/N_0)]^{1/3}. \quad (7)$$

3. EXTRINSIC CRYSTALS: THE EFFECT OF DYNAMIC AGING OF DISLOCATIONS

The simplest and most widely used method for taking into account the dynamic aging of dislocations consists in decreasing the driving stress by the magnitude of the "dry friction" which is proportional to the excess concentration of impurities in the dislocation core, $\tau \longrightarrow \tau - \beta c$ [17]. Somewhat different models of dynamic aging of dislocations, whose motion proceeds according to the kink mechanism [18] (as is typical of dislocations in semiconductors), were developed in [5] and [19]. A simpler approach [19] will be used here; this approach can be incorporated into the Alexander–Haasen model and makes it possible to obtain an analytical solution.

The kinetics of variation in the impurity concentration c at a dislocation that moves with the velocity V is described by the following equation:

$$\frac{dc}{dt} = \frac{V}{a}\left[rc_0 - c\exp\left(-\frac{a}{Vt_m}\right)\right]. \quad (8)$$

Here, c_0 is the impurity concentration observed in the crystal bulk and calculated per lattice site; the radius of trapping of impurities by the dislocation r is measured in lattice parameters and is assumed to be constant; and t_m is the migration time of impurities. The first term in square brackets in Eq. (8) describes the increase in the impurity concentration at a dislocation due to trapping, and the second term describes a detachment of impurities during the time of overcoming the Peierls barrier a/V. According to experimental data, the velocity of dislocations in silicon depends linearly on the driving force; therefore, we have $V = B(\tau - \beta c)$.

Let us now describe (see [20]) qualitative characteristics of variation in the excess impurity concentration at a dislocation in relation to a stress that is either constant or varies slowly. Assuming a rapid completion of transient processes, we determine the quasi-steady state from the condition $dc/dt \longrightarrow 0$. This condition defines an attractor that, according to Eq. (8), consists of two branches, $V = B(\tau - \beta c) \approx 0$ and

$$rc_0 - c\exp\left[-\frac{a}{t_m B(\tau - \beta c)}\right] = 0. \quad (9)$$

As a result, we obtain the pattern shown in Fig. 2. Specifically, temporal variation in the excess impurity concentration at dislocations generated at somewhat different points in time for linearly increasing stress $\tau = \dot{\tau} t$ is shown in Fig. 2; this variation was calculated by numerically solving Eq. (8). Depending on the initial instant of time, the impurity concentration tends either to the branch of large values of c ($c \approx \tau/\beta$), which leads to complete immobilization of dislocations, or to the branch with small values of c, which corresponds to almost free motion of dislocations. Thus, the separating value of the stress τ_s and the corresponding point in time t_s, which determine the bifurcation point of solutions with a radical change in the type of dynamic behavior of dislocations, are important. As can be seen from expression (9), the value of τ_s corresponds to the minimum of the function $\beta c + a/(t_m B \ln(c/rc_0))$ with respect to c; this minimum can be easily determined numerically. The expression $c_s \approx rc_0[1 + 0.879(a/(\tau_m B\beta rc_0))^{0.587}]$ represents a satisfactory approximation for a minimum value c_s. This expression yields the following dependence of τ_s on the impurity concentration and other parameters:

$$\tau_s = \beta rc_0\left\{1 + 0.879\left(\frac{a}{Bt_m\beta rc_0}\right)^{0.587} + \frac{a}{Bt_m\beta rc_0\ln[1 + 0.879(a/Bt_m\beta rc_0)^{0.587}]}\right\}. \quad (10)$$

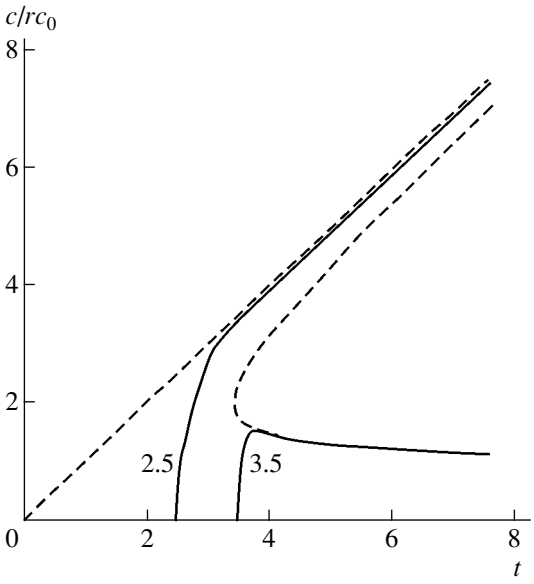

Fig. 2. Two types of evolution of the concentration of impurities at a dislocation in relation to the point in time of generation of this dislocation $t_m = 2.5$ and 3.5 (time is measured in units of $\beta rc_0/\dot{\tau}$, and the parameters are chosen to be equal to $a/(t_m B\beta rc_0) = 1$ and $B(\beta rc_0)^2/(a\dot{\tau}) = 10$). The dashed line represents the attractor for solutions of Eq. (8).

At $\tau < \tau_s$, aging occurs under the conditions of almost complete drag of impurities; in this case, aging can be described by the following simplified variant of Eq. (8):

$$\frac{dc}{dt} \approx \frac{Brc_0}{a}(\tau - \beta c). \quad (11)$$

In contrast, if $\tau > \tau_s$, the impurity drag is insignificant and can be disregarded in the first approximation. The existence of a bifurcation point and the corresponding

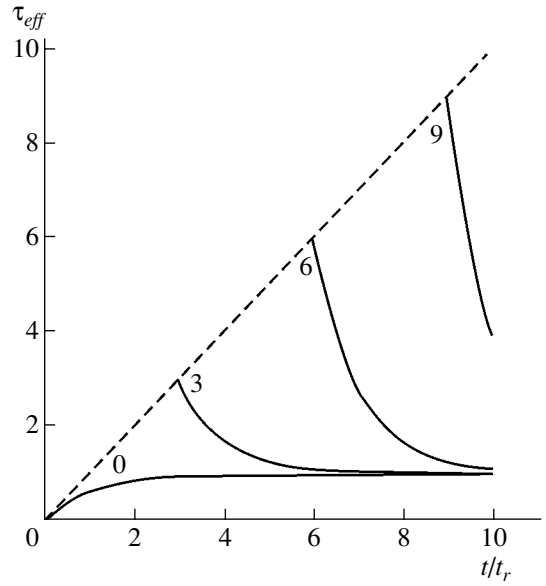

Fig. 3. Kinetics of effective stress (measured in units of $S\dot{\varepsilon}\, t_r$) for various values of points in time corresponding to the generation of dislocations; these points are indicated on the lines and are expressed in units of t_r.

variation in the dynamic behavior of dislocations makes it possible to explain a number of special features of deformation in extrinsic semiconductor crystals.

4. INCLUSION OF DYNAMIC AGING IN THE ALEXANDER–HAASEN MODEL

The number of impurities collected by a dislocation is controlled by its path length, which depends on the point in time corresponding to the generation of this dislocation. As a result, various dislocations in the ensemble under conditions of their intense multiplication are subjected to a different retarding force. In order to take into account the dependence of the dislocation velocity on the age of an individual dislocation, one has to modify the common description of plasticity. For extrinsic semiconductors, this description should include the age of dislocations, in addition to such characteristics as the Burgers vector and the mobility of dislocations [6]. Let us now perform the required modification of the theory.

Initial dislocations that are present in a crystal and have the density N_0 have a chance to acquire a certain impurity concentration c_s before the onset of deformation due to static aging. The starting stress βc_s that should be overcome for dislocations to start moving and for the process to set in is related to the initial impurity atmosphere around a dislocation. Thus, there is initially only elastic strain; as a result, the stress increases linearly up to the point in time $t_s = bc_s/(S\dot{\varepsilon})$. Dislocations then start to move and multiply, and plastic flow arises. Special measures are sometimes taken to immobilize the inherent dislocations [7].

Dislocations generated at different points in time t_m move with different velocities $V(t, t_m)$ at the instant of time t under consideration and, consequently, make dissimilar contributions to the plastic-strain rate $\dot{\varepsilon}_p$. For example, the conventional Orowan equation is valid now only for partial contributions of dislocations generated at almost coinciding points in time within a short interval δt_m with $\delta\dot{\varepsilon} = \delta N(t_m)bV$, where $\delta N(t_m) = \rho(t_m)\delta t_m$ and $\rho(t_m)$ is the generation rate of dislocations. After summing all the contributions, we obtain the following generalized Orowan relation:

$$\dot{\varepsilon}_p = bBN_0[\tau - \tau_i - \beta c_i(t)] + bB\int_0^t dt_m \rho(t_m)[\tau - \tau_i - \beta c(t, t_m)]. \quad (12)$$

Here, $c_i(t)$ is the concentration of impurities at initial dislocations. Equation (3) for multiplication of dislocations is modified in a similar way; i.e.,

$$\frac{dN}{dt} = \rho(t) = wBN_0[\tau - \tau_i - \beta c_i(t)]^2 + wB\int_0^t dt_m \rho(t_m)[\tau - \tau_i - \beta c(t, t_m)]^2. \quad (13)$$

Let us apply the system of Eqs. (12) and (13) to the description of the initial portion of the stress–strain curve and to the calculation of the upper yield stress for a semiconductor strengthened owing to impurities. In order to solve the model equations analytically, we will use the descriptive qualitative pattern of evolution of the excess impurity concentration at dislocations (see Section 3). In the first stage of deformation at $t < t_s = \tau_s/(S\dot{\varepsilon})$ (the quantity τ_s is defined by expression (10)), one can use the simplified concept that impurities are completely dragged by dislocations and employ Eq. (11). At $\tau \approx S\dot{\varepsilon}t$, a solution to this equation taking into account the initial condition at a newly generated dislocation $c(t_m, t_m) = 0$ is given by

$$c(t, t_m) = \frac{S\dot{\varepsilon}}{\beta}\{t - t_r - (t_m - t_r)\exp[-(t - t_m)/t_r]\}. \quad (14)$$

Here, $t_r = a/(B\beta r c_0)$. As can be seen from solution (14), a transient process takes place for the time $t - t_m \sim t_r$; the state with c varying according to the law $c \approx (S\dot{\varepsilon}/B)(t - t_r)$ is established after completion of this process. The impurity concentration at initial dislocations $c_i(t)$ varies according to the same law. The above condition for the short duration of transient processes can be expressed quantitatively as $t_r \ll t_s$.

Figure 3 shows the temporal variation in the effective stress $\tau = \beta c$ that sets in motion the dislocations generated at different points in time. The major contribution to the generation of dislocations during the time t is made by a small interval of generation times t_m that are close to t, $t - t_m \sim t_r$; in this case, the effective stress is maximal, and, as follows from formula (14), $\tau - \beta c \approx S\dot{\varepsilon} t_m \exp[-(t - t_m)/t_r]$. Substituting this expression into Eq. (13) and differentiating the result with respect to time, we obtain the following simplified differential equation (instead of the original integral equation):

$$\frac{d\rho}{dt} = \frac{2N_0 t_r}{t_*^3} + \left(\frac{t^2}{t_*^3} - \frac{2}{t_r}\right)\rho. \tag{15}$$

The solution of this equation defines an increase in the population of dislocations under conditions of drag of impurities at $t > (2\beta r c_0/aw)^{1/2}/(S\dot{\varepsilon})$; i.e.,

$$N_d(t) = \int \rho(t_m) dt_m \approx N_0 \exp\left\{\frac{1}{3}\left(\frac{t}{t_*}\right)^3 - \frac{2\beta r c_0}{a} Bt + \frac{2}{3}\frac{B}{S\dot{\varepsilon}\sqrt{w}}\left(\frac{2\beta r c_0}{a}\right)^{3/2}\right\}. \tag{16}$$

Only exponential contributions are completely represented in solution (16); the variation in the preexponential factor is disregarded since this variation is insignificant for what follows. As can be easily seen from expression (16), the population of dislocations grows more slowly in an extrinsic semiconductor ($c_0 \neq 0$) than in an intrinsic material ($c_0 = 0$). This stage of retarded growth continues up to the point in time $t = t_s$.

Dislocations generated during the second stage ($t > t_s$) do not have any significant impurity atmosphere. Consequently, the evolution of the density of these dislocations obeys the conventional Alexander–Haasen equation for an intrinsic semiconductor. The difference between this case and that of an intrinsic semiconductor consists in the fact that the initial condition is imposed on the dislocation density at $t = t_s$ when $N \approx N_d(t_s)$ rather than at $t = 0$ when $N = N_0$. Using Eq. (16), we obtain the following modified expression for effective initial dislocation density N_{0i}:

$$N_{0i} = N_0 \exp\left[-\frac{2\beta r c_0}{a} Bt_s + \frac{2}{3}\frac{B}{S\dot{\varepsilon}\sqrt{w}}\left(\frac{2\beta r c_0}{a}\right)^{3/2}\right]. \tag{17}$$

Consequently, dynamic aging reduces the generation rate of dislocations at the first stage of deformation and does not affect the process at the later stage ($t > t_s$). If the point of the peak in the stress–strain curve (i.e., the position of the upper yield stress) corresponds to the instant of time $t_u > t_s$, the resulting decrease in the dislocation density can be attributed effectively to a decrease in the initial dislocation density. All the special features of deformation in the vicinity of the upper yield stress will be described by the Alexander–Haasen model if N_0 is replaced by N_{0i}. Different values of initial dislocation density and impurity concentration may correspond to the same value of N_{0i}. However, the stress–strain curves adjusted to the same scale should be identical for both intrinsic and extrinsic semiconductors. Such an equivalence was directly observed by Sumino *et al.* [7] as an approximate agreement between the stress–strain curves for silicon that was grown by the floating-zone method and had an initial dislocation density N_0 of 1.7×10^4 cm^{-2} and for silicon that was grown by the Czochralski method, contained 10^{18} cm^{-3} oxygen atoms, and had $N_0 \times 2 \times 10^6$ cm^{-2}. In a broader sense, the universality of the stress–strain curves should become clear after a scaling transformation, similar to that employed in Fig. 1. As a result of this scaling, the stress–strain curves in the portion under consideration become dependent on only one combined parameter N_{0i}/N_*, which makes it possible to compare the shape of the yield-stress peak in an intrinsic semiconductor with that in an extrinsic semiconductor.

A decrease in the dislocation density leads to a strengthening of the material, which manifests itself, in particular, in an increase in the upper yield stress. This strengthening has a somewhat peculiar nature and is not related to the retardation of dislocations by impurities at the current point in time along the stress–strain curve. Such a retardation is negligibly small at high stresses that correspond to the upper yield stress. The strengthening is caused by the sensitivity of the stress–strain curve to the initial conditions. In intrinsic semiconductor crystals, this sensitivity manifests itself in the dependence of the stress–strain curve on the initial dislocation density, which is clearly observed experimentally. In extrinsic semiconductors, the initial stage of the process at comparatively low stresses also turn out to be important; at this stage, impurities have a significant effect on the multiplication rate of dislocations.

Quantitatively, the modified upper yield stress can be calculated by substituting N_{0i} from Eq. (17) for N_{0i} into expression (7); i.e.,

$$\tau_u \approx \left\{\tau_{u0}^3 + 6\frac{\beta r c_0}{aw}\tau_s - 2\left(\frac{2\beta r c_0}{aw}\right)^{3/2}\right\}^{1/3}. \tag{18}$$

Here, τ_{u0} is the upper yield stress for an impurity-free semiconductor. The concentration dependence of the upper yield stress as predicted by formula (18) is shown in Fig. 4. By way of illustration, experimental data [9] for silicon with an oxygen impurity are shown in the inset. As can be seen from Fig. 4, the strain-rate sensitivity of the yield stress is lowered in an extrinsic semiconductor. The temperature dependence of the impurity contribution to the upper yield stress is controlled by the combination of parameters Bt_m, which appears in the expression for τ_s (10). Consequently, the final result

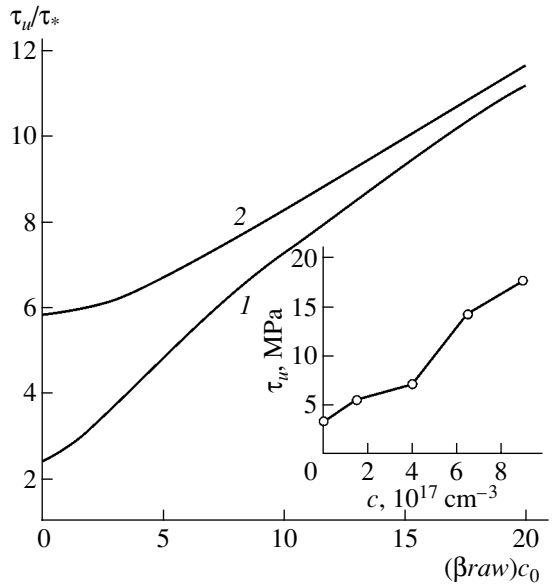

Fig. 4. Concentration dependences of the upper yield stress for two strain rates that differ by an order of magnitude: (curve *1*) $\dot{\varepsilon}_1$ and (curve *2*) $\dot{\varepsilon}_2 = 10\dot{\varepsilon}_1$. The values of the parameters used in the calculation are $\ln(N_*/N_0) = 5$, $a^2w/(t_mB) = 1$, and $\tau_* aw = 1$. For a qualitative comparison, the experimental data in [9] for silicon with an oxygen impurity ($T = 900$°C, $N_0 = 10^6$ cm^{-2}, and $\dot{\varepsilon} = 1.1 \times 10^{-4}$ s^{-1}) are shown in the inset.

depends on the difference between the activation energies for migration of impurities in the vicinity of the dislocation core and for the mobility of dislocations themselves. Therefore, in the case of mobile impurities (such as interstitial oxygen in silicon), the contribution of impurities decreases with increasing temperature and, in contrast, increases if there are low-mobility substitutional impurities.

Formula (18) is valid if $t_u > t_s$ with impurities detaching from the dislocations as the stress increases. Experimental data in [4, 7, 9] apparently indicate that this situation is realized in silicon with a relatively high oxygen concentration. In the opposite case ($t_u < t_s$), the effect of impurities on the mobility of dislocations extends to the portion of the stress–strain curve in the vicinity of the yield-stress peak. In this situation, the kinetics of multiplication of dislocations should be described by the model of complete drag of impurities (i.e., by formula (16)). As a result, the quantity τ_u is determined from the equation

$$\tau_u \approx \left\{ \tau_{u0}^3 + 6\frac{\beta r c_0}{aw}\tau_u - 2\left(\frac{2\beta r c_0}{aw}\right)^{3/2} \right\}^{1/3}. \qquad (19)$$

Since the mobility of impurities does not appear in Eq. (19), the temperature dependence of τ_u becomes less heavy as the impurity concentration increases.

5. CONCLUSION

We now summarize the main results of this study.

(i) The Alexander–Haasen model for multiplication of dislocations is generalized taking into account the effect of dynamic aging of dislocations. The combined model accounts for the experimentally observed [7–11] fact that extrinsic semiconductors are strengthened to a greater extent than intrinsic semiconductors.

(ii) An analytical expression for the dependences of the upper yield stress in a semiconductor crystal on the impurity concentration and other parameters that characterize the material properties, the impurity type, and the conditions of deformation is derived.

(iii) It is shown that dynamic aging of dislocations is accompanied by an abrupt change in the mobility of dislocations as the stress increases. This circumstance gives rise to two distinctly different stages of deformation with a significant effect of impurities on the mobility and multiplication of dislocations only at the first stage. As a result, the strengthening in the vicinity of the yield-stress peak may be caused by the effect of impurities on the initial stage of deformation, as is observed for silicon with a comparatively high concentration of oxygen. This fact may also explain the similarity of the stress–strain curves for impurity-free and extrinsic semiconductor crystals.

REFERENCES

1. K. Sumino, in *Defects and Properties of Semiconductors: Defect Engineering*, Ed. by J. Chikawa, K. Sumino, and K. Wada (KTK, Tokyo, 1987), p. 227.
2. M. G. Mil'vidskiĭ and V. B. Osvenskiĭ, *Structural Defects in Single Crystals of Semiconductors* (Metallurgiya, Moscow, 1984).
3. H. Alexander and P. Haasen, Solid State Phys. **22**, 27 (1968).
4. H. Alexander, in *Dislocations in Solids*, Ed. by F. R. N. Nabarro (North-Holland, Amsterdam, 1986), Vol. 7, Chap. 35, p. 113.
5. D. Maroudas and R. A. Brown, J. Mater. Res. **6**, 2337 (1991).
6. B. V. Petukhov, Fiz. Tekh. Poluprovodn. (St. Petersburg) **36**, 129 (2002) [Semiconductors **36**, 121 (2002)].
7. K. Sumino, H. Harada, and I. Yonenaga, Jpn. J. Appl. Phys. **19**, L49 (1980).
8. K. Sumino, I. Ionenaga, M. Imai, and T. Abe, J. Appl. Phys. **54**, 5016 (1983).
9. I. Yonenaga and K. Sumino, J. Appl. Phys. **56**, 2346 (1984).

10. J. Rabier and A. George, Rev. Phys. Appl. **22**, 1327 (1987).
11. V. Orlov, H. Richter, A. Fischer, *et al.*, Mater. Sci. Semicond. Process. **5**, 403 (2002).
12. M. Imai and K. Sumino, Philos. Mag. A **47**, 599 (1983).
13. V. I. Nikitenko, in *Dynamics of Dislocations* (Naukova Dumka, Kiev, 1975), p. 7.
14. A. George and J. Rabier, Rev. Phys. Appl. **22**, 941 (1987).
15. B. V. Petukhov, Kristallografiya **46**, 909 (2001) [Crystallogr. Rep. **46**, 835 (2001)].
16. J. R. Patel, Discuss. Faraday Soc. **38**, 201 (1964).
17. Y. Estrin and L. P. Kubin, in *Continuum Models for Materials with Micro-Structure*, Ed. by H.-B. Mulhaus (Wiley, New York, 1995), p. 395.
18. J. P. Hirth and J. Lothe, *Theory of Dislocations*, 2nd ed. (Wiley, New York, 1982; Atomizdat, Moscow, 1972).
19. B. V. Petukhov, Zh. Tekh. Fiz. **60** (10), 64 (1990) [Sov. Phys. Tech. Phys. **35**, 1150 (1990)].
20. B. V. Petukhov, Zh. Tekh. Fiz. **73**, 82 (2003) [Tech. Phys. **48**, 880 (2003)].

Translated by A. Spitsyn

Semiconductors, Vol. 38, No. 4, 2004, pp. 376–379. Translated from Fizika i Tekhnika Poluprovodnikov, Vol. 38, No. 4, 2004, pp. 391–394.

ATOMIC STRUCTURE AND NONELECTRONIC PROPERTIES OF SEMICONDUCTORS

Electric Transport in Gallium Antimonide Single Crystals Involving Molten GaSb–Sn Inclusions

A. M. Orlov*, A. A. Skvortsov, and A. A. Salanov**

Ulyanovsk State University, Ulyanovsk, 432970 Russia

**e-mail: OrlovAM@ulsu.ru*

***e-mail: scvor@sv.uven.r*

Submitted April 15, 2003; accepted for publication June 18, 2003

Abstract—Electromigration of molten tin-based inclusions in single-crystal *p*-GaSb:Zn(111) was studied. It was shown that molten inclusions are displaced by a current ($j = (1–4) \times 10^5$ A/m^2) toward a negative electrode in the temperature range $T = 750–920$ K. The mechanism of this phenomenon was shown to be related to concentration changes in the bulk of molten inclusions. It was noted that the inclusion transport is initiated by two competing processes: the temperature changes at phase interfaces caused by the Peltier heat and the electric transport, leading to the redistribution of components, depending on their effective charges in the melt. The size dependence of the velocity of inclusion motion W in the bulk of a single-crystal matrix was determined: W increases with the inclusion size. The numerical values of the thermoelectric parameters of all the contacting phases were experimentally determined using independent methods. This made it possible, fitting the theory to the experimental data, not only to estimate quantitatively the effective charge Z^* of a molten semiconductor, but also to explain the size dependence of the activation barrier overcome by a drifting inclusion. © *2004 MAIK "Nauka/Interperiodica".*

Major problems in the practical application of heavily doped single crystals are associated with second-phase inclusions, which drastically affect electric, optical, magnetic, and other properties of crystals [1–6]. This problem is especially urgent in semiconductor electronics, where the occurrence of a second phase (including a molten one) is often explained by local contact melting of metallization layers exposed to a high-density pulsed current [7–9]. Therefore, the problem of electromigration of molten inclusions in semiconductors has attracted much attention. This problem has been most thoroughly studied, both theoretically [1, 2, 6] and experimentally [5, 7, 8], using the elemental semiconductors Si and Ge as an example. Except for a few studies on gallium arsenide [2, 5], almost no such investigations were performed with compound semiconductors. Thus, we attempted to detect and analyze in detail the electric transport of second-phase tin-based inclusions in gallium antimonide single crystals.

As a starting material, we used Czochralski-grown *p*-GaSb:Zn single crystals with a resistivity of 0.138–0.073 Ω cm and majority-carrier mobility μ = 420–448 cm^2/(V s).

Bars shaped as rectangular parallelepipeds $4 \times 4 \times 15$ mm in size were cut from crystals. The growth-dislocation density N_d in samples did not exceed 4×10^3 cm^{-2}.

The main source of molten inclusions was a tin film ($m \le 0.3$ mg) electrochemically deposited [7] onto a [111] end face attached to an analogous face of another sample. Electric annealing of samples was carried out in an inert atmosphere. Samples were placed in a resistively heated quartz cell (Fig. 1) installed in the chamber of an ALA-TOO system (IMASh-20-78 type). Five-millimeter graphite inserts prevented the interaction between the samples and heat-resistant stainless steel electrodes.

Before the experiment, the chamber was pumped out to a residual pressure of 10 Pa and filled with argon at a small overpressure. The temperature was measured by a platinum–platinum-rhodium thermocouple placed in the immediate vicinity of the sample (see Fig. 1).

At temperatures above the eutectic temperature, contact melting of components occurs with the formation of a liquid film, which rapidly disperses into sepa-

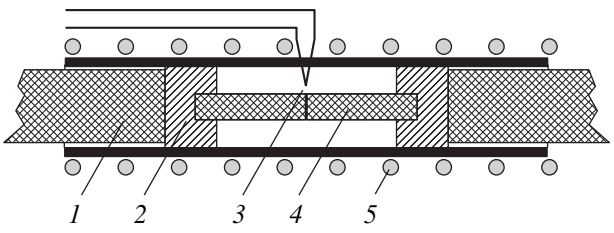

Fig. 1. Schematic representation of the electric annealing cell: (*1*) steel electrodes, (*2*) graphite inserts, (*3*) thermocouple, (*4*) sample with an electrolytically deposited metal film, and (*5*) nichrome spiral around a quartz tube.

1063-7826/04/3804-0376$26.00 © 2004 MAIK "Nauka/Interperiodica"

rate drops during electromigration.[1] Inclusions were always displaced by a current ($j = (1–4) \times 10^5$ A/m^2) toward a negative electrode; however, their velocity depended on their size l.[2]

It was ascertained that the inclusion formation from the liquid film is completed by melt penetration into the bulk of the single-crystal matrix to a depth of 2–5 μm. The small thickness of the initial film leads to its instability and dispersion into separate molten regions. This process is facilitated by deviations of the velocity vector from the orientation axis of the film and other random factors. The latter are mostly wetting and fusion defects and structural imperfections caused by dislocations and other defects, as well as distortions of the temperature and electric field configurations. In this case, the time to reach the steady state of each drop formed is determined by the relaxation time (see [1]),

$$\tau = l^2/D \approx 0.1–2.5 \text{ s},$$

where $l = 10–50$ μm and $D \approx 10^{-9}$ m^2/s is the mutual diffusivity in the melt at a total time of electric annealing of 2–4 h.

The inclusion size l and the depth of penetration into the matrix from the starting position were determined by sequential removal of N layers 5–7 μm thick followed by identification of inclusions using an MII-4 microscope. The longest size measured along the motion direction was determined by the extremum of the dependence $l = f(N)$ plotted for each drop (Fig. 2).

Figure 3 shows the typical results, which satisfy the empirical dependence

$$W/j = a + bl. \quad (1)$$

Here, W/j is the specific migration rate. The numerical values of a and b are listed in the table.

To reveal the origin of forces driving inclusions in the electric field, we will consider the equations (see [6])

$$\frac{W}{j} = -\frac{V\beta\bar{C}}{N_A}\left(\frac{\delta\rho eZ^*}{kT} + \frac{VPL}{N_A 2\lambda kT^2}l\right), \quad (2)$$

$$\frac{W}{j} = -\frac{VD\bar{C}}{N_A}\left(\frac{\rho eZ^*}{kT} + \frac{VPL}{\delta N_A 2\lambda kT^2}l\right), \quad (3)$$

which take into account the electric transport contribution (Z^* is the effective charge of the molten semiconductor) and the Peltier heat (P is the Peltier coefficient) released at the face and back sides of each inclusion during direct current flow. The following designations are used in Eqs. (2) and (3): β is the melting–crystallization rate constant; V is the specific melt volume; $\bar{C}$ and D are the equilibrium concentration and the diffusivity of semiconductor molecules in the melt,

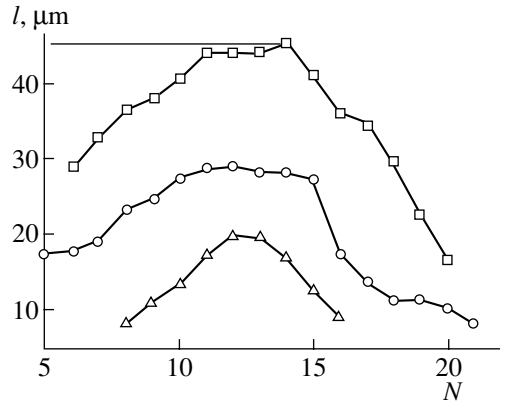

Fig. 2. Definition of the largest inclusion size l by sequential removal of N layers; the annealing temperature $T = 853$ K.

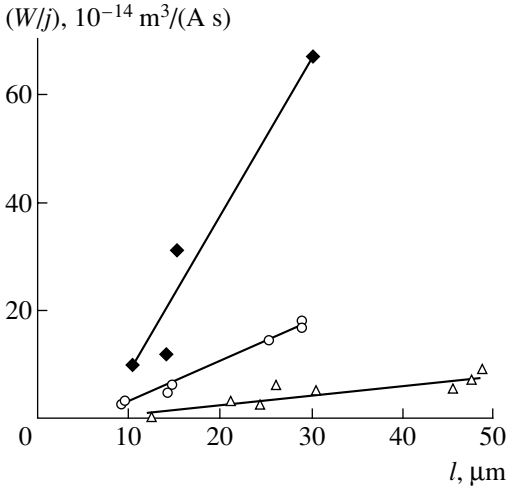

Fig. 3. Dependence of the specific migration rate of inclusions on their size for annealing temperature $T = 853$ (triangles), 873 (circles), and 913 K (diamonds).

respectively; N_A is Avogadro's number; δ is the thickness of the diffusion layer near the phase interface; ρ is the melt resistivity; e is the elementary charge; k is the Boltzmann constant; L is the heat of transition of a unit volume of the solid phase into the melt; and λ is the melt thermal conductivity, which is estimated by the Viedemann–Franz law. Equation (2) is valid when the inclusion motion is controlled by the dissolution–crystallization processes at the phase interfaces. Equation (3) holds true when transport processes in the inclusion volume become dominant. Let us consider these situations in more detail.

Relation (1) is in full agreement with the theory if the Peltier coefficient P and Z^* in Eqs. (2) and (3) are set to be negative and positive, respectively. As for the controlling stage, it can be estimated by the activation barrier E overcome by an inclusion during its motion in the single-crystal matrix, as well as from the relation

[1] The GaSb–Sn phase diagram corresponds to a degenerate eutectic [10, 11].

[2] The velocity of inclusions is assumed to be positive when they move along electric field lines.

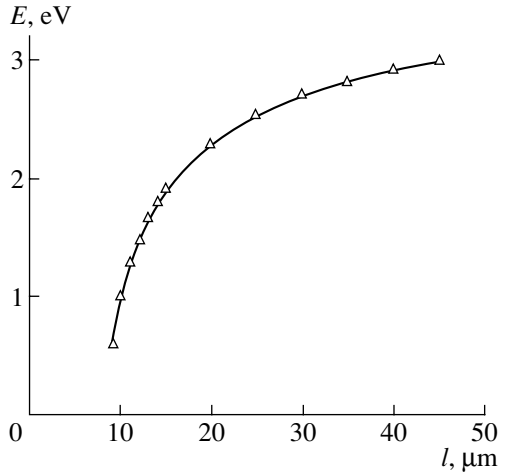

Fig. 4. Size dependence of the apparent activation energy of electric transport of molten GaSb–Sn inclusions in gallium antimonide.

between $\beta\delta$ and D [6]. We calculated E using the temperature dependences $W = f(T)$ plotted for the entire range of l. Analysis of these results (Fig. 4) suggests a mixed diffusion–kinetic control during the migration of molten inclusions. Only for large inclusions (l > 70–100 μm), almost total stabilization of the activation barrier occurs, which is controlled in this case only by the processes of melting–crystallization of active regions in the matrix contacting with inclusions. This is understandable, since with large values of l, $bl \gg a$ and $W/j \approx bl$ in Eqs. (1)–(3), which predetermines the constant activation energy E for such inclusions and the dominant role of thermoelectric phenomena in their transport.

At the same time, when $bl \ll a$, the main driving force for the melt components is diffusion electric transport; hence, $W/j \approx a$ and the activation barrier E should also be constant. The absence of a corresponding plateau in the dependence $E = f(l)$ (Fig. 4) indicates only the short range of l, although the determined values of E are typical of diffusion control (E_{dif} < 0.65 eV). All these factors suggest that most of the inclusions under consideration move in the transition diffusion–kinetic region with significantly reduced diffusion control.

Calculated and experimental data on the electromigration of GaSb–Sn melt inclusions in the bulk of a GaSb single crystal

Parameter	Dimension	Temperature T		
		853 K	873 K	913 K
X_{Sn}	at %	44	38	26
α_L, 10^{-6}	V/K	–18	–23	–8
α_S, 10^{-6}	V/K	–121	–109	–87
a, 10^{-14}	m^3/(A s)	–0.8	–4.2	–20.3
b, 10^{-8}	m^2/(A s)	0.18	0.76	2.89
V, 10^{-5}	m^3/mol	2.5	2.6	2.8
P, 10^{-3}	V	–88	–75	–72
β, 10^{-3}	m/s	0.58	2.6	8.8
Z*, 10^{-3}	–	48	49	58

Another important feature of the above results is a clear manifestation of mutually compensating contributions from the quantities P and Z^*. Indeed, the Peltier heat is released at the face side of each inclusion, while this heat is absorbed at the back side (where the crystal grows in the case of liquid epitaxy). This forces the inclusion to move to the negative electrode. However, the electric transport direction is opposite, since the melt is enriched in GaSb ($Z^* > 0$) at the cathode side and depleted with GaSb at the anode side. Therefore, very small inclusions ($l \longrightarrow 0$), in contrast to larger ones (see Fig. 3), are forced to migrate toward the positive electrode.

As for a quantitative estimation of β, P, and Z^*, it requires determination of the thermoelectric parameters of all the contacting phases. The Peltier coefficient in relations (2) and (3) can be readily estimated using the corresponding values of the Seebeck coefficients α for the solid phase (S) and melt (L),

$$P = P_S - P_L = (\alpha_S - \alpha_L)T. \quad (4)$$

We used the contact method for measuring the thermoelectric power (see [12, 13] for more details). The measurements were carried out in an inert atmosphere (Ar) with respect to the chromel (C) and/or alumel (A) parts of two thermocouples with a temperature gradient of 5–10 K between them. Recalculation to the magnitudes of α_L for the analyzed alloys was carried out taking into account the data of [14]. The alloy under study, placed into a U-shaped cell, contacted with the CA thermocouples via thin graphite caps. An additional miniature resistive heater with a bifilar winding was placed onto one of the shoulders of the U-shaped cell. The thermoelectric power of each alloy was measured in the range T = 300–1100 K. A single value of α_L fitted in composition and temperature with the inclusion parameters, taking into account the phase diagram of GaSb–Sn [11], was selected from the entire set of such data. These results (see Fig. 5) were used to estimate the numerical value of P using Eq. (4), where the value of α_S was taken from [12]. The values of P determined in such a way were used to calculate β (by the slope of straight lines $W/j \approx f(l)$) and the effective charge Z^* by the section cut in the vertical axis. These data are listed in the table.

Thus, the electrostimulated motion of molten Sn-based inclusions in p-GaSb was studied in the temperature range 750–920 K. The size dependences of the migration rate W/j were determined. The contributions of the electric transport and Peltier heat to the resulting rate of inclusion displacement by a current were estimated. It was shown that the contribution of the Peltier heat increases with the inclusion size and becomes dominant at l > 70 μm. Numerical values of the effec-

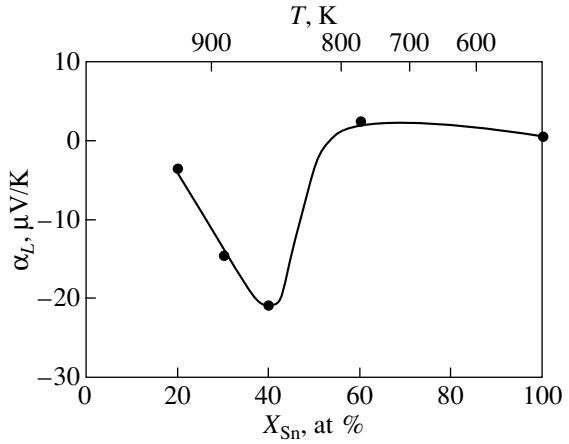

Fig. 5. Dependence of the Seebeck coefficient α_L for Sn- and GaSb-based inclusions on the temperature T of molten phases and the tin content X_{Sn} in these phases.

tive charge of a molten semiconductor and the thermoelectric parameters of the phase interface were determined. It was shown that the electric transport of inclusions in a semiconductor matrix proceeds under mixed diffusion–kinetic control.

REFERENCES

1. Ya. E. Geguzin and M. A. Krivoglaz, *Migration of Macroscopic Inclusions in Solids*, 2nd ed. (Moscow, Nauka, 1985; Consultants Bureau, New York, 1973).
2. D. K. Belashchenko, *Transport Phenomena in Liquid Metals and Semiconductors* (Atomizdat, Moscow, 1970).
3. J. P. Dekker, C. A. Volkert, E. Arzt, and P. Gumbsch, Phys. Rev. Lett. **87**, 35901 (2001).
4. A. Bonapasta, Phys. Rev. B **65**, 045308 (2002).
5. Ho Mon-Shu, Hwang Ing-Shouh, and Tsong Tien, Phys. Rev. Lett. **84**, 5792 (2000).
6. D. K. Belashchenko, A. M. Orlov, and V. I. Parkhomenko, Izv. Akad. Nauk SSSR, Neorg. Mater. **10**, 1728 (1975).
7. A. M. Orlov, A. A. Skvortsov, and B. M. Kostishko, Teplofiz. Vys. Temp. **3**, 404 (1997).
8. I. N. Larionov, N. M. Roĭzin, V. M. Nogin, and É. T. Avrasin, Fiz. Tverd. Tela (Leningrad) **9**, 1414 (1967) [Sov. Phys. Solid State **9**, 1103 (1967)].
9. A. M. Orlov, A. A. Skvortsov, and A. A. Salanov, Pis'ma Zh. Tekh. Fiz. **27** (19), 76 (2001) [Tech. Phys. Lett. **27**, 834 (2001)].
10. *Physical Chemistry*, Ed. by B. P. Nikol'skiĭ (Khimiya, Moscow, 1987).
11. E. I. Eroshinkova, A. M. Zakharov, and V. G. Olenicheva, *Phase Diagrams of Metal Systems Published in 1982–1983* (Metallurgiya, Moscow, 1985).
12. V. M. Glazov, S. N. Chizhevskaya, and N. N. Glagoleva, *Liquid Semiconductors* (Nauka, Moscow, 1967; Plenum, New York, 1969).
13. V. M. Glazov, M. Wobst, and V. I. Timoshenko, *Methods of Investigation of the Properties of Liquid Metals and Semiconductors* (Metallurgiya, Moscow, 1989).
14. R. R. Heikes, *Ure Termoelectrodity* (Interscience, New York, 1961).

Translated by A. Kazantsev

Semiconductors, Vol. 38, No. 4, 2004, pp. 380–386. Translated from Fizika i Tekhnika Poluprovodnikov, Vol. 38, No. 4, 2004, pp. 395–400.

ELECTRONIC AND OPTICAL PROPERTIES OF SEMICONDUCTORS

Microwave Photoconductivity and Photodielectric Effect in Thin PbS Films Obtained from Thiocarbamide Coordination Compounds

N. L. Sermakasheva*, G. F. Novikov*^, Yu. M. Shul'ga*, and V. N. Semenov**

**Institute of Problems of Chemical Physics (Chernogolovka Branch), Russian Academy of Sciences, Chernogolovka, Moscow oblast, 142432 Russia*

^e-mail: novikov@icp.ac.ru

***Voronezh State University, Universitetskaya pl. 1, Voronezh, 394893 Russia*

Submitted August 14, 2003; accepted for publication September 9, 2003

Abstract—The dependences of photoresponse parameters of the microwave absorption caused by the effect of a short pulse of a nitrogen laser (337 nm, 10 ns) in micrometer-thick PbS films on the frequency of a microwave oscillator, intensity of light, and conditions of the film growth are investigated by a cavity method in the 3-cm frequency band. The films were obtained by pyrolysis of aerosol of thiocarbamide coordination compounds at a substrate temperature of 250–500°C. Using the analysis of frequency dependences of the photoresponse, the microwave photoconductivity and the photodielectric effect, which cause a variation in the cavity quality factor and a variation in its resonance frequency, respectively, are investigated separately. © *2004 MAIK "Nauka/Interperiodica".*

1. INTRODUCTION

Lead sulfide is a narrow-gap (E_g = 0.41 eV) optical-sensitive material with a large static permittivity and a high mobility of electrons and holes and is widely used in photoresistors and infrared sensors. Based on PbS, unique multichannel photodetectors for space detection systems were developed [1]. Most of the new photodetectors are fabricated from polycrystalline layers and heterostructures; therefore, the investigation of electron-ion processes in thin films is of great interest.

The wide application of polycrystalline semiconductors in microelectronics was severely restricted for a long time by the existence of numerous defects in them, mainly grain boundaries and dislocations. These defects considerably reduce the majority-carrier mobility and the minority-carrier lifetime. By varying the grain size and orientation and using controlled doping, it is possible to attain a substantial variation in properties of these materials. As was noted, the polycrystallinity became a hope for future achievements, rather than a problem [2]. However, without understanding which elementary processes with the involvement of electrons, ions, and holes proceed at which centers, it is difficult to have hopes of obtaining materials with specified properties.

In this paper, we report the results of studying thin PbS films by a contactless method of microwave photoconductivity. As it originated as a steady-state method [3] and then developed into the present two-pulse method [4], this technique occupies a special place among the methods for studying elementary reactions with the participation of charged particles in polycrystalline or microdisperse systems. Its advantage is related to the small drift shift of charges in the microwave fields applied [5], which allows one to substantially reduce the effect of intercrystallite barriers and contact phenomena on the results of the investigation.

2. EXPERIMENTAL

2.1. Synthesis of PbS Films

The PbS films were obtained by the method of sputtering a water solution of the thiocarbamide coordination compound $[Pb((NH_2)_2CS)_2Cl_2]$ with deposition on a heated substrate [6]. The substrate temperature (T) was varied from 250 to 500°C. To prepare the complexes, $PbCl_2 \cdot 2.5H_2O$ of ultrahigh purity grade and $(NH_2)_2CS$ were used. The film was deposited onto a smooth surface of Pyroceram in several stages, since the film grows very rapidly and is easily etched off by the initial solution. The higher T, the more rapidly the film grows and is etched off and the more difficult it is to obtain a continuous film. In the film obtained, the chlorine impurity ($Cl_S^{\times}$) is contained; as T increases, the amount of chlorine impurity decreases. This method allows one to change the impurity composition gradually and to control the defect structure. According to the published data [6], the PbS films obtained under such conditions have *n*-type conductivity.

1063-7826/04/3804-0380$26.00 © 2004 MAIK "Nauka/Interperiodica"

2.2. X-Ray Powder Diffraction Analysis

The X-ray powder diffraction patterns were recorded using a DRON ADP-1 diffractometer (CuK_α radiation, Ni filter).

2.3. Method of Microwave Photoconductivity

The method is based on recording the variation in the power of the electromagnetic wave (3-cm band) reflected from the cavity with the sample. The variation is caused by the effect of the pulse of light on the sample. The method is described in detail in [7]. A TE_{101} rectangular reflection cavity (volume $V \approx 5.1$ cm^3) was used. The quality factor of the loaded cavity $Q_L \approx 10^3$. The sample in a quartz cell was placed into the antinode of the electric field. An LGI-505 laser with the wavelength $\lambda = 337$ nm and a pulse width of 8–10 ns was used for the illumination. The area of the sample subjected to the laser irradiation was ~0.06 cm^2. The time resolution of the setup was 50 ns.

If the variations in Q_L due to the photoconductivity (Q_σ) are relatively small and the resonance frequency f_0 is invariable, the relative variation in the reflected power, which is determined by the effect of light, is given by

$$\frac{\Delta P_Q}{P_0} \approx R\frac{1}{Q_\sigma}. \quad (1)$$

Here, P_0 is the incident power and R is the proportionality factor, which is determined only by the properties of the cavity for the samples of a small volume relative to V, and

$$Q_\sigma^{-1} \propto \sigma = en\mu_d,$$

where e is the elementary charge, and n and μ_d are the concentration and the drift mobility of the charge carriers generated.

However, in general, due to the variations in the complex sample permittivity $\varepsilon^* = \varepsilon' - i\varepsilon''$, the photoresponse under the effect of light may consist of two components, $\Delta P = \Delta P_f + \Delta P_Q$. They are determined by the variation in the cavity quality factor (ΔP_Q) and in the resonance frequency (ΔP_f), respectively. The ΔP_Q magnitude is determined mainly by the variation in the imaginary part of permittivity $\Delta\varepsilon''$. Both components ε' and ε'' can contribute to the shift of the resonance frequency Δf_0 [8, 9]:

$$-\frac{\Delta f_0}{f_0} \propto \Delta\varepsilon' + \frac{(\Delta\varepsilon'')^2}{\varepsilon' + 2}. \quad (2)$$

2.4. Method for Separating the Contributions of Variations in the Quality Factor and Resonance Frequency in the Microwave Photoresponse

To separate ΔP_Q and ΔP_f and to determine Δf_0, the frequency dependence of the photoresponse ΔP_f was analyzed in the vicinity of the resonance frequency at $f \approx f_0$. The resonance curves for the tuned microwave path not too far from the resonance frequency are described by the Lorentz function. The resonance curve for the unilluminated sample (in the dark) is

$$y_1(f) = 1 - \frac{A'}{1 + 4[(f - f_0)/\delta f'_{1/2}]^2}; \quad (3)$$

for the illuminated sample this curve is

$$y_2(f) = 1 - \frac{A''}{1 + 4[(f - f_0 - \Delta f_0)/\delta f''_{1/2}]^2}, \quad (4)$$

where y_1 and y_2 are the dimensionless quantities normalized to the incident microwave power; A' and A'' are the dimensionless amplitudes of resonance curves for the cavity with the unilluminated and the illuminated sample, respectively; and $\delta f'_{1/2}$ and $\delta f''_{1/2}$ are the half-widths of the resonance curves. The microwave response is proportional to the difference between expression (4) and (3):

$$\Delta P(f) \propto y_2 - y_1. \quad (5)$$

The amplitudes, the shift of the resonance curve, and the half-width of the resonance curve under illumination $\delta f''_{1/2}$ were determined by varying these quantities as the parameters in the sum of squared deviations of theoretical curve (5) from the experimental values. Matching was carried out by two methods. In the first method, which was described previously in [7], all the parameters in function (5) were simultaneously varied directly. In the second method, the parameters were initially varied and resonance curve (3) for the unilluminated sample was matched; then the other parameters of function (5) were varied. The results were similar.

The contribution of the microwave conductivity to the photoresponse at $f \approx f_0$ was defined as $\Delta P_Q \propto A'' - A'$, and the photodielectric response ΔP_f was defined as the difference $\Delta P - \Delta P_Q$.

3. RESULTS AND DISCUSSION

3.1. Results of the X-Ray Powder Diffraction Analysis

The X-ray diffraction patterns of the Pyroceram substrate and one of the samples investigated are shown in Fig. 1. The interplanar spacings, which were calculated from the positions of diffraction peaks, were analyzed. The analysis showed that the main crystalline phase of the samples under investigation is the face-centered cubic (fcc) PbS phase (the coincidence of ten peaks in the angle range 2θ measured).

The size of the PbS crystallites in the direction normal to the [220] plane was estimated from the formula $D_{220} = \lambda/\beta\cos\theta$, where λ is the wavelength of the X-ray radiation and β is the half-width of the diffraction peak (220). This size initially increases and then decreases as T increases (table), attaining a maximum at T =

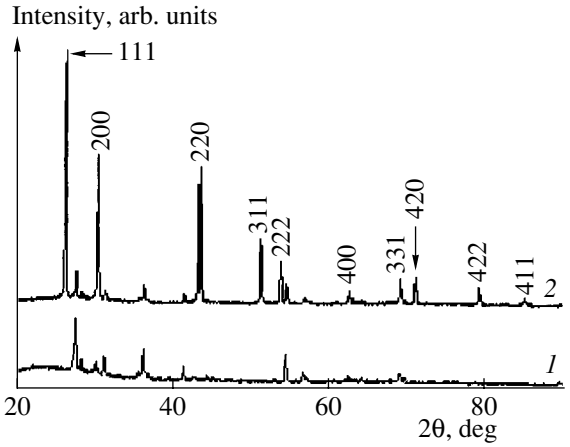

Fig. 1. X-ray powder diffraction patterns of (*1*) the substrate and (*2*) the PbS film grown at $T = 300$°C.

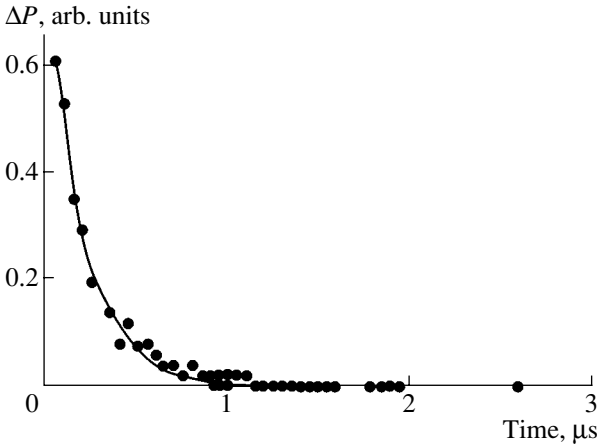

Fig. 2. Photoresponse of the Cl-doped PbS film grown at $T = 350$°C.

350°C. To estimate the size, the diffraction peak (220) was chosen, since it is observed against a uniform background and does not overlap with other peaks. The fcc lattice constant decreased steadily to $T = 450$°C (table) and then increased at $T = 500$°C to the value observed at $T = 300$°C. For all T, the fcc lattice constant was noticeably less than that for pure PbS, which was equal to $a = 5.9362$ Å [10].

A decrease in the unit-cell parameter can be determined by the partial substitution of S atoms by atoms of Cl, O, or another element with a smaller atomic radius. However, it is most likely that the decrease in interplanar spacings observed is caused by vacancies in the S sublattice.

From measurements of intensity attenuation of diffraction peaks for the substrate, the film thickness d is estimated (table). For the estimate, we used the known mass attenuation factors of the radiation for elements (see [11]). In making the estimate, we also assumed that the attenuation factor for the film material is the same as for pure PbS. It can be seen from the table that, as T increases, the film thickness decreases for all samples, excluding the film obtained at 250°C, which falls out of this series.

Constant of the fcc lattice a, average size D_{220} of the PbS particles, and film thickness d

Synthesis temperature T, °C	a, Å	D_{220}, Å	d, μm
250	5.932	413	6.3–6.9
300	5.928	430	12.0–12.5
350	5.924	445	7.8–8.4
400	5.920	394	2.9–3.5
450	5.916	395	3.3–4.0
500	5.928	384	2.6–3.1

3.2. Two Components of the Photoresponse

In general, the photoresponse parameters for all the samples depended heavily on the temperature of the film growth. The experimental curves of photoresponse decays at the resonance frequency after completing the pulse of the laser radiation were described by the exponential function, the hyperbolic function, or the sum of two functions (two exponential ones or a hyperbolic and an exponential one). Hyperbolic components noticeably manifested themselves only for high intensities of light, which corresponded to the photon flux in the pulse $I > 10^{14}$ photon/cm^2.

For example, Fig. 2 shows the photoresponse at the resonance frequency for the PbS film grown at $T = 350$°C. It can be seen from Fig. 2 that the kinetics of the photoresponse decay is described well by a single exponential function with a characteristic decay time of ~200 ns. For the films grown at higher substrate temperatures, the photoresponse is characterized by two exponential components. These are the fast component with the characteristic times $\tau_1 \approx 100$–800 ns and the slow component with the characteristic times $\tau_2 \approx 3$–16 μs:

$$\Delta P(t) \propto A_1 \exp\{-t/\tau_1\} + A_2 \exp\{-t/\tau_2\}. \qquad (6)$$

Here, A_1 and A_2 are the amplitudes of components, and t is the time reckoned from the end of the laser pulse.

The shape of the frequency dependence of the photoresponse was also different for samples grown at different T. Figure 3 shows the frequency dependences of the photoresponse at the point in time $t = 50$ ns for several samples. For the films grown at $T < 350$°C (Fig. 3a), the shape of the frequency dependence relative to the resonance frequency is asymmetric. The photoresponse at the resonance frequency is very small. As T increases to 450°C, the shape of the frequency dependence becomes increasingly symmetric (Fig. 3b). For the temperature of the film growth $T = 500$°C (Fig. 3c),

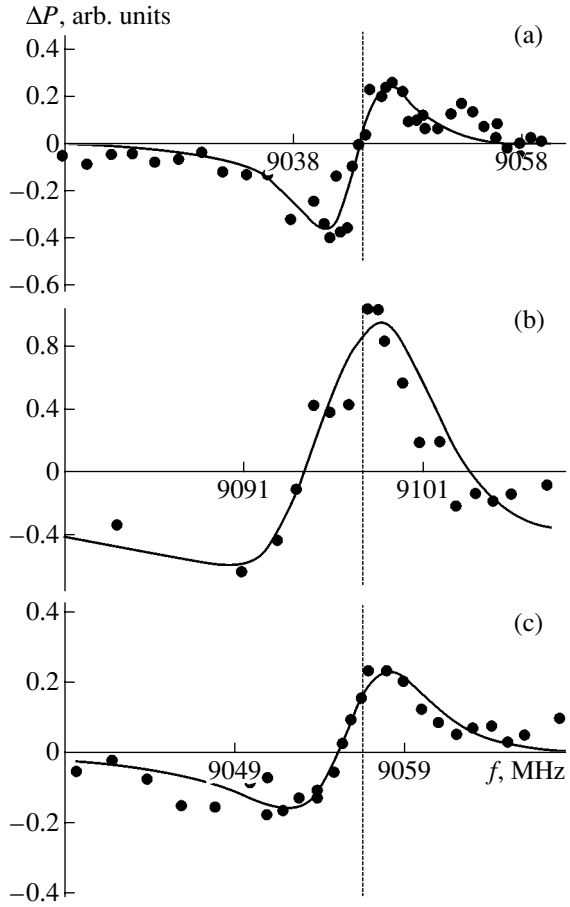

Fig. 3. Frequency dependences of the photoresponse for the films grown at temperatures of (a) 250, (b) 450, and (c) 500°C. $I = 3.1 \times 10^{13}$ cm^{-2} (per pulse). The resonance frequency is shown by the dotted line.

the frequency dependence of the photoresponse becomes asymmetric again.

Figure 4 shows the growth-temperature dependence of characteristic parameters of the photoresponse, which are determined at a resonance frequency with the approximation of decay curves by formula (6). The data for the sample grown at $T = 250$°C are given for the frequency corresponding to the photoresponse peak (at the resonance frequency, the amplitude is equal to zero). Two characteristic temperature ranges are observed, namely, 250–300°C and 350–500°C. At low temperatures of the film growth ($T < 350$°C), τ_1 remains virtually constant. At $T > 300$°C, A_1 starts to increase sharply; τ_1 also increases steadily. Further, A_1 increases by approximately an order of magnitude at $T = 350$–450°C.

It is difficult to relate the decrease in the amplitude of the fast component A_1 for the PbS film grown at $T = 500$°C (Fig. 4) with the decrease in the film thickness. The reason is that its thickness is only 10% less than that of the film grown at $T = 400$–450°C (see table). It is more probable that the nature of the photoresponse changes for the films grown at $T > 450$°C. Indeed,

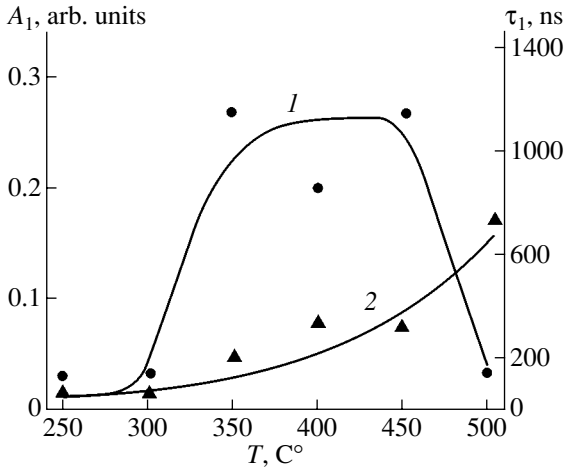

Fig. 4. Growth-temperature dependence of (*1*) amplitude and (*2*) characteristic decay time of the fast component for Cl-doped PbS. $I = 1.3 \times 10^{13}$ photon/cm^2 (per pulse).

despite the low reproducibility of the data for the films grown at $T = 500$°C, it can be seen that the average value of τ_1 increases steadily to limiting temperatures. However, the frequency dependence becomes asymmetric (Fig. 3). The asymmetry of the frequency dependence may serve as the cause of the apparent drop in the photoresponse amplitude at the resonance frequency.

As noted above, the analysis of special features of the variation in the shape of the frequency dependences of the photoresponse with time allows us to separate the contributions ΔP_Q and ΔP_f for all times after completion of the laser pulse. Thus, we can obtain the time dependences of the microwave photoconductivity and photodielectric effect. In addition, the magnitude and sign of Δf_0 in formula (2) depend on both parts of the complex permittivity (real and imaginary). Therefore, based on frequency dependences of the photoresponse, we can clarify the state of charge carriers responsible for the photoresponse.

The results of separation of contributions of the microwave photoconductivity and the photodielectric effect based on the frequency dependences of Fig. 3 for $T = 450$ and 500°C are shown in Figs. 5 and 6. It can be seen that, in the first case, the above quantities decrease with the same rate. This fact in accordance with relationship (2) indicates that the first term on the right-hand side of relationship (2), i.e., the variation in the real part of permittivity, is responsible for the negative shift of the resonance frequency. Hence, one may conclude that, for the films obtained at $T = 450$°C, the charge carriers in the band and at shallow traps are in equilibrium for $t > 50$ ns. A similar situation is apparently characteristic of all films grown at $T \le 450$°C.

The special features of the decay curves for microwave photoconductivity and of the photodielectric effect for the film grown at 500°C (Fig. 6) for $t > 800$ ns are similar. It seems likely that, starting from this point

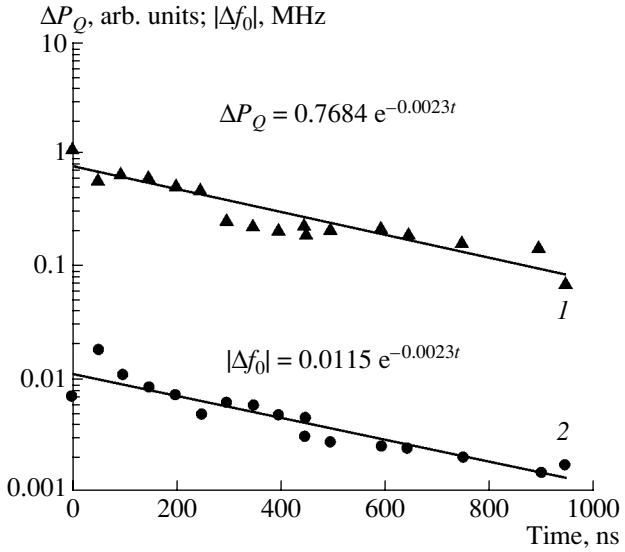

Fig. 5. Kinetics of decay of (*1*) P_Q and (*2*) $|\Delta f_0|$ for the PbS film grown at $T = 450$°C. $I = 3.1 \times 10^{13}$ photon/cm^2 (per pulse).

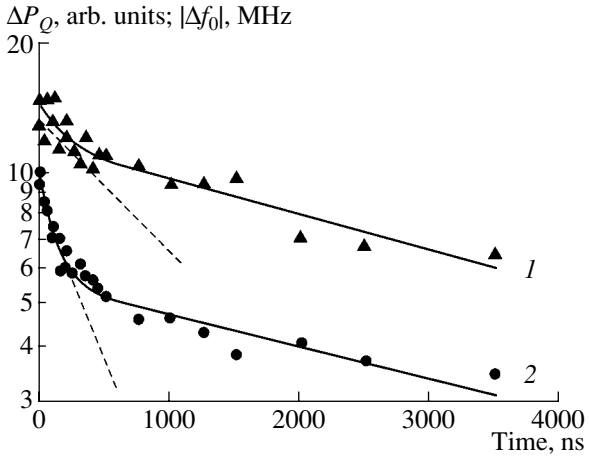

Fig. 6. Kinetics of decay of (*1*) ΔP_Q and (*2*) $|\Delta f_0|$ for the PbS film grown at $T = 500$°C. $I = 3.1 \times 10^{13}$ photon/cm^2 (per pulse).

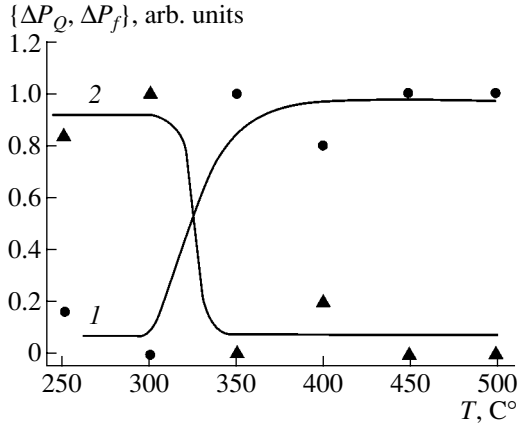

Fig. 7. Relative contributions of (*1*) ΔP_Q and (*2*) ΔP_f to the photoresponse in relation to the temperature of growth of the PbS films. $I = 3 \times 10^{13}$ photon/cm^2.

in time, similarly to the films grown at a lower temperature, the equilibrium between the charge carriers in the band and the shallow acceptors is established. However, for $t < 800$ ns, the decay rate of the shift of the resonance frequency of the cavity is higher by a factor of approximately 2 than the decay rate of variation of the quality factor.

One can suggest two causes for such a difference in rates. The first cause is the additional contribution of charge carriers of the other sign to the photoresponse. Deri and Spoonhower discussed such a situation for the microwave photoconductivity of a wide-gap silver bromide semiconductor [8]. However, this point of view did not find convincing support. The second cause, which is more probable, is the contribution of free charge carriers that were never captured by traps. In the latter case, according to relationship (2), the second term on the right-hand side of the relationship, i.e., the variation in the negative part of the permittivity, is responsible for the negative shift of the resonance frequency.

Figure 7 shows the contributions ΔP_Q and ΔP_f at the initial point in time after the laser radiation pulse for films grown at different temperatures. These contributions were calculated based on data similar to those shown in Fig. 4. To make allowance for the spread of the quality factor for a cavity with different unilluminated samples, the curves are normalized to the total amplitude of the photoresponse ΔP. It can be seen that, at temperatures below 350°C and above 350°C, the photodielectric effect ΔP_f and photoconductivity ΔP_Q make the main contribution to the absorption of the cavity, respectively.

3.3. The Nature of Charge Carriers Responsible for the Photoresponse

Usually, the observation of the effect of the positive or the negative impurity charge on the kinetics of decay of the photoresponse is considered as a reliable method for determining the sign of free charge carriers in measurements of the microwave absorption caused by the effect of light on wide-gap semiconductors. However, for narrow-gap semiconductors, specifically, for PbS, the interpretation of such data is problematic, and work in this area has not yet been completed. However, it is reasonable to assume that electrons will mainly contribute to microwave absorption under illumination in *n*-PbS.

If we accept this assumption, we can consider the dependence of the relation between contributions of free and localized electrons to the photoresponse of the

microwave absorption on the temperature of film growth. According to [8], the electrons localized at shallow traps should cause the largest negative frequency shift. Therefore, the asymmetric frequency dependence of the amplitude of the photoresponse (Fig. 3a) with respect to the resonance frequency (at $\Delta f_0 < 0$) is indicative of the negligibly small contribution of the free carriers. As T increases to 450°C, the shape of the frequency dependence becomes increasingly symmetric (the absolute value of Δf_0 decreases), which may be associated with an increase in the contribution of free electrons. At T = 500°C (Fig. 3c), the frequency dependence of the photoresponse becomes asymmetric again, which is indicative of a new variation in the relation between contributions of free and trapped electrons.

The above inferences are consistent with the decay kinetics for variations in the quality factor and frequency, if we assume that mainly free electrons contribute to the microwave photoconductivity due to variations in ε". At the same time, the electrons captured by traps mainly contribute to the photodielectric effect due to variations in ε'. The correlation between variations in the shift of the frequency and a quality factor at $t >$ 800 ns (Fig. 6) is probably indicative of the equilibrium established between electrons in the conduction band and electrons at the traps by this point in time.

The decay kinetics for ΔP_Q (Fig. 5, curve *1*) and $|\Delta f_0|$ (Fig. 5, curve *2*) for PbS grown at T = 450°C noticeably differs from the data of Fig. 6. The fast components are absent here, and the variations in both quantities are correlated, as in the previous case, at times $t >$ 800 ns. It is probable that the electrons released a second time from the traps mainly contribute to the microwave conductivity in this case. Thus, the decay rate of the photoresponse is determined by the competition of two processes, namely, the thermal release of localized electrons from traps and electron recombination at the traps with interstitial ions. At T = 500°C, the free electrons that are never captured by the traps mainly contribute to the cavity absorption at times $t <$ 800 ns. The detailed nature of the traps is not clear, especially given the fact that PbS is a narrow-gap semiconductor. However, we can still consider the effect of synthesis conditions on the film properties.

3.4. Effect of Synthesis Conditions on the Electronic–Ionic Processes

First, note that the characteristic time of decay of the fast component of the photoresponse gradually increases in general over the entire temperature range of the film growth (Fig. 4). This fact indicates that the annihilation rate of carriers gradually decreases. In principle, this behavior can be due to a decrease either in the trap concentration or in the defect concentration (interstitial ions).

However, the data shown in Figs. 4 and 7 and those listed in the table are indicative of finer specific features. Specifically, one can see that substantial variations in the properties of the synthesized PbS films are observed in the temperature range T_{cr} = 300–350°C. Indeed, in the region $T = T_{cr}$, the amplitude of the fast component of the photoresponse increases by an order of magnitude (Fig. 4, curve *1*), and the grain size increases (table). Taking into account that defects of the type of interstitial Pb ions (Pb_i) effectively reduce the grain size, we should assume that the concentration of defects of the Pb_i type decreases drastically as the substrate temperature is increased to T_{cr}.

In the region $T > T_{cr}$, the variations in the cavity quality factor, i.e., Δε", mainly contribute to the photoresponse. This circumstance is clearly indicative of an increase in the contribution of free charge carriers to the photoresponse. However, the character of the photoresponse in this region varies more gradually. The amplitude of the fast component of the photoresponse is virtually constant, although the decay time continues to increase. It is probable that no radical variations in the defect density occur in this region. Most likely, qualitative variations in defect types occur in this region. For example, taking into account the model of the thiocarbamide complex [12], we may assume that defects of the Cl_S type are formed in films obtained by the pyrolysis method. As the substrate temperature increases, Cl atoms evaporate, defects of the V_S type remain in the film, and the concentration of vacancy defects increases with the temperature. It seems likely that, with a further increase in temperature, the vacancies V_S are filled with oxygen, and the O_S defects are formed. These defects are not active traps for electrons.

ACKNOWLEDGMENTS

We thank Yu.V. Meteleva for her help in synthesizing the PbS films.

This study was supported by the Russian Foundation for Basic Research, project nos. 03-03-32202 and 02-03-32322.

REFERENCES

1. V. G. Butkevich, E. R. Globus, G. A. Kazantsev, Yu. P. Butrov, and L. Ya. Lebedeva, *Photodetectors on the Basis of Lead Chalcogenides in GUP NPO Orion and Perspectives of Development*, http://www.vimi.ru/appl-phys/appl-99/99-2/99-2-16r.htm.
2. S. Pizzini, N. Butta, M. Acciary, and M. Acciarri, Springer Proc. Phys. **54**, 178 (1991).
3. V. G. Erofeichev and L. I. Kurbatov, Fiz. Tverd. Tela (Leningrad) **1**, 133 (1959) [Sov. Phys. Solid State **1**, 119 (1959)].

4. G. F. Novikov, B. I. Golovanov, A. V. Chukalin, and N. A. Tikhonina, Zh. Nauchn. Prikl. Fotogr. **42** (4), 1 (1997).
5. R. J. Deri and J. P. Spoonhower, Photograph. Sci. Eng. **28** (3), 92 (1984).
6. Ya. A. Ugaĭ, O. B. Yatsenko, V. N. Semenov, and E. M. Averbakh, Izv. Akad. Nauk SSSR, Neorg. Mater. **9**, 2055 (1973).
7. G. F. Novikov, S. G. Nemanov, and M. V. Alfimov, Opt. Spektrosk. **75**, 1244 (1993) [Opt. Spectrosc. **75**, 733 (1993)].
8. R. J. Deri and J. P. Spoonhower, Phys. Rev. B **25**, 2821 (1982).
9. Yu. V. Meteleva, A. V. Naumov, N. L. Sermakasheva, *et al.*, Khim. Fiz. **20** (9), 39 (2001).
10. *Powder Diffraction File* (JCPDS International Centre for Diffraction Data, Swarthmore, Pa., 1989), No. 5-592.
11. Ya. S. Umanskiĭ, Yu. A. Skakov, A. N. Ivanov, and L. N. Rastorguev, *Crystallography, X-Ray Diffraction, and Electron Microscopy* (Metallurgiya, Moscow, 1982), p. 632.
12. V. N. Semenov, Doctoral Dissertation (Voronezh, 2002).

Translated by N. Korovin

Semiconductors, Vol. 38, No. 4, 2004, pp. 387–392. Translated from Fizika i Tekhnika Poluprovodnikov, Vol. 38, No. 4, 2004, pp. 401–406.

ELECTRONIC AND OPTICAL PROPERTIES OF SEMICONDUCTORS

Capacitance Study of Electron Traps in Low-Temperature-Grown GaAs

P. N. Brunkov*, A. A. Gutkin*, A. K. Moiseenko*, Yu. G. Musikhin*, V. V. Chaldyshev*, N. N. Cherkashin*, S. G. Konnikov*, V. V. Preobrazhenskiĭ, M. A. Putyato**, and B. R. Semyagin****

**Ioffe Physicotechnical Institute, Russian Academy of Sciences, St. Petersburg, 194021 Russia*

***Institute of Semiconductor Physics, Siberian Division, Russian Academy of Sciences, Novosibirsk, 630090 Russia*

Submitted September 8, 2003; accepted for publication September 10, 2003

Abstract—Electron traps in GaAs grown by MBE at temperatures of 200–300°C (LT-GaAs) were studied. Capacitance deep level transient spectroscopy (DLTS) was used to study the Schottky barrier on *n*-GaAs, whose space-charge region contained a built-in LT-GaAs layer ~0.1 μm thick. The size of arsenic clusters formed in LT-GaAs on annealing at 580°C depended on the growth temperature. Two new types of electron traps were found in LT-GaAs layers grown at 200°C and containing As clusters 6–8 nm in diameter. The activation energy of thermal electron emission from these traps was 0.47 and 0.59 eV, and their concentration was ~10^{17} cm^{-3}, which is comparable with the concentration of As clusters determined by transmission electron microscopy. In LT-GaAs samples that were grown at 300°C and contained no arsenic clusters, the activation energy of traps was 0.61 eV. The interrelation between these electron levels and the system of As clusters and point defects in LT-GaAs is discussed. © *2004 MAIK "Nauka/Interperiodica".*

1. INTRODUCTION

A specific feature of GaAs grown by MBE at 200–300°C temperature (LT-GaAs) is a strong deviation from the stoichiometry [enrichment with As (up to 1.5 at %)], which results in a high concentration of intrinsic point defects, such as interstitial atoms As_i and the antisite defect As_{Ga} [1]. The postgrowth annealing of epitaxial LT-GaAs layers at temperatures $T > 500$°C results in the formation of nanoscale As clusters [2, 3]. In this case, the epitaxial layer is characterized by high resistivity [4], and the lifetime of carriers in it can be extremely small, less than 1 ps [5–7]. It is believed that these properties, which are the basis for the application of LT-GaAs in various devices, are related to the formation of nanoscale As clusters and/or deep-level defects in the matrix of the material. At the same time, the parameters and properties of the electron traps that define the Fermi level position and fast recombination of carriers, as well as the factors governing their behavior, are either scantily known or completely unknown [4, 8–10]. A high-sensitivity method of capacitance deep level transient spectroscopy (DLTS) in structures with a potential barrier [11] is widely used in the studies of carrier traps in semiconductor materials. However, problems in the application of this method arise when the barrier is formed directly on a thick LT-GaAs layer, because of the high resistivity of the material. To obviate this difficulty, the authors of [4, 10] used a structure in which a thin LT-GaAs layer was confined between the layers of low-resistivity GaAs grown at 620°C and was located within the space-charge region (SCR) of the barrier formed on the surface of this structure. In these studies, the maximum thickness of the LT-GaAs layers was 26 nm. They were grown at 250°C and annealed at 620°C, which might be insufficient to ensure the concentration of the excess As necessary for the formation of clusters, because of As diffusion into the neighboring GaAs layers [12].

We report the results of a study of electron traps in LT-GaAs layers that was performed by capacitance DLTS in the Schottky barrier based on low-resistivity *n*-GaAs containing a 0.1-μm-thick LT-GaAs layer. This thickness of the LT-GaAs layer is sufficient for the formation of As clusters several nanometers in size during annealing [13, 14]. To reveal the role of clusters in the formation of electron traps, a comparative study of structures that differ only in the amount of excess As in the LT-GaAs layers was carried out.

2. EXPERIMENTAL

The samples for study were grown by MBE in a two-chamber Katun' machine on (100) n^+-GaAs substrates doped with Si to 2×10^{18} cm^{-3}. The structures comprised three layers: a ~0.5-μm-thick *n*-GaAs layer (the temperature of epitaxy T_s = 580°C), a ~0.1-μm-thick LT-GaAs layer, and a second ~0.5-μm-thick *n*-GaAs layer (T_s = 580°C). The epitaxial layers of the structures were uniformly doped with Si to a concentration of ~2×10^{16} cm^{-3}. Two types of samples were grown, with the LT-GaAs growth temperatures T_s = 200 and 300°C, referred to below as LT200 and LT300,

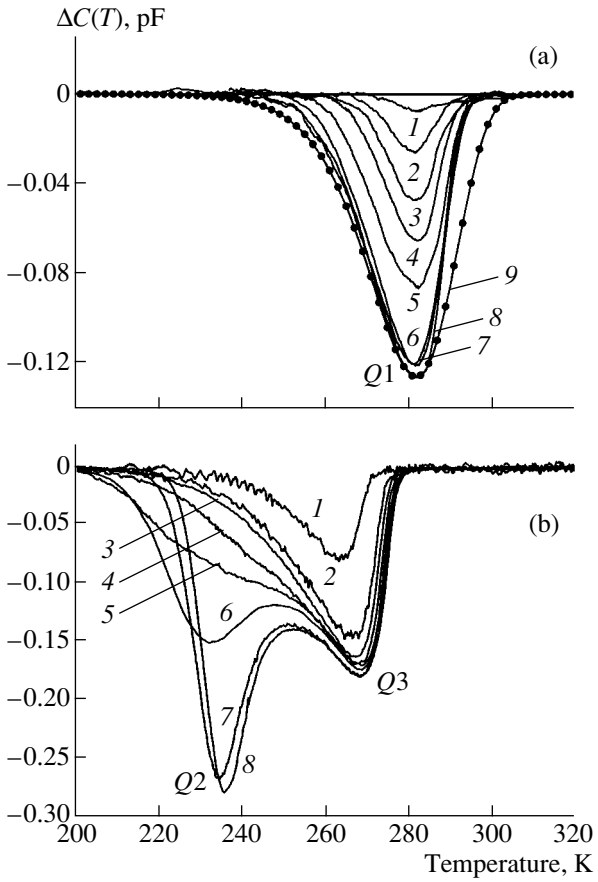

Fig. 1. DLTS spectra of samples (a) LT300 and (b) LT200. The emission rate window of the double-strobe integrator was 6.8 s^{-1} (t_1 = 133.8 ms, t_2 = 160.6 ms). (a) V_b = –9 V; V_p: (*1*) 1.0, (*2*) 2.0, (*3*) 3.0, (*4*) 4.0, (*5*) 6.0, (*6*) 7.0, (*7*) 8.0, (*8*) 9.0 V, and (*9*) simulated DLTS spectrum for *Q*1 trap in sample LT300. (b) V_b = –10 V; V_p: (*1*) 2.0, (*2*) 4.0, (*3*) 5.0, (*4*) 6.0, (*5*) 6.25, (*6*) 6.75, (*7*) 8.0, and (*8*) 10.0 V.

respectively. Growing the upper layers at high temperature for 0.5 h caused the precipitation of the excess As and the formation of a system of nanoscale As clusters in the LT-GaAs layer. A cross-sectional transmission electron microscopy (TEM) study of the samples showed that As clusters of ~6–8 nm in size, with a concentration of ~10^{17} cm^{-3}, were formed in LT200 structures [13, 14]. Arsenic clusters were not found in LT300 structures. This may be due to the fact that in this case the size of clusters was smaller than the resolution (3 nm) of the TEM apparatus.

The Schottky barriers were formed by sputtering Au onto the surface of samples through the openings in the mask, which were 0.35 mm in diameter. Ohmic contacts on the n^+ substrate were produced by firing-in an AuGe alloy at 400°C.

The DLTS spectra $\Delta C(T)$ were recorded using a computerized system with a Boonton-72B capacitance bridge operating at a frequency of 1 MHz, with an amplitude of the probing signal of 150 mV. The ratio of the sampling times t_2 and t_1 in the two-strobe integrator was chosen as 1.2 in order to improve energy resolution while retaining sufficient sensitivity.

In the DLTS study of the structures described above, it must be kept in mind that the negative charge of electrons captured by the LT-GaAs layer after the filling pulse is so large that the boundary of the SCR can be shifted into the heavily doped substrate on which the structure is grown. We therefore performed the DLTS measurements only at minimum possible bias voltages, which provided the recharging of traps in the LT-GaAs layer. In addition, methods based on the analysis of the isothermal relaxation of the capacitance, $C(t)$, were used.

3. EXPERIMENTAL RESULTS

One type of electron trap, *Q*1, was found in the spectra of samples LT300 (Fig. 1a). At fixed bias V_b = –9 V, the height of the *Q*1 peak remained virtually unchanged when the amplitude of the filling pulse, V_p, decreased from 9 to 7 V. A further decrease in V_p resulted in a fast decrease in the height of the *Q*1 peak (Fig. 1a). A comparison of the dependences of the *Q*1 peak amplitude and the capacitance at the end of the filling pulse on the filling bias demonstrated that an abrupt decrease in the *Q*1 peak amplitude starts at the moment when the boundary of the layer in which the levels are being filled shifts into the LT-GaAs layer (the capacitance of the barrier becomes virtually independent of the filling bias). This means that *Q*1 traps are localized in LT-GaAs layer. In this case, the decrease in their filling as the filling pulse amplitude V_p further decreases is related to the depression of the quasi-Fermi level in the LT-GaAs layer during the filling pulse. One should also note that the temperature position of the *Q*1 peak did not change, and the relaxation of the capacitance $C(t)$ had a standard form [11].

Two types of electron traps, *Q*2 and *Q*3, were found in the spectra of samples LT200 (Fig. 1b). As in the case of *Q*1 traps in LT300 structures, the dependence of the amplitude of *Q*2 and *Q*3 peaks on the amplitude of the filling pulse indicates their localization in the LT-GaAs layer of structure LT200. The decrease in the amplitude of peak *Q*2 begins at higher amplitudes of the filling pulse compared to peak *Q*3 (Fig. 1b). The reason is that the level of *Q*3 is lower than that of *Q*2 in the band gap of GaAs. It is also worth noting that the *Q*2 peak broadens as the amplitude of the filling pulse V_p decreases, whereas the shape of the *Q*3 peak is independent of the parameters of the filling pulse.

To investigate the cause of this behavior, we studied the isothermal relaxation of capacitance ($C(t)$) at the bias voltage V_b = –10V for different amplitudes of the filling pulse (V_p). A portion of quasi-constant capacitance is observed at the beginning of the $C(t)$ curve at V_p = 10 V in the temperature range 230–260 K (Fig. 2a). The length of this portion decreases as the temperature increases, and it virtually disappears at temperatures above 270 K. The capacitance of 11.5 pF in the quasi-

constant capacitance portion of $C(t)$ (Fig. 2a) yields the width of the SCR $W \approx 1$ μm. This approximately corresponds to the total thickness of epitaxial layers in the LT200 structure; i.e., the boundary of the SCR lies within the heavily doped n^+-GaAs substrate. Because of this circumstance, the electron emission from deep traps in the SCR has only a weak effect on the position of this boundary and, consequently, on the capacitance of the structure. The shift of the SCR boundary into the substrate is due to the fact that the negative charge captured by traps during the filling pulse strongly exceeds the charge of shallow donors in the epitaxial GaAs layer adjacent to the substrate. As electrons are emitted from the deep level, the boundary of SCR is shifted from the heavily doped n^+-GaAs substrate to the weakly doped n-GaAs epitaxial layer, and the relaxation behavior of the $C(t)$ capacitance becomes standard. As the temperature rises, the rate of the electron emission increases; thus, the duration of the portion of quasi-constant capacitance in the $C(t)$ curve decreases (Fig. 2a).

The presence of the quasi-constant-capacitance portion in $C(t)$ distorts the shape of the DLTS spectrum $\Delta C(T)$ obtained in the double-strobe integration mode, when the difference between the $C(t)$ values in the instants of time t_1 and t_2 is measured [11]. As can be seen in Fig. 1b, the $Q2$ peak in the DLTS spectrum recorded with a filling pulse amplitude of $V_p = 10$ V is "cut" at the low-temperature side, when at least one of the two strobes falls within the quasi-constant-capacitance portion of $C(t)$ (Fig. 2a). This results in an effective shift of the position of the $Q2$ peak (Fig. 1b) and does not allow the parameters of a trap to be correctly determined. In addition, the amplitude of the $Q2$ peak somewhat decreases.

The change in the relative amplitude of the filling pulse (V_p) from 10 to 2 V results in a decrease in the density of electrons captured by $Q2$ traps, so at $V_p = 5$V the amplitude of the $Q2$ peak nearly falls to zero (Fig. 1b). In this situation, the negative charge in the LT-GaAs layer decreases, and the SCR boundary comes out of the heavily doped substrate. This makes it possible to select the amplitude V_p of the filling pulse, which is necessary in order to measure the DLTS spectrum correctly. Optimal conditions for the LT200 sample were obtained at $V_p = 6.75$ V (Fig. 1b). As can be seen in Fig. 2b, the relaxation curves of the capacitance $C(t)$, which correspond to these conditions, have virtually no portion of quasi-constant capacitance.

Figure 3 shows temperature dependences of the rate of electron emission from deep traps $Q1$, $Q2$, and $Q3$ in the form of Arrhenius plots. From these plots we determined the parameters of traps, the activation energy, E_{act}, and the capture cross-section, σ_∞; they are listed in the table.

The DLTS spectra for $Q1$, $Q2$, and $Q3$ electron traps, simulated using the parameters listed in the table, are shown in Fig. 1a and Figs. 4a and 4b. As can be seen

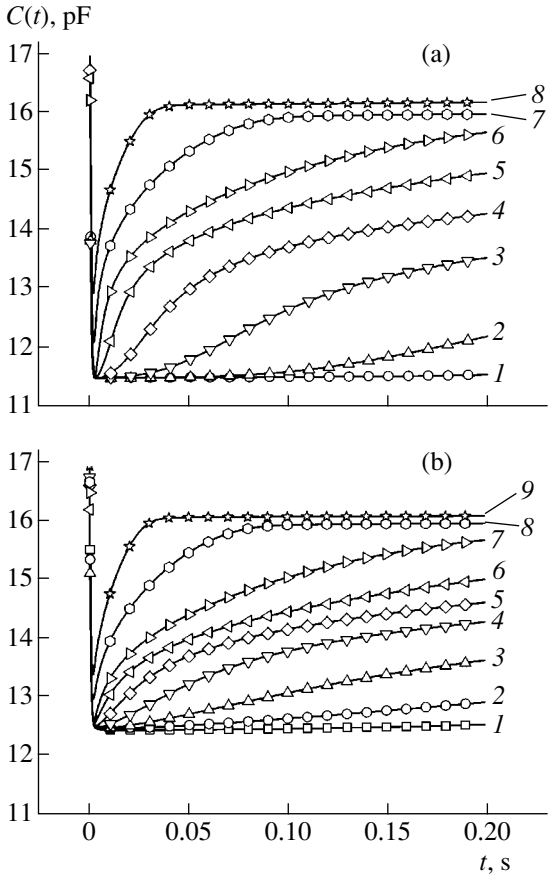

Fig. 2. Relaxation of capacitance $C(t)$ of sample LT200 at the bias $V_b = -10$ V at different temperatures. (a) $V_p = 10$ V; T: (*1*) 220, (*2*) 230, (*3*) 240, (*4*) 250, (*5*) 260, (*6*) 270, (*7*) 280, and (*8*) 290 K. (b) $V_p = 6.75$ V; T: (*1*) 210, (*2*) 220, (*3*) 230, (*4*) 240, (*5*) 250, (*6*) 260, (*7*) 270, (*8*) 280, and (*9*) 290 K.

from the comparison of Figs. 4a and 4b, the existence of the portion of quasi-constant capacitance $C(t)$ does modify the $Q2$ peak of the DLTS spectrum on its low-temperature side. The distinct difference between the simulated and experimental DLTS spectra (Fig. 4a) in the temperature range between the $Q2$ and $Q3$ peaks can be attributed to the existence of deep levels in the energy range between the levels of $Q2$ and $Q3$.

As can be seen in Figs. 1a and 4a, the high-temperature edge of the $Q2$ and $Q3$ peaks in the simulated DLTS spectra is significantly wider than in the experimental ones. The reason for this difference is not clear.

Parameters of electron traps

Trap type	E_{act}, eV	σ_∞, cm^2
$Q1$	0.61	3.4×10^{-14}
$Q2$	0.47	8.6×10^{-15}
$Q3$	0.59	7.3×10^{-14}

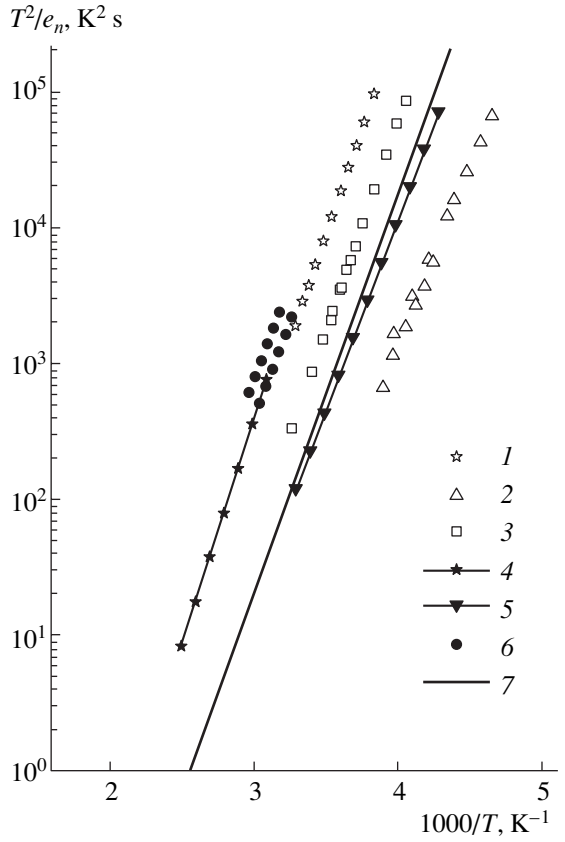

Fig. 3. Arrhenius plots for electron traps in LT-GaAs. (*1*–*3*) this study (*Q*1, *Q*2, and *Q*3, respectively); (*4*) *LTE*1 [8], (*5*) *EAL*2 [10], (*6*) *LT*1 [9], and (*7*) *EL*3 [10, 16].

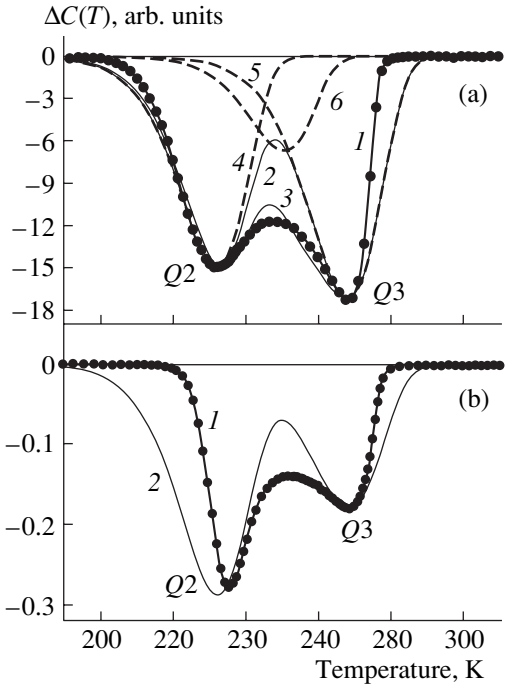

Fig. 4. Comparison of experimental and simulated DLTS spectra for sample LT200. The emission rate window of the double-strobe integrator was 6.8 s^{-1} (t_1 = 133.8 ms, t_2 = 160.6 ms). (a) V_b = –10 V, V_p = 6.75 V. (b) V_b = –10 V, V_p = 10 V. (*1*) experiment; (*2*–*6*) simulation: (*2*) (*Q*2 + *Q*3), (*3*) (*Q*2 + *Q*3 + *EL*3), (*4*) *Q*2, (*5*) *Q*3, and (*6*) *EL*3.

The activation energy of thermal emission of electrons from deep traps can be determined also from the analysis of the relaxation of capacitance $C(t)$, even if there exists the portion of quasi-constant capacitance (Fig. 2a). The principle of the method is as follows. Let us assume that, in the process of thermal emission of electrons from some type of deep traps at the temperature T, the capacitance of the structure reaches some fixed value C_0 during the time interval $t_0(T)$. Then, disregarding the temperature dependences of the contact potential and dielectric constant, the charge emitted by this trap during the time $t_0(T)$ is independent of the temperature T. Consequently, the product $e_n(T)\,t_0(T)$, where $e_n(T)$ is the rate of thermal emission of electrons from the trap level, is a constant. Plotting the dependence of $t_0(T)T^2$ against $1/T$ in a semilogarithmic scale, we can determine the activation energy E_{act} of thermal emission of electrons from this trap, in accordance with the relation

$$E_{act} = k\frac{\ln[t_0(T_1)T_1^2] - \ln[t_0(T_2)T_2^2]}{1/T_1 - 1/T_2},$$

where k is the Boltzmann constant, and T_1 and T_2 are the two temperature values.

Using this method, we analyzed the relaxation curves $C(t)$ measured at the LT200 structure (Fig. 2a). Since the emission rates for *Q*2 and *Q*3 traps differ greatly (Fig. 3), the relaxation of the capacitance $C(t)$ is related to the depletion of *Q*2 traps at the initial stage and *Q*3 traps at the final stage of the process. Therefore, having chosen a value of C_0 capacitance near the portion of quasi-constant capacitance in the range 12–13 pF, we obtained the thermal activation energy E_{act} = 0.46–0.49 eV, which is in good agreement with the activation energy for *Q*2 traps obtained by DLTS (see table). At the same time, using C_0 near its constant value in the range 14.5–15 pF, we obtained an activation energy of E_{act} = 0.58–0.64 eV, which is close to the value for *Q*3 traps.

The determination of the concentrations of *Q*1, *Q*2, and *Q*3 traps from the dependence of the peak height in the DLTS spectrum on the filling pulse amplitude V_p [15] is hindered by the strong variation of this concentration with the coordinate and its high value, as well as by the proximity of the SCR boundary to the region being probed. However, an approximate evaluation can be made on the basis of the change in the capacitance $C(t)$ of the structure when deep traps are depleted. Taking into account that the boundary of the SCR region in the LT200 sample enters the heavily doped substrate when the *Q*2 level is completely filled, this estimate shows that the concentration of *Q*2 traps in the LT-GaAs layer

is not lower than 2×10^{17} cm^{-3}, and the concentration of $Q3$ traps is nearly half this value. In sample LT300, the concentration of $Q1$ traps in the LT-GaAs layer is ~1×10^{17} cm^{-3}.

4. DISCUSSION

As is well known [1–3, 16], in the process of LT-GaAs growth at 200–300°C, the excess As forms antisite defects As_{Ga}, which induce the formation of $EL2$ electron traps [17], with an activation energy of ~0.8 eV. These point defects govern the properties of unannealed LT-GaAs. During the annealing (in our case, in growing the n-GaAs buffer layer at 580°C in the course of 30 min) the excess As forms clusters, and the concentration of As_{Ga} defects strongly decreases. The absence of this level in the DLTS spectra indicates that the As_{Ga} concentration in LT-GaAs layers of the structures under study is presumably below 10^{15} cm^{-3}. Thus, As_{Ga} point defects in sample LT300, as well as in LT200, transformed into more intricate complexes or clusters of various size.

The growth conditions of sample LT300 assumed that there was a concentration of excess As of ~10^{18} cm^{-3} in the LT-GaAs layer [16]. This excess As content should lead to total compensation of all the shallow levels and the Fermi level position deep in the band gap, both before and after the annealing. However, this amount of excess As is not sufficient for the formation of large (>3 nm in diameter) clusters under the annealing conditions used in our case. This fact was confirmed by TEM study. One type of electron traps, $Q1$, was found in sample LT300 (Fig. 1a). As can be seen from the Arrhenius plot (Fig. 3), these traps may be identified with $LTE1$ [8] and $LT1$ [9] traps, observed earlier by current spectroscopy in structures containing LT-GaAs layers. It should be emphasized that LT-GaAs layers [8] were grown at 300°C and presumably contained no As clusters more than 3 nm in diameter, similarly to the layers of the same kind studied in our case. The thickness of the LT-GaAs layers studied in [9] was ~4 nm, and apparently they also did not contain a sufficient excess of As to form large clusters [12]. Thus, $Q1$ level can be attributed to complexes, associates of point defects, or small (<3 nm) clusters related to the excess of As.

In the case of the LT200 sample, the growth conditions provided an excess As concentration in the LT-GaAs layer at the level of 10^{20} cm^{-3}. During the subsequent growing of the n-GaAs buffer layer at 580°C, this excess As provided the formation of As clusters 6–8 nm in diameter with a concentration of 4×10^{16} cm^{-3} in the LT-GaAs layer. It is necessary to note that, owing to the coalescence mechanism (Ostwald ripening) of cluster formation, small clusters, and also complexes and associates of point defects, should coexist with large clusters in the material. Two types of electron traps, $Q2$ and $Q3$, which differ from $Q1$ traps, were

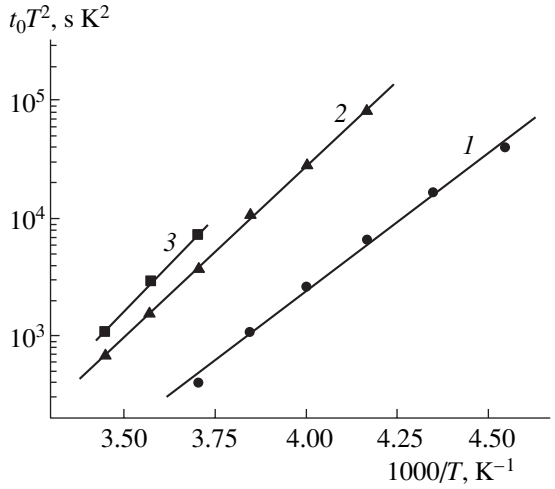

Fig. 5. Temperature dependences of time t_0 for LT200 structure at $V_b = -10$ V, $V_p = 10$ V at different fixed capacitances C_0: (*1*) 12.0, (*2*) 14.5, and (*3*) 15.0 pF.

observed in the LT200 structure (Fig. 3). It is worth noting, however, that the difference in activation energies between $Q2$ and $Q3$ is 0.02 eV, which is on the order of the experimental error, and the difference in their capture cross-sections is not too pronounced. This implies that $Q3$ traps are similar in nature to $Q1$ traps.

The only structural difference between the LT200 and LT300 samples is the presence of large As clusters in the former. It is possible that these clusters are the reason for the $Q2$ levels observed in LT200. As can be seen in Fig. 4a, the DLTS spectrum simulated for the LT200 sample, with only $Q2$ and $Q3$ traps taken into account, agrees poorly with the experiment in the temperature range between the $Q2$ and $Q3$ peaks. The cause of this discrepancy may be that the model of the two discrete peaks does not reflect the existing size distribution of clusters. If this distribution is taken into account, an additional signal in the DLTS spectrum might appear between the $Q2$ and $Q3$ peaks, which are related to the largest and smallest clusters. An alternative explanation could be the existence of $EL3$ traps [4, 8, 17] in sample LT200, with their peak lying between the $Q2$ and $Q3$ peaks, in accordance with the Arrhenius plot (Fig. 3). Indeed, taking the $EL3$ level into account in calculating the DLTS spectrum considerably improves the agreement between calculation and experiment (Fig. 4a).

The $Q2$ traps found in this study with a thermal activation energy of 0.47 eV may be responsible for the position of the Fermi level in the LT-GaAs layer; this, in turn, defines the formation of a potential barrier 0.5 eV in height at the interface between this material and low-resistivity GaAs. We determined the height of this barrier in LT200 samples earlier by analyzing the capacitance–voltage characteristics [13].

5. CONCLUSION

The results obtained suggest that the type and concentration of the dominant traps in LT-GaAs layers depend on the growth temperature of these layers. In LT-GaAs layers grown at 200°C and containing As clusters ~6–8 nm in size, two new types of electron trap were observed: $Q2$ ($E_{act} = 0.47$ eV, $\sigma_\infty = 8.6 \times 10^{-15}$ cm^2) and $Q3$ ($E_{act} = 0.59$ eV, $\sigma_\infty = 7.3 \times 10^{-14}$ cm^2); their concentration is on the same order of magnitude as the concentration of As clusters. In LT-GaAs layers grown at 300°C with a lower concentration of excess As, $Q1$ traps were found ($E_{act} = 0.51$ eV, $\sigma_\infty = 3.4 \times 10^{-14}$ cm^2). Analysis of the sample structure and growth conditions suggest that levels $Q1$ and $Q3$ can be attributed to complexes, associates of point defects, or small (<3 nm) clusters associated with excess As, and level $Q3$, to large (6–8 nm) As clusters.

ACKNOWLEDGMENTS

This study was supported by the Russian Foundation for Basic Research (project no. 03-02-16607).

REFERENCES

1. M. Kaminska, Z. Liliental-Weber, E. R. Weber, *et al.*, Appl. Phys. Lett. **54**, 1881 (1989).
2. M. R. Melloch, K. Mahalingam, N. Otsuka, *et al.*, J. Cryst. Growth **111**, 39 (1991).
3. N. A. Bert, A. I. Veĭnger, M. D. Vilisova, *et al.*, Fiz. Tverd. Tela (St. Petersburg) **35**, 2609 (1993) [Phys. Solid State **35**, 1289 (1993)].
4. T.-C. Lin and T. Okumura, Jpn. J. Appl. Phys. **35**, 1630 (1996).
5. A. C. Warren, N. Katzenellenbogen, D. Grischkowsky, *et al.*, Appl. Phys. Lett. **58**, 1512 (1991).
6. P. A. Loukakos, C. Kalpouzos, I. E. Perakis, *et al.*, Appl. Phys. Lett. **79**, 2883 (2001).
7. P. A. Loukakos, C. Kalpouzos, I. E. Perakis, *et al.*, J. Appl. Phys. **91**, 9863 (2002).
8. C. H. Goo, W. S. Lau, T. C. Chong, and L. S. Tan, Appl. Phys. Lett. **69**, 2543 (1996).
9. C. Steen, V. Oechsner, V. Donshev, *et al.*, in *Proceedings of 4th Symposium on Non-Stoichiometric III–V Compounds, Asilomar, USA, 2002*, Ed. by P. Specht, T. R. Weatherford, P. Kiesel, T. Marek, and S. Malzer (Friedrich–Alexander–Univ., Erlangen–Nurnberg, 2002), p. 37.
10. T. C. Lin, H. T. Kaibe, and T. Okumura, Jpn. J. Appl. Phys. **33**, L1651 (1994).
11. D. V. Lang, J. Appl. Phys. **45**, 3023 (1974).
12. V. V. Chaldyshev, N. A. Bert, A. E. Kunitsyn, *et al.*, Fiz. Tekh. Poluprovodn. (St. Petersburg) **32**, 1161 (1998) [Semiconductors **32**, 1036 (1998)].
13. P. N. Brunkov, V. V. Chaldyshev, N. A. Bert, *et al.*, Fiz. Tekh. Poluprovodn. (St. Petersburg) **32**, 1170 (1998) [Semiconductors **32**, 1044 (1998)].
14. P. N. Brunkov, V. V. Chaldyshev, A. V. Chernigovskiĭ, *et al.*, Fiz. Tekh. Poluprovodn. (St. Petersburg) **34**, 1109 (2000) [Semiconductors **34**, 1068 (2000)].
15. Jian H. Zhao, Jyh-Chwen Lee, Z. Q. Fang, *et al.*, J. Appl. Phys. **61**, 5303 (1987).
16. L. G. Lavrent'eva, M. D. Vilisova, V. V. Preobrazhenskiĭ, and V. V. Chaldyshev, Izv. Vyssh. Uchebn. Zaved., Fiz. **45** (8), 3 (2002).
17. G. M. Martin, A. Mitonneau, and A. Mircea, Electron. Lett. **13**, 191 (1977).

Translated by D. Mashovets

Semiconductors, Vol. 38, No. 4, 2004, pp. 393–396. Translated from Fizika i Tekhnika Poluprovodnikov, Vol. 38, No. 4, 2004, pp. 407–411.

SEMICONDUCTOR STRUCTURES, INTERFACES, AND SURFACES

Oscillations of Induced Photopleochroism in ZnO/GaAs Heterojunctions

S. E. Nikitin*, Yu. A. Nikolaev*, V. Yu. Rud', Yu. V. Rud'*, E. I. Terukov*, N. Fernelius***, and J. Goldstein*****

**Ioffe Physicotechnical Institute, Russian Academy of Sciences, ul. Politekhnicheskaya 26, St. Petersburg, 194021 Russia*
***St. Petersburg State Technical University, ul. Politekhnicheskaya 29, St. Petersburg, 195251 Russia*
e-mail: yuryrud@mail.ioffe.ru
****Air Force Wright Lab., Wright Patterson AFB, OH, USA*
Submitted July 14, 2003; accepted for publication July 16, 2003

Abstract—Anisotype and isotype ZnO/GaAs heterojunctions were formed by magnetron sputtering of thin *n*-ZnO:Al films on epitaxial layers of *n*- and *p*-GaAs. It is shown that the heterostructures obtained have a high photosensitivity (~5×10^3 V/W at 300 K) in a wide spectral range (1.5–3.2 eV), which oscillates due to the radiation interference in thin ZnO films. Under oblique incidence of linearly polarized radiation on a ZnO film, photopleochroism is induced in a heterojunction, whose value oscillates within ~1–55% at $\theta = 85°$. The photopleochroism oscillations are also due to the radiation interference in the ZnO film. It is concluded that the heterojunctions obtained are promising candidates for selective photodetectors of linearly polarized radiation. © *2004 MAIK "Nauka/Interperiodica".*

The detection of induced photopleochroism in isotropic diamond-like semiconductors that occurs under oblique incidence of linearly polarized radiation has opened up real possibilities for applying cubic III–V semiconductors in new generation optoelectronics [1, 2]. Even the first investigations of this phenomenon in III–V crystals showed the possibility of designing polarimetric photodetectors with unprecedently high polarization efficiency of photoconversion: ~0.22 A/W K [3–6]. Recently, wide-gap oxides, which have high conductivity and optical transparency, have found increasing application in semiconductor optoelectronics. Specifically, the use of wide-gap oxides makes it possible to attain a high quantum efficiency of solar cells [7–10]. In this study, we report the first results of the investigations of the polarization photosensitivity of heterojunctions formed from GaAs and thin ZnO layers.

Heterostructures were fabricated by deposition of ZnO:Al films using dc magnetron sputtering of a pressed ZnO:Al target in argon. Epitaxial layers of *p*-GaAs:Mn with hole density $p \approx 10^{17}$ cm^{-3} at T = 300 K and *n*-GaAs with electron density $n \approx 10^{13}$ cm^{-3} at 300 K, grown on semi-insulating GaAs(100), were used as substrates. In order to dope ZnO films, aluminum was introduced into the target [10], which made it possible to obtain *n*-ZnO:Al films with electron density $n \approx 5 \times 10^{20}$ cm^{-3} at T = 300 K. The ZnO films showed high adhesion to the surface of epitaxial GaAs.

Measurements of the steady-state current–voltage characteristics $I(U)$ showed rectification in both anisotype *n*-ZnO:Al/*p*-GaAs:Mn and isotype *n*-ZnO:Al/*n*-GaAs heterojunctions. It is noteworthy that the forward direction always corresponds to the negative polarity of an applied bias voltage on the *n*-ZnO:Al film, which is in agreement with the approximate energy-level diagram of the heterojunctions under study. As an example, a typical current–voltage characteristic of an anisotype heterojunction is shown in Fig. 1. At $U < 0.3$ V, the forward current increases exponentially with an ideal-

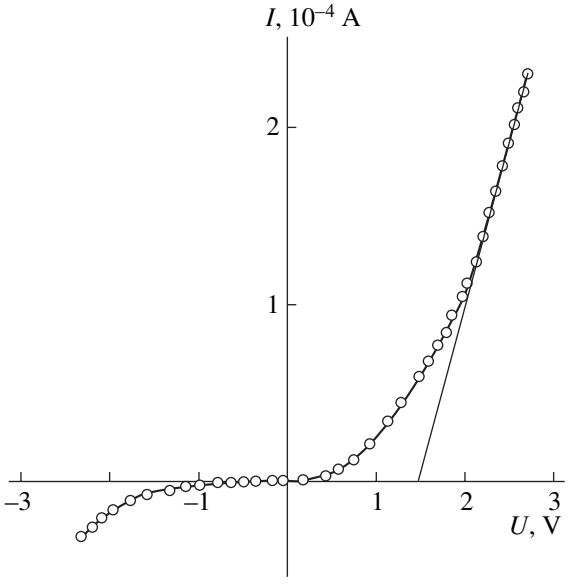

Fig. 1. Steady-state current–voltage characteristic of an *n*-ZnO:Al/*p*-GaAs:Mn heterojunction at T = 300 K. The forward direction corresponds to the positive polarity of applied bias voltage on *p*-GaAs:Mn.

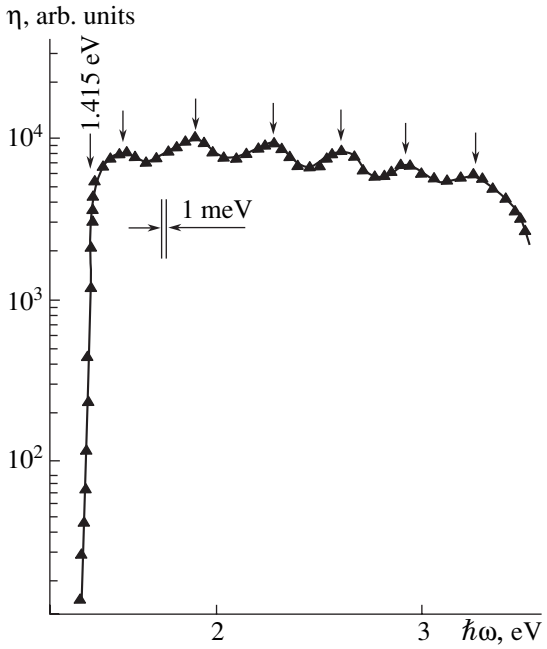

Fig. 2. Spectral dependence of the relative quantum efficiency of photoconversion for an *n*-ZnO:Al/*p*-GaAs:Mn heterojunction in unpolarized light at $T = 300$ K. Sample *2*, illumination from the side of the *n*-ZnO:Al film.

ity factor of about 2.4. This suggests that the forward current is governed by the recombination processes in the active region of the structures obtained [11]. As can be seen from Fig. 1, at $U > 2$ V, the forward portion of the current–voltage characteristic obeys the relation

$$I = (U - U_0)/R_0, \quad (1)$$

where the residual resistance $R_0 \approx 10^4\ \Omega$ and the cutoff voltage $U_0 \approx 1.4$ V. The value of the cutoff voltage (multiplied by the elementary charge) is close to the band gap width E_G of gallium arsenide [12]. The reverse current in anisotype heterojunctions generally obeys the power law $I \propto U^\gamma$, where $\gamma \approx 1.1$ at $U \leqslant 0.3$ V. With a further increase in U in the range 0.5–2.5 V, γ becomes as high as ~3. The behavior of the reverse current–voltage characteristics suggests a low quality of the periphery of the anisotype heterojunctions, for which the rectification coefficient (i.e., the ratio of the forward to reverse current) is $K \approx 10$ (at $U \approx 1.5$ V). In the case of isotype heterojunctions, the residual resistance of the structures increases to $R_0 \approx 10^8\ \Omega$, which is controlled by the low doping level of *n*-GaAs layers. The reverse currents in these heterojunctions are about 10^{-8} A at $U = 10$ V and $T = 300$ K.

The photovoltaic effect in the *n–p*- and *n–n*-heterojunctions obtained is significant when they are illuminated from the side of the *n*-ZnO:Al film. For the best anisotype heterojunctions, the maximum voltaic photosensitivity is $S_U^m \approx 500$ V/W, and the maximum current photosensitivity $S_I^m \approx 0.5$ mA/W at $T = 300$ K. In the case of isotype heterojunctions, $S_U^m \approx 5 \times 10^3$ V/W. These parameters are well reproduced and do not show any degradation. It should also be noted that the sign of photoresponse in the heterojunctions obtained is independent of (1) the location of the light probe (~0.2 mm in diameter) upon its shift across the surface, (2) the energy of incident photons, and (3) the radiation intensity. Thus, we can attribute the observed photosensitivity of the heterojunctions to the only active region arising at the interface.

A spectral dependence of the relative quantum efficiency of photoconversion $\eta(\hbar\omega)$, typical of the heterojunctions illuminated from the side of the *n*-ZnO film, is shown in Fig. 2. It is noteworthy that the spectra $\eta(\hbar\omega)$ of anisotype and isotype heterojunctions are similar. The main features of the photosensitivity spectra of the ZnO/GaAs heterojunctions are as follows.

The long-wavelength edge of η has an exponential form and is characterized by a large gradient, $S = \delta(\ln\eta)/\delta(\hbar\omega) \approx 80$–$90\ \text{eV}^{-1}$, which is typical of direct-gap diamond-like semiconductors [12]. The kink in the region corresponding to the transition from the exponential dependence on the curves $\eta(\hbar\omega)$ to a weaker dependence for all the *n–p*- and *n–n*-heterojunctions under study is located at the same energy, $\hbar\omega_0 \approx 1.415$ eV, which is consistent with the band gap width of gallium arsenide [12]. It can also be seen from Fig. 2 that, at $\hbar\omega > E_G$, the photosensitivity attains the maximum value and remains high with increasing $\hbar\omega$. The short-wavelength falloff occurs, as rule, at 3.2–3.4 eV, which is close to the band gap width of thin ZnO films [12–14]. Hence, the window for the intensity of incident radiation, which is typical of ideal heterojunctions, manifests itself in the heterojunctions under investigation. Due to this effect, the photosensitivity remains high in the interval between the band gap widths of the heterojunction components. In this case, one should bear in mind that the set of functional parameters of the materials in contact does not meet the requirements for ideal matching. Apparently, the manifestation of the window effect may be the result of matching between a thin ZnO film and a bulky GaAs substrate. In this context, we can assume that the concentration of mismatch defects at the heterojunction interface is rather low and the recombination at the interface is almost absent.

The oscillations observed in the spectra $\eta(\hbar\omega)$ of the heterostructures when they are exposed to unpolarized radiation should be considered one of the main specific features of the photosensitivity of the heterojunctions under consideration (see Fig. 2). These oscillations can be characterized by the ratio of the maximum and minimum values of the quantum efficiency of photoconversion: $\Delta = \eta^{max}/\eta^{min}$. For the heterojunctions under study, Δ ranges from 1.2 to 1.4. Higher values of Δ are observed for anisotype heterojunctions and Δ decreases with increasing $\hbar\omega$. Obviously, additional investiga-

tions are required to explain these facts; at the same time, the presence of oscillations in the spectra $\eta(\hbar\omega)$ indicates the homogeneity of ZnO films.

The spectral positions of the maxima and minima of η are different for heterojunctions from different sets, which accounts for the influence of the deposition conditions on the properties of *n*-ZnO:Al films. The thickness of the film was estimated from the spectra $\eta(\hbar\omega)$ using the expression for the refractive index [15]

$$n = \lambda_m\lambda_{m-1}/2d(\lambda_m - \lambda_{m-1}), \quad (2)$$

where λ_m is the wavelength of unpolarized radiation at $\eta = \eta^{max}$ and m is the number of the maximum; the value $n = 2$ was taken for ZnO [12]. The estimation gave a value of $d \approx 0.7$–0.9 μm, which is in satisfactory agreement with the results of direct measurements of the thickness of ZnO:Al films.

The total width of the photosensitivity spectra of both anisotype and isotype heterojunctions, $\delta \approx 1.85$–2.0 eV, characterizes the structures obtained as potential broadband converters of unpolarized radiation with the possibility of using the fine structure for spectral tuning of their photosensitivity.

The investigations performed showed that polarization photosensitivity in the heterojunctions under consideration arises only under conditions of oblique incidence of linearly polarized radiation on the outer specular surface of the thin-film component of a structure, which suggests the appearance of induced photopleochroism [1, 2]. At fixed angles of incidence $\theta > 0°$, the short-circuit photocurrent in the heterojunctions periodically depends on the azimuthal angle φ between the vector of the electric field of a light wave **E** and the plane of incidence [1, 2]:

$$i = i^p\cos^2\varphi + i^s\sin^2\varphi. \quad (3)$$

Here, i^p and i^s are the photocurrents in the cases when the vector **E** ∥ PIR and **E** ⊥ PIR is parallel and perpendicular to the plane of incidence, respectively.

Under conditions of oblique incidence of linearly polarized radiation on the front surface of ZnO/GaAs heterojunctions, a transformation of the spectra $\eta(\hbar\omega)$ occurs and is governed by the orientation of the vector **E** with respect to the plane of incidence (Fig. 3, curves *1*, *2*). In this case, the long-wavelength edge remains exponential, and the value of $\hbar\omega_0$ is almost the same for the *s* and *p* polarizations of radiation: $\hbar\omega_0 = 1.415$ eV. The latter circumstance is due to the fact that the GaAs substrate does not suffer any perturbations that lead to a change in E_G. With an increase in the photon energy ($\hbar\omega > E_G$), the polarization of radiation significantly affects both the quantitative and qualitative characteristics of the photosensitivity spectrum. The minima of η^s correspond to the maxima of η^p, and the maxima of η^s correspond to the minima of η^p. As a result, at a fixed angle of incidence, a set of photon energies is clearly distinguished in the spectra of quantum efficiency; at these energies, the difference

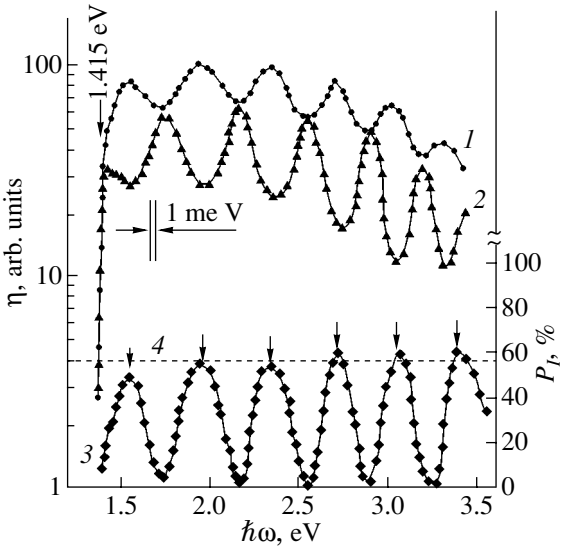

Fig. 3. Spectral dependences of the relative quantum efficiency of photoconversion for an *n*-ZnO:Al/*p*-GaAs:Mn heterojunction at $T = 300$ K: (*1*) *p* polarization, η^p; (*2*) *s* polarization, η^s; and (*3*) the coefficient of induced photopleochroism P_I. $\theta \approx 85°$. (*4*) Calculated value of P_I for the air/ZnO interface, according to [16].

between the values of η^p and η^s is maximum or minimum ($\eta^p \approx \eta^s$ in the latter case). According to [2], these features are due to the interference of incident radiation in the ZnO film.

Figure 3 also shows the experimental spectral dependence of the coefficient of induced photopleochroism in the ZnO/GaAs heterojunctions at $\theta \approx 85°$ (curve *3*), found from the relation [2]

$$P_I = (\eta^p - \eta^s)/(\eta^p + \eta^s). \quad (4)$$

It can be seen that, at the photon energies $\hbar\omega \approx 1.55$, 1.95, 2.34, 2.71, 3.05, and 3.34 eV, which correspond to maximum differences between the quantum efficiencies for the *p* and *s* polarizations, maxima in the spectrum $P_I(\hbar\omega)$ are observed (Fig. 3, curve *3*). It is noteworthy that the maximum experimental values P_I^{max} are similar to the theoretical estimate of the coefficient of induced photopleochroism (Fig. 3, curve *4*), based on the data of [2, 16]. As can be seen from Fig. 3 (curve *4*), the coefficient P_I calculated according to [16] is almost independent of the photon energy. The reason is that the radiation interference was disregarded in [16]. Due to the effects of interference, distinct minima are observed in the experimental spectrum $P_I(\hbar\omega)$ of the heterojunctions under study. The values P_I^{min} are close to zero in the minima because, in this case, bleaching for the *p* and *s* polarizations is attained simultaneously, whereas the photon energies $\hbar\omega \approx 1.75$, 2.16, 2.55, 2.88, and 3.34 eV correspond to the condition of disappearance of the induced photopleochroism ($P_I^{min} \longrightarrow 0$).

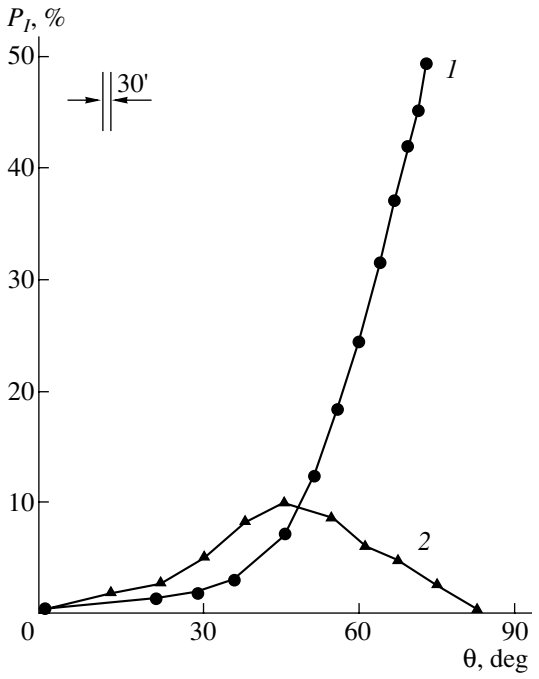

Fig. 4. Dependences of the coefficient of induced photopleochroism on the angle of incidence of linearly polarized radiation θ in the region of an interference (*1*) maximum and (*2*) minimum for an *n*-ZnO:Al/*p*-GaAs:Mn heterojunction at T = 300 K. Illumination from the side of the *n*-ZnO:Al film.

Figure 4 shows typical experimental dependences of the coefficient of induced photopleochroism on the angle of incidence of radiation in the vicinity of a maximum (curve *1*) and a minimum (curve *2*) of P_I. It can be seen that, near maxima in the spectrum $P_I(\hbar\omega)$, the dependence of the coefficient of induced photopleochroism on the angle of incidence is in agreement with theory [16] and obeys a parabolic law:

$$P_I \propto \theta^2. \quad (5)$$

In this case, the value of P_I corresponds to the refractive index of ZnO [12]. In the vicinity of a minimum in the spectrum $P_I(\hbar\omega)$, the experimental dependence $P_I(\theta)$ (Fig. 4, curve *2*) does not correspond to expression (5) and the experimental value of the coefficient P_I is much smaller compared to the theoretical value [16]. According to [2], this difference (due to the interference of radiation of *p* and *s* polarizations in the thin ZnO film) indicates a fairly high interference bleaching of heterojunctions by the ZnO:Al film when the following condition is satisfied: $P_I \longrightarrow 0$.

The similarity of the coefficient $P_I^{\max}$ for the ZnO/GaAs heterojunctions to the theoretical estimates (Fig. 3, curve *3*) suggests that such heterojunctions can be used as selective photodetectors of linearly polarized radiation, in which tuning of the spectral range and adjustment of the coefficient P_I are performed by varying the angle of incidence and the conditions of deposition of ZnO films. The phenomenon revealed—the disappearance of induced photopleochroism ($P_I \longrightarrow 0$)—can be used in monitoring the bleaching of heterojunctions containing thin-film components.

Thus, the method of magnetron sputtering of ZnO:Al targets makes it possible to deposit thin (~1 μm) ZnO films on the surface of GaAs single crystals and fabricate heterojunctions showing oscillations (from 55 to 1–2%) in the spectrum of induced photopleochroism in the region of high quantum efficiency of photoconversion in the range 1.5–3.2 eV, which opens up the possibility of using GaAs-based heterojunctions in new generation optoelectronics.

REFERENCES

1. Yu. V. Rud', Izv. Vyssh. Uchebn. Zaved., Fiz. **29**, 68 (1986).
2. F. P. Kesamanly, V. Yu. Rud', Yu. V. Rud', and G. V. Shok, Fiz. Tekh. Poluprovodn. (St. Petersburg) **33**, 513 (1999) [Semiconductors **33**, 483 (1999)].
3. S. G. Konnikov, D. Melebaev, V. Yu. Rud', and M. Serginov, Pis'ma Zh. Tekh. Fiz. **18** (12), 38 (1992) [Sov. Tech. Phys. Lett. **18**, 382 (1992)].
4. S. G. Konnikov, D. Melebaev, V. Yu. Rud', *et al.*, Pis'ma Zh. Tekh. Fiz. **19** (4), 57 (1993) [Tech. Phys. Lett. **19**, 124 (1993)].
5. S. G. Konnikov, G. D. Melebaeva, D. Melebaev, *et al.*, Pis'ma Zh. Tekh. Fiz. **18** (24), 32 (1992) [Sov. Tech. Phys. Lett. **18**, 806 (1992)].
6. S. G. Konnikov, D. Melebaev, V. Yu. Rud', *et al.*, Jpn. J. Appl. Phys. **32**, 515 (1993).
7. N. Mardeesich, in *Proceedings of 15th IEEE Photovoltaic Special Conference* (Kissimee, 1981); IEEE Electron Device Lett., No. 4, 446 (1981).
8. Yu. A. Nikolaev, V. Yu. Rud', Yu. V. Rud', *et al.*, Fiz. Tekh. Poluprovodn. (St. Petersburg) **36**, 1128 (2002) [Semiconductors **36**, 1048 (2002)].
9. S. E. Nikitin, Yu. A. Nikolaev, I. K. Polushina, *et al.*, Fiz. Tekh. Poluprovodn. (St. Petersburg) **37**, 1329 (2003) [Semiconductors **37**, 1291 (2003)].
10. E. Aperathirtis, Z. Hatzpoulos, M. Androulidaki, *et al.*, Sol. Energy Mater. Sol. Cells **45**, 161 (1997).
11. S. M. Sze, *Physics of Semiconductor Devices*, 2nd ed. (Wiley, New York, 1981; Mir, Moscow, 1984).
12. *Physicochemical Properties of Semiconductor Materials: Handbook*, Ed. by A. V. Novoselova and V. B. Lazarev (Nauka, Moscow, 1979).
13. A. Shileika, Surf. Sci. **37**, 730 (1973).
14. H. Ohta, H. Miroguch, and M. Hirano, Appl. Phys. Lett. **82**, 823 (2003).
15. G. S. Landsberg, *Optics* (Nauka, Moscow, 1976).
16. G. A. Medvedkin and Yu. V. Rud', Phys. Status Solidi A **67**, 333 (1981).

Translated by Yu. Sin'kov

Semiconductors, Vol. 38, No. 4, 2004, pp. 397–401. Translated from Fizika i Tekhnika Poluprovodnikov, Vol. 38, No. 4, 2004, pp. 412–416.

SEMICONDUCTOR STRUCTURES, INTERFACES, AND SURFACES

Electron–Phonon Damping Factor for the Landau Quantization of 2D Electrons with a Fine Structure of the Energy Spectrum

V. I. Kadushkin

Ryazan' State Pedagogical University, ul. Svobody 46, Ryazan', 390000 Russia

e-mail: kadush@ttc.ryazan.ru

Submitted April 29, 2003; accepted for publication August 26, 2003

Abstract—The drift of degenerate 2D electrons in the channel of the heterojunction potential well is considered. In a quantizing magnetic field **B**, the electrons scan the defects of the heteroboundary, which perturb their momentum and energy equilibrium state (T, T_D^0). The stationary nonequilibrium state (T, T_D^*) is attained by electron–phonon relaxation in energy and momentum. The experimentally observed nonlinear dependence $T_D(T)$ is explained by the admixture of deformation acoustic phonons to the interaction of 2D electrons with piezoelectric phonons. © *2004 MAIK "Nauka/Interperiodica".*

1. INTRODUCTION

From the pioneering studies [1, 2] to the present day [3, 4], the effects of quasiparticle interactions have attracted constant interest. This is due to the fact that electron–electron and/or electron–phonon interactions, for example, play a decisive role in transport phenomena. Among the most significant effects, we cite hot electron effects, quantum corrections to conductivity, and Landau damping in bulk (3D) and two-dimensional (2D) semiconductor compounds with a degenerate electron gas. The anomalies of low-temperature magnetotransport related to the filling of several confinement subbands with 2D electrons are well known [5–9].

In the experiments with $Al_xGa_{1-x}As$(Si)/GaAs [10, 11], nonmonotonic dependences of the time $\tau_q^{\exp}(T, n_s)$ of nonthermal (collisional) Landau level broadening on temperature and the concentration of degenerate 2D electrons were observed. A qualitative interpretation of the observed features was suggested in [10, 11]. This interpretation took into account the competition between the channels of *e–e* electron–electron interactions in a complex system with a degenerate electron gas; it was shown that $\tau_{ee}^{\text{th}} \approx \tau_q^{\exp}$. The studies of *e–e* relaxation processes in 2D electron systems with a fine structure of the energy spectrum and of the spatial electron-density distribution were performed in [12–14]. It was shown that Landau damping is controlled by the *n* satellite of the *p* component of the excited confinement subband (the notation of electronic components is given below; see Fig. 1). The analysis of the expressions for $\tau_{ee}^{\text{th}}(T)$ has shown that the nonlinear dependence of $\tau_q^{\exp}(T)$ is related to the excitation of 2D plasmons with frequency $\omega = kT/\hbar$ determined by the concentration of the *n* satellite. It was possible to explain the features of the $\tau_q^{\exp}(T)$ dependence in the case of filling both one ground subband [15] and two confinement subbands [10].

In this study, we consider the dynamics of destruction of Landau quantization and analyze the role of electron–phonon relaxation as a factor stabilizing the destruction process on the basis of a physical model of *e–e* interactions [10–14]. We show that features of the temperature dependence $\tau_q^{\exp}(T)$ can be explained by

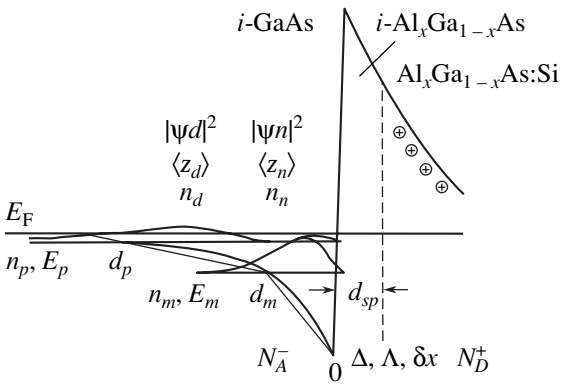

Fig. 1. Energy diagram of the conduction band $E_C(z)$ of a heterojunction with two occupied confinement subbands E_m and E_p and with concentrations n_m and $n_p = n_n + n_d$; $\langle z_{m,p} \rangle$ are the centroids of $|\psi_{m,p}|^2$ for the *m* and *p* electron states, and d_{sp} is the width of the undoped spacer. The sources of perturbation of the 2D electronic system are (+) ionized donors N_D^+ (the doping impurity is Si), (N_A^-) acceptors from the residual atmosphere, (Λ, Δ) growth islands, and (δx) variations in the heteroboundary mole fraction.

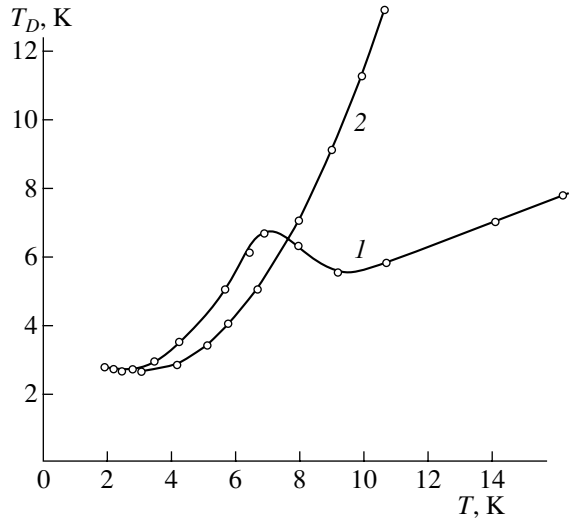

Fig. 2. Characteristic temperature dependence of the collisional broadening of Landau levels for samples with (*1*) two and (*2*) one occupied confinement subbands. The parameters of the samples are given in the table. The anomaly of T_D (*1*) is related to the admixture of DA phonons to the PA relaxation of 2D electrons in the *p* subband.

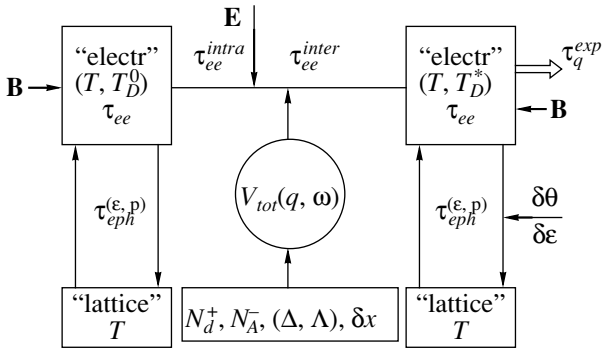

Fig. 3. Outline of interactions in the electron–lattice system with the excitation of the stationary nonequilibrium state $(T,\ T_D^*)$ by the external perturbation $V_{tot}(\mathbf{q}, \omega)$; defects of the potential well of the heterojunction are scanned by the electric field **E** in the equilibrium state $(T,\ T_D^0)$ in a quantizing magnetic field **B** of defects $(N_D^+, \ldots)$ in the potential well of heterojunction. The characteristics of the states are $(T,\ T_D^0)$ T = const, **B** = const, **E** = 0 ($V(\mathbf{r}, t^0)$ = const); $(T,\ T_D^*)$ T = const, **B** = const, **E** ≠ 0 ($V(\mathbf{r}, t) = V_{tot}(\mathbf{q}, \omega)$).

the admixture of deformation acoustic (DA) phonons to the interaction of electrons with piezoelectric acoustic (PA) phonons.

2. MODEL

The electron-density distribution $|\psi(z)|^2$ and the energy structure of a single heterojunction $Al_{0.28}Ga_{0.72}As(Si)/GaAs$ with doping level $N_D \approx 10^{18}$ cm^{-3} and background (acceptor) impurity density $N_A \approx 6 \times 10^{15}$ cm^{-3} are shown in Fig. 1. When calculating $\tau_{ee}^{\text{th}}(T)$, we approximated the potential well $E_C(z)$ by a triangular profile with kinks at the confinement levels $E_m = E_c(d_m)$ and $E_p = E_c(d_p)$ [14]. Landau quantization is destroyed by the *m*–*n* electron interaction, whether it be the *m* component or the *n* satellite of the *p* component that is affected by the external perturbation $V_{tot}(\mathbf{q}, \omega)$. Due to intrasubband and intersubband *e*–*e* interaction, the perturbation extends over the entire 2D electron system and affects the form of $\tau_q^{\text{exp}}(T)$. The *n* satellite of the *p* component occupies a key position with respect to the perturbation sources $(N_D^+, \ldots)$ and to the basic concentration of the 2D electrons localized in the *m* component. It should be noted that the centroid of $|\psi_m(z)|^2$ and $|\psi_n(z)|^2$ are spatially compatible.

Table.

Sample no.	Component		
	1		2
Parameter	*m* component	*p* component	*m* component
n_s, 10^{11} cm^{-2}	9.4	0.6	8.6
$\varepsilon_F - \varepsilon_{m,p}$, meV	32	2.0	29.2
$\sqrt{8ms^2(\varepsilon_F - \varepsilon_{m,p})}$, K	19.4	4.9	18.4
$kT/\hbar s$, 10^6, cm^{-1}	2.1 (T = 8 K)		
$2\pi/d_{m,p}$, 10^6 cm^{-1}	21	2.1	19
$k_{F_{m,p}}$, 10^6 cm^{-1}	2.5	1.0	2.3
$\sqrt{8ms^2\varepsilon_B}$, K		8.5	
q_{TF}, 10^6 cm^{-1}		2.0	67
$\varepsilon_{m,p}$, meV	68.0	98	96.2
ε_F, meV	100		

This situation is illustrated in Fig. 2, where the dependence $T_D(T)$ is shown for the cases where two-dimensional subbands (sample *1*, curve *1*) or a one-dimensional subband (sample *2*, curve *2*) are occupied. The parameters of the samples are given in the table. We see that the feature of the curve $T_D(T)$ for sample *1* in the temperature range 6.5–9 K (nonlinearity of oscillatory type) does not appear for sample *2*.

We consider 2D electrons, the crystal lattice, and the perturbation source as a thermodynamic system "electron–lattice–$V_{tot}(\mathbf{q}, \omega)$" in equilibrium; the heat bath has temperature T (Fig. 3). Electrons interact with each other and with the crystal lattice, and the corresponding relaxation times are τ_{ee} and τ_{eph}. At low temperatures and in a quantizing magnetic field **B**, an equilibrium (in

energy and momentum) state of 2D electrons can be described in terms of harmonic oscillators with the cyclotron frequency $\omega = (e/m^*)B$.

The "*e–e*" interaction is strong such that $\tau_{ee} \ll \tau_p \ll \tau_\varepsilon$, where τ_p and τ_ε are the momentum and energy relaxation times; therefore, the electronic states are correlated and coherent. The states of electrons in cyclotron orbits are coherent if the lifetime in the orbit is longer than the mean free-path time (momentum relaxation time). The initial phase of the electronic state is controlled by the appearance of the electron in the cyclotron orbit and is random. However the electron motion in the orbit is synchronized. This allows one to apply the random phase approximation (RPA) to the description of properties of such magnetized 2D electrons. It should be noted that, for the heterojunctions that we studied, $n_s \approx (0.5–2) \times 10^{12}$ cm^{-2} and the reduced Wigner radius $r_s^* = r_s/a_B$ is 0.6–1.2, so the use of the RPA approximation is not completely justified.

Collisions of electrons with lattice defects ($N_D^+, \ldots$) destroy the ground quantum state (cyclotron orbits). This is reflected in a broadening of Landau levels and results (together with other mechanisms [16]) in a finite value of the amplitude of oscillations of kinetic coefficients. The collisions are taken into account by introducing the reducing Dingle factor $R_D \propto \exp(-2\pi^2 kT_D/\hbar\omega)$, where T_D is the Dingle temperature expressed in terms of nonthermal collisional broadening time τ_q as

$$T_D = \hbar/2\pi k\tau_q. \quad (1)$$

In the absence of an external electric field, the temperature T_D^0 is associated with the equilibrium state of the electron gas. This parameter determines the degree of randomization of 2D electrons that are in thermal equilibrium with the crystal lattice (T, T_D^0) in a quantizing magnetic field **B**. We note that perturbations of the potential well profile in the 2D channel induced by various defects are stationary, $V(\mathbf{r}, t^0)$. The approach to the equilibrium state (T, T_D^0) between the 2D electrons and the crystal lattice in a quantizing magnetic field is schematically illustrated in Fig. 3 (on the left-hand side). The stationary state (T, T_D^0) of the system is established due to an energy–momentum relaxation with the characteristic time $\tau_{eph}^{(\varepsilon, p)}$.

3. RELAXATION MODES AND CHANNELS IN THE (T, T_D^0) STATE

The mechanism of destruction of the quantum Landau state (T, T_D^0) and of the excitation of a new equilibrium stationary state (T, T_D^*), which, however, is nonequilibrium with respect to the initial equilibrium state (T, T_D^0), is illustrated on the right-hand side in Fig. 3. The application of an electric field **E** displaces the 2D electron system along the channel of the heterojunction potential well. Moving electrons "scan" the spatial distribution of defects in the heterojunction ($N_d^+, \ldots$). An observer in the reference frame bound with the 2D electrons sees the result of scanning defects $E_C(z)$ as $V_{tot}(\mathbf{q}, \omega)$. The external electric field **E** appears to be only a tool used for time scanning external (with respect to the 2D electrons) perturbations. This is reflected in the transition from $V(\mathbf{r}, t)$ to the Fourier transform $V_{tot}(\mathbf{q}, \omega)$.

The character of collisions in the 2D electron system changes under the effect of $V_{tot}(\mathbf{q}, \omega)$. Now even for T = const and **B** = const, in addition to the equilibrium broadening kT_D^0, the perturbation $V_{tot}(\mathbf{q}, \omega)$ induced by the external field **E** contributes to broadening, and a new equilibrium state with broadening kT_D^* is established. This new equilibrium state (T, T_D^*) should be considered as nonequilibrium with respect to the state (T, T_D^0).

The initial equilibrium state (T, T_D^0) corresponds to the conditions T = const, **B** = const, and **E** = 0 ($V(\mathbf{r}, t^0)$). The perturbed nonequilibrium state (T, T_D^*) is excited under the conditions T = const, **B** = const, and **E** ≠ 0 ($V(\mathbf{r}, t) = V_{tot}(\mathbf{q}, \omega)$). Naturally, the measurements of T_D (and, respectively, of τ_q) are performed in most of the experiments in the magnetic field sweeping mode at **E** = const and T = const. This situation differs from the conditions under which the broadening kT_D is measured by the de Haas–van Alphen effect [16].

The stationarity of the nonequilibrium state (T, T_D^*) is ensured by the electron–phonon mechanism. In this state, the effect of the perturbation $V_{tot}(\mathbf{q}, \omega)$) induced by the external electrical field **E** in our 2D electron system is not accumulated. The state is stabilized by dissipation to the heat bath producing the momentum–energy relaxation with characteristic time $\tau_{eph}^{(\varepsilon, p)}$ (the right-hand side in Fig. 3).

This situation is completely analogous to electron heating. In this case, the energy derived by electrons from an electric field increases their average energy and the electron temperature T_e becomes different from the lattice temperature T. The increase in T_e continues until, with a constant external source power, an energy balance is attained due to the efficient channel of electron energy relaxation to the heat bath; for T = const, T_e is also stabilized. This situation is controlled by the energy relaxation time $\tau_{eph}^{(\varepsilon)}$. The variation in the input power from the external source affects the energy output rate from electrons to the heat bath and stabilizes the new steady-state temperature T_e.

Theoretical studies of momentum–energy relaxation of 2D electrons were carried out in [17] and the results were repeatedly applied to the analysis of experiments [18–20]. In the table, we list the parameters of the electron subsystem of the heterostructure sample whose $E_C(z)$ dependence is shown in Fig. 1 (sample no. 12 in [10]).

Below, we analyze the parameters and experimental conditions corresponding to different modes and channels of momentum and energy relaxation. Following Karpus [17], we distinguish between the modes of small-angle ($\delta\theta$) and quasi-elastic ($\delta\varepsilon$) relaxation and consider the channels of interaction of electrons with piezoelectric (PA) and deformation (DA) acoustic phonons.

For sample *1* for the *m* component, the small-angle low-temperature scattering mode ($\delta\theta$) is realized in the entire temperature range,

$$T, T_D \ll \sqrt{8m^*s^2(E_F - E_m)}, \qquad (2)$$

where *s* is the velocity of sound. It can be seen from the data in the table that the quasi-elastic scattering mode ($\delta\varepsilon$) is not realized, since the conditions

$$\sqrt{8m^*s^2E} \ll T, \quad T_D \ll \sqrt{8m^*s^2E_{m,p}} \qquad (3)$$

are obviously not satisfied for any of the components of the 2D electron system.

For the *p* component, the temperature range 1.6–12 K must be divided into two parts with respect to the temperature $\sqrt{8m^*s^2(E_F - E_m)} \approx 5$ K: (*1*) $T < 5$K and (*2*) $T > 5$K. Under the conditions $E_F - E_p \ll E_p$ for the *p* component of the 2D electron system, the small-angle relaxation mode for $T < 5$K is realized by a narrow margin. Therefore, in the region $T < 5$ K, the PA channel of a momentum–energy relaxation is dominant and the loss rate is temperature-dependent, $(\tau_{eph}^{\varepsilon,p})^{-1} \propto T$ [17]. The nonlinearity in the dependence $T_D(T)$ in the neighborhood of $T \approx 5$ K can be explained by the transition from pure PA relaxation in the $\delta\theta$ mode to (PA + DA) relaxation. We recall that $T_D \propto \tau_q^{-1}$ and the establishment of the stationary state (T, T_D^*) is controlled by $\tau_{eph}^{\varepsilon,p}$, which characterizes the drain rate of $V_{tot}(\mathbf{q}, \omega)$ from the 2D electron system to the heat bath. This is illustrated on the right-hand side of the diagram in Fig. 3.

According to review [21], momentum relaxation rates for the PA and DA mechanisms are temperature-dependent, since $(\tau_{eph}^{p}(\mathrm{PA}))^{-1} \propto T^6$ and $(\tau_{eph}^{p}(\mathrm{DA}))^{-1} \propto T^4$, regardless of the detailed form of temperature conditions (2) and (3).

If the estimation of the relaxation modes illustrated above by sample 1 with the introduction of the boundary temperature (≈5K) is applied to sample 2, we see that only the small-angle scattering mode $\delta\theta$ is effective in the entire temperature range. Therefore, there are no grounds to expect any anomalies in $T_D(T)$, in agreement with the experiment (Fig. 2, curve *2*). We note that the energy level $E_p(z)$ for sample 2 lies above the Fermi level E_F by 1.2 meV.

Let us discuss momentum relaxation. Nonthermal broadening is governed by small-angle collisions, which is in agreement with the previous discussion of the modes of relaxation from the state (T, T_D^0) to (T, T_D^*). The quasi-momentum transferred from 2D electrons to the heat bath during relaxation to the stationary state (T, T_D^*) is $q \propto \min\{q_\perp, q_\parallel\}$, where $q_\perp$ and $q_\parallel$ are the momentum components along the axis and in the heterostructure plane. For the quasi-momentum components, we have $q_\perp \propto \min\{2\pi/d, kT/\hbar s\}$, $d \in \{d_m, d_p\}$, and $q_\parallel \propto \min\{2k, kT/\hbar s\}$ [17]. The characteristic scales d_m, d_p, and $kT/\hbar s$ are given in the table. Comparing them, we may conclude that the stationarity of the state (T, T_D^*) is controlled by $q(q_\perp, q_\parallel) \propto kT/\hbar s$, i.e., by thermal longitudinal acoustic phonons. In our estimations, we used the value $s = s_L = 5.4 \times 10^5$ cm/s [22].

4. SUMMARY

In [10–14], we demonstrated the dominant role of the *n* satellite of the *p* component in the mechanism of the *e–e* interaction–induced destruction of Landau quantization in complicated 2D electronic systems. Due to spatial proximity to the sources of external perturbation $V_{tot}(\mathbf{q}, \omega)$ and to the *m* component of the 2D electrons, the *n* satellite occupies the key position in the hierarchy of *e–e* interactions.

This statement was confirmed by our analysis of the dynamics of the approach to the stationary quantum state (T, T_D^*), which is nonequilibrium with respect to (T, T_D^0). On the one hand, the external perturbation $V_{tot}(\mathbf{q}, \omega)$ affects the *n* satellite, which spreads it over the entire 2D system of degenerate electrons in time τ_{ee}^{inter}. On the other hand, the *n* satellite plays the role of a channel that controls the approach to the stationary nonequilibrium state (T, T_D^*). This channel ensures energy–momentum relaxation to the heat bath; as a result, the perturbation $V_{tot}(\mathbf{q}, \omega)$ is not accumulated in the electron system in the presence of strong intersubband *e–e* interaction. The spatial and energy parameters of the *p* component and the experimental conditions appear to be most appropriate both for responding to external perturbations and for relaxation of the excitation to the heat bath by the (PA)–(PA + DA) channel in the small-angle mode.

When the situation is examined more closely, an apparent inconsistency appears. Indeed, $\tau_{eph}^{\varepsilon,p}$ (PA, DA) varies with the magnetic field like $\propto B^{-(4-5)}$ for quantizing magnetic fields [23, 24]. Accordingly, it becomes

incorrect to determine the factor of nonthermal broadening in $T_D(T)$ by $\delta(1/B)$ from the magnetic field dependence exhibiting Shubnikov–de Haas oscillations in a finite interval of B [10]. However, this apparent contradiction is resolved if we note that the sources of perturbation of a coherent system of 2D electrons in a quantizing magnetic field are the heteroboundary defects $V_{tot}(\mathbf{q}, \omega)$. The *e–e* interaction (intrasubband and intersubband) is the tool spreading the destruction over the entire 2D electronic system. In this case $\tau_q^{\exp} \approx \tau_{ee}(T)$ [13]. The interaction of electrons with PA and DA phonons ensures the stationarity of the states (T, T_D^0) and (T, T_D^*) and the equilibrium of the 2D electronic system with the crystal lattice of the sample. In addition, we must pay attention to the following fact. In semiconductor III–V compounds, the following hierarchy of relaxation times holds: $\tau_{ee} < \tau_{ei}^p \ll \tau_{ep}^{\varepsilon, p}$; i.e., at low temperatures the energy and momentum relaxation times for scattering by piezoelectric and deformation acoustic phonons both for the bulk and for the two-dimensional case are much greater than the relaxation times for scattering by ionized impurities and for *e–e* scattering. The important role played by *e–ph* interactions (for PA and DA phonons) in the destruction of Landau quantization is due to the appreciable magnetic field dependence of $\tau_{eph}^{\varepsilon, p}$ (PA) and $\tau_{eph}^{\varepsilon, p}$ (DA) [23]. The analysis of experiments [24] has shown that the corresponding relaxation times decrease in a quantizing magnetic field by four to five orders of magnitude compared to the case $B = 0$.

ACKNOWLEDGMENTS

This study was supported by the Ministry of Industry, Science, and Technology of the Russian Federation (grant 4.15.99 of the program "Promising Areas of Research in the Physics of Condensed Matter" and by state contract no. 40.012.1.11153 of the program "Research and Design in Priority Areas of the Development of Science and Technology," section "Fundamental Studies in the Field of the Physical Sciences") and by the Ministry of Education of the Russian Federation (grant nos. E 00-3.4-75 and E 02-3.4-319).

REFERENCES

1. L. D. Landau and A. S. Kompaneets, Zh. Éksp. Teor. Fiz. **5**, 276 (1935).
2. B. I. Davydov, Zh. Éksp. Teor. Fiz. **7**, 1069 (1937).
3. V. F. Gantmakher and I. B. Levinson, *Scattering of Charge Carriers in Metals and Semiconductors* (Nauka, Moscow, 1984).
4. S.-C. Lee and J. Galbraith, Physica B (Amsterdam) **272**, 237 (1999); Phys. Rev. B **62**, 15327 (2000); G. D. Mahan and L. M. Woods, Phys. Rev. B **60**, 5276 (1999); G. D. Mahan, *Many-Particle Physics*, 3rd ed. (Kluwer Academic, New York, 2000).
5. Zh. I. Alferov, S. V. Ivanov, P. S. Kop'ev, *et al.*, Fiz. Tekh. Poluprovodn. (Leningrad) **19**, 1199 (1985) [Sov. Phys. Semicond. **19**, 734 (1985)].
6. R. Fletcher, E. Zaremba, M. D'Jorio, *et al.*, Phys. Rev. B **38**, 7866 (1988).
7. S. Ben Amor, L. Dmowski, and J. C. Portal, Appl. Phys. Lett. **57**, 2925 (1990).
8. R. T. Coleridge, Semicond. Sci. Technol. **5**, 961 (1990).
9. D. R. Leadley, R. J. Nicolas, J. J. Harris, and C. T. Foxon, Solid-State Electron. **32**, 1473 (1989); Semicond. Sci. Technol. **5**, 1081 (1990).
10. V. I. Kadushkin and F. M. Tsahhaev, Phys. Low-Dimens. Semicond. Struct., No. 1/2, 93 (2000).
11. V. I. Kadushkin, Izv. Vyssh. Uchebn. Zaved., Fiz. **43**, 52 (2000).
12. V. I. Kadushkin and A. B. Dubois, Radiotekh. Élektron. (Moscow), No. 5, 305 (2002).
13. V. I. Kadushkin, Yu. N. Gorbunova, A. B. Dubois, *et al.*, Phys. Low-Dimens. Semicond. Struct., No. 11/12, 27 (2002).
14. A. B. Dubois, Candidate's Dissertation (Ryazan. Gos. Pedagog. Univ., Ryazan, 2003).
15. V. I. Kadushkin, Fiz. Tekh. Poluprovodn. (St. Petersburg) **26**, 1323 (1992) [Sov. Phys. Semicond. **26**, 739 (1992)].
16. D. Shoenberg, *Magnetic Oscillations in Metals* (Cambridge Univ. Press, Cambridge, 1984; Mir, Moscow, 1986).
17. V. Karpus, Fiz. Tekh. Poluprovodn. (Leningrad) **20**, 12 (1986) [Sov. Phys. Semicond. **20**, 6 (1986)]; Fiz. Tekh. Poluprovodn. (Leningrad) **22**, 439 (1988) [Sov. Phys. Semicond. **22**, 268 (1988)].
18. V. I. Kadushkin and A. P. Senichkin, Fiz. Tekh. Poluprovodn. (Leningrad) **24**, 1109 (1990) [Sov. Phys. Semicond. **24**, 699 (1990)].
19. A. M. Kreshchuk, M. Yu. Martisov, T. A. Polyanskaya, *et al.*, Fiz. Tekh. Poluprovodn. (Leningrad) **22**, 604 (1988) [Sov. Phys. Semicond. **22**, 377 (1988)]; A. M. Kreschuk, M. Yu. Martisov, T. A. Polyanskaya, *et al.*, Solid State Commun. **65**, 1189 (1988).
20. G. N. Gol'tsman and K. V. Smirnov, Pis'ma Zh. Éksp. Teor. Fiz. **74**, 532 (2001) [JETP Lett. **74**, 474 (2001)].
21. B. K. Ridley, Rep. Prog. Phys. **54**, 169 (1991).
22. A. Dragys and J. Kundrotas, *Handbook on Physical Properties of Ge, Si, GaAs, and InP* (Sci. Encicl., Vilnius, 1994).
23. J. L. Schmit, J. Appl. Phys. **41**, 2876 (1970).
24. V. I. Ivanov-Omskiĭ, R. Link, and A. A. Mal'kova, Fiz. Tekh. Poluprovodn. (Leningrad) **12**, 855 (1978) [Sov. Phys. Semicond. **12**, 504 (1978)].

Translated by I. Zvyagin

Semiconductors, Vol. 38, No. 4, 2004, pp. 402–405. Translated from Fizika i Tekhnika Poluprovodnikov, Vol. 38, No. 4, 2004, pp. 417–421.

SEMICONDUCTOR STRUCTURES, INTERFACES, AND SURFACES

Oxide–*p*-InSe Heterostructures with Improved Photoelectric Characteristics

V. N. Katerinchuk* and Z. D. Kovalyuk

Frantsevich Institute of Materials Science Problems, National Academy of Sciences of Ukraine, Chernovtsy, 58001 Ukraine

**e-mail: chimsp@unicom.cv.ua*

Submitted July 30, 2003; accepted for publication September 9, 2003

Abstract—Heterostructures consisting of *p*-InSe and native oxide were formed by thermal oxidation of indium selenide crystals in air. Long-term (for 1–5 days) oxidation of InSe substrates at 450°C leads to changes in both the photosensitivity spectral band and the photoelectric parameters of the heterostructures compared to samples oxidized for 5–15 min. These changes are due to the layer-by-layer formation of additional oxide phases on the semiconductor surface. For the best heterostructures, the open-circuit voltage attains 0.6 V and the short-circuit current density is 30–35 mA/cm^2 under saturation conditions. The electrical characteristics of the heterostructures are distorted by the effect of series resistance, which complicates the determination of the potential-barrier height and the mechanism of current flow through the barrier. © *2004 MAIK "Nauka/Interperiodica".*

1. INTRODUCTION

The layered structure of InSe crystals offers an advantage over other semiconductors in the preparation of high-quality substrates and heterostructures. The surface obtained by cleaving single-crystal ingots is specular; it remains chemically inert under normal conditions. Indium selenide substrates can be prepared as thin as a few micrometers, which is more characteristic of semiconductor films than of bulk crystals. The band gap of InSe is 1.2 eV at room temperature. This value is very close to optimum from the point of view of the efficiency of solar cells. Therefore, the interest in InSe as a potential material for solar cells remains high. Research in this field is aimed at both developing different types of photosensitive InSe-based heterostructures and optimizing their parameters.

Heterostructures based on InSe can be formed by thermal oxidation of InSe substrates in air [1]. During oxidation, an oxide film is formed on the substrate surface, and the oxide–semiconductor system acquires diode properties. The heterostructures thus formed show photosensitivity only when *p*-InSe crystals are used. The phase composition of an oxide film depends on the temperature and time oxidation conditions [1–6]. A change in the phase composition of an oxide leads to changes in the potential barrier of a heterostructure and the photosensitivity characteristics. In [2–5], attention was focused on the chemical nature of oxides formed on an InSe surface under different temperature and time conditions. Different oxide phases were revealed by X-ray diffraction, cathodoluminescence, and Raman scattering methods. Investigation of temperature and time conditions of formation of a potential barrier in oxide–*p*-InSe heterostructures was performed in [6]. Specifically, it was concluded in [6] that photoelectric parameters of heterostructures deteriorate as the oxidation time increases from 30 to 120 min.

The experimental results obtained in this study indicate a significant improvement in the photoelectric characteristics of heterostructures consisting of *p*-InSe and native oxide as a result of relatively long-term (over several days) oxidation at T = 450°C. It is shown that, under saturation conditions, the open-circuit voltage in such heterostructures attains maximum (the half-width of the InSe band gap). Spectral studies of the photosensitivity of these structures show that, along with In_2O_3, an intermediate compound with a band gap of about 2.0 eV is formed and a barrier arises between the basic semiconductor and this intermediate layer during long-term oxidation.

2. EXPERIMENTAL

We used *p*-InSe:Cd single crystals grown by the Bridgman method to prepare heterostructures. Depending on the impurity concentration, the resistivity of *p*-InSe samples varied from 10^3 to 10^4 Ω cm. The grown ingots were cut into wafers 4–5 mm thick and then cleaved into plane-parallel plates 0.3–0.4 mm thick. The InSe samples thus obtained were oxidized in air at T = 450°C in an electric temperature-controlled furnace. The oxidation temperature was chosen on the basis of the results of testing and selecting heterostructures with the best photoelectric parameters from the samples fabricated under different conditions: at temperatures from 200 to 500°C with a step of 50 K and oxidation times from 5 to 60 min with a step of 5 min. The long-term oxidation of InSe was performed for 1–5 days with a step of one day. After oxidation, the

samples were cleaved again to leave an oxide film on one side only. All the other sides covered with oxide were cut off. Some samples prepared in this way were placed in evacuated cells and subjected to thermal annealing at the same temperature to reveal other phase changes in the basic material. Ohmic contacts were prepared from pure indium, which wets the surfaces of both the oxide and the semiconductor fairly well. To exclude nonohmic behavior of the contact between indium and *p*-InSe, the surface of the latter was mechanically damaged [7].

The photosensitivity spectra of the fabricated heterostructures were measured at room temperature using an MDR-3 monochromator with a resolution of 26 Å. The samples were illuminated from the oxide-film side. All the spectra were normalized to the number of incident photons.

The capacitance–voltage (*C–V*) characteristics of the heterostructures under investigation were measured using an E8-2 capacitance bridge. The relative error in the capacitance measurements did not exceed 5×10^{-3}. In order to determine the mechanism of current flow through a barrier, static current–voltage (*I–V*) characteristics of forward-biased heterostructures were measured.

3. EXPERIMENTAL RESULTS AND DISCUSSION

3.1. Spectral and Photovoltaic Characteristics

The photosensitivity spectra of the heterostructures based on InSe oxidized at $T = 450$°C for different times are shown in Fig. 1. The shape of the spectra is typical of heterostructures: the spectra are limited from the left and right. The energy positions of the photosensitivity-band edges, which are determined by the light absorption in the heterostructure components, amount to 1.2, 2.0, and 3.7 eV. The long-wavelength limit of the photoresponse is the same for all the samples; it is related to the light absorption in the basic material (InSe). The short-wavelength limit is related to the absorption in the oxide film. As can be seen from Fig. 1a, the oxidation time of InSe significantly affects the position of the high-energy edge of the spectrum and, hence, the phase composition of the oxide. Short-term (5–15 min) oxidation of InSe (curve *6*) leads to the formation of a film of indium trioxide In_2O_3, whose optical and electric properties were investigated by us in [1]. The X-ray diffraction identification of the In_2O_3 phase on an InSe surface was performed later in [2]. The passage from short- to long-term oxidation of InSe substrates is accompanied by the formation of a new oxide phase. This fact manifests itself in the appearance of the high-energy edge of photosensitivity at 2.0 eV in the spectral dependences (curves *1–5*).

On the basis of Raman spectroscopic data, it was suggested in [3] that it is the $In_2(SeO_4)_3$ compound that corresponds to the phase with the photosensitivity edge at 2.0 eV. It was also suggested in [2–6] that the oxide film may contain inclusions of other phases, for example, β-In_2Se_3 and γ-In_2Se_3 (the band gap widths of these compounds are 1.27 and 2.0 eV, respectively). In order to verify this suggestion and check the possibility of forming other phases in the In–Se system, we studied the In_2O_3–*p*-InSe heterostructures fabricated by 15-min oxidation (Fig. 1a, curve *6*). The samples were annealed in vacuum at the same temperature (450°C) at which the substrates were oxidized. It was found that the photoresponse spectra of the corresponding samples showed no formation of new chemical phases (Fig. 1b). As can be seen from Fig. 1b, the photoresponse spectrum of the annealed samples (curves *2–4*) changes only insignificantly in comparison with the spectrum of the unannealed samples (curve *1*), while the short-wavelength photosensitivity is controlled by the light absorption in the In_2O_3 oxide. Moreover, the photoelectric characteristics of the heterostructures annealed in vacuum are much worse than those of the heterostructures oxidized in air.

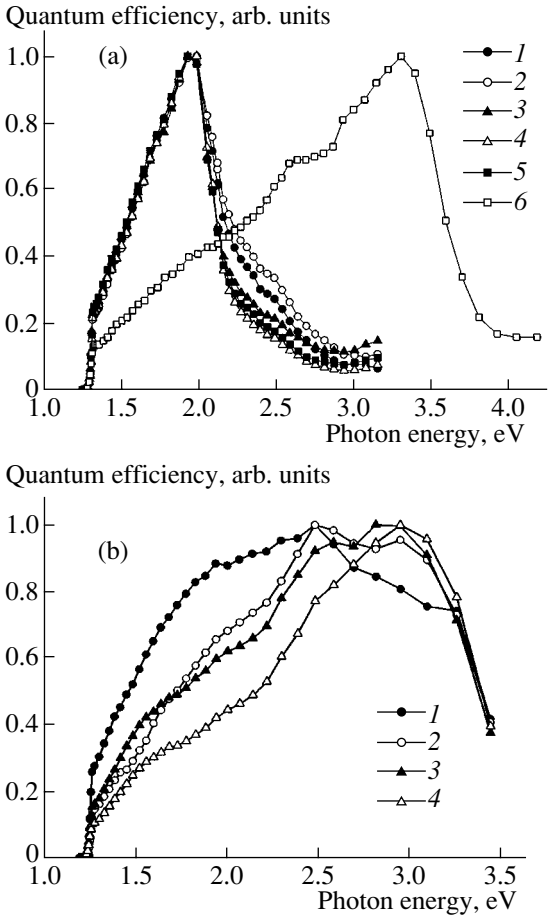

Fig. 1. Spectra of relative quantum efficiency of the oxide–*p*-InSe heterostructures at room temperature. The oxidation temperature 450°C. (a) Oxidation for (*1*) 1, (*2*) 2, (*3*) 3, (*4*) 4, and (*5*) 5 days and (*6*) 15 min. (b) Oxidation for 15 min (*1*) without annealing and (*2–4*) with annealing in vacuum (after oxidation) for (*2*) 0.5, (*3*) 1, and (*4*) 2 days.

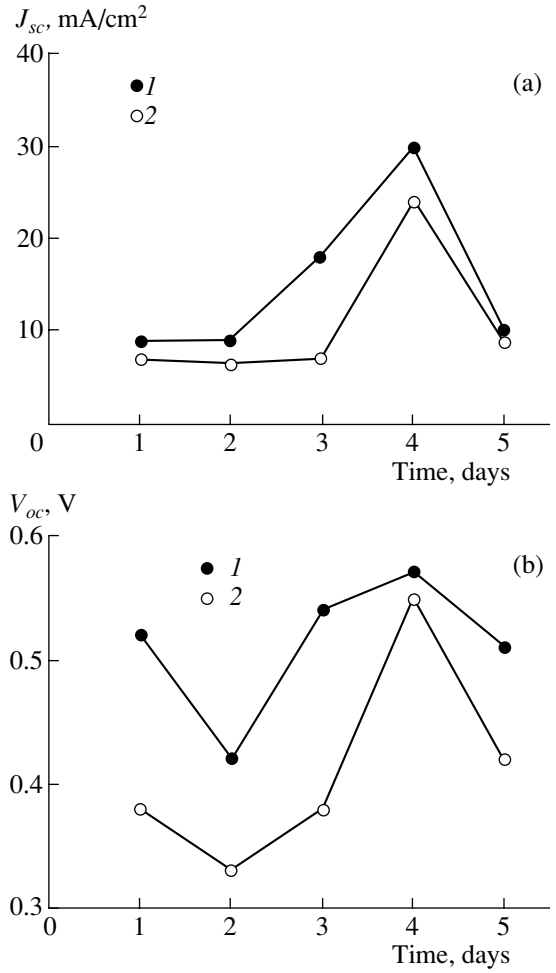

Fig. 2. Dependences of (a) the current density and (b) the open-circuit voltage on oxidation time for two sets of samples of oxide–*p*-InSe heterostructures (*1*, *2*). The intensity of illumination 100 mW/cm^2.

It can also be seen from Fig. 1a that the falloff of photoresponse for the short-wavelength edge is more abrupt for curves *4* and *5* in comparison with curves *1–3*. This circumstance indicates that, with an increase in oxidation time, the $In_2(SeO_4)_3$ layer becomes thicker. Nevertheless, this layer remains too thin to exclude completely the absorption of photons with an energy exceeding 2.0 eV. The front film In_2O_3, limiting the penetration of oxygen into the crystal bulk, impedes the growth of thicker $In_2(SeO_4)_3$ films. The $In_2(SeO_4)_3$ phase occupies the intermediate position between InSe and In_2O_3, and a potential barrier is formed at the interface between the InSe and the intermediate phase.

Relative comparison of the photoresponse of the heterostructures oxidized for different times shows that its value changes significantly. An increase in the oxidation time leads to an increase in the absolute value of the short-circuit photocurrent by more than an order of magnitude. The photocurrents in the samples represented by curves *1* and *4* differ by about a factor of 20.

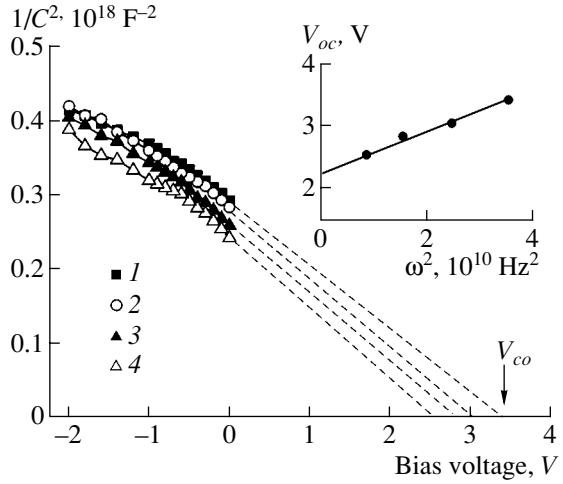

Fig. 3. Capacitance–voltage characteristics of the oxide–*p*-InSe heterostructures at frequency f = (*1*) 30, (*2*) 25, (*3*) 20, and (*4*) 15 kHz. The measurements were performed at 295 K. The inset shows the frequency dependence of the capacitance cutoff voltage.

Figure 2 shows the dependences of the short-circuit current density (I_{sc}) and the open-circuit voltage (V_{oc}) in the heterostructures under study on oxidation time. The testing was performed for two groups of samples exposed to light with a power of 100 mW/cm^2. It can be seen from Fig. 2 that the general trend toward improvement of the photoelectric parameters is observed for both groups of samples. It was found that oxidation of substrates at T = 450°C for four days yields the best results.

3.2. Capacitance–Voltage and Current–Voltage Characteristics

The rectifying properties of heterostructures with improved photoelectric parameters, obtained by long-term oxidation with the formation of an intermediate oxide layer, are of interest. Measurements of *C–V* characteristics were performed on the samples oxidized at T = 450°C for four days, i.e., the samples with the best photoelectric parameters. The height of the potential barrier in the heterostructures was determined from the *C–V* characteristics shown in Fig. 3. All the measured *C–V* characteristics are linear in the $1/C^2$–*V* coordinates, which is indicative of an abrupt *p–n* junction. As can be seen from Fig. 3, a change in the frequency of a probe signal leads to a shift of the *C–V* characteristic. The frequency dependence of the *C–V* characteristics is caused by the effect of the series resistance of heterostructures [8]. As follows from [8], in order to find the actual value of the barrier height (qV_D), one has to approximate the frequency dependence of the cutoff voltage (V_{co}) to zero frequency in the $V_{co} - \omega^2$ coordinates ($\omega = 2\pi f$, f is the frequency of the test signal). The approximated values of V_{co} turned out to be highly overestimated in comparison with the band gap width of InSe (qV_D = 2.25 eV) (see Fig. 3, inset). Measure-

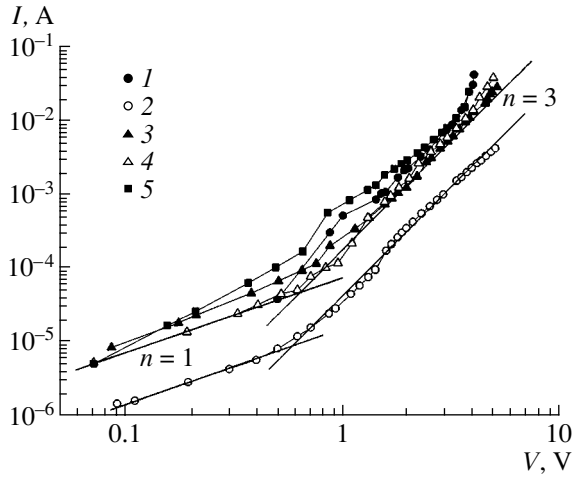

Fig. 4. Forward portions of the current–voltage characteristics of the oxide–*p*-InSe heterostructures. Oxidation time is (*1*) 1, (*2*) 2, (*3*) 3, (*4*) 4, and (*5*) 5 days. The exponent n in the dependence $I \propto V^n$ is indicated. The measurements were performed at 295 K.

ments of the *C–V* characteristics on some samples (more than three) showed that the potential-barrier height determined from these characteristics ranges within 1–3 eV and the results are not reproducible. In our opinion, the reason is that the measured capacitance is the sum of two capacitances connected in series, one of which is the sought barrier capacitance and the other results from the nonohmic behavior of the current-collecting contact with the substrate. Both the capacitances are due to the formation of depleted regions in the substrate at two opposite sides, front and rear. Thus, the capacitance of the rear region is not constant since it depends on the conditions under which the sample surface is damaged before the contact formation. Therefore, the corresponding value of $1/C^2$ shifts up in the ordinate axis. This shift results in higher values of cutoff voltage and an overestimated barrier height. We also found some discrepancy between the results of measurements for different samples. The only reliable parameter that can be obtained from the *C–V* characteristics shown in Fig. 3 is the concentration of uncompensated acceptor impurities $N_A–N_D$ in the substrate. The slope of the *C–V* characteristics corresponds to a value of 10^{15} cm^{-3}. A value of the same order of magnitude was obtained for the concentration of major carriers in *p*-InSe:Cd in [9].

In order to study the mechanisms of current flow through heterostructures consisting of *p*-InSe and native oxide, we measured the forward portions of the *I–V* characteristics (see Fig. 4). In the logarithmic coordinates, the *I–V* characteristics of all the heterostructures obtained by oxidation for different times exhibit two similar dependences: $I \propto V$ and $I \propto V^3$. Cubic dependence is observed in the *I–V* characteristics at large forward biases in an interval of several orders of magnitude of current. We failed to find an exponential dependence of current on voltage in heterostructures formed by long-term oxidation. The cause of this may be, as in the case of *C–V* characteristics, a depleted layer in the rear contact region, which makes the main contribution to the series resistance of a heterostructure. The theory of space-charge-limited currents predicts that an ohmic portion and a cubic dependence can be observed simultaneously in *I–V* characteristics, which we found experimentally in [10]. The results of the investigations of both *I–V* and *C–V* characteristics indicate that an additional depleted region arises in heterostructures consisting of *p*-InSe and native oxide, while the efficiency of forming an ohmic contact with the substrate using mechanical damage of the surface of the latter is rather low.

4. CONCLUSION

It is shown that oxidation of *p*-InSe crystals in air leads to the formation of a potential barrier in the oxide–semiconductor system, while a change in the oxidation conditions affects the photoelectric parameters of heterostructures. Under saturation conditions, the maximum values of the open-circuit voltage (0.6 V) and the short-circuit current density (30–35 mA/cm^2) were obtained for *p*-InSe samples oxidized in air at 450°C for four days. The changes in the photosensitivity spectra of the heterostructures are due to the formation of oxide phases In_2O_3 and $In_2(SeO_4)_3$. The electrical characteristics of the heterostructures under study differ from ideal due to the effect of the series resistance. The main reason for the appearance of the series resistance is the nonohmic behavior of the current-collecting contact with the basic semiconductor.

REFERENCES

1. V. N. Katerinchuk and M. Z. Kovalyuk, Pis'ma Zh. Tekh. Fiz. **18**, 70 (1992) [Sov. Tech. Phys. Lett. **18**, 394 (1992)].
2. O. A. Balitskii, R. V. Lutsiv, V. P. Savchyn, and J. M. Stakhira, Mater. Sci. Eng. B **56**, 5 (1998).
3. O. A. Balitskii, V. P. Savchyn, and V. O. Yukhymchuk, Semicond. Sci. Technol. **17**, L1 (2002).
4. V. P. Savchyn and C. B. Kutsay, Thin Solid Films **361–362**, 123 (2000).
5. O. A. Balitskii, N. N. Berchenko, V. P. Savchyn, and J. M. Stakhira, Mater. Chem. Phys. **65**, 130 (2000).
6. S. I. Drapak, V. B. Orletskiĭ, Z. D. Kovalyuk, and V. V. Netyaga, Fiz. Tekh. Poluprovodn. (St. Petersburg) **37**, 196 (2003) [Semiconductors **37**, 187 (2003)].
7. A. G. Milnes and D. L. Feucht, *Heterojunctions and Metal–Semiconductor Junctions* (Academic, New York, 1972; Mir, Moscow, 1975), Chap. 9.
8. A. M. Goodman, J. Appl. Phys. **34**, 329 (1963).
9. J. Martinez-Pastor, A. Segura, J. L. Valdes, and A. Chevy, J. Appl. Phys. **62**, 1477 (1987).
10. M. A. Lampert and P. Mark, *Current Injection in Solids* (Academic, New York, 1970; Mir, Moscow, 1973), Chap. 13.

Translated by Yu. Sin'kov

Semiconductors, Vol. 38, No. 4, 2004, pp. 406–409. Translated from Fizika i Tekhnika Poluprovodnikov, Vol. 38, No. 4, 2004, pp. 422–425.

SEMICONDUCTOR STRUCTURES, INTERFACES, AND SURFACES

Photosensitivity of the Structures Based on Quinary Solid Solutions of the Isoelectronic Series of Germanium

A. A. Vaĭpolin*, Yu. A. Nikolaev*, V. Yu. Rud', Yu. V. Rud'*, and E. I. Terukov***

**Ioffe Physicotechnical Institute, Russian Academy of Sciences, Politekhnicheskaya ul. 26, St. Petersburg, 194021 Russia*

***St. Petersburg State Polytechnical University, St. Petersburg, 195251 Russia*

Submitted October 1, 2003; accepted for publication October 2, 2003

Abstract—The temperature dependence of resistivity and the spectrum of optical absorption are investigated for $(Cu_2GaSe_3)_{0.6}(3GaAs)_{0.4}$ single crystals. Photosensitive structures of several types (Schottky barriers, welded structures, and photoelectrochemical cells) have been developed. The rectification and the photovoltaic effect are observed for the structures obtained. The revealed specific features of photosensitivity in structures and possibilities for their practical application as photoconverters are also discussed. © *2004 MAIK "Nauka/Interperiodica".*

The formation of semiconductor solid solutions is based on isovalent or heterovalent atomic substitution, which is widely used in semiconductor electronics for obtaining materials with required fundamental properties [1]. In recent years, the isovalent solid solutions of III–V compounds became most widespread in the development of semiconductor lasers and photoconverters [1–3].

Along with binary phases, the investigations of the interatomic interaction have also been developed for systems with a more complex composition, namely, for ternary and more complex compounds [1, 4, 5]. Specifically, pioneering investigations of the chemical interaction in the $(Cu_2GaSe_3)_x(3GaAs)_{1-x}$ system, which were carried out even prior to the investigation of solid solutions of III–V compounds, led to the growth of first single crystals of quinary single-phase solid solutions, which include as much as ~40 mol % of GaAs [4]. Such solutions are unique in their own way, since they contain the maximum number of elements positioned in the germanium series of the periodic table. This specific feature automatically provided satisfaction of the condition for proximity of ion radii of atoms forming the tetrahedral phase, which is necessary for obtaining equilibrium solid solutions [2]. Up to now, heterovalent solid solutions based on binary III–V compounds have been practically not investigated [6]. This paper is concerned with experimental investigations of the physical properties of single crystals of the $(Cu_2GaSe_3)_x(3GaAs)_{1-x}$ solid solution ($x = 0.6$) and the development of the first photosensitive structures based on them.

In order to form the photosensitive structures, we used homogeneous crystals of the $(Cu_2GaSe_3)_x(3GaAs)_{1-x}$ solid solution grown by the gas-transport reactions method [4]. The largest dimensions of the single-crystal wafers grown were ~$5 \times 5 \times 1$ mm^3 with the most developed postgrowth mirror face (111). According to X-ray diffraction investigations, the single crystals of the $(Cu_2GaSe_3)_{0.6}(3GaAs)_{0.4}$ have a face-centered cubic (fcc) lattice. The space group is $F43m$, and the unit cell parameter $a = 5.6054 \pm 0.0004$ Å at $T = 300$ K. According to Vegard's law [4], this corresponds to $x = 0.6$. From the sign of the thermoelectric power, all the $(Cu_2GaSe_3)_{0.6}(3GaAs)_{0.4}$ single crystals obtained have *n*-type conductivity. A high resistivity $\rho = 10^8$–10^9 Ω cm at $T = 300$ K is characteristic of the crystals of the solid solution with $x = 0.6$. In the case of GaAs, such a value is attained only due to the doping [2]. As the temperature increases from 300 to 400 K, the resistivity of crystals usually follows Arrhenius' law (Fig. 1),

$$\rho = \rho_0 \exp(E/kT), \qquad (1)$$

in which the activation energy of the levels $E = 0.50$–0.53 eV may by associated with the thermalization of electrons from a deep donor level into the conduction band on the assumption of strong compensation [7].

For single-crystal samples of the $(Cu_2GaSe_3)_{0.6}(3GaAs)_{0.4}$ solid solution, the spectra of optical transmission were also measured at $T = 300$ K. From these spectra, the coefficient of optical absorption was found from the relationship [8]

$$\alpha = \frac{1}{d}\ln\left(\frac{(1-R_0)^2}{2T_0} + \sqrt{\left[\frac{(1-R_0)^2}{2T_0}\right]^2 + R_0^2}\right), \qquad (2)$$

where d is the wafer thickness and the reflectance $R_0 = 0.3$.

A typical spectral dependence $\alpha(\hbar\omega)$ for single crystals of the solid solution of the *n*-type of conductivity is shown in Fig. 2 (curve *1*). It can be seen from Fig. 2 that α starts to increase rapidly at energy $\hbar\omega \geq 1.17$ eV. This value may be used as a preliminary estimate of the band gap E_g of the $(Cu_2GaSe_3)_{0.6}(3GaAs)_{0.4}$ solid solution. In the coordinates $(\alpha\hbar\omega)^2$–$\hbar\omega$ (Fig. 2,

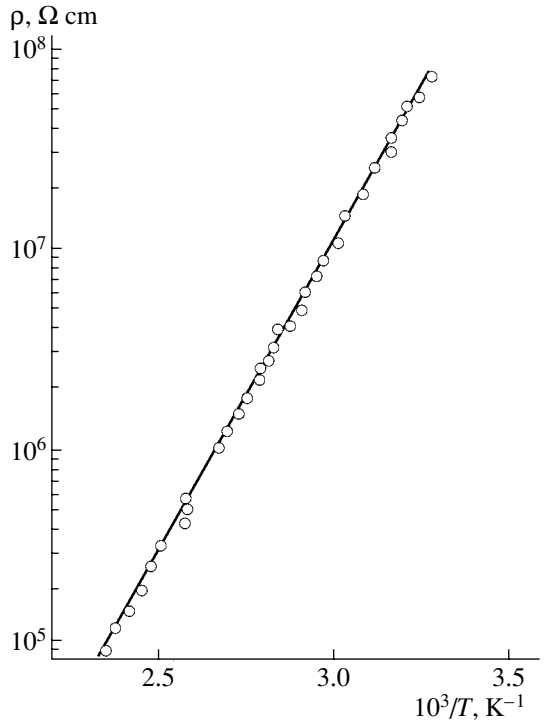

Fig. 1. Temperature dependence of resistivity of a $(Cu_2GaSe_3)_{0.6}(3GaAs)_{0.4}$ single crystal (sample 2).

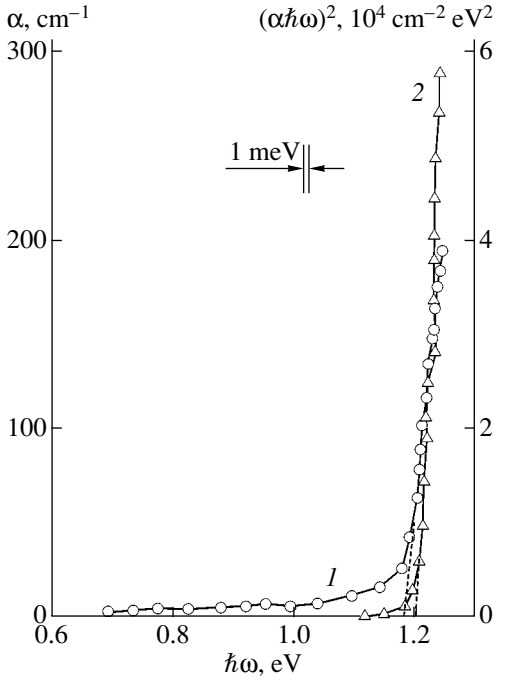

Fig. 2. Dependences of (*1*) coefficient of optical absorption α and (*2*) $(\alpha\hbar\omega)^2$ magnitude on the energy of incident photons for an *n*-$(Cu_2GaSe_3)_{0.6}(3GaAs)_{0.4}$ single crystal at T = 300 K.

curve *2*), a linear portion is observed. The extrapolation of this dependence to $(\alpha\hbar\omega) \longrightarrow 0$, according to [9], allows us to determine the band gap $E_g \simeq 1.20$ eV at T = 300 K.

With allowance made for the theory of fundamental optical absorption in semiconductors [9], the fulfillment of the quadratic law $(\alpha\hbar\omega)^2 \propto \hbar\omega$ allows us to state that the band-to-band transitions for quinary solid solutions are direct, similarly to the GaAs binary compound [2, 6]. Figure 3 shows the dependence of the band gap on the composition of the $(Cu_2GaSe_3)_x(3GaAs)_{1-x}$ solid solution. This dependence is almost linear, which may indicate that the energy-band structure in the limits of this system remains invariable and is similar to that characteristic of the initial compounds forming this system. This applies primarily to GaAsm, since data on the band structure of the Cu_2GaSe_3 ternary compound are still lacking [6].

For $(Cu_2GaSe_3)_{0.6}(3GaAs)_{0.4}$ homogeneous single crystals, attempts were also made to develop several types of photosensitive structures. If these attempts were successful, this would open up possibilities for applying photoelectric spectroscopy for research into new semiconductor phases with a statistical distribution of five elements isoelectronic to Ge (Cu, Ga, Ge, As, and Se) at the sites of the sphalerite lattice.

Rectification was observed in preliminary investigations of the current–voltage characteristics of the contact of single-crystal wafers of the quinary solid solution with thin films of several metals (In, Cu, Ag). The forward direction corresponds to the positive polarity of the external bias at the In film. The rectification factor K, which was defined as the forward-to-reverse current ratio for the external biases $U \simeq 5$–10 V, was usually not large, and for the best structures $K \simeq 5$ at T = 300 K.

Along with the deposition of thin metal films, in some cases we succeeded in obtaining rectifying struc-

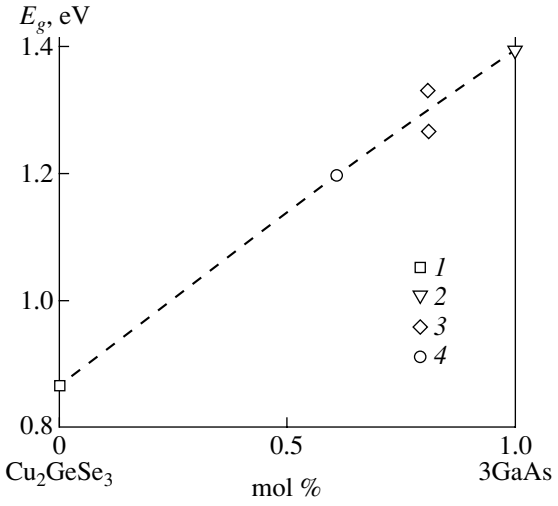

Fig. 3. Composition dependence of the band gap for the $(Cu_2GaSe_3)_x(3GaAs)_{1-x}$ system at T = 300 K. Published data: (*1*, *2*) [6], (*3*) [4], and (*4*) this study.

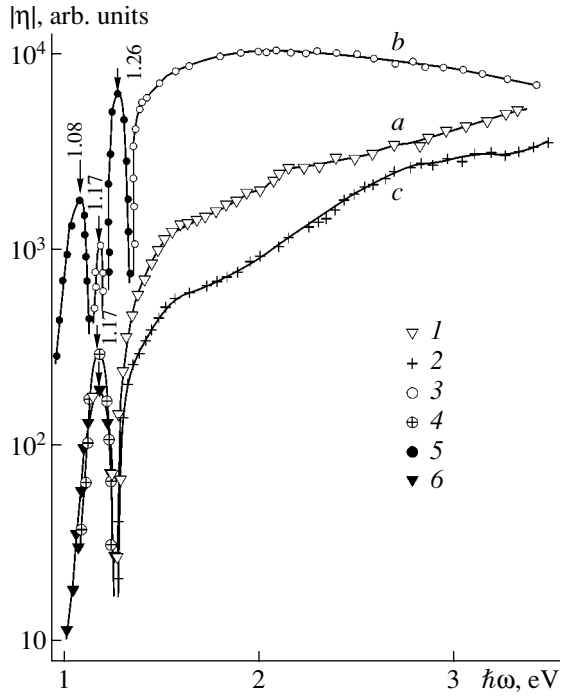

Fig. 4. Spectral dependences of the relative quantum efficiency of photoconversion $\eta(\hbar\omega)$ (*a*) for the In/*n*-$(Cu_2GaSe_3)_{0.6}(3GaAs)_{0.4}$ surface-barrier structure, (*b*) for the welded structure, and (*c*) for the H_2O/*n*-$(Cu_2GaSe_3)_{0.6}(3GaAs)_{0.4}$ photoelectrochemical cell in nonpolarized light at $T = 300$ K. The barrier-contact side of the structures was illuminated. The sign of photovoltage at the crystal for the data (*1–3*) and (*4–6*) corresponds to plus and minus, respectively.

tures due to the electrical discharge between thin ($d \simeq$ 0.1 mm) Pt or Ag conductors near the surface of the solid solution wafer. Such discharge caused the formation of structures (henceforth, welded structures) with the rectification $K \simeq 2$–3 at 300 K. The forward direction corresponded to a negative external bias at the solid solution crystal, similarly to Schottky barriers at the same crystals. We may assume that the discharge caused the variation in the composition of the solid solution in the surface region of the crystal, which led to the formation of the active region.

Finally, the contacts of natural mirror planes of the solid solution wafers with a liquid electrolyte (distilled water) also exhibited rectification with the largest value $K \simeq 10$. The polarity of the forward direction was the same as for the previous structures. The residual resistance (the base resistance) for the Schottky barriers, welded structures, and photoelectrochemical cells based on $(Cu_2GaSe_3)_{0.6}(3GaAs)_{0.4}$ solid solutions was almost the same, $R_0 \simeq (1–5) \times 10^8$ Ω at $T = 300$ K. Apparently, this behavior of the resistance is caused by the fact that the value of R_0 for the structures so different by nature is mainly determined by the electrical properties of the solid solution. The reverse portions of the steady-state current–voltage characteristics had the form $I \propto U^\gamma$, where the exponent $\gamma \simeq 1.1$–2, and increased as the bias voltage increases. This specific feature of the reverse characteristic may be caused by imperfections at the periphery of the first structures based on these crystals.

With the illumination of structures of different types with nonpolarized radiation, the photovoltaic effect is observed. This effect is most pronounced with the illumination of the barrier-contact side of the structures. The highest voltage photosensitivity was observed for In/$(Cu_2GaSe_3)_{0.6}(3GaAs)_{0.4}$ Schottky barriers: $S_U^m \simeq 10^2$ V/W at $T = 300$ K. It should be also noted that the photovoltage sign for the structures based on these crystals in the region of highest photosensitivity corresponds to the rectification direction.

Typical spectral dependences of the relative quantum efficiency of photoconversion $\eta = f(\hbar\omega)$ for each type of structure developed are given in Fig. 4 as an example. It can be seen that the Schottky barriers, welded structures, and photoelectrochemical cells are photosensitive over a wide spectral range from 1 to 3.5 eV. The spectral dependences $\eta(\hbar\omega)$ in structures that are so different by nature are found to be very similar. This may be grounds to assume that the photosensitivity spectra are determined by the interaction of the incident light with the quinary solid solution crystals.

The main special features of the photosensitivity spectra are as follows. The highest photosensitivity in the structures fabricated is attained within the fundamental band of the solid solution ($x = 0.6$). For the surface-barrier structure and for the electrochemical cell based on the solid solution, as can be seen from Fig. 4 (curves *a*, *c*), the photosensitivity continues to increase at $\hbar\omega > E_g$ as the photon energy increases. The latter circumstance may indicate that the barriers fabricated provide effective suppression of the surface recombination of photogenerated pairs. However, it should be noted that, in the $\eta(\hbar\omega)$ spectrum for the welded structure (curve *b*) for $\hbar\omega > 2.3$ eV, the photosensitivity ceases to increase and even decreases. Thus, from the point of view of providing a high efficiency of collection of photogenerated pairs, the welded structures are inferior to the surface-barrier structures and photoelectrochemical cells.

The second important specific feature of the $\eta(\hbar\omega)$ spectra of the structures obtained is the inversion of the conductivity sign for $\hbar\omega < E_g$ with respect to the region $\hbar\omega > E_g$ (Fig. 4). Along with this, anomalies are also found in the luminance–voltage characteristics. These anomalies clearly manifest themselves in the vicinity of the energy $\hbar\omega \simeq 1.24$ eV and consist in the fact that the photovoltage does not level off as the intensity of light increases but, on the contrary, decreases. For some structures, specific features in the form of alternating photocurrent peaks of different polarity [for example, see Fig. 4 (curve *b*)] extend over the entire spectral range of photosensitivity up to $\hbar\omega \simeq 3.6$ eV. It is not

inconceivable that all the above-listed anomalies of the $\eta(\hbar\omega)$ spectra may be indicative of the manifestation of self-organization effects in quinary solid solutions. It is evident that additional research in this field is required to gain insight into the observed anomalies of the photosensitivity of the structures.

Thus, we showed that photosensitive structures based on quinary solid solutions of elements of the isoelectronic series of germanium could be developed. These structures may find application in wide-gap photoconverters, including solar cells. However, in the latter case, the problem of doping should be resolved with allowance made for possible processes of self-organization, whose probability may considerably increase in multicomponent phases.

REFERENCES

1. N. A. Goryunova, *The Chemistry of Diamond-Like Semiconductors* (Leningr. Gos. Univ., Leningrad, 1963; Chapman and Hall, London, 1965).
2. O. Madelung, *Physics of III–V Compounds* (Wiley, New York, 1964; Mir, Moscow, 1967).
3. Zh. I. Alferov, V. M. Andreev, and N. N. Ledentzov, in *Ioffe Institute. 1918–1998* (Ioffe Physicotechnical Inst., St. Petersburg, 1998).
4. G. K. Averkieva, G. V. Berdichevskiĭ, A. A. Vaĭpolin, *et al.*, Izv. Akad. Nauk SSSR, Neorg. Mater. **4**, 1064 (1968).
5. A. A. Vaĭpolin, Fiz. Tverd. Tela (Leningrad) **31** (12), 165 (1989) [Sov. Phys. Solid State **31**, 2119 (1989)].
6. *Physicochemical Properties of Semiconductor Materials: A Handbook*, Ed. by A. V. Novoselova and V. B. Lazarev (Nauka, Moscow, 1979).
7. J. S. Blakemore, *Semiconductor Statistics* (Pergamon Press, Oxford, 1962; Mir, Moscow, 1964).
8. H. Y. Fan and M. O. Becker, in *Proceedings of Conference of Semiconductor Materials* (Academic, New York, 1951).
9. S. M. Sze, *Physics of Semiconductor Devices*, 2nd ed. (Wiley, New York, 1981; Mir, Moscow, 1973).

Translated by N. Korovin

Semiconductors, Vol. 38, No. 4, 2004, pp. 410–418. Translated from Fizika i Tekhnika Poluprovodnikov, Vol. 38, No. 4, 2004, pp. 426–435.

LOW-DIMENSIONAL SYSTEMS

Energy States in Short-Period Symmetrical and Asymmetrical $(GaAs)_N/(AlAs)_M$ Superlattices: The Effect of the Boundary Conditions

K. E. Glukhov*^, A. I. Bercha*, D. V. Korbutyak, and V. G. Litovchenko****

**Uzhgorod National University, Uzhgorod, 88000 Ukraine*

^e-mail: kglukhov@issp.univ.uzhgorod.ua

***Institute of Semiconductor Physics, National Academy of Sciences of Ukraine, Kiev, 03028 Ukraine*

Submitted May 27, 2003; accepted for publication June 4, 2003

Abstract—Obtained experimental data on low-temperature photoluminescence are used to numerically simulate the energy states in symmetrical and asymmetrical short-period $(GaAs)_N/(AlAs)_M$ superlattices with the (001) orientation. The matrix formalism in the envelope-function method is employed to study trends in the behavior of the miniband spectrum in models with different boundary conditions. It is shown that correct information about the type of transitions in the materials under consideration can be obtained even if the boundary conditions are diagonal. The effect of corrections on the miniband spectrum that arise when mixing of the states belonging to the Γ and *X* valleys is taken into account and a δ-functional potential localized at the heterointerface is present is studied. © *2004 MAIK "Nauka/Interperiodica".*

1. INTRODUCTION

A great amount of experimental material on the electronic properties of $(GaAs)_N/(AlAs)_M$ superlattices (SLs) with crystallographic orientation (001) has been amassed to date [1–13], and this material is being added to all the time. In addition, the energy-band structure of starting bulk materials that form these SLs has been adequately studied. As a result, these SLs are convenient test objects to consider theoretically and subsequently check the results of simulation. Furthermore, these heterostructures are of interest because they could be used in the fabrication of new semiconductor lasers that operate in the visible region of the spectrum.

According to a number of recent reports [14–19], the envelope-function method can be used to describe the energy states even in short-period SLs ($N \le 10$, $M \le 10$). Indeed, even preliminary calculation based on the Bastard model [20] show that the envelope-function method can be used to obtain qualitative agreement of theoretical results related to a short-period $(GaAs)_N/(AlAs)_M$ SL (001) with corresponding experimental data [21].

It is comparatively easy and convenient to use the envelope-function approximation to simulate the SL energy states and identify the experimentally obtained energies of transitions between these states. Nevertheless, the correct solution of the problem requires subsequent consideration of the dependence of energy states on the boundary conditions at the heterointerfaces. These conditions have not been taken into account in preliminary simulation performed for a number of symmetrical and asymmetrical short-period $(GaAs)_N/(AlAs)_M$ SLs [8, 10]. These SLs are of great interest since it has been found recently that asymmetrical short-period $(GaAs)_N/(AlAs)_M$ SLs are direct-gap structures [8–10] (it is noteworthy that symmetrical short-period $(GaAs)_N/(AlAs)_M$ ($N < 10$) SLs are indirect-gap structures, as is confirmed, for example, by the results of calculating the energy-band structure using the method of semiempirical pseudopotential [22]). The observed fact that the structures are direct-gap, as well as the amplification of light (observed, in particular, in SLs with the ratio of monolayers in a period $N/M = 6/3$) [23]), may pave the way for the fabrication of semiconductor lasers that are designed for the red region of the spectrum and have an active zone based on unstrained $(GaAs)_N/(AlAs)_M$ layers. It is worth noting that semiconductor lasers for the wavelength range 690–730 nm are not commercially produced at present. It follows from the above that there is a need for additional, both theoretical and experimental, study of the fact that the asymmetrical SLs under consideration are direct-gap structures.

Taking the above considerations into account, we decided to study experimentally the spectra of low-temperature photoluminescence (PL) for a group of symmetrical and asymmetrical $(GaAs)_N/(AlAs)_M$ SLs (with N/M = 10/10, 10/5, 8/4, and 6/3) subjected to various levels of excitation. We used the envelope-function method to calculate the energy states in the conduction band for the above SLs and also for SLs with N/M = 7/7 and 5/5 taking into account the Γ, *X*, and *L* valleys; the results are reported in this paper. We also analyzed theoretically the dependence of energy gaps on the diagonal and nondiagonal elements of the transition matrix

and on the strength of Γ–*X* mixing in order to determine the most important quantities under consideration.[1]

When simulating the energy states, we used the published data on the energies that corresponded to peaks in the low-temperature PL spectra [1–13] and also the data obtained by us previously [23, 24] and in this study.

It is worth noting that experimental values of energy gaps may differ somewhat from energy spacings between lower minibands since the transitions observed in a low-temperature PL spectrum typically involve excitons. It is also noteworthy that published experimental data feature a certain spread that depends mainly on the history of the samples, which makes it difficult to compare these data with the results of calculations. Furthermore, additional deviations are observed in the energies of the quantum-confinement levels; these deviations are caused by the roughness of the heterointerfaces and give rise to fluctuations (on the order of several monolayers) of the effective position of the heterointerface [25]. Therefore, for the sake of definiteness, we use the results of our own experimental studies in the simulations.

2. EXPERIMENTAL

We studied the spectra of low-temperature PL for short-period $(GaAs)_N/(AlAs)_M$ SLs with ratios of the number of monolayers in a period N/M = 6/3, 8/4, 10/5, and 10/10.[2] All the SL samples were grown by molecular-beam epitaxy on semi-insulating GaAs substrates with a (001) orientation. The SL period was measured using X-ray diffractometry. The relative deviation from the nominal thickness of the layers was ~1%. The spectra of low-temperature PL were measured under conditions of high excitation levels. The second harmonic of a pulsed YAG:Nd^{3+} laser with a wavelength of 533 nm was used for excitation. The pulse width was 7 ns, and the power in the pulse was as high as 10 MW/cm^2. The spectra were measured using an MDR-24 monochromator and a photomultiplier; the results of studying the low-temperature PL of the same samples at low excitation levels were reported in [7–9].

The spectra of low-temperature PL $I_{PL}(h\nu)$ at high excitation levels I_{ex} for $(GaAs)_N/(AlAs)_M$ SLs with N/M = 10/10 and 10/5 are shown in Figs. 1a and 1c. The spectra of the other aforementioned asymmetrical SLs are similar to that of an SL with N/M = 10/5. The energy positions of the PL peaks are listed in Table 1. A new band comes into existence in the high-energy portion of the PL spectrum of the sample with N/M = 10/10 as the excitation level becomes higher (Fig. 1a). This band is related to the radiative recombination of electrons in the Γ valley and heavy holes (Γ ⟶ *hh*) and has been observed before [11, 12]. The other band (observed also at low excitation levels [7–9]) is related to the indirect transitions of electrons from an indirect valley of the conduction band to the energy band of heavy holes (*X* ⟶ *hh*) [4, 7–9]. The difference between the energies of transitions Γ ⟶ *hh* ($\Delta E_{\Gamma-hh}$) and *X* ⟶ *hh* (ΔE_{X-hh}) is 67 meV.

Table 1. Results of calculating the transition energies in the diagonal approximation and comparison of these results with experimental data

SL (N/M)	Type	α*	$\Delta E_{\Gamma-hh}$		ΔE_{X-hh}	
			calculation	experiment	calculation	experiment
(10/5)	I	−0.198	1.836	1.836	1.843	–
(8/4)	I	−0.228	1.886	1.890	1.887	–
(6/3)	I	−0.002	1.913	1.913	1.938	–
(10/10)	II	−0.275	1.881	1.880	1.800	1.813
(7/7)	II	−0.040	1.961	1.961	1.857	1.880
(5/5)	II	−0.500	2.297	–	1.944	1.862

Note: The energies are expressed in electronvolts.

A different situation arises for an asymmetrical SL with N/M = 10/5 (Fig. 1c). An additional band in the high-energy portion of the PL spectrum is not observed at high levels of excitation. This fact, along with the differences in the dependences of intensities of PL bands on the excitation level (see Figs. 1b, 1d), indicates that the nature of the ground state in the conduction band in symmetrical GaAs/AlAs SLs differs from that in corresponding asymmetrical SLs. This inference to a certain extent confirms the conclusion [7–9] that asymmetrical short-period GaAs/AlAs SLs are direct-gap structures. However, it is worth noting that, in order to make the conclusions more tenable, one should carry out additional studies of the same samples using other experimental methods (time-resolved PL, measurements of PL excitation spectra, and low-temperature PL measured with the samples subjected to a hydrostatic pressure).

3. SIMULATION OF THE ENERGY STATES

In approximate calculations of SL energy states using the envelope-function method, one of the simplified models (for example, the Kronig–Penney or Bastard model) is often used a priori. Good agreement between the results of calculating the energy gaps and the experimentally determined and identified transition energies is attained by choosing properly the magnitudes of the band offsets at the heterointerface and the charge-carrier effective masses within the accuracy of their experimental determination [26]; this accuracy may be rather low. Despite the fact that the aforementioned models are simplified, they are still valuable in approximate calculations [21]. On the one hand, this approach leads to certain problems when it is necessary to describe a series of similar SLs or if there are several, simultaneously observed, PL peaks that correspond to

[1] The results of such studies were first reported in [10].

[2] We acknowledge the contribution of Professor K. Ploog (Paul Drude Institute, Berlin), who provided us with the SL samples.

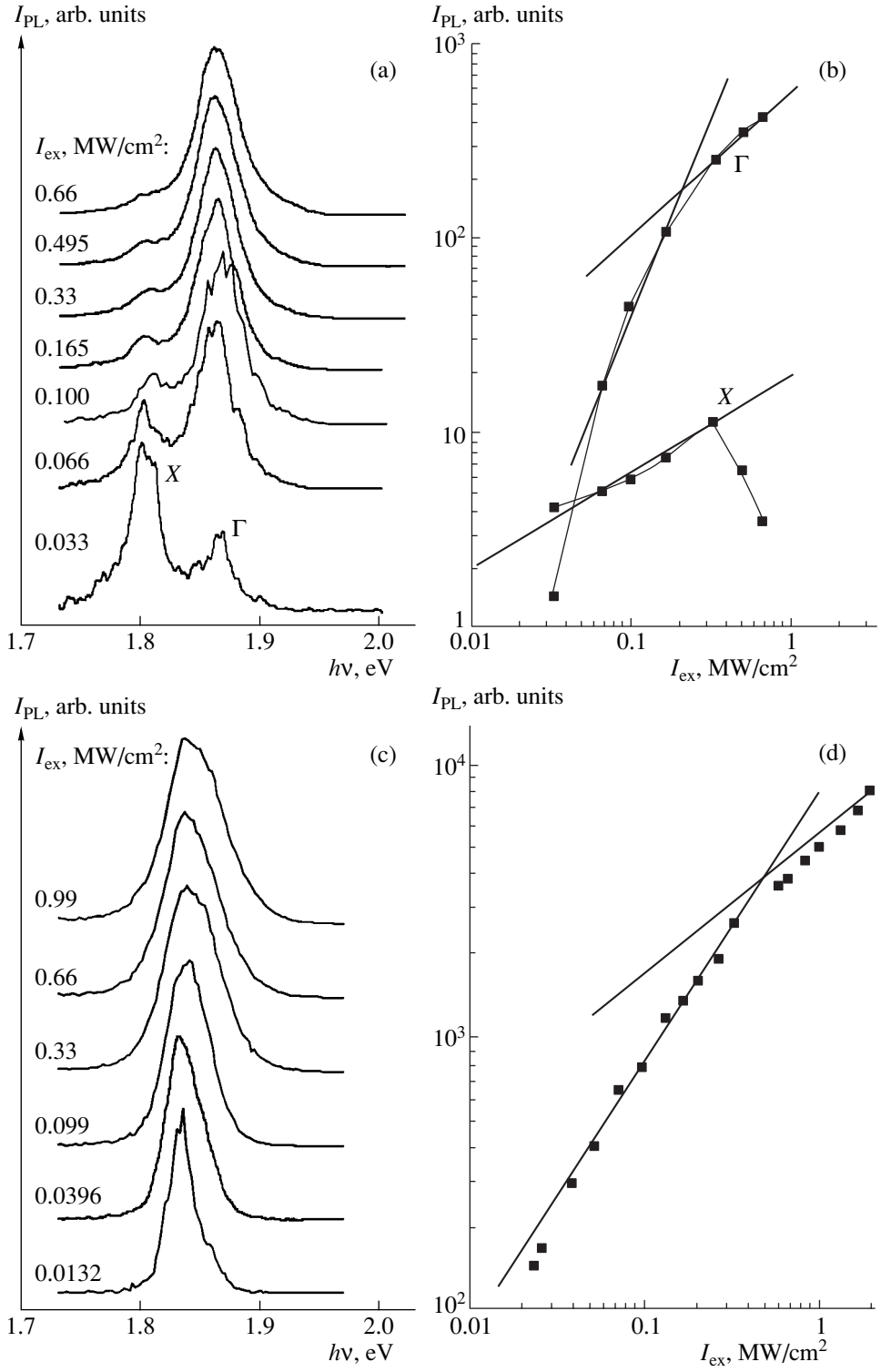

Fig. 1. (a, c) Spectra of low-temperature photoluminescence at various levels of excitation and (b, d) dependences of the photoluminescence intensity (I_{PL}) on the excitation level I_{ex} for $(GaAs)_N/(AlAs)_M$ superlattices with N/M = (a, b) 10/10 and (c, d) 10/5.

transitions of charge carriers from different valleys. These problems are caused by the fact that, when a sample or a valley is changed, certain parameters of bulk materials (for example, the magnitudes of the band offsets) should be redefined in the context of this approach. These parameters should be independent of the geometrical characteristics of SLs. On the other hand, it is well known that the choice of the boundary conditions may greatly affect the results of calculating the SL miniband spectrum. This circumstance has stim-

ulated detailed studies of whether it is possible to obtain satisfactory calculated data by choosing the appropriate boundary conditions. The matrix formalism of the envelope-function method [27] is a convenient approach that makes it possible to carry out the aforementioned study. In this case, the problem of determining the miniband spectrum of a short-period $(GaAs)_N/(AlAs)_M$ is reduced to solving the following equation:

$$\left|\mathbf{S}_w\mathbf{T}_{wb}\mathbf{S}_b\mathbf{T}_{bw} - e^{-i\lambda}\mathbf{I}\right| = 0. \quad (1)$$

Here, $\mathbf{S}_i$ are the transfer matrices that relate the values of envelope functions to their first derivatives at the inner boundaries of the ith layer ($i = w, b$); $\mathbf{T}_{wb} = (\mathbf{T}_{bw})^+$ are the interface matrices that specify the boundary conditions; I is a unity matrix; and λ is a quantity that depends on the wave vector and is assumed to be equal to zero in our calculations, which corresponds to the center of the SL Brillouin zone. Consideration of this point within the Brillouin zone is related to the fact that the minima of the miniband spectrum are located at this point; these minima are used to determine the energy gaps. Henceforth, the subscript *w* refers to GaAs layers and the subscript *b* refers to AlAs layers.

When calculating the states in the conduction band of the SLs under consideration, we have to take into account the multivalley character of the energy spectrum of GaAs and AlAs; there are several minima at almost the same energies at the Γ, *X*, and *L* points of the Brillouin zone in the vicinity of the conduction-band bottom for the aforementioned constituent semiconductors. In addition, in semiconductors with a zinc blende structure (including GaAs and AlAs), the top of the valence band is formed by three bands: a band of heavy holes (*hh*), a band of light holes (*lh*), and a band split off owing to the spin–orbit coupling. However, since we are interested only in the lower minibands that determine the type of SL and are known to be formed from the Γ and X_z states of the conduction band and the Γ states (*hh*) of the valence band of bulk materials, we will restrict our consideration to these states only.

In the approximation under consideration, the transfer matrices have a block form; i.e.,

$$\mathbf{S}_i = \begin{bmatrix} S_i^{\Gamma_1} & O & O & O \\ O & S_i^{X_{1z}} & O & O \\ O & O & S_i^{X_{3z}} & O \\ O & O & O & S_i^{hh} \end{bmatrix}. \quad (2)$$

Here, $O = \begin{bmatrix} 0 & 0 \\ 0 & 0 \end{bmatrix}$ and S_i^ν are the one-band transfer matrices that have the form

$$S_i^\nu = \begin{bmatrix} \cos(k_i^\nu d_i) & (m_i^\nu/k_i^\nu)\sin(k_i^\nu d_i) \\ -(k_i^\nu/m_i^\nu)\sin(k_i^\nu d_i) & \cos(k_i^\nu d_i) \end{bmatrix}, \quad (3)$$

if the ith layer is a potential well for charge carriers in the νth valley, and

$$S_i^\nu = \begin{bmatrix} \cosh(k_i^\nu d_i) & (m_i^\nu/k_i^\nu)\sinh(k_i^\nu d_i) \\ (k_i^\nu/m_i^\nu)\sinh(k_i^\nu d_i) & \cosh(k_i^\nu d_i) \end{bmatrix} \quad (4)$$

in the case where this layer represents a barrier. Here, m_i^ν are the bulk charge-carrier effective masses in the ith layer for the νth valley, and k_i^ν are the corresponding components of the wave vector of the bulk material along the SL growth direction (we are only interested in the case of normal orientation of the wave vector).

The interface transfer matrices $\mathbf{T}_{wb}$ also have a block structure and are given by

$$\mathbf{T}_{wb} = \begin{bmatrix} T_{wb}^{(\Gamma_1,\Gamma_1)} & T_{wb}^{(\Gamma_1,X_{1z})} & T_{wb}^{(\Gamma_1,X_{3z})} & O \\ T_{wb}^{(X_{1z},\Gamma_1)} & T_{wb}^{(X_{1z},X_{1z})} & T_{wb}^{(X_{1z},X_{3z})} & O \\ T_{wb}^{(X_{3z},\Gamma_1)} & T_{wb}^{(X_{3z},X_{1z})} & T_{wb}^{(X_{3z},X_{3z})} & O \\ O & O & O & T_{wb}^{(hh,hh)} \end{bmatrix}, \quad (5)$$

where $T_{wb}^{(\nu,\mu)} = (T_{wb}^{(\nu,\mu)})^+$ are the one-band interface matrices that ensure continuity of the envelope function and its derivative at the interface and are related to the νth and μth valleys. Quasi-diagonal representation (5) is caused by the fact that we disregard the interaction between the conduction and valence bands.

The nondiagonal blocks $T_{wb}^{(\nu,\mu)}$ with $\nu \neq \mu$ describe the mixing of the νth and μth valleys. The structure of these matrices is subjected to certain restrictions related to the symmetry of the states that are mixed. However, as is shown by numerical calculations [28, 29], not all of the symmetry-allowed elements of $T_{wb}^{(\nu,\mu)}$ matrices are important in the heterostructures under consideration. For example, it follows from the estimations of the values of the matrix elements in the tight-binding approximation [29] that the envelope functions of all valleys can be joined directly, whereas derivatives of these functions can involve an "admixture" that is proportional to the envelope function of a specific valley (in the case under consideration, the X_{1z} and X_{3z} valleys), depending on the parity of *M*.

In our preliminary consideration [10], in order to ensure agreement with the calculated transition energies determined from the peaks in the low-temperature PL spectra and identified with the $\Gamma \longrightarrow hh$ and $X \longrightarrow hh$ transitions in an SL with $N/M = 10/10$ and also with a $\Gamma \longrightarrow hh$ transition in an SL with $N/M = 10/5$, we used the generalized one-parameter diagonal boundary con-

Table 2. Values of material parameters of bulk GaAs and AlAs as used in the simulation [26]

Parameter	GaAs	AlAs
a_0, Å	5.65330	5.66139
m_e^{Γ}/m_0	0.067	0.150
$m_e^{X_1}/m_0$	1.300	1.100
$m_e^{X_3}/m_0$	1.578	1.117
m_e^{L}/m_0	0.210	0.213
m_{hh}^{Γ}/m_0	0.450	0.500

Note: a_0 is the lattice constant and m_e^{ν}/m_0 and m_{hh}^{ν}/m_0 are the relative effective masses of electrons and heavy holes in the ν^{th} valley.

ditions (the diagonal approximation) that corresponded to diagonal interface matrices [30]

$$T_{wb}^{\nu,\nu} = \begin{bmatrix} (m_b^{\nu}/m_w^{\nu})^{\alpha} & 0 \\ 0 & (m_w^{\nu}/m_b^{\nu})^{\alpha} \end{bmatrix} \quad (6)$$

and disregarded the effect of Γ–X mixing (i.e., we assumed that $T_{wb}^{\nu,\mu} = O$ at $\nu \neq \mu$).

We performed numerical simulation in diagonal approximation [10] with a fixed choice of parameters of constituent compounds in an SL (see Table 2). The offset of the valence bands ΔE_v is, as mentioned above, an important parameter in simulating the SL energy states and is chosen as $\Delta E_v = 0.53$ eV (or $r \equiv \Delta E_v/\Delta E_g \approx 35\%$, where ΔE_g is the offset of the band gaps); this value coincides with that used by Ivchenko *et al.* [31] and is in satisfactory agreement with experimentally determined value $r = (34 \pm 2)\%$ [26]. This approach made it possible to determine the quantities $\alpha = \alpha^*$ that ensured that the calculated energy gaps were consistent with the experimental data. The results of simulation in the chosen approximation are listed in Table 1.

We should note here that the energy gaps obtained using boundary conditions (6) at $\alpha = 0$ are in satisfactory agreement with experimental data in relation to the SL type. However, the energy-gap values were found to be underestimated, whereas, at $\alpha = -1/2$, the qualitative agreement was violated and the calculated energies of transitions were found to exceed the corresponding experimental data.

It is worth noting that the parameter α that appears in boundary conditions (6) comes into existence owing to a generalized expression for the kinetic-energy operator in the case of the spatial-dependent effective mass; i.e.,

$$\hat{T} = \frac{1}{2} m^{\alpha} \hat{p} \frac{1}{m^{1+2\alpha}} \hat{p} m^{\alpha}. \quad (7)$$

An expression similar to (7) was suggested first in [32] and was then studied in detail in [32–36]. Thus, the above representation of the kinetic-energy operator in the effective-mass approximation is widely used at present for materials with spatially dependent parameters [16]. However, there have been contradictory published data on the values of α. For example, it was found [35] that the best agreement between calculated energy gaps and experimental values was attained at $\alpha = 0$ (i.e., $\hat{T} = \hat{p}(1/m)\hat{p}$); at the same time, the value $\alpha = -1/2$ ($\hat{T} = (1/\sqrt{m})\hat{p}^2(1/\sqrt{m})$) was used in [36]. In more recent publications [16–19], complex expressions are reported for α; these expressions relate α to special features of the potential profile for an individual barrier in the heterostructure. However, it is worth noting that a direct use of the aforementioned theoretical expressions [16] in order to determine the numerical value of α is difficult due to the fact that the values of the parameters appearing in these expressions are not known. In addition, since the expressions for the quantity α were obtained [16] for a single-barrier heterostructure, they are apparently best suited for estimating the value of α in SLs with periods that are not too small. It is noteworthy that a very specific relation between the values of the momentum matrix elements and the magnitudes of the band offsets at the heterojunction corresponds to the cases of $\alpha = 0$ and $\alpha = -1/2$ [16–18]; apparently, this relation cannot be valid for SLs. This reasoning indirectly confirms the fact that intermediate values of α can be used in simulations. Therefore, in our calculations, we treat the quantity α as an adjustable parameter that can take values from the interval $(-1/2, 0)$.

The positions of energy levels [10] related to the Γ and X_z states of the conduction band and also to the Γ states of the valence band depend to a different extent on the value of α, which is caused by the large difference in the relevant effective masses. The states related to the Γ valley of the conduction band are found to be most sensitive to variations in α. This circumstance, along with the very weak corresponding dependence of positions of the states of the X electrons and Γ holes, makes it possible to use a single parameter α common to all the states under consideration.

A comparison with the experimental values (Table 1) shows that the results obtained using the diagonal approximation are in unexpectedly good agreement with experimental data for SLs that have values of N and M that are not too small. The deterioration in the agreement between calculation and experiment with small values of the thickness of layers is evidently a result of the effect of factors that are not taken into account in the model under consideration. These factors include the mixing of states in different valleys and an increase in the relative role of the abrupt change in

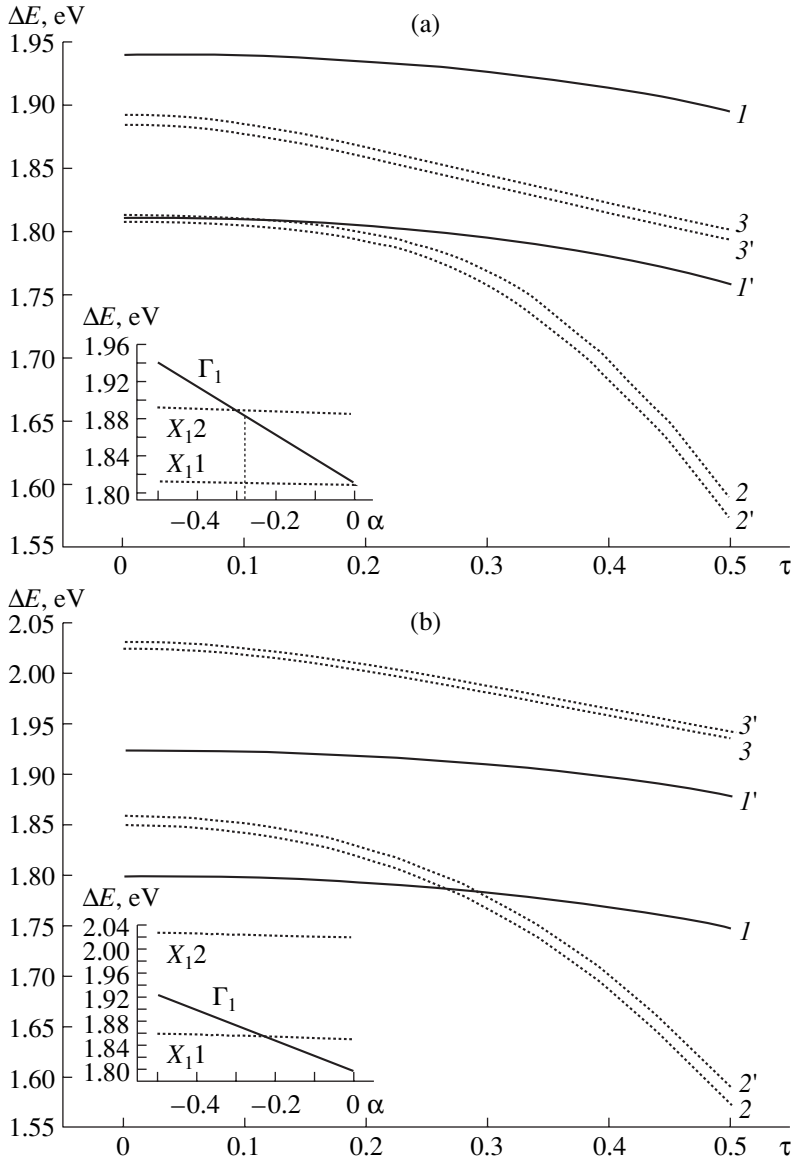

Fig. 2. Dependences of the energy gaps ΔE on the parameter τ at $\alpha = (1–3)\ 0$ and $(1'–3')\ –1/2$ and on α (insets) for $(GaAs)_N/(AlAs)_M$ with N/M = (a) 10/10 and (b) 10/5. Curves *1* and *1'* correspond to the Γ_1 valley and curves *2*, *3*, *2'*, and *3'* correspond to the X_1 valley. $X_1 1$ and $X_2 2$ designate the edges of the first and second minibands that originate from the X_1 valley of the bulk material.

periodic potential at the heterointerface, and they should manifest themselves to a greater extent with decreasing barrier thickness. This rest of this paper is devoted to clarifying the pattern in the behavior of the miniband spectrum when all the above effects are taken into account.

First of all, we consider the evaluation of the effect of nondiagonal elements of the single-band interface matrices $T_{wb}^{(\nu,\nu)}$ on the miniband spectrum; these elements give rise to a linear relation between the envelope function and its derivative at the heterointerface. The corresponding boundary conditions can be obtained by considering the equation for envelope functions with the kinetic-energy operator given by formula (7); a δ-functional addition to the potential with the strength U_δ appears in this equation. In this case, the diagonal matrices $T_{wb}^{(\nu,\nu)}$ ($\nu = \mu$) can be written as

$$T_{wb}^{(\nu,\nu)} = \begin{bmatrix} (m_b^\nu/m_w^\nu)^\alpha & 0 \\ (U_\delta/\hbar)[1/(m_w^\nu)^\alpha + 1/(m_b^\nu)^\alpha] & (m_w^\nu/m_b^\nu)^\alpha \end{bmatrix}. \quad (8)$$

The presence of the aforementioned δ-functional addition is caused by the difference between the scattering of a Bloch wave at a jump of the actual periodic potential and the scattering at the piecewise constant potential of the model [36]. In the first approximation, the term proportional to $\delta(z)$ corrects this difference.

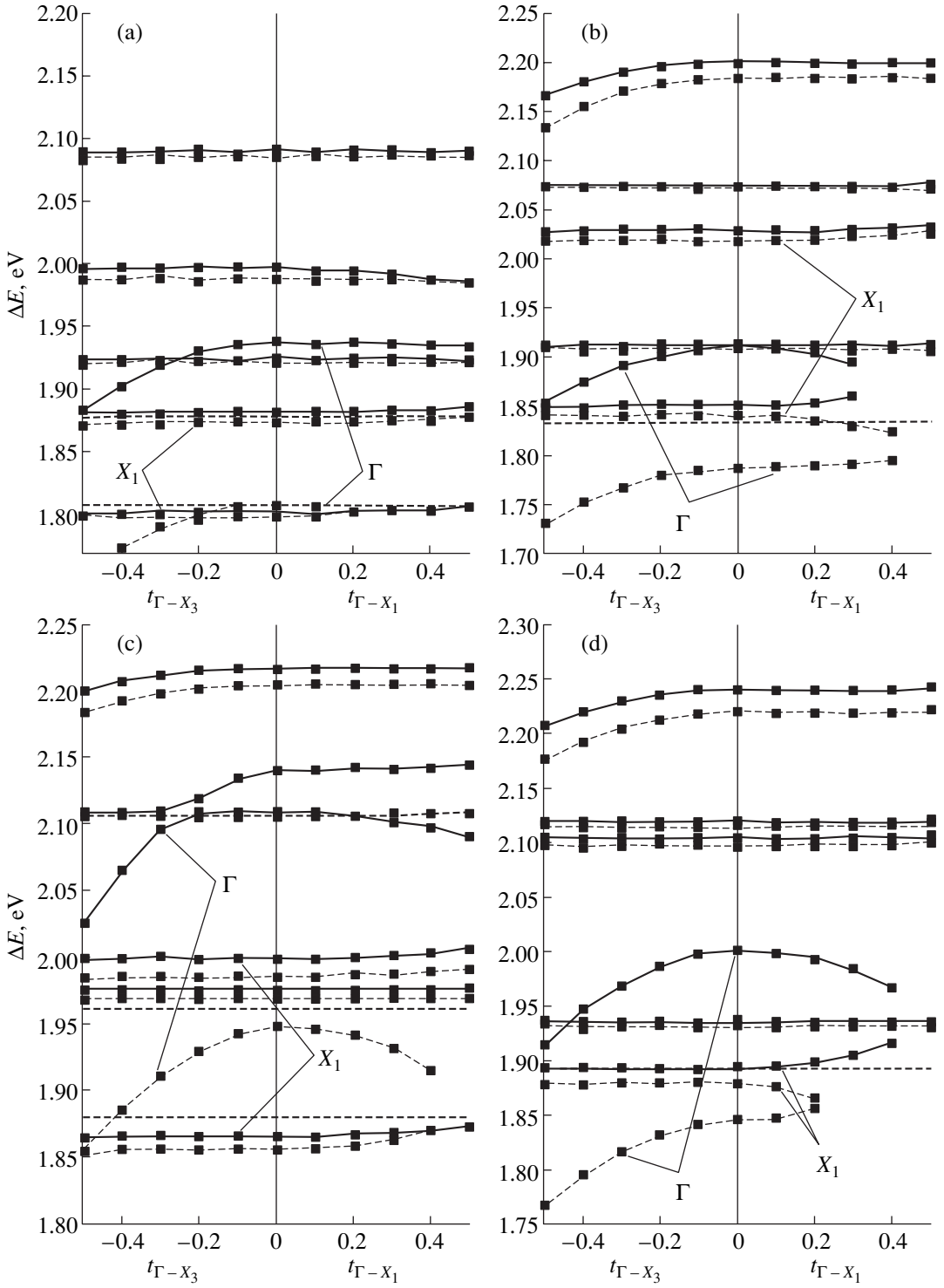

Fig. 3. Dependences of the energy gaps ΔE on the strength of the Γ–X mixing at $\alpha = 0$ (dashed lines) and $\alpha = -1/2$ (solid lines) for $(GaAs)_N/(AlAs)_M$ superlattices with N/M = (a) 10/10, (b) 10/5, (c) 7/7, and (d) 8/4.

In simulating the energy states, we assumed that the value of α was fixed ($\alpha = 0$ or $\alpha = -1/2$), whereas the quantity τ expressed in terms of U_δ as $\tau = (U_\delta/\hbar)[1/(m_w^\nu)^\alpha + 1/(m_b^\nu)^\alpha]$ was used as the parameter of the model. The convenience of this consideration is caused by the fact that the energy states in the interval $\alpha \in (-1/2, 0)$ vary almost linearly [10].

The results of numerical calculation of the energy-gap dependences on the value of τ for an SL with N/M = 10/10 and 10/5 are shown in Fig. 2; it can be seen that

an increase in the strength of a δ-functional scatterer leads to a decrease in the energies of both the $\Gamma \longrightarrow hh$ and $X \longrightarrow hh$ transitions in the SLs under consideration. The dependence of the energy states under investigation on the parameter α at $\tau \equiv 0$ (see Fig. 2, insets) shows, on the one hand, that, since at $\alpha = -1/2$ the calculated values of the energy gaps are found to exceed the experimental values (see Table 1), the introduction of the parameter τ brings about a certain improvement in the agreement between the results of calculations and experimental data. On the other hand, it is evident that, since the calculated transition energies obtained at $\alpha = 0$ are found to be too low, the introduction of the quantity τ only increases the deviation of calculated energies from experimental values. The best agreement between calculated energy gaps and experimental values can be attained using intermediate values of α and τ. In this case, the values of τ can be different for fitting the Γ–*hh* and *X*–*hh* energy gaps at the same value of α, or, on the contrary, one can fix the value of τ and vary the parameter α.

The mixing of the Γ- and *X*-valley states is another factor that affects the miniband-spectrum structure. In order to separate the effect of this factor on the energy spectrum, in the following discussion we assume that $\tau = 0$.

A large number of publications [16, 22, 29, 37–39] are devoted to Γ–*X* mixing and its dependence on the geometric characteristics of SLs. Specifically, they discuss the extent to which Γ–X_1 and Γ–X_3 mixing affects the miniband spectrum. In this study, we use (as above) the matrix method in order to simulate the mixing effect.

It is worth noting that we considered the effects under investigation separately for the cases of Γ–X_1 and Γ–X_3 mixing. The form of nondiagonal blocks $T_{wb}^{(\nu, \mu)}$ was chosen as

$$T_{wb}^{(\Gamma, X_{1z})} = \begin{bmatrix} 0 & 0 \\ 0 & t_{\Gamma X_1} \end{bmatrix} \quad \text{and} \quad T_{wb}^{(\Gamma, X_{3z})} = \begin{bmatrix} 0 & 0 \\ 0 & 0 \end{bmatrix}$$

when considering Γ–X_1 mixing and

$$T_{wb}^{(\Gamma, X_{1z})} = \begin{bmatrix} 0 & 0 \\ 0 & 0 \end{bmatrix} \quad \text{and} \quad T_{wb}^{(\Gamma, X_{3z})} = \begin{bmatrix} 0 & 0 \\ t_{\Gamma X_3} & 0 \end{bmatrix}$$

when considering Γ–X_3 mixing.

The dimensionless parameters $t_{\Gamma X_i}$ and $2Ut_{\Gamma X_i} m_0 a_0^2/\hbar^2$ ($i = 1, 3$) appear in the boundary conditions and control the strength of mixing.

Two factors, i.e., whether the number *M* is odd or even and whether the SL under investigation is symmetrical or asymmetrical, are important when considering the effect of Γ–*X* mixing on the miniband spectrum. Therefore, the short-period SLs can be divided in calculations into four groups according to the aforementioned criteria. The $(GaAs)_N/(AlAs)_M$ SLs with *N*/*M* = 10/10, 10/5, 7/7, and 8/4 can be considered as representatives of the above groups. These SLs illustrate the main tendencies in the behavior of the miniband spectrum when the effect of Γ–*X* mixing is taken into account. In Fig. 3, we show the dependences of the energy gaps between the minima of the minibands on the parameters $t_{\Gamma X_i}$ at $\alpha = 0$ and $\alpha = -1/2$ for short-period SLs. The results of calculations show that satisfactory agreement with experimental values (to within ~10 meV) can be attained for the SLs under consideration in the case of even *M* due to variations in the parameters of the Γ–X_3 mixing at $\alpha = -1/2$. The situation turned out to be different in the case of an odd number of monolayers *M*; i.e., taking mixing into account does not improve the agreement between calculated energies and the corresponding experimental values. It is worth noting here that one theoretical study [39] indicates that there is neither Γ–X_1 nor Γ–X_3 mixing at the center of the Brillouin zone for an ideal SL with an abrupt heteroboundary and an odd number *M*. Thus, the energy gaps calculated on the assumption that there is mixing of the states in the short-period SLs under consideration are in inadequate agreement with experimental data, which may indirectly support the conclusion that the SLs under study are of high quality.

It is also worth noting that a good agreement between calculated and experimental data can be attained for all types of SLs under consideration by both taking into account the Γ–*X* mixing and modifying the boundary conditions due to variations in the parameter α. Indeed, specific values α* that can be used to attain satisfactory agreement between experimental data and the results of calculations even in the diagonal approximation are characteristic of all the short-period SLs under investigation; small corrections caused by Γ–*X* mixing can improve this agreement. This circumstance is especially important if it is necessary to correct the positions of the *X* levels, whose dependence on α is weak, as mentioned above.

4. CONCLUSION

The above results of experimental investigations into the spectra of low-temperature photoluminescence in short-period $(GaAs)_N/(AlAs)_M$ superlattices (SLs) with *N*/*M* = 6/3, 8/4, 7/7, 10/10, 10/5, and 5/5 under high excitation levels are consistent with previous conclusions [9, 10] that asymmetrical short-period (GaAs)/(AlAs) SLs are direct-gap structures. This type of asymmetrical SLs can be described theoretically even in the context of the simplest Kronig–Penney model using the parameters of the constituent compounds. Satisfactory qualitative agreement between the calculated and the experimental values of the energy gaps between the minibands is attained by choosing appropriately the parameters of the bulk materials and the magnitudes of the band offsets at the heterointerface within the accuracy of the experimental determination of the above quantities for each SL. However, in the case of considering a set of SLs, it appears more consistent in calculations to fix the above parameters and

introduce other physical parameters into the model; these new parameters should be related naturally to the boundary conditions.

The performed simulation, whose parameters were related to the boundary conditions, showed that it is possible to obtain values of the energy gaps that are in good qualitative and satisfactory quantitative agreement with experimental data for the SLs under study. The results of calculations indicate that the miniband spectrum of the short-period (GaAs)/(AlAs) SLs is predominantly affected by diagonal elements of the interface matrix $\mathbf{T}_{wb}$.

We also studied the trends in the evolution of the miniband-spectrum when only the effect of Γ–X mixing is taken into account or if there is a δ-functional addition to the potential for fixed limiting values of the parameter α that modifies the diagonal part of the boundary conditions.

These studies showed that, at $\alpha = 0$, only taking Γ–X mixing into account cannot ensure satisfactory agreement between calculated values of the energy gaps between the minibands and experimental data for the aforementioned SLs. In contrast to this situation, it is possible to fit the calculation to the experiment for SLs with an even number M in the case of $\alpha = -1/2$.

The obtained numerical values of $t_{\Gamma X_1}$ and $t_{\Gamma X_3}$ confirm the theoretical conclusions [39] that the mechanism of Γ–X_3 mixing is prevalent, which indirectly indicates that the heteroboundaries in the investigated SLs are of high quality, since these conclusions are based on a model of an ideal heterojunction.

Variation in the value of α in the interval $(-1/2, 0)$ combined with consideration of the effects of mixing and the δ-functional addition to the potential at the heterointerface make it possible to obtain agreement between the calculated and experimental values of transition energies to within ~10 meV.

ACKNOWLEDGMENTS

We thank A. Zukauskas and G. Tamulaitis for their help in organizing measurements of low-temperature photoluminescence at high levels of excitation.

REFERENCES

1. J. P. van der Ziel and A. C. Gossard, J. Appl. Phys. **48**, 3018 (1977).
2. T. Isu, Tiang De Sheng, and K. Ploog, Appl. Phys. A **43**, 75 (1987).
3. E. Finkman, M. D. Struge, and M. C. Tamargo, Appl. Phys. Lett. **149**, 1299 (1986).
4. E. Finkman, M. D. Struge, M. H. Meynadier, *et al.*, J. Lumin. **39**, 57 (1987).
5. K. Takahashi, T. Nayakawa, T. Suyama, *et al.*, J. Appl. Phys. **63**, 1729 (1988).
6. G. Danan, B. Etienne, F. Mollot, *et al.*, Phys. Rev. B **35**, 6207 (1987).
7. V. G. Litovchenko, D. V. Korbutyak, S. Krylyuk, *et al.*, Phys. Rev. B **55**, 10621 (1997).
8. D. V. Korbutyak, S. G. Krilyuk, V. G. Litovchenko, *et al.*, Ukr. Fiz. Zh. **43** (1), 116 (1998).
9. S. Krylyuk, D. V. Korbutyak, V. G. Litovchenko, *et al.*, Appl. Phys. Lett. **74**, 2596 (1999).
10. A. I. Bercha, D. V. Korbutyak, S. Krylyuk, *et al.*, Funct. Mater. **6**, 545 (1999).
11. V. G. Litovchenko, A. I. Bercha, D. V. Korbutyak, *et al.*, Thin Solid Films **217**, 62 (1992).
12. R. Cingolani, L. Baldassare, M. Ferrara, *et al.*, Phys. Rev. B **40**, 6101 (1989).
13. R. Cingolani, K. Ploog, G. Scamarcio, and L. Tapfer, Opt. Quantum Electron. **22**, 201 (1990).
14. G. F. Karavaev and Yu. S. Tikhodeev, Fiz. Tekh. Poluprovodn. (Leningrad) **25**, 1237 (1991) [Sov. Phys. Semicond. **25**, 745 (1991)].
15. B. A. Foreman, Phys. Rev. B **54**, 1909 (1996).
16. É. E. Takhtamirov and V. A. Volkov, Zh. Éksp. Teor. Fiz. **116**, 1843 (1999) [JETP **89**, 1000 (1999)].
17. É. E. Takhtamirov and V. A. Volkov, Zh. Éksp. Teor. Fiz. **117**, 1221 (2000) [JETP **90**, 1063 (2000)].
18. V. A. Volkov and É. E. Takhtamirov, Usp. Fiz. Nauk **167**, 1123 (1997) [Phys. Usp. **40**, 1071 (1997)].
19. E. E. Takhtamirov and V. A. Volkov, Semicond. Sci. Technol. **12**, 77 (1997).
20. G. Bastard, Phys. Rev. B **24**, 5693 (1981).
21. M. Recio, J. L. Gastano, and F. Briones, Jpn. J. Appl. Phys. **27**, 1204 (1988).
22. Yu. I. Polygalov and A. S. Poplavnoĭ, Fiz. Tekh. Poluprovodn. (Leningrad) **24**, 328 (1990) [Sov. Phys. Semicond. **24**, 201 (1990)].
23. V. G. Litovchenko, D. V. Korbutyak, A. I. Bercha, *et al.*, Appl. Phys. Lett. **78**, 4085 (2001).
24. A. I. Bercha, V. I. Gavrilenko, D. V. Korbutyak, and V. G. Litovchenko, Ukr. Fiz. Zh. **35**, 35 (1990).
25. V. L. Al'perovich, N. T. Moshegov, V. V. Popov, *et al.*, Fiz. Tverd. Tela (St. Petersburg) **39**, 2085 (1997) [Phys. Solid State **39**, 1864 (1997)].
26. Sadao Adachi, *Properties of Aluminium Gallium Arsenide* (Gunma Univ., Japan, 1992).
27. N. F. Gashimzade and E. L. Ivchenko, Fiz. Tekh. Poluprovodn. (Leningrad) **25**, 323 (1991) [Sov. Phys. Semicond. **25**, 195 (1991)].
28. T. Ando, S. Wakahara, and H. Akera, Phys. Rev. B **40**, 11609 (1989).
29. T. Ando and H. Akera, Phys. Rev. B **40**, 11619 (1989).
30. E. L. Ivchenko and G. Pikus, *Superlattices and Other Heterostructures. Summetry and Optical Phenomena* (Springer, Berlin, 1995), p. 370.
31. E. L. Ivchenko, A. Yu. Kaminskiĭ, and I. L. Alaĭner, Zh. Éksp. Teor. Fiz. **104**, 3401 (1993) [JETP **77**, 609 (1993)].
32. O. von Roos, Phys. Rev. B **27**, 7547 (1983).
33. R. A. Morrow and K. R. Brownstein, Phys. Rev. B **30**, 678 (1984).
34. R. A. Morrow, Phys. Rev. B **35**, 8074 (1987).
35. I. Galbraith and G. Duggan, Phys. Rev. B **38**, 10057 (1988).
36. Q.-G. Zhu and H. Kroemer, Phys. Rev. B **27**, 3519 (1983).
37. Y. Fu, M. Willander, E. L. Ivchenko, and A. A. Kiselev, Phys. Rev. B **47**, 13498 (1993).
38. C. Gourdon, D. Martins, P. Lavallard, and E. L. Ivchenko, Acta Phys. Pol. A **100**, 409 (2001).
39. I. L. Aleĭner and E. L. Ivchenko, Fiz. Tekh. Poluprovodn. (St. Petersburg) **27**, 594 (1993) [Semiconductors **27**, 330 (1993)].

Translated by A. Spitsyn

Semiconductors, Vol. 38, No. 4, 2004, pp. 419–430. Translated from Fizika i Tekhnika Poluprovodnikov, Vol. 38, No. 4, 2004, pp. 436–447.

LOW-DIMENSIONAL SYSTEMS

Resonant Γ–*X* Tunneling in Single-Barrier GaAs/AlAs/GaAs Heterostructures

Yu. N. Khanin*, E. E. Vdovin, and Yu. V. Dubrovskiĭ

Institute of Microelectronics Technology and Ultrahigh-Purity Materials, Russian Academy of Sciences, Chernogolovka, Moscow oblast, 142432 Russia

**e-mail: khanin@ipmt-hpm.ac.ru*

Submitted June 16, 2003; accepted for publication June 30, 2003

Abstract—The electron transport through single-barrier GaAs/AlAs/GaAs heterostructures is studied. This transport is caused by resonant tunneling between the two-dimensional states related to the Γ valley of the GaAs conduction band and various two- or zero-dimensional donor states related to the lower *X* valleys of the AlAs conduction band. The resonant electron tunneling both via various two-dimensional states related to the X_z and X_{xy} valleys in AlAs (the X_z and X_{xy} states) and via related states of Si donors X_z^D and X_{xy}^D was observed. This circumstance made it possible to determine the binding energies of these states ($E_B(X_z^D) \approx 50$ meV and $E_B(X_{xy}^D) \approx 70$ meV, respectively) directly from the results of identification of resonance features in transport characteristics. An analysis of the structure of experimental resonances corresponding to tunneling between the Γ and *X* Landau levels in a magnetic field made it possible to determine the transverse effective mass in the *X* valleys of AlAs ($m_t = (0.2 \pm 0.02)m_0$). An additional fine structure of donor resonances is observed in experimental transport characteristics. This fine structure is caused by resonant tunneling of electrons through the states of the donors that are located in various atomic layers of the AlAs barrier (in the growth direction) and therefore have different binding energies. © *2004 MAIK "Nauka/Interperiodica".*

1. INTRODUCTION

Experimental discovery of an appreciable effect of quantum states that belong to the *X* valleys in the AlAs conduction band on electrical properties of GaAs/AlAs heterostructures [1] has stimulated intense tunneling-transport [2–5] and optical [6, 7] studies of both the spectra of quantum states and the mechanisms of tunneling transitions between electronic states related to valleys in the conduction band. These valleys are located at different symmetry points of the Brillouin zone and are characterized by different effective masses (different mechanisms of intervalley transitions Γ–*X*). The dependence of properties of GaAs/AlAs heterostructures on the AlAs *X* states is related to the following combination of special features of the energy-band structure for the materials that form these heterostructures. AlAs is an indirect-gap semiconductor with the bottom of the conduction band located near the *X* point of the Brillouin zone, whereas GaAs is a direct-gap semiconductor with the bottom of the conduction band located at the center of the Brillouin zone (at the point Γ)[6]. Therefore, as can be seen from Fig. 1a, the profile of the *X* minimum in the conduction band along the GaAs/AlAs/GaAs heterostructure forms a quantum well (QW) for electrons in the AlAs layer. It is noteworthy that the difference between the energies of the minima in the valleys Γ (GaAs) and *X* (AlAs) amounts to a mere ~0.12 eV [3]. It is the resonant tunneling of electrons from the states Γ in GaAs via the *X* states of the QW in the AlAs layer that leads [1–3] to a modification of the transport characteristics of the heterostructures under consideration. In addition, it was shown that the effective-mass anisotropy in the *X* valleys (see Fig. 1b) in a thin AlAs layer (QW) leads to the appearance of two different types of quasi-confined states (different staircases of two-dimensional (2D) subbands) formed by the X_z and X_{xy} valleys. The latter feature different effective masses in the direction of the *z* quantization [2, 3, 6]. The energies of dimensional quantization of corresponding 2D states X_z and X_{xy} (the energy of the minima in the subbands X_z and X_{xy}) are governed by the values of the longitudinal ($m_l \approx 1.1m_0$) and transverse ($m_t \approx 0.19m_0$) effective masses in the AlAs *X* valleys, respectively; as a result, these energies differ markedly. This effect is often referred to as the splitting of the *X* valleys (to be more precise, of the *X* subbands) or as a reduction of the multiplicity of the valley degeneracy under conditions of quantization. In addition, another factor affecting the mutual energy arrangement of subbands X_z and X_{xy} was discovered. This factor consists in the presence of a biaxial stress in the AlAs layer, which arises owing to a 0.12% mismatch of the GaAs and AlAs lattice constants and leads to a decrease in the energy of subbands X_{xy} in respect to the energy of subbands X_z (see [6] and the references cited therein). In a number of studies concerned with GaAs/AlAs hetero-

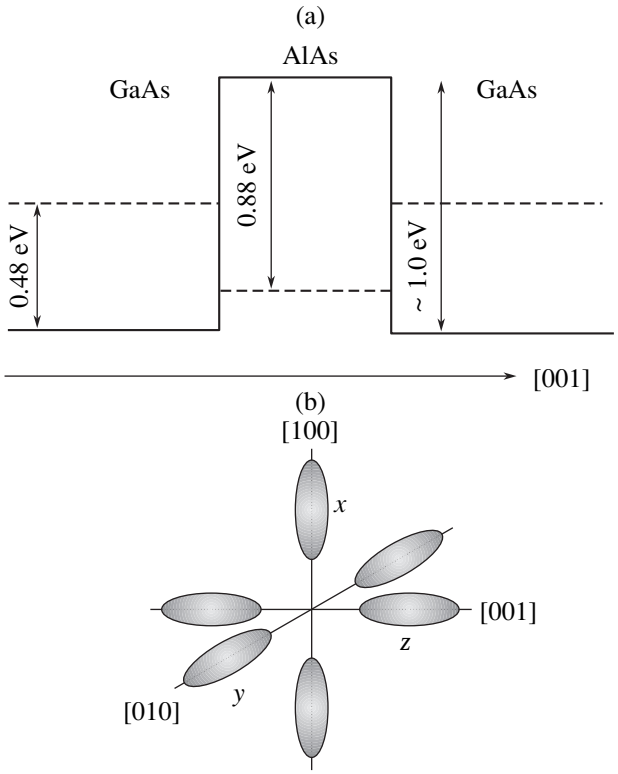

Fig. 1. (a) Energy diagram of the Γ and *X* minima in the conduction band along the GaAs/AlAs/GaAs heterostructure; (b) schematic representation of isoenergetic surfaces corresponding to the six equivalent AlAs *X* valleys in the *k* space.

structures, the manifestation of quasi-confined states X_z and X_{xy} was observed and attempts to reveal the factors that affect the relative positions of these states were undertaken. Nevertheless, there is now considerable disagreement about the origin of the ground state (X_z or X_{xy}) in the *X* well of a certain width [2–6, 8–10]. In this context, it is stated that the nature of the ground state largely controls the optical and electrical properties of GaAs/AlAs heterostructures. The aforementioned controversy is caused to a great extent by the appreciable uncertainty in band-structure parameters such as the principal effective masses m_l and m_t in the AlAs *X* valleys, the energy gaps between the minima Γ (GaAs) and *X* (AlAs) in the conduction band, and the magnitude of splitting of the X_z and X_{xy} valleys due to the biaxial stress (see [11–14] and the references cited therein). The values of the above parameters used in our calculations represent merely one of the possible sets determined experimentally.

Optical studies of thick (1–7 μm) AlAs epitaxial layers doped with silicon (the most widely used donor impurity in GaAs/AlAs heterostructures) showed that the Si donors in this semiconductor are related to the *X* valleys. The Si states are adequately described by the hydrogen-like model in the context of the effective-mass method in which the intervalley and spin–orbit coupling effects are disregarded. This model is equivalent to the model of independent *X* valleys, which is commonly used to describe the states of substitutional donor impurities that reside at the sites of Group III elements; these states are related to the *X* valleys [7]. In other words, the Si donors in AlAs give rise to single-type hydrogen-like states related to independent (noninteracting) *X* valleys. As a result, the Si ground state is found to be threefold degenerate in the absence of additional factors that reduce the degeneracy multiplicity (these factors may include, for example, stresses in the lattice); otherwise (if the valleys interact), the above state splits along with the *X* valleys. The above inferences were specifically supported by observation of splittings of the Si ground donor state into the states related to the X_z and X_{xy} valleys. These splittings correspond to relative variations in energies of minima in the X_z X_{xy} valleys in stressed AlAs layers grown on GaAs substrates and bonded to Si substrates; the stresses are caused by a mismatch of the GaAs and Si lattice constants ($a_{\mathrm{GaAs}} < a_{\mathrm{AlAs}} < a_{\mathrm{Si}}$). The Si states are not split in an unstressed AlAs layer separated from the substrate.

Weber [15] considered theoretically the hydrogen-like donors whose states (like those of Si donors) can be treated as related to the independent *X* valleys; the donors under consideration were located in a thin AlAs layer confined by GaAs layers (i.e., in a quantum *X* well). In this case, the X_z and X_{xy} valleys are nonequivalent owing to dimensional quantization and biaxial stress in the AlAs layer. In turn, this circumstance gives rise to a corresponding difference in the donor energy states related to the above valleys. The binding energies of "ground" states of hydrogen-like donors associated with the X_z and X_{xy} valleys (the lower X_z and X_{xy} subbands) were calculated in relation to the QW width and the location of the donor in this QW. When calculating the binding energy, the effective-mass anisotropy and the effect of QW potential were taken into account. The effect of biaxial stress in the AlAs layer on the binding energy was disregarded. The term "ground" states is used above because the donor states under consideration are ground ones only with respect to the *X* valleys to which these states are related (X_z or X_{xy}). The mutual arrangement of these states is governed by the binding energies and the energies of the minima in the X_z and X_{xy} subbands for a given QW width and by the location of a donor atom in the QW. The results of calculations showed that the absolute values of binding energies for the ground states of hydrogen-like donors were large (~50 meV); there was an appreciable difference (~20 meV) between these energies for the donors located at the center of the *X* well and those related to the X_z and X_{xy} valleys. This circumstance is conducive to experimental observation and identification of the states related to the X_z and X_{xy} valleys for the practically important donors such as Si in thin AlAs layers with the use of resonant-tunneling spectroscopy. In addition, it was shown that the absolute values of binding energies changed appreciably as the donor location in the well

varies (for example, the binding energy of the ground state related to the X_{xy} valleys changed by 25 meV when a donor atom was transferred to the edge of a 10-nm-thick well).

Experimental studies of the structure of donor levels in the band gap of thin AlAs layers are in the initial stage. Optical studies of GaAs/AlAs heterostructures with AlAs doped with silicon showed that there is a single nonsplit donor level related to the *X* valleys in AlAs [16]. Anomalous values of the longitudinal and transverse effective masses in the *X* valleys ($m_l \approx 2.62m_0$ and $m_t \approx 0.44m_0$) had to be used in order to account for the energy of the above level [15]. Resonant-tunneling spectroscopy makes it possible to determine directly the binding energies for donor states under conditions of observation of resonances that correspond to 2D subbands in a QW and to the donor states related to these subbands. This inference was confirmed by tunneling experiments aimed at determining the binding energies of donors in conventional Γ QWs in GaAs/AlAs/GaAs heterostructures [17–19]. However, only one tunneling resonance, presumably related to a Si donor state associated with *X* valleys in general, was detected in a single study published so far, and this concerned tunneling through an AlAs barrier layer doped with Si [20] (the concepts related to the splitting of the X_z and X_{xy} valleys and to differences in the binding energies of relevant donor states were disregarded). Thus, various Si donor states related to the X_z and X_{xy} valleys in thin AlAs layers have not in fact been detected experimentally so far.

In this paper, we report the results of studying the electron transport that occurs through single-barrier GaAs/AlAs/GaAs heterostructures and is caused by resonant-tunneling transitions between the Γ states in GaAs and the *X* states in the AlAs barrier. These results include the following.

(i) We observed the resonant tunneling of electrons both through the states X_z and X_{xy} and through the X_z^D and X_{xy}^D states, which made it possible to determine the binding energies for the X_z^D and X_{xy}^D states of donors located at the center of the AlAs barrier: $E_B(X_z^D) \approx$ 50 meV and $E_B(X_{xy}^D) \approx 70$ meV. These energies were determined directly from the results of identification of resonance features in the transport characteristics. It is also shown on the basis of identification of experimental resonances using the self-consistent calculations of potential profiles across the heterostructure that the energy position of the X_z^D and X_{xy}^D states is largely governed by the following two factors. The first factor is spatial confinement in the AlAs layer. The width of the *X* QW affects both the energies of the X_z and X_{xy} states (the energies corresponding to the minima of the X_z and X_{xy} subbands) (see [6]) and the binding energies for the X_z^D and X_{xy}^D donor states [15]. The second factor is the biaxial stress in the AlAs layer, which is caused by a mismatch of the AlAs and GaAs lattice constants and gives rise to the splitting of the X_z and X_{xy} valleys (as reported also in [6]). The magnitude of this splitting determined by us from the identification procedure amounted to ~23 meV and coincided with the value determined in [6]. Furthermore, we used the value of the difference in energies for the minima Γ (GaAs) and *X* (AlAs) $\Delta_{\Gamma-X} = 120$ meV, which coincided with the average value reported by Teissier *et al.* [3].

(ii) We observed special features in the transport characteristics of the structures in a magnetic field that was parallel to the current ($B \parallel I$). These features were caused by resonant tunneling of electrons between the Γ and *X* states of the Landau levels formed in the presence of a magnetic field in the near-barrier accumulation GaAs layer and in the AlAs barrier, respectively. An analysis of the structure of experimental resonances that corresponded to the above tunneling allowed us to determine the transverse effective mass (m_t) in the AlAs *X* valleys and confirmed the result of identifying the main low-energy resonance in the transport characteristics at $B = 0$. The transverse effective mass determined, $m_t = (0.2 \pm 0.02)m_0$, almost coincides with the value used in practice previously ($0.19m_0$) but differs from the values that have been used when interpreting the experimental data in the majority of publications cited above.

(iii) We observed an additional fine structure of donor resonances in the experimental transport characteristics; this structure is caused by resonant tunneling of electrons through the states of donors that are located in different atomic layers of the AlAs "barrier" (in the growth direction) and have, as a consequence, different binding energies. An investigation into the behavior of the fine structure in relation to variations in a magnetic field shows that the binding energy and, accordingly, the characteristic spatial extent of the wave function of donor states X^D depend heavily both on the magnetic field and on the location of the donor atom in the AlAs barrier, which is consistent with theoretical predictions [15, 21]. The features of the latter dependence allowed us to resolve the resonance-related fine structure caused by tunneling transitions of electrons through the states of donors located in neighboring atomic layers of AlAs. Thus, it is shown that the resonant-tunneling spectroscopy can be used to determine the difference between the binding energies of donors located in neighboring atomic layers of the AlAs barrier.

2. RESONANT TUNNELING OF ELECTRONS THROUGH SPATIALLY CONFINED AND DONOR *X* STATES IN THE ALAS BARRIER AND DETERMINATION OF BINDING ENERGIES FOR THE DONOR STATES RELATED TO THE X_z AND X_{xy} VALLEYS

The samples studied by us were single-barrier heterodiodes fabricated on the basis of symmetrical GaAs/AlAs/GaAs heterostructures with spacers. These

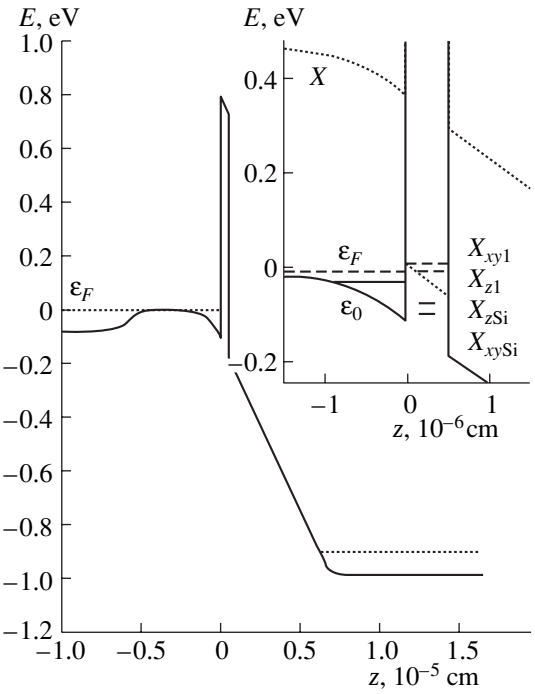

Fig. 2. The potential profile for the Γ minimum of the Brillouin zone along a single-barrier GaAs/AlAs/GaAs heterostructure at voltage $V = 900$ mV. The profiles of the Γ and X minima in the vicinity of the AlAs layer are shown in the inset.

samples were designed in such a way that a 2D accumulation layer for electrons was formed near the AlAs barrier if an external voltage V_b is applied (see Fig. 2). As a result, the processes of resonant Γ–X tunneling occur between 2D electronic Γ states in the accumulation layer and 2D or zero-dimensional donor X states in the AlAs barrier.

An increase in V_b leads to a decrease in the energy of X states with respect to the Γ states in the emitter. Since the processes of Γ–X tunneling occur predominantly without conservation of the wave vector k_{xy} that is transverse to the transport direction [22], a new channel for Γ–X tunneling comes into existence each time the energy of the bottom of a specific subband or the energy of the donor state X^D coincide with the Fermi energy in the emitter accumulation layer. The emergence of a new channel for resonant tunneling through the X states results in a sharp increase in the current.

The heterostructures used in the fabrication of experimental samples were grown by molecular-beam epitaxy on a heavily doped N^+-GaAs substrate with (001) orientation at a substrate temperature of 570°C. These heterostructures had the following sequence of layers:

a 400-nm-thick N^+-GaAs layer with an electron concentration of 2×10^{18} cm^{-3};

a 50-nm-thick N^--GaAs layer with an electron concentration of 2×10^{16} cm^{-3};

a 10-nm-thick layer of undoped GaAs;

a 5-nm-thick layer of undoped AlAs;

a 10-nm-thick layer of undoped GaAs;

a 50-nm-thick N^--GaAs layer with an electron concentration of 2×10^{16} cm^{-3}; and

a 400-nm-thick N^+-GaAs layer with an electron concentration of 2×10^{18} cm^{-3}.

It is noteworthy that, although the AlAs barrier layer was nominally undoped, a high concentration of Si donor impurities was present in this layer owing to the diffusion of impurities from the heavily doped N^+ layer in the course of growth and to a residual Si concentration in the growth chamber. The presence of a high concentration of donor impurities in the AlAs barrier was confirmed in our studies on the basis of analysis of the Shubnikov–de Haas oscillations in a magnetic field that was parallel to the current ($B \parallel I$) [23, 24]. The calculated profile of the Γ minimum in the conduction band of the experimental structure at $V_b = 900$ mV is shown in Fig. 2. The profiles of the Γ and X minima in the vicinity of the AlAs layer are shown in the inset in Fig. 2.

We measured the current–voltage (I–V) characteristics and also the $dI/dV = f(V)$ and $d^2I/dV^2 = f(V)$ in the magnetic-field range from 0 to 14 T at temperatures of 0.4–30 K. The dependences $dI/dV = f(V)$ and $d^2I/dV^2 = f(V)$ were measured using the conventional modulation method.

An I–V characteristic of the experimental sample measured at a temperature of 4.2 K in the absence of a magnetic field is shown in Fig. 3a. As can be seen, a drastic increase in the current occurs at a voltage of about 900 mV; this increase is caused, as will be shown below, by the emergence of a channel of resonant tunneling through the states of the lower X_{z1} subband in the AlAs barrier. The range of the measured current densities from 10 to 100 A/cm^2 observed by us corresponds to the emergence of the channel for Γ–X_{z1} tunneling and coincides with the current densities reported in previous publications [20, 25] where similar structures with a 5-nm-thick AlAs barrier were studied. In addition, the shape of the I–V characteristics in the region of emergence of the channel for the Γ–X tunneling reported previously [20, 22, 25] was similar to that observed by us. Deviations from monotonicity in the I–V characteristics at voltages that are below the threshold of the Γ–X_{z1} tunneling are denoted in Fig. 3a as an "excess current" and manifest themselves as two resonance special features in the $dI/dV = f(V)$ characteristic (see Fig. 3b). A similar special feature of the transport characteristics of single-barrier GaAs/AlAs/GaAs heterostructures, in which a thin region in the vicinity of the middle of the AlAs barrier layer was doped intentionally with Si, was reported in [20]. This feature was attributed to the manifestation of resonant tunneling through single-type donor X^D states in the barrier; these states are related to the X valleys in general, without any consideration of the complex structure of the X states in a thin AlAs layer.

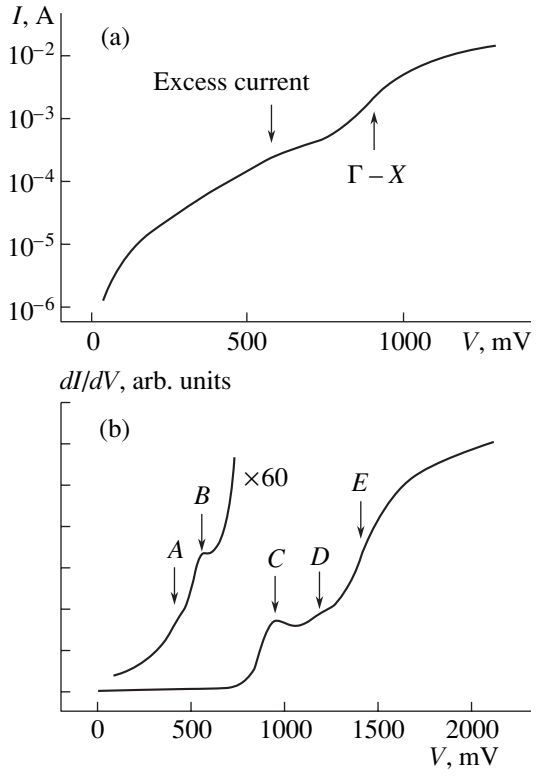

Fig. 3. (a) Current–voltage characteristic of an experimental sample at $T = 4.2$ K; (b) the characteristic $dI/dV = f(V)$.

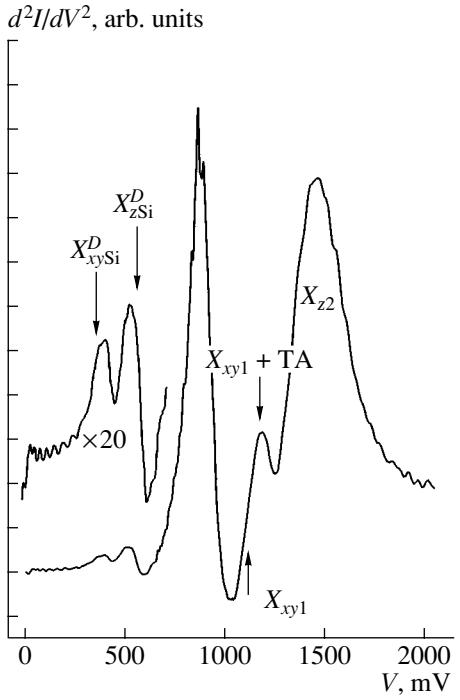

Fig. 4. Dependence $d^2I/dV^2 = f(V)$ for an experimental sample at 4.2 K. Arrows indicate the calculated values of voltages for which the Fermi energy in the accumulation layer coincides with energies of the donor or spatially confined X states in the AlAs layer.

In Fig. 3b, we show the $dI/dV = f(V)$ characteristic measured at a temperature of 4.2 K. Three distinct steplike features in this characteristic, which are denoted by C, D, and E, are caused by the successive emergence of new channels for resonant Γ–X tunneling. We relate features C and E to the thresholds for elastic-tunneling transitions through the X_{z1} and X_{z2} states, whereas feature D corresponds to the threshold for inelastic-tunneling transitions through the X_{xy1} states with the involvement (emission) of transverse acoustic (TA) phonons in AlAs. The two poorly pronounced features A and B at voltages that are lower than the threshold for tunneling through the states X_{z1} are more distinct in Fig. 4, where the dependence $d^2I/dV^2 = f(V)$ is shown. We relate the features A and B to the thresholds for resonant tunneling through the silicon donor states X_z^D and X_{xy}^D.

We identified the special features in experimental transport characteristics using the self-consistent calculations of both potential profiles for the minima in the conduction band and energy levels of electronic states. The results of calculations were then used to determine the voltage V_b required for the initiation of any of the aforementioned processes of Γ–X tunneling. It is noteworthy that, in order to correct the results of self-consistent calculations, we used experimental voltage dependences of both the electron concentration in the accumulation layer and the electric-field strength in the barrier region. These dependences were determined from an analysis of the Shubnikov–de Haas oscillations, which had been previously studied by us in detail [23]. When carrying out the calculations, we also took into account both the anisotropy of the effective mass in the X valleys of AlAs and the splitting of the X_{xy} and X_z valleys due to biaxial stress in the AlAs layer. As a result, we calculated the energies of the X_{xy} and X_z states (the energies of the minima in the subbands X_{xy} and X_z) in relation to the applied voltage. The tunneling transitions with the involvement of phonons were included in the simulation by adding the phonon energy $\hbar\omega_{ph}$ to the energy of the X state under consideration. We then determined the threshold voltages that corresponded to the onset of various processes of resonant tunneling. The threshold voltages for resonant tunneling through the silicon donor states X_z^D and X_{xy}^D were calculated using the data reported in [15]. In the latter publication, the binding energies of hydrogen-like donors related to the X_{xy} and X_z were calculated taking into account the effective-mass anisotropy and the spatial confinement in the AlAs layer (the effect of the QW walls). The binding energies of hydrogen-like donors related to the X_{xy} and X_z valleys and located at the center of the 5-nm-thick AlAs barrier should be equal, according to [15], to 68 and 51 meV, respectively. The arrows in Fig. 4 indicate the calculated values of threshold voltages for

which the energies of the *X* states in the barrier coincide with the Fermi energy in the accumulation emitter layer. As can be seen from Fig. 4, the positions of the peaks in the dependence $d^2I/dV^2 = f(V)$ are in satisfactory agreement with calculated values of threshold voltages. It is also worth noting that the positions of the peaks in the dependence $d^2I/dV^2 = f(V)$ correspond with good accuracy to the conditions of thresholds for resonant tunneling without conservation of the wave vector k_{xy} that is transverse to the transport direction (see, for example, [26]). In order to attain the best agreement between the results of calculations and experimental data, we used the following values of the longitudinal and transverse effective masses in the *X* valley of GaAs: $m_l \approx 1.1m_0$ and $m_t \approx 0.19m_0$; these values are the most widely used. The difference in energies between the Γ (GaAs) and *X* (AlAs) minima was set equal to 120 meV, which coincided with the average of the values reported by Teissier *et al.* [3]. The magnitude of the splitting of the X_{xy} and X_z valleys due to the biaxial stress in the AlAs layer was taken to be equal to 23 meV in accordance with the data reported by van Kesteren *et al.* [6].

As can be seen from Fig. 4, the feature corresponding to elastic tunneling through the X_{xy1} states is not observed. However, we observed the feature caused by tunneling through the X_{xy1} states with emission of the *X*-valley TA phonons in AlAs ($\hbar\omega_{TA}$ = 12 meV). The ratio between the amplitudes of special features corresponding to the tunneling transitions Γ–X_z, Γ–X_{xy}, and Γ–(X_{xy} + TA) observed previously [3, 22], was similar to that shown in Fig. 4 and was accounted for by the corresponding relation between the rates of tunneling transitions $P_{\Gamma-X_z} \gg P_{\Gamma-(X_{xy}+\mathrm{TA})} \gg P_{\Gamma-X_{xy}}$. This relation between the transition rates is also confirmed by the results of studying the photoluminescence spectra of GaAs/AlAs heterostructures (see [3, 6]). The low probability of elastic-tunneling transitions to the states in the outer X_{xy} valleys is caused by the fact that, in order for these transitions to be accomplished, a large change in the transverse wave vector is required. The magnitude of this change *q* is comparable to the value of the wave vector at the boundary of the Brillouin zone; i.e., we have $q \approx 2\pi/a$, where *a* is the lattice constant.

As already mentioned above, the most plausible causes of the presence of the Si donor impurities in the barrier is the diffusion of these impurities from the heavily doped regions during growth and the residual (background) Si concentration in the growth chamber. As a result, the Si donors are found to be almost uniformly distributed in the AlAs layer and, since the binding energy of donors depends on their location in the layer [15], the resonant tunneling through the states of donors located in different atomic layers of AlAs occurs at different values of applied voltage. This circumstance could result in an appreciable broadening of experimental donor resonances. However, the resonant tunneling through donor states located near the middle of the AlAs layer is the most probable process and makes the major contribution to the total current [27]; furthermore, the binding energies of these states are highest [15]. As a result, tunneling transitions through the "middle" (central) donor states give rise to fairly abrupt (in the sense of the magnitude of variation in the current per unit voltage) thresholds for tunneling through various types of the donor states (X_{xy}^D and X_z^D) in the AlAs layer in general and correspond with good accuracy to the peaks in the dependence $d^2I/dV^2 = f(V)$. The above reasoning allowed us to use the identification of the resonance special features of the experimental characteristic $d^2I/dV^2 = f(V)$ to directly determine the binding energies of central states X_{xy}^D and X_z^D as $E_B(X_{xy}^D) \approx 70$ meV and $E_B(X_z^D) \approx 50$ meV, respectively; these values are in good agreement with theoretical results [15].

Additional studies of the Γ–*X* tunneling in a magnetic field that was parallel to the transport direction, $B \parallel I$ ($B \parallel z$), allowed us to confirm the results of identifying special feature *C* in the characteristic $dI/dV = f(V)$ at $B = 0$ as a threshold for resonance Γ–X_{z1} transitions and determine the transverse effective mass m_t in the *X* valleys of AlAs. Application of a magnetic field $B \parallel I$ gives rise to quantization of the electron motion in the *xy* plane, which manifests itself in the formation of the Landau levels with energies $(n_{\Gamma,X} + 1/2)\hbar\omega_c$, where $n_{\Gamma,X}$ are the numbers of the Landau levels in the Γ and *X* subbands, respectively; $\omega_c = eB/m^*_{\Gamma,X}$ is the cyclotron frequency; and $m^*_{\Gamma,X}$ is the cyclotron mass. Finley *et al.* [2] studied the magnetotunneling in GaAs/AlAs/GaAs heterostructures that were similar to those in our studies. The resonance transitions of electrons between the states of various Γ Landau levels in the accumulation layer and *X* Landau levels in the AlAs barrier were observed as peaks in the experimental dependences $d^2I/dV^2 = f(V)$ at voltages that corresponded to a coincidence of these state energies with

$$eB = \alpha\{\Delta E_{\Gamma-X} + \hbar eB[(n_X + 1/2)/m^*_X - (n_\Gamma + 1/2)/m^*_\Gamma]\}, \quad (1)$$

where $\Delta E_{\Gamma-X}$ is the difference between the energies of the minima in the Γ and *X* subbands and α is the factor of proportionality between the applied voltage and relative variation in energies of the Γ and *X* states.

The identification of resonance features in the characteristics $dI/dV = f(V)$ (Fig. 5) was based on the approach suggested by Finley *et al.* [2]. We used the voltage dependences of the electron concentration in the accumulation layer and the electric-field strength in the AlAs barrier layer (and the emitter near-barrier GaAs layer). These dependences had been previously determined from an analysis of the Shubnikov–de Haas oscillations [23] and/or from the aforementioned self-

consistent calculations. Knowledge of the above dependences allowed us to determine the number of Landau levels below the Fermi level in the accumulation layer for various values of the voltage *V*, as well as the assumed values of *B* and *V* at which the resonance features corresponding to transitions between the Γ and *X* Landau levels should be observed. The identification procedure is appreciably simplified by the fact that only two Landau levels with numbers $n_\Gamma = 0, 1$ are found below the Fermi level in the accumulation layer at $V < 1.4$ V and $B > 9$ T, in which case the most pronounced features in the experimental characteristics $dI/dV = f(V)$ are observed. In addition, it was assumed initially that the observed structure of resonance features was caused by transitions via the X_{z1} states of the Landau levels. Indeed, as shown by Finley *et al*. [2], a manifestation of Γ–X_{xy} between the Landau levels in the transport characteristics is complicated by the less pronounced (diffuse due to the broadening of the levels) structure of the X_{xy} Landau levels as a result of the fact that the cyclotron mass corresponding to the X_{xy} Landau levels far exceeds the cyclotron mass for the X_z Landau levels. As a result, we found that the most clearly pronounced features observed in the dependence $dI/dV = f(V)$ at $B > 5$ T and indicated by arrows in Fig. 5 corresponded to transitions between the Γ and X_{z1} states of the Landau levels with the following sets of indices (n_Γ, n_X): (2, 2), (1, 1), and (0, 0). We then fitted the assumed calculated resonance voltages determined using formula (1) to experimental data using the cyclotron mass m_X^* as the adjustable parameter. The fit was performed sequentially for each set of features with a fixed magnetic field, which allowed us to set the same value of $\Delta E_{\Gamma-X}$ in formula (1) for all the special features in a set. Furthermore, the value of α was also assumed to be the same in each aforementioned case, which was verified using the self-consistent calculations and corresponded to the experimental data with satisfactory accuracy (≤5%). The value $m_\Gamma^* = 0.067m_0$ used by us is treated as reliably established. The best agreement with experimental data (shown in the inset in Fig. 5) was attained for $m_X = (0.2 \pm 0.02)m_0$, which coincided with the commonly used value of the transverse effective mass in the *X* valleys of AlAs ($m_t = 0.19m_0$).

If $B \parallel z$, the cyclotron motion of electrons occurs in the *xy* plane. For electrons in the X_z states, the cyclotron motion in the *k* space corresponds to the circular motion over the surface of constant-energy ellipsoids in the X_z valley. As a result, the cyclotron mass corresponding to the X_z states of the Landau levels is equivalent to the transverse effective mass m_t^* in the *X* valleys. However, the electrons located at the X_{xy} states move in the *k* space along elliptic orbits over the surface of the X_z and X_y constant-energy ellipsoids. Therefore, the cyclotron mass is given by the expression $(m_t^* m_l^*)^{1/2} \approx 0.5m_0$. Thus, the value of the cyclotron mass $m_X^* \approx m_t^*$ determined by us confirms the identification of features in the dependence $dI/dV = f(V)$ in a magnetic field $B \parallel I$ (Fig. 5) as a consequence of the Γ–*X* transitions between the Landau levels. In addition, this result is yet another confirmation of the fact that feature *C* in Fig. 3 is caused by the Γ–X_{z1} resonance transitions, as was previously established on the basis of self-consistent calculations at $B = 0$. Finally, it should be noted that the value of m_t^* determined by us differs from the value obtained from an analysis of the Γ–X_z magnetotunneling between the Landau levels [2]. Contradictory values of the transverse effective mass m_t^* have been also reported in many recent publications mentioned in Section 1.

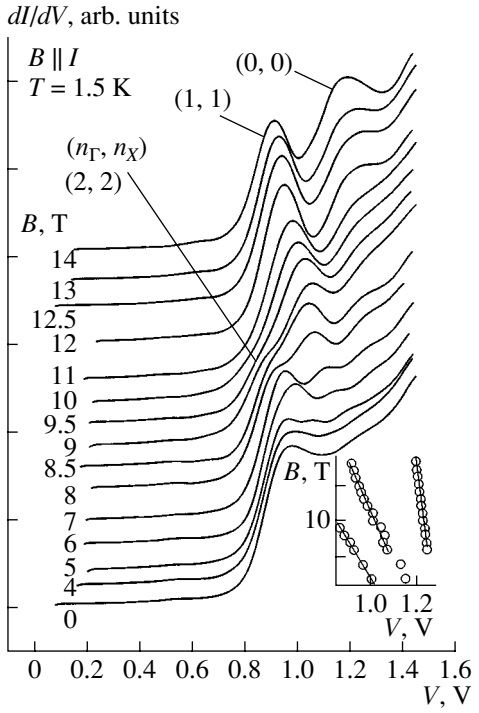

Fig. 5. Experimental dependences $dI/dV = f(V)$ at $T = 1.5$ K in the range of magnetic fields $B \parallel I$ from 0 to 14 T. Positions of the conductivity peaks for various values of *B* are shown in the inset.

3. THE FINE STRUCTURE OF DONOR RESONANCES AS A MANIFESTATION OF TUNNELING TRANSITIONS VIA THE STATES OF DONORS LOCATED IN DIFFERENT ATOMIC LAYERS OF THE AlAs BARRIER

In the previous section, we reported the observation of special features in the transport characteristics of single-barrier GaAs/AlAs/GaAs heterostructures. These features are caused by resonant-tunneling transitions via the Si donor states related to the X_{xy} and X_z valleys

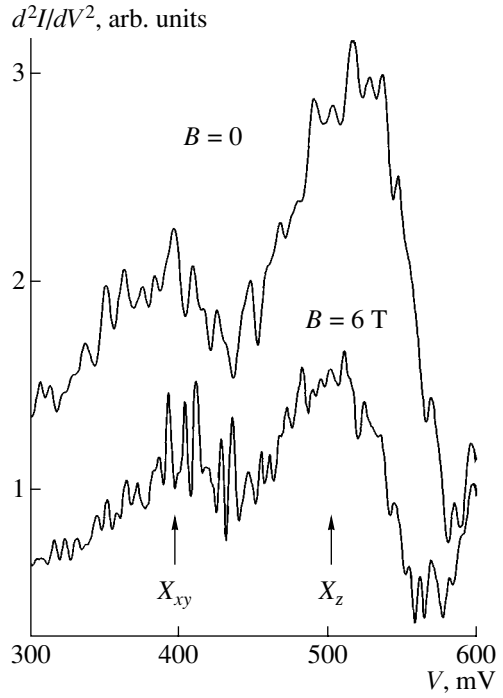

Fig. 6. Experimental dependences $d^2I/dV^2 = f(V)$ in the region of the X_{xy} and X_z donor resonances at $B = 0$ and $B = 6$ T. $T = 1.5$ K.

in the thin AlAs layer; we also determined the binding energies of these states. In this section, we report on the observation of an additional fine structure in the aforementioned features of transport characteristics (donor resonances); this fine structure is caused by tunneling transitions via the states of Si donors that are located at various possible sites (in the growth direction z) in the AlAs layer (i.e., in different atomic layers of AlAs) and, consequently, have different values of the binding energy, as shown by Weber [15].

Previously, the fine structure of donor resonances was observed in the studies of tunneling through structures with a QW in GaAs whose central layers were doped with donor impurities [28, 29]. However, in that case, the fine structure turned out to be mesoscopic conductivity fluctuations caused by statistical fluctuations of quasi-continuous density of localized donor states. These statistical fluctuations are related to appreciable fluctuations of electrostatic potential in the QW region that are induced by charged impurities that are randomly distributed in the depletion region of the doped collector contact. Therefore, the energies of the donor states in the GaAs QW was mainly governed by random fluctuations of the electrostatic potential in the QW region rather than by the dependence of the binding energy on the donor location. As a result, the donor-state energies were also found to be random.

Theoretical calculations showed that the dependence of binding energy of hydrogen-like donors on their location in the AlAs layer is much greater than the similar dependence for donors in the GaAs layer [15, 30, 31]. For example, the difference between the binding energies at the center and at the boundary of the 5-nm-thick AlAs layer (as in the case under consideration) and, consequently, the difference between the binding energies of donors located in neighboring atomic layers exceeds the corresponding values for a GaAs layer with the same thickness by almost an order of magnitude. As a result, possible random fluctuations of the electrostatic potential can no longer greatly affect the energies of donor states in the AlAs layer. This circumstance allowed us to resolve the fine structure of donor resonances; the components of this structure correspond to resonant tunneling via similar donor states located in various atomic layers of the AlAs barrier. The evolution of the fine structure in a strong magnetic field that is parallel to the current direction is observed by us and can be accounted for using the concept that tunneling occurs via the states of donors located at various sites in the AlAs layer. It is also assumed according to the theory [15, 21] that there are heavy dependences of the donor-state energies on the location of donors and on the magnetic field. As a result, the above evolution is an independent confirmation of the interpretation of the fine structure. Thus, in this section, we show that resonance spectroscopy can be used to measure the difference between the binding energies of donors located in neighboring atomic layers of the AlAs barrier.

An additional fine structure of donor resonances in transport characteristics measured at $T = 1.5$ K either in a magnetic field $B = 6$ T parallel to the current or in the absence of a magnetic field is shown in Fig. 6. The large-scale features of the characteristic $d^2I/dV^2 = f(V)$ in Fig. 6 correspond, as we showed above, to resonant tunneling through the groups of donor states related to the X_{xy} and X_z valleys in AlAs in general. In contrast, individual features of the fine structure correspond to tunneling transitions via the single-type (X_{xy}^D or X_z^D) states of donors located in various atomic layers of AlAs. The fine structure of donor resonances was also observed in the absence of a magnetic field; however, this structure became more pronounced as the magnetic field increased. It is noteworthy that we observed virtually no variation in the number of individual features as components of the fine structure with increasing magnetic field. An increase in the amplitudes of the fine-structure features with increasing magnetic field may be caused by the following two factors. First, the application of a magnetic field leads to an additional localization of the donor states (an increase in their binding energies) and, as a result, to a decrease in the broadening of corresponding energy levels. Second, the density of states at the Fermi level in the accumulation layer (this density has a great effect on the amplitudes of resonance features) can be much higher in the presence of a magnetic field (if a specific Landau level is close to the Fermi level) than the density of states in the absence of a magnetic field. Thus, we may state that a magnetic

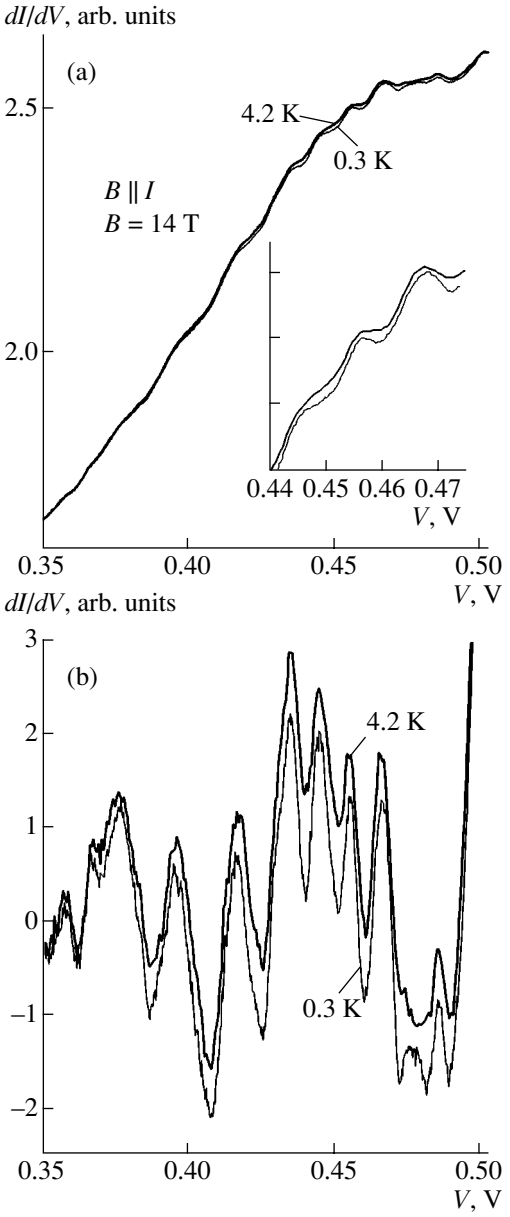

Fig. 7. (a) Experimental characteristics $dI/dV = f(V)$ in the region of the donor resonance X_{xy} in a magnetic field $B = 14$ T (parallel to the current) at temperatures of 0.3 and 4.2 K; (b) the characteristics $dI/dV = f(V)$ after subtraction of the monotonic component.

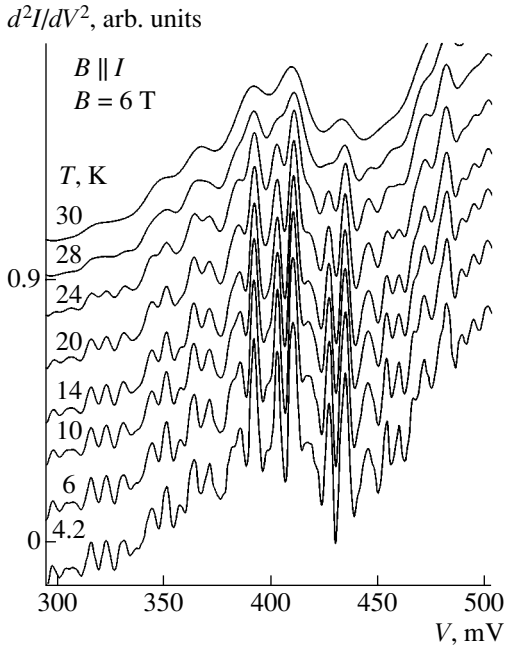

Fig. 8. Experimental dependences $d^2I/dV^2 = f(V)$ in the region of the donor resonance X_{xy} in a magnetic field $B = 6$ T (parallel to the current) in the temperature range 4.2–30 K.

field just enhances the fine structure without changing its nature. At $B > 10$ T, the fine structure is clearly pronounced even in the dependences $dI/dV = f(V)$ (see Fig. 7 for $B = 14$ T). It should be noted that relatively large amplitudes of the fine-structure features in the low-energy donor resonance X_{xy} in Fig. 6 are caused only by the fact that the Landau level with $n = 2$ is located near the Fermi level at $B = 6$ T (and at values of B that are close to 6 T) in the range of voltages at which the Fermi level position in the accumulation layer coincides with the donor states; tunneling through the latter gives rise to the fine structure of the donor resonance X_{xy}. In this situation, the density of states at the Fermi level is relatively high. At higher voltages that correspond to tunneling through the donor X_z^D states, the aforementioned Landau level is still some distance from the Fermi level. Accordingly, the density of states at the Fermi level is relatively low. Naturally, as the magnetic field increases, the situation with amplitudes of features in the fine structure of the X_{xy} and X_z donor resonances becomes opposite. The fine structure is found to be specific but highly reproducible for each sample, even after thermal cycling. In addition, the fine structure is to a certain extent regular (Fig. 6) with an average period of about 15 mV, which corresponds to the energy difference of 1.2 meV, taking into account the factor of proportionality between the relative variation in the energies of donor states and applied voltage; this factor was determined from the self-consistent calculations.

An increase in temperature to 20 K ($kT \approx 1.25$ meV) leads, as can be seen from Fig. 8, to an appreciable suppression of the majority of features in the fine structure as a result of thermal broadening of the Fermi distribution function in the accumulation layer; the fine structure almost completely disappears at $T = 30$ K. The decrease in temperature from 4.2 to 0.3 K (Fig. 7) led to an increase in the amplitudes of the fine-structure features, the resolution of an additional feature at $V \approx 0.48$ V, and the manifestation of an even finer structure (i.e., substructure) in certain features. Thus, the number of features in the fine structure remains virtually constant in the temperature range 0.3–20 K. This observa-

tion indicates that the smallest difference between the donor-state energies exceeds kT in the above temperature range.

We now consider the experimental data reported above in more detail taking into account that there are two alternative plausible reasons for the appearance of the fine structure. First, as the studies of the Γ–Γ tunneling in two-barrier GaAs/AlAs heterostructures showed, the fine structure can be caused by the roughness of interfaces [32]. However, the donor binding energy in AlAs depends more heavily on the location of the donor in the layer than on the thickness of the layer itself [15]. For example, a variation in the thickness of an AlAs layer by two monolayers (a typical magnitude of roughness of heterosurfaces in the case of molecular-beam epitaxy) leads to changes in the binding energies of central donors X_{xy}^D and X_z^D by 4 and 2 meV, respectively. In contrast, the experimentally observed difference between the binding energies of donors located in the center (middle) of the 5-nm-thick AlAs layer and those located on the layer boundary is approximately equal to 30 and 20 meV for the X_{xy}^D and X_z^D donors, respectively. Therefore, we assume that the roughness of interfaces cannot give rise to the fine structure in the situation under consideration. Second, the presence of donors in the QW of the GaAs/AlAs structure can give rise to mesoscopic fluctuations of differential conductivity; these fluctuations are caused by statistical fluctuations in the quasi-continuous density of localized donor states [28, 29]. The conductivity fluctuations manifest themselves as the fine structure of donor resonances. Both the amplitudes and the number of observed fluctuations in the conductivity (or their typical period with respect to voltage) decreased simultaneously as temperature increased from 0.5 to 4.2 K and finally ceased to exist. In order to explain this temperature dependence of fluctuations, the modified Larkin–Matveev theory of mesoscopic fluctuations was used [33]. The donor states in AlAs are found to be localized to a much greater extent than those in GaAs, and the binding energies of Si donors located in neighboring atomic layers of AlAs differ to a much greater extent (nearly by an order of magnitude) than those in GaAs [15]. Therefore, random fluctuations of electrostatic potential affect the spectrum of donor states in AlAs to a much lesser extent. As a result, the spectrum of donor states in the AlAs layer is mainly controlled by the dependence of the binding energy on the donor location. Both the regularity in the arrangement of features in the fine structure under investigation and the agreement between the number of observed features and the number of possible positions of Si donors in the 5-nm-thick AlAs layer confirm that fluctuations of electrostatic potential insignificantly affect the spectrum of donor states in AlAs in the experimental situation under consideration. The fine structure of the donor resonance X_{xy} (as well as of the resonance X_z) included 22 features, whereas Si donors can be located in 20 different atomic layers in a 5-nm-thick AlAs layer. The difference between the binding energies of the donors X_{xy} located at the center and the boundary of the AlAs layer is equal to 35 meV in the case under consideration [15]. Therefore, the average difference between corresponding donor levels should be approximately equal to 1.65 meV. The average difference between voltages related to neighboring features in the observed fine structures was equal to 15 mV and corresponded to the energy difference of 1.2 meV, which is in satisfactory agreement with the previous estimate. As noted above, the features of the fine structure are suppressed to a great extent as temperature is increased from 0.3 to 20 K. However, the number and shape of the features remain virtually unchanged in this case. A further increase in temperature from 20 to 30 K leads to the complete disappearance of the fine structure. In our opinion, such an evolution of the fine structure with increasing temperature is caused by the temperature-related broadening of the Fermi distribution function in the accumulation layer and, thus, represents an additional confirmation of the suggested interpretation of the fine structure. We believe that, under the conditions of our experiment, random fluctuations of electrostatic potential lead only to additional inhomogeneous broadening of the states of donors located in different atomic layers.

The modification of transport characteristics of our samples in a magnetic field $B \parallel I$ was found to be quite complex, since this modification was caused in part by the Landau quantization in the accumulation layer and in part by changes in the fine structure. Therefore, in order to clarify the effect of the magnetic field on the fine structure, we studied in detail the transport in high magnetic fields ($B > 12$ T). Under these conditions, only a single Landau level is found below the Fermi level in the accumulation layer (in the voltage range corresponding to the donor resonance X_{xy}). A shift of this Landau level with increasing B can produce only monotonic changes in the accumulation-layer parameters and, consequently, monotonic shifts of the resonance features. As can be seen from Fig. 9a, where the fine structure of the donor resonance X_{xy} is shown in the range of $B \parallel I$ from 12.75 to 14 T at $T = 0.4$ K, the peaks in the fine structure shift to lower voltages with increasing magnetic field. The dependence of positions of the peaks in the experimental curve on the value of B is shown in Fig. 9b. The fine-structure peaks in the region of the donor resonance X_{xy} shift with the rates from 8 to 20 mV/T in the voltage range 300–500 mV; the rate of this shift is a steadily increasing function of the voltage (Fig. 9b). The results of our self-consistent calculations showed that, in the voltage range under consideration (300–500 mV), the ratio between the applied voltage and the voltage drop across the AlAs layer varied only very slightly (from 12 to 12.7) and could not appreciably affect the shift of resonance peaks as B varied. In addition, it was shown that, in the voltage and magnetic-field ranges under consideration, variations in the

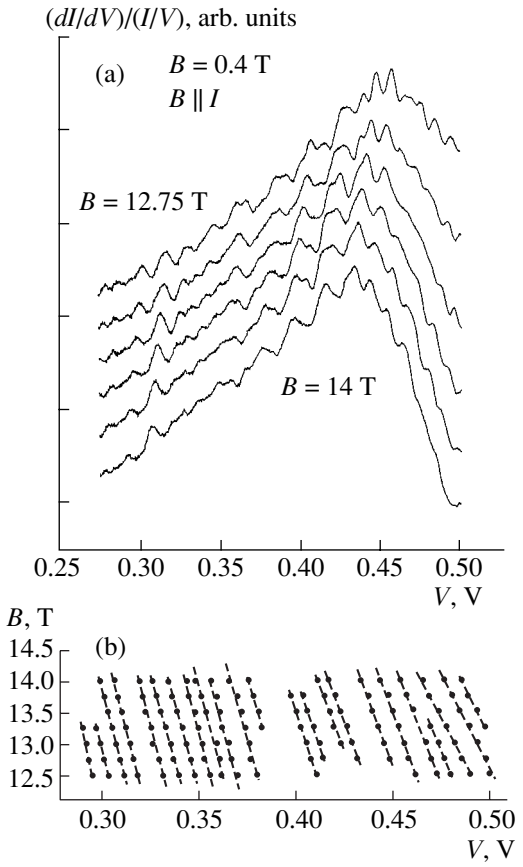

Fig. 9. (a) Experimental characteristics $dI/dV = f(V)$ in the region of the donor resonance X_{xy} at $T = 0.4$ K in the range of magnetic fields from 12.75 to 14 T (the field was parallel to the current); (b) positions of the fine-structure peaks for various values of the magnetic field.

accumulation-layer parameters as a result of a shift of the Landau levels were also insignificant and could not account for the very large difference between the rates of shifts of the peaks as observed experimentally. Therefore, we rely on theoretical predictions [15, 27] and believe that this difference in the rates is related to the fact that the binding energy of the states with lesser localization for donors located near the boundary of the AlAs layer depends much more heavily on B than the binding energy of more highly localized states of the donors located near the middle of the AlAs layer. We note for clarity that the low-energy features of the fine structure correspond to tunneling transitions through the states of donors located near the middle of the AlAs layer. Thus, the behavior of the fine structure when the magnetic field is varied represents an independent experimental confirmation of the fact that individual features of the fine structure are caused by resonant tunneling through the states of donors located in various atomic layers of AlAs. In addition, this behavior confirms the strong dependence of the binding energy for the X donors on their location in the AlAs layer; this dependence has been predicted theoretically [15].

4. CONCLUSION

We now summarize the results of these studies of transport through single-barrier GaAs/AlAs/GaAs heterostructures. We observed special features in the transport characteristics; we unambiguously related these features to manifestations of resonant Γ–X tunneling through quasi-confined X states and through various donor X^D states in the AlAs layer. The features were identified using both the self-consistent calculations of voltages that corresponded to the thresholds of resonant transitions and the results of analysis of the Shubnikov–de Haas oscillations in the structures under consideration. The results of identification show that the energies of the donor X^D states are predominantly controlled by spatial confinement in the AlAs layer (the quantum-well width) and by biaxial stress, which gives rise to splitting of the X_{xy} and X_z valleys. The aforementioned spatial confinement affects the energies of the X_{xy} and X_z states and the binding energies of the donor states X^D_{xy} and X^D_z. In addition, the aforementioned results allowed us to directly determine the binding energies of "central" donor states X^D_{xy} and X^D_z as $E_B(X^D_{xy}) \approx 70$ meV and $E_B(X^D_z) \approx 50$ meV, respectively. An analysis of the evolution of the structure of resonance features caused by tunneling transitions between the Γ and X Landau levels with a variation in a magnetic field made it possible to determine the transverse effective mass m_t^* in the AlAs X valleys. This analysis also confirmed the result of identification of the main low-energy resonance in the transport characteristics in the absence of a magnetic field as a manifestation of the Γ–X_{z1} tunneling transitions. We also observed an additional fine structure of the donor resonances in the experimental transport characteristics. This structure is caused by resonant tunneling of electrons through the states of donors that are located in different atomic layers of the AlAs barrier (in the growth direction) and, correspondingly, have different binding energies. Studies of the behavior of the fine structure in a magnetic field $B \parallel I$ confirm that the binding energy of the donor X states depends heavily on the location of donors in the AlAs layer and on magnetic field; these dependences were predicted theoretically. As a result, we show that it is possible to use resonant-tunneling spectroscopy to study the states of donors located in neighboring atomic layers of the AlAs barrier and measure the difference in the binding energies of these donors.

ACKNOWLEDGMENTS

We thank T.G. Andersson for providing us with the heterostructures and Prof. V.A. Tulin and K.S. Novoselov for fruitful discussions and the interest they showed in this study.

This study was supported in part by the Russian Foundation for Basic Research (the program on the physics and technology of nanostructures) and INTAS (grant no. 01-2362).

REFERENCES

1. E. E. Mendez, W. I. Wang, E. Calleja, and C. E. T. Goncalves da Silva, Appl. Phys. Lett. **50**, 1263 (1987).
2. J. J. Finley, R. J. Teissier, M. S. Skolnick, *et al.*, Phys. Rev. B **54**, 5251 (1996).
3. R. J. Teissier, J. J. Finley, M. S. Skolnick, *et al.*, Phys. Rev. B **54**, 8329 (1996).
4. J. M. Smith, P. C. Klipstein, R. Grey, and G. Hill, Phys. Rev. B **58**, 4708 (1998).
5. J. M. Smith, P. C. Klipstein, R. Grey, and G. Hill, Phys. Rev. B **57**, 1740 (1998).
6. H. W. van Kesteren, E. C. Cosman, P. Dawson, *et al.*, Phys. Rev. B **39**, 13426 (1989).
7. E. R. Glaser, T. A. Kennedy, B. Molnar, *et al.*, Phys. Rev. B **43**, 14540 (1991).
8. K. Maezawa, T. Mizutani, and S. Yamada, J. Appl. Phys. **71**, 296 (1992).
9. S. Yamada, K. Maezawa, W. T. Yuen, and R. A. Stradling, Phys. Rev. B **49**, 2189 (1994).
10. D. Scalbert, J. Cernogora, C. Benoit a la Guillaume, *et al.*, Solid State Commun. **70**, 945 (1989).
11. D. Landheer, H. C. Liu, M. Buchanan, and R. Stoner, Appl. Phys. Lett. **54**, 1784 (1989).
12. P. Lefebvre, B. Gil, H. Mathieu, and R. Planel, Phys. Rev. B **40**, 7802 (1989).
13. M. Goiran, J. L. Martin, J. Leotin, *et al.*, Physica B (Amsterdam) **177**, 465 (1992).
14. B. Rheinlander, H. Neumann, P. Fischer, and G. Kuhn, Phys. Status Solidi B **K167**, 49 (1972).
15. G. Weber, Appl. Phys. Lett. **67**, 1447 (1995).
16. S. T. Lee, A. Petrou, M. Dutta, *et al.*, Phys. Rev. B **51**, 1942 (1995).
17. M. W. Delow, P. H. Beton, C. J. M. Langerak, *et al.*, Phys. Rev. Lett. **68**, 1754 (1992).
18. J. W. Sakai, P. C. Main, P. H. Beton, *et al.*, Appl. Phys. Lett. **64**, 2563 (1994).
19. J. W. Sakai, T. M. Fromhold, P. H. Beton, *et al.*, Phys. Rev. B **48**, 5664 (1993).
20. H. Fukuyama and T. Waho, Jpn. J. Appl. Phys. **34**, L342 (1995).
21. J. M. Shi, F. M. Peeters, G. Q. Hai, and J. T. Devreese, Phys. Rev. B **44**, 5692 (1991).
22. J. J. Finley, R. J. Teissier, M. S. Skolnick, *et al.*, Phys. Rev. B **58**, 10619 (1998).
23. Yu. V. Dubrovskii, Yu. N. Khanin, I. A. Larkin, *et al.*, Phys. Rev. B **50**, 4897 (1994).
24. Yu. V. Dubrovskiĭ, Yu. N. Khanin, T. G. Andersson, *et al.*, Zh. Éksp. Teor. Fiz. **109**, 868 (1996) [JETP **82**, 467 (1996)].
25. Y. Carbonneau, J. Beerens, H. C. Liu, *et al.*, Appl. Phys. Lett. **62**, 1955 (1993).
26. M. Tsuchiya and H. Sakaki, Jpn. J. Appl. Phys. **30**, 1164 (1991).
27. I. P. Roche, G. P. Whittington, P. C. Main, *et al.*, J. Phys.: Condens. Matter **2**, 4439 (1990).
28. P. McDonnell, T. J. Foster, P. C. Main, *et al.*, Solid-State Electron. **40**, 409 (1996).
29. P. C. Main, T. J. Foster, P. McDonnell, *et al.*, Phys. Rev. B **62**, 16721 (2000).
30. R. L. Greene and K. K. Bajaj, Solid State Commun. **45**, 825 (1983).
31. L. E. Oliveira, Phys. Rev. B **38**, 10641 (1988).
32. Y. C. Kang, M. Suhara, K. Furuya, *et al.*, Jpn. J. Appl. Phys. **34**, 4417 (1995).
33. A. I. Larkin and K. A. Matveev, Zh. Éksp. Teor. Fiz. **93**, 1030 (1987) [Sov. Phys. JETP **66**, 580 (1987)].

Translated by A. Spitsyn

Semiconductors, Vol. 38, No. 4, 2004, pp. 431–436. Translated from Fizika i Tekhnika Poluprovodnikov, Vol. 38, No. 4, 2004, pp. 448–454.

LOW-DIMENSIONAL SYSTEMS

Tuning the Energy Spectrum of InAs/GaAs Quantum Dots by Varying the Thickness and Composition of the Thin Double GaAs/InGaAs Cladding Layer

I. A. Karpovich*, B. N. Zvonkov, S. B. Levichev, N. V. Baidus, S. V. Tikhov, D. O. Filatov, A. P. Gorshkov, and S. Yu. Ermakov

Nizhni Novgorod State University, Nizhni Novgorod, 603950 Russia

**e-mail: fdp@phys.unn.ru*

Submitted July 7, 2003; accepted for publication July 14, 2003

Abstract—It is shown that the ground state transition energy in quantum dots in heterostructures grown by atmospheric-pressure MOCVD can be tuned in the range covering both transparence windows of the optical fiber at wavelengths of 1.3 and 1.55 μm by varying the thickness and composition of the thin GaAs/$In_xGa_{1-x}As$ double cladding layer. These structures also exhibit a red shift of the ground state transition energy of the $In_xGa_{1-x}As$ quantum well (QW) as a result of the formation of a hybrid QW $In_xGa_{1-x}As$/InAs (wetting layer) between the quantum dots (QDs). The Schottky diodes based on these structures are characterized by an increased reverse current, which is attributed to thermally activated tunneling of electrons from the metal contact to QD levels. © *2004 MAIK "Nauka/Interperiodica".*

1. INTRODUCTION

Quantum dot heterostructures (QDH) with self-organized InAs/GaAs quantum dots (QDs) have attracted particular interest owing to the prospects for their application in optoelectronics, especially in the design of high-efficiency laser diodes for fiber-optic communication lines [1, 2]. A problem of current interest is growing structures that emit in the maximum transparence window of optical fibers at a wavelength of ≈1.55 μm, which corresponds to the energy of the ground state transition in QDs, $E_0(QD) \approx 0.8$ eV. A possible solution to this problem is to clad the InAs QD layer with an $In_xGa_{1-x}As$ quantum well (QW) layer, which results in the red shift of $E_0(QD)$ [3–5]. Laser structures that emit in the maximum-transparence window of optical fibers at a wavelength of 1.3 μm were produced by this method [6]. In similar structures with an enhanced In content in the QW layer ($x = 0.35$–0.45), photoluminescence at 1.52 μm was observed, but the quantum efficiency was low [7]. The main reason for the red shift of $E_0(QD)$ in combined QW/QD layers is either the relaxation of elastic stress in QDs, caused by the reduction of the lattice mismatch on the QW/QD interface [3, 6], or the increase in the QD effective size, related to the decomposition of the QW solid solution, which is stimulated by the presence of InAs clusters [4, 5].

These effects can be manifested to various extents in structures grown by different methods in different conditions. Earlier [8], we studied the effect of cladding the QD layer with a QW layer in structures grown by MOCVD at atmospheric pressure. Unlike QDH grown by MBE [3] and low-pressure MOCVD [7], in which the red shift of the QD energy spectrum $\Delta E_0(QD)$ exceeds 100 meV, the red shift in structures obtained in [8] is relatively small, $\Delta E_0(QD) < 30$ meV. However, these structures demonstrate very low $E_0(QD)$, less than 0.85 eV at room temperature, even without cladding the QD layer with a QW layer [9]. It is suggested that, owing to diffusion mixing of In and Ga, an interlayer of a solid solution is formed on the GaAs/InAs heterointerface, which relieves elastic stresses in QDs. It seems reasonable that in this situation the deposition of an external QW layer can exert only a small influence on the transition energy.

In the same structures, a considerable red shift of the ground state transition energy ($\Delta E_0(QD) \approx 100$ meV) in InGaAs QDs has been observed when the QW layer was deposited onto the QD layer; the effect was attributed to the formation of a hybrid QW, InGaAs + InAs (wetting layer, WL) in the space between QDs.

The present study is concerned with the influence exerted by the thickness and composition of the QW material, as well as the thickness of the external GaAs cladding layer, on the energy spectrum of combined QW/QD layers in structures grown by MOCVD at atmospheric pressure.

2. EXPERIMENTAL

Heterostructures were grown on semi-insulating (100) GaAs substrates. An *n*-GaAs buffer layer, 0.6 μm in thickness, with an electron density of $\sim 5 \times 10^{16}$ cm^{-3}, was grown at a temperature of 650°C; then the temperature was lowered to 520°C, and the following layers were deposited: InAs QDs (five monolayers),

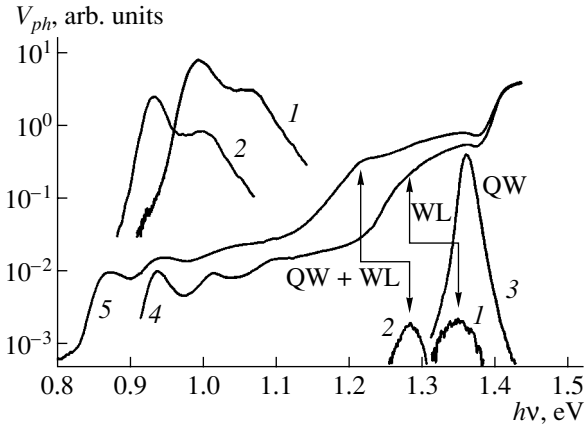

Fig. 1. Effect of cladding the QD layer with a QW layer on PL and PSE spectra. (*1*, *2*) PL spectra of QDH (77 K), (*3*) PL spectrum of a structure with a single QW (77 K), and (*4*, *5*) PSE spectra (300 K); (*1*, *4*) a structure with a separate QD layer, (*2*, *5*) a structure with a combined QW/QD layer. Arrows: PL peaks and edges of the photosensitivity bands from QWs in these structures.

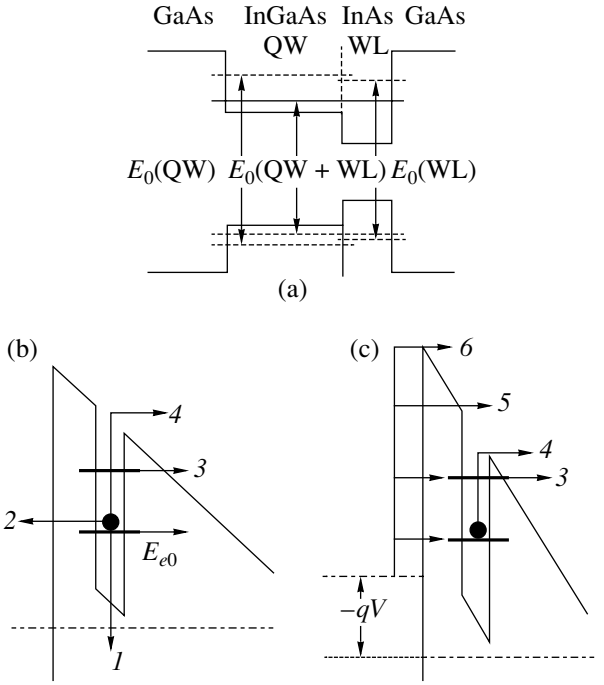

Fig. 2. Energy diagrams: (a) hybrid quantum well (QW + WL) (dashed lines show levels in separate QWs); (b) interface between metal and QDH with a thin cladding layer; (c) the same, with reverse bias applied to the contact.

$In_xGa_{1-x}As$ QW (x = 0.2–0.3, well width L = 2–12 nm), and the external GaAs layer with thickness d_c = 3–30 nm. For better uniformity of the QDs, the InAs layer was doped with Bi in the course of deposition [10].

According to atomic force microscopy (AFM) data, QDs uncovered by selective etching of the cladding layer [10] were 40–50 nm in lateral size, 4–5 nm in height, and had a surface density of $\sim 1 \times 10^{10}$ cm^{-2} in the structures obtained. The spectral dependences of photoluminescence (PL) under excitation with a He–Ne laser and of the photovoltage at the semiconductor/electrolyte interface (PSE) and across the Schottky barriers with a golden blocking contact were studied. The electrolyte was a (1 : 1) mixture of 1*M* KCl aqueous solution with glycerol. To exclude the impact of the light absorption in the electrolyte on PSE spectra, which was significant at $h\nu < 0.9$ eV, the structures were illuminated through the substrate. This resulted in the cutoff of spectra in the intrinsic absorption range of GaAs. The PSE experimental technique was described in detail in [11].

3. RESULTS AND DISCUSSION

3.1. Structures with a Single QD Layer

Structures with a single QD layer and a relatively thick GaAs cladding layer ($d_c \approx 30$ nm) were used as a reference for the determination of the red shift of E_0(QD) in structures with a thinner cladding layer [at $d_c > 30$ nm, E_0(QD) is virtually independent of the cladding layer thickness]. The growth conditions for these structures were chosen so that the ground state transition energy E_0(QD) ≈ 0.95 eV corresponded to the PL emission wavelength $\lambda_0 \approx 1.3$ μm. Figure 1 shows typical spectra of such a structure: PL at 77 K (curve *1*) and PSE at 300 K (curve *4*). Although the intensity of QD PL was high even at room temperature, weak emission lines related to the InAs wetting layer and QW in combined QW/QD layers are better resolved in the PL spectra recorded at 77 K.

At $d_c \approx 30$ nm, QDs experience the electric field of the surface barrier, ~30 kV/cm (Fig. 2b); this ensures a virtually 100% emission of photoexcited electrons and holes from QDs to the matrix, which is necessary to obtain the maximum normalized photosensitivity of QDs, i.e., the maximum ratio of the photosensitivity in the range of QD absorption to the intrinsic photosensitivity of the GaAs matrix. The dominant mechanisms of emission are presumably thermal above-barrier emission (transition *4*) and thermally activated tunneling emission (transition *3*) through the triangular barrier lowered by the field. It is worth noting that when the QD layer is built in the quasi-neutral region of the structure (at $d_c \approx 300$ nm), the photosensitivity in the range of the ground state transition is strongly depressed (as low as the detection limit [11]), which indicates a nearly total termination of the electron and hole emission from the QD ground state levels to the matrix.

The photosensitivity related to QDs was one to two orders of magnitude weaker that related to QWs (the edges of QW photosensitivity bands are marked by arrows in Fig. 1), which may be attributed to the difference between the absorption coefficients of QDs and QWs. The surface barrier does not interfere with the

observation of the QD PL (Fig. 2b, transition *1*), because at the high level of the PL photoexcitation in the intrinsic absorption range of GaAs it is flattened, and the rate of the radiative recombination of electrons and holes exceeds the rate of their emission from the QD.

3.2. Structures with a Combined QW/QD Layer

Figure 1 shows how the capping of the QD layer with an external $In_xGa_{1-x}As$ ($x = 0.2$, $L = 5$ nm) QW layer modifies the PSE and PL spectra in structures with a thick GaAs cladding layer. In the combined QW/QD layer, the red shift ΔE_0(QD) in PSE spectra was ~70 meV, and the minimum E_0(QD) was ≈0.87 eV at 300 K (curve *5*). With correction made for the temperature shift of spectra, these data are in good agreement with the PL spectra recorded at 77 K (curves *1*, *2*). It was found that the red shift of E_0(QD) disappears if a 5-nm-thick GaAs spacer is deposited between the QW and QD layers.

Along with the two factors mentioned above, the red shift of the QD spectrum may be related to the decrease of the effective barrier in the QD on the InAs/InGaAs interface. However, in the structures under study the principal factor is the relaxation of elastic stress in QDs. This is specifically confirmed by the fact that in QD layers grown on the surface, and also in those uncovered by selective etching of the GaAs cladding layer, when the capping InGaAs layer is absent and the barrier height on the free surface of QDs even increases, a strong (~300 and 150 meV, respectively) red shift of E_0(QD) is also observed [12]. Below we will present additional arguments in favor of this conclusion.

It is noteworthy that the stress relaxation reduces E_0(QD) not only by virtue of the reduction of elastic strain in QDs, but also because it facilitates the growth of larger pseudomorphic clusters, QDs. The final stage of their formation continues for some time during the deposition of the InAs/InGaAs cladding layer and after the termination of this process, which is especially typical of MOCVD [13], which is usually done at higher temperatures than MBE.

As can be seen in Fig. 1, the structures under study also demonstrate the red shift of the ground state transition energy in the QW layer deposited onto the QD layer. In the single-QW structure with x and L defined above, the ground state transition energy in the QW is E_0(QW) ≈ 1.37 eV at 77 K (curve *3*). It is close to the ground state transition energy in the QW of the InAs WL in the structure with a single QD layer, E_0(WL) ≈ 1.36 eV (curve *1*). In structures with a combined QW/QD layer, the peak of PL from QW lies at an energy of 1.285 eV (curve *2*). This shift is related to the formation of a hybrid QW (QW + WL), whose profile is shown in Fig. 2a. Calculations of the energy spectrum of such steplike QWs taking account of the Kane dispersion law for electrons and elastic stresses in the QW [14] have shown a satisfactory agreement with experiment. The table contains the data calculated for structures whose spectra are shown in Fig. 1.

Calculated and experimental ground state transition energies at 77 K in different types of QWs

Layer type	QW	WL	QW + WL
Parameters: x; L, nm	0.2; 5	1; 0.6	
E_0(QW), eV (calculated)	1.38	1.36	1.3
E_0(QW), eV (experiment)	1.37	1.36	1.29

The calculations show that the electron ground state E_{e0} always lies in the wide part of a steplike potential well, but the heavy-hole level E_{hh0} is found to be in the potential well of the WL at some specific values of parameters x and L, which should lead to a strong decrease in the overlap integral of the envelopes of electron and hole wave functions and, consequently, in the band-to-band optical absorption coefficient and photosensitivity. Specifically, this occurs in a structure with the combined QW/QD layer, whose parameters are listed in the table. For this structure, the calculated level E_{hh0} lies in the potential well of the WL, though close to its edge (20 meV below it). However, the normalized photosensitivity of the hybrid QW (QW + WL) and the QW of the WL are nearly equal (compare curves *4* and *5*). This means that level E_{hh0}, as well as E_{e0}, lies in the wide part of the hybrid well, as shown in Fig. 2a. We believe that this disagreement with the calculated results, which was also observed for some other structures, can be attributed to the deviation of the structure profile from the ideal steplike form as a result of diffusion processes.

3.3. Structures with a Surface QW/QD Layer

A significantly stronger red shift of E_0(QD) was obtained in structures with a surface QW/QD layer. In these structures, the QW layer served as the cladding layer for QDs. The thinning of the GaAs cladding layer from 25 to 5 nm in a structure with a single QD layer reduced E_0(QD) in PSE spectra from 0.95 to 0.86 eV (Fig. 3, curves *1*, *2*), which also indicates the decisive role of elastic stress in this effect. When $In_{0.2}Ga_{0.8}As$ was deposited instead of a GaAs layer of the same thickness, E_0(QD) decreased to 0.78 eV (curve *3*). When the QD layer was built-in between two similar QWs ($x = 0.2$, $L = 5$ nm), a relatively weak additional red shift of E_0(QD) to 0.755 eV was observed (curve *4*), but the QD uniformity deteriorated significantly, which is indicated by the fact that the structure of the spectrum related to excited states of QDs is weakly pronounced. It is worth noting that E_0(QD) decreases to ~0.7 eV in structures in which the surface QD layer is not covered by a QW layer [11].

In this type of structure, the red shift of the photosensitivity spectrum is followed by a decrease in the energy of the ground state transition peak in respect to

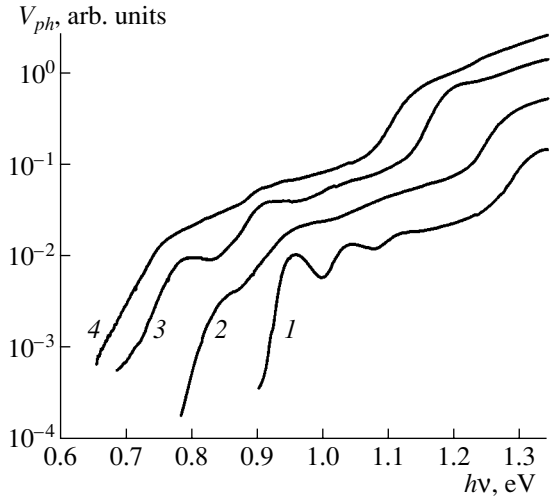

Fig. 3. Effect of the cladding layer thickness and composition in structures with the surface QW/QD layer on PSE spectra. Composition and thickness (nm): (*1*) GaAs (25); (*2*) GaAs (5); (*3*) $In_{0.2}Ga_{0.8}As$ (5); and (*4*) QD layer built-in between two $In_{0.2}Ga_{0.8}As$ QWs (5).

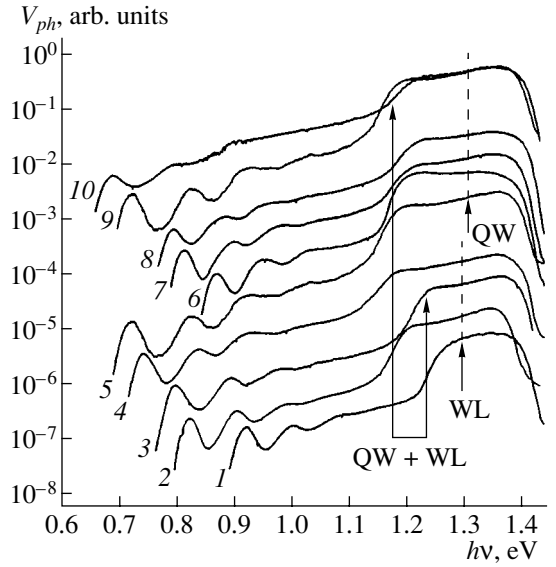

Fig. 4. Effect of parameters of a double cladding layer on PSE spectra of QDH. QW parameters, *x*, *L* (nm): (*1*) without QW; (*2*) 0.2, 5; (*3*) 0.2, 4; (*4*) 0.3, 4; (*5*) 0.3, 2; (d_c = 25 nm for curve *1* and 5 nm for curves *2–5*). The thickness of GaAs cladding layer, d_c: (*6*) 20, (*7*) 10, (*8*) 7, (*9*) 5, and (*10*) 3 nm. For curves *6–10*, the QW parameters are $x = 0.3$, $L = 2$ nm.

that of peaks associated with the excited states of QDs (compare curves *2–4* with curve *1*), and by a strong quenching of the PL, which may be attributed to the appearance of a recombination channel directly on the QD surface. Its effect is stronger in the range of the ground state transition, because the probability of emission of nonequilibrium electrons and holes from the QD to the matrix from the ground state levels is much less than from the excited state levels. Although the ground state transition energy is even lower than 0.8 eV in structures with surface QW/QD layers, a significant disadvantage of these structures is the low intensity of QD PL, which is due to the strong influence of the surface recombination.

Similar to the case of structures with a relatively thick cladding layer, structures with surface QW/QD layers exhibit red shift in the spectrum of the hybrid QW (curves *3*, *4*). For curve *4*, the shift is about 150 meV in respect to the WL. It is noteworthy that, in the structure with a thin GaAs cladding layer, a small red shift in the wetting layer spectrum is also observed (compare curves *2* and *1*), which indicates that its thickness is larger than in structures with a thick cladding layer. Increasing the cladding layer thickness and the related buildup of the elastic stress in the WL lead to the reconstruction of its structure, which consists in thinning it via the formation of small-size QDs [9].

3.4. Structures with a Thin GaAs/InGaAs Double Cladding Layer

One might expect that the deposition of a thin enough GaAs cladding layer onto the combined QW/QD layer would depress the surface recombination channel in QD and that no considerable blue shift of E_0(QD) would occur. As shown in [15], when a narrower-gap semiconductor (GaAs) is covered with a thin layer of lattice-matched wider-gap material ($In_{0.5}Ga_{0.5}P$), the rate of surface recombination in GaAs strongly decreases. The effect is attributed to barriers arising on the InGaP/GaAs interface, which constrain the electron and hole recombination flows to the defective outer surface of InGaP (the effect is named heteroepitaxial passivation of the surface). In the structures under study, the GaAs layer should act as a passivating coating in respect to the combined QW/QD layer. The pseudomorphism of this layer naturally provides the lattice matching and, consequently, low density of the surface states on the GaAs/InGaAs interface. Indeed, our experiment has shown that the deposition of a thin GaAs layer can provide both the relaxation of elastic stress and a reduction of the surface recombination rate.

Figure 4 shows the influence of parameters of a thin double layer on PSE spectra. In a set of structures in which the impact of QW parameters *x* and *L* on the spectra was investigated (curves *2–5*), a 5-nm-thick GaAs cladding layer was deposited onto the QW. As stated above, a layer of this thickness does not produce strong elastic stress in the underlying QD layer. Increasing the In content in QW from 0.2 to 0.3 nm and decreasing the QW width from 12 to 2 nm raise the red shift of E_0(QD). The last result seems unexpected; it is inconsistent with the data in [3], where, on the contrary, the red shift decreased as *L* decreased. The minimum E_0(QD) = 0.72 eV ($\lambda_0 = 1.7$ μm) was obtained at $x = 0.3$ and $L = 2$ nm.

To elucidate the impact of the thickness of the external GaAs layer on E_0(QD), a set of structures was produced, with the same QW parameters ($x = 0.3$, $L = 2$ nm), which corresponded to the maximum red shift, but with different values of d_c. As can be seen in Fig. 4 (curves *6–10*), the energy of the QD ground state transition decreases gradually as d_c decreases in the range 20–3 nm. This result is additional confirmation of the assertion that the principal cause of the red shift of E_0(QD) is the relaxation of elastic stress in the QD, and this relaxation depends on the total thickness of the double cladding layer and on its composition.

Figure 5 shows PL spectra at 300 K for the last set of structures. The PL peak positions coincide with PSE peaks to within the ordinary experimental scatter over the wafer (~10 meV). The PL intensity in these structures remained nearly the same as in structures with a thick GaAs cladding layer; only for $d_c = 3$ nm was the PL intensity reduced by a factor of 3–4. Both PSE (Fig. 4) and PL (Fig. 5) spectra indicate a high quality of structures with a thin GaAs/InGaAs double cladding layer. The FWHM for the ground state transition peaks usually did not exceed 35 meV, and up to three peaks associated with excited states were observed in PSE spectra along with the clearly pronounced ground state transition peaks. As far as we know, the value E_0(QD) ≈ 0.68 eV ($\lambda_0 = 1.8$ μm) obtained in this set of structures represents a record-breaking low value for the GaAs/InAs system. The variation of x, L, and d_c parameters of the thin double cladding layer makes it possible to control the wavelength of the QD emission in the range 1.3–1.8 μm; 1.55-μm emission can be obtained at different combinations of these parameters.

3.5. Schottky Diodes

In view of the problems arising in the fabrication of laser diode structures with a *p–n* junction on QDH with a thin double cladding layer, it seems interesting to discuss the possibility of producing LEDs with a Schottky barrier based on this type of structure. For $d_c \geq 7$ nm, the PL spectra of Schottky diodes with a gold contact based on structures with a combined QW/QD layer were virtually the same as the PSE spectra on the QDH/electrolyte interface. However, at smaller (3 and 5 nm) d_c, comparable with the QD height, the band of the QD photosensitivity disappeared from the spectra of Schottky diodes, whereas the band of photosensitivity related to the hybrid QW was still retained (these spectra are shown by dashed lines in Fig. 4).

Clusters, i.e., QDs, are hardly observable in the AFM images obtained from the surfaces of these QDHs. The smooth nanoscale profile indicates that the thickness of the QW and GaAs layers on top of QDs is significantly lower than the rated thickness. In this context, the disappearance of the QD photosensitivity band in structures with $d_c < 7$ nm may be related to the situation when the tunneling of electrons and holes from QDs to metal (Fig. 2b, transition *2*) with subsequent

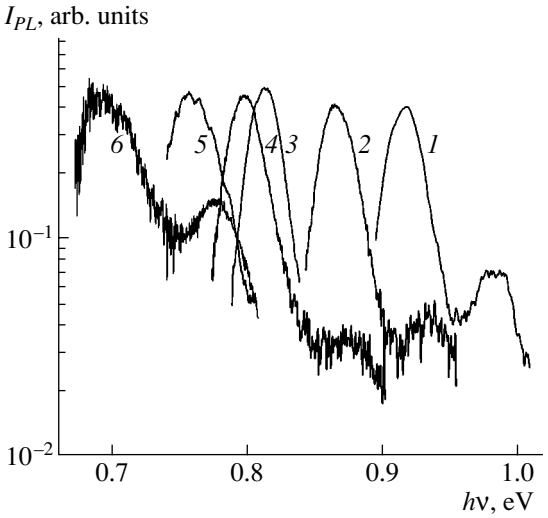

Fig. 5. Effect of the GaAs cladding layer thickness on PL spectra of QDH (300 K). d_c: (*1*) 25 (without QW); (*2*) 20; (*3*) 10; (*4*) 7; (*5*) 5; and (*6*) 3 nm. For curves *2–6*, the QW parameters are $x = 0.3$, $L = 2$ nm.

nonradiative recombination becomes more probable than the emission of nonequilibrium electrons from QDs to the bulk (transitions *3*, *4*). This is also confirmed by the absence of the QD PL in these diode structures, although QD PL is observed under photoexcitation of areas of the structure outside the metal electrode.

The combined QW is in a more advantageous position as regards the emission of electrons to the bulk, since its emission barrier is significantly lower than in the QD, and the thickness of the cladding layer, which impedes the electron tunneling to metal, is close to the rated value. Therefore, the related photosensitivity band is retained in Schottky diodes even at $d_c = 3$ nm. We compared the PL spectra obtained during photoexcitation of structures under the metallic electrode and outside of it, and also the photovoltage spectra of Schottky diodes and QDH/electrolyte junctions. It appeared that the deposition of ~20-nm-thick Au and Pt electrodes does not significantly affect the E_0(QD) value; thus, polycrystalline metal layers do not produce additional stress in the QD layer, even at the minimum thickness of the cladding layer.

The presence of a QW/QD layer in the vicinity of the metal contact raises the forward and reverse currents of the diodes (Fig. 6), and the magnitude of this change strongly depends on the thickness of the cladding layer, d_c. The effect decreases with small and large thicknesses. The maximum increase in the reverse current (nearly three orders of magnitude), was observed at $d_c = 7$ nm (curve *4*). In this case, the activation energy determined from the temperature dependence of the reverse current decreased from 0.8 to 0.35 eV as the bias increased in the range 0.1–5 V.

An exponential increase in the reverse current of Schottky diodes on GaAs at fairly high bias voltages is

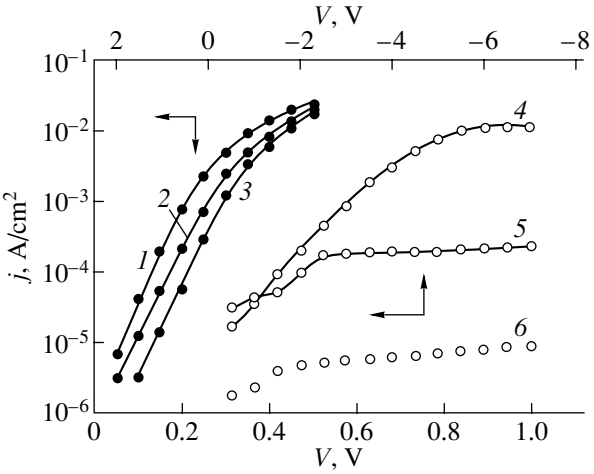

Fig. 6. Current–voltage characteristics of Schottky diodes on QW/QD structures (350 K): (*1–3*) direct bias; (*4–6*) reverse bias. QW parameters: $x = 0.3$, $L = 2$ nm. The thickness of GaAs cladding layer, d_c: (*1*, *4*) 7; (*2*, *5*) 20 nm; (*3*, *7*) homogeneous GaAs layer.

attributed to thermally activated tunnel emission across the vertex of a triangular barrier (Fig. 2c, transition *5*) [16]. In Schottky diodes with quantum-confinement layers lying in the vicinity of the metal contact, the electron tunneling from the metal to QD levels becomes possible when these levels approach the Fermi level in the metal (Fig. 2c). The electron emission from these states occurs by the possible mechanisms *3* and *4*. Evidently, the maximum enhancement of current corresponds to some optimum distance between the QD layer and the metal. When the distance is too small, a large bias is necessary to bring the QD levels close to the Fermi level in metal; with a large distance this is easily achieved, but the probability of the electron tunneling across the barrier decreases drastically.

4. CONCLUSION

The dependence of the ground state transition energy in InAs QDs on the parameters of a thin $GaAs/In_xGa_{1-x}As$ double cladding layer (the width and composition of the QW and the thickness of the external GaAs layer) in heterostructures grown by MOCVD has been determined. It is shown that the variation of these parameters makes it possible to control the transition energy in InAs QDs in the range 0.72–0.95 eV, which covers both transparence windows of optical fiber at 1.3 and 1.55 μm wavelengths, with a high yield of photoemission. The structures obtained can be used in lasers with surface photo- or electron excitation. Recently, room-temperature electroluminescence in the range 1.3–1.5 μm was obtained from similar structures with the Schottky barrier and cladding layer δ-doped with carbon [17].

ACKNOWLEDGMENTS

The authors are grateful to V. Ya. Aleshkin for the software used in the calculation of the energy spectrum in steplike QWs and for valuable discussions.

This study was supported by the Russian Foundation for Basic Research (project nos. 03-02-17178 and 01-02-16441) and by the Joint Program of the Ministry of Education of Russia and CRDF (US Civilian R&D Foundation) [BRHE (Basic Research and Higher Education) Program, REC-001].

REFERENCES

1. N. N. Ledentsov, V. M. Ustinov, V. A. Shchukin, *et al.*, Fiz. Tekh. Poluprovodn. (St. Petersburg) **32**, 385 (1998) [Semiconductors **32**, 343 (1998)].
2. M. Grundmann, Physica E (Amsterdam) **5**, 167 (2000).
3. K. Nishi, H. Saito, S. Sugou, and J.-S. Lee, Appl. Phys. Lett. **74**, 1111 (1999).
4. B. V. Volovik, A. F. Tsatsul'nikov, D. A. Bedarev, *et al.*, Fiz. Tekh. Poluprovodn. (St. Petersburg) **33**, 990 (1999) [Semiconductors **33**, 901 (1999)].
5. A. R. Kovsh, A. E. Zhukov, N. A. Maleev, *et al.*, Fiz. Tekh. Poluprovodn. (St. Petersburg) **33**, 1020 (1999) [Semiconductors **33**, 929 (1999)].
6. V. M. Ustinov, N. A. Maleev, A. E. Zhukov, *et al.*, Appl. Phys. Lett. **74**, 2815 (1999).
7. J. Tatebayashi, M. Nishioka, and Y. Arakawa, Appl. Phys. Lett. **78**, 3469 (2001).
8. I. A. Karpovich, B. N. Zvonkov, D. O. Filatov, *et al.*, Poverkhnost, No. 11, 27 (2000).
9. B. N. Zvonkov, I. A. Karpovich, N. V. Baidus, *et al.*, in *Proceedings of 25th International Conference on Physics of Semiconductors*, Ed. by N. Miura and T. Ando (Osaka, 2000), p. 397.
10. B. N. Zvonkov, I. A. Karpovich, N. V. Baidus, *et al.*, Fiz. Tekh. Poluprovodn. (St. Petersburg) **35**, 92 (2001) [Semiconductors **35**, 93 (2001)].
11. I. A. Karpovich, A. P. Gorshkov, B. N. Zvonkov, *et al.*, Fiz. Tekh. Poluprovodn. (St. Petersburg) **35**, 564 (2001) [Semiconductors **35**, 543 (2001)].
12. I. A. Karpovich, N. V. Baidus, B. N. Zvonkov, *et al.*, Nanotechnology **12**, 425 (2001).
13. N. V. Baidus, B. N. Zvonkov, D. O. Filatov, *et al.*, Poverkhnost, No. 7, 71 (2000).
14. G. Ji, D. Huang, U. K. Reddy, *et al.*, J. Appl. Phys. **62**, 3366 (1987).
15. I. A. Karpovich and M. V. Stepikhova, Fiz. Tekh. Poluprovodn. (St. Petersburg) **32**, 182 (1998) [Semiconductors **32**, 164 (1998)].
16. N. A. Torkhov, Fiz. Tekh. Poluprovodn. (St. Petersburg) **35**, 823 (2001) [Semiconductors **35**, 788 (2001)].
17. N. V. Baidus, B. N. Zvonkov, P. B. Mokeeva, *et al.*, in *Proceedings of Meeting on Nanophotonics* (IFM Ross. Akad. Nauk, Nizhni Novgorod, 2003), Vol. 2, p. 351.

Translated by D. Mashovets

Semiconductors, Vol. 38, No. 4, 2004, pp. 437–446. Translated from Fizika i Tekhnika Poluprovodnikov, Vol. 38, No. 4, 2004, pp. 455–464.

LOW-DIMENSIONAL SYSTEMS

Studies of Physical Phenomena in Semiconductor Nanostructures Using Samples with Laterally Nonuniform Layers: Photoluminescence of Tunneling-Coupled Quantum Wells

Yu. V. Khabarov*, V. V. Kapaev, and V. A. Petrov*****

**Institute of Ultrahigh-Frequency Semiconductor Electronics, Russian Academy of Sciences, Moscow, 117105 Russia*

e-mail: yukhabar@mtu-net.ru

***Lebedev Physical Institute, Russian Academy of Sciences, Leninskiĭ pr. 53, Moscow, 117924 Russia*

****Institute of Radio Engineering and Electronics, Russian Academy of Sciences, ul. Mokhovaya 18, Moscow, 101999 Russia*

Submitted August 27, 2003; accepted for publication September 9, 2003

Abstract—The previously suggested spectral-correlative method for studying nanostructures is applied to an analysis of photoluminescence of tunneling-coupled and isolated quantum wells in structures with laterally nonuniform layers. This method made it possible to use a single wafer to study the dependences of intensities of photoluminescence lines and their energy positions on the tunneling-barrier width for a system of tunneling-coupled GaAs–InGaAs–GaAs wells and on the quantum-well widths in a system of isolated AlGaAs–GaAs–AlGaAs quantum wells. Good agreement between the results of calculations and experimental data can be attained if it is assumed that a constant transverse electric field affecting the processes of trapping of charge carriers by quantum wells exists in a structure with tunneling-coupled quantum wells. The dependence of photoluminescence parameters on the width of isolated quantum wells is sensitive to the profile of heterointerfaces and to the processes of trapping the charge carriers by quantum wells. © *2004 MAIK "Nauka/Interperiodica".*

1. INTRODUCTION

Previously [1], a new method of correlative spectroscopy based on the use of laterally nonuniform semiconductor layers was suggested for studying physical phenomena in semiconductor nanostructures. This method was later used to study photoluminescence (PL) in structures with quantum wells (QWs) [2]. As a continuation of these studies, we report here the results of applying this method to investigations of PL of tunneling-coupled QWs in structures with laterally nonuniform layers. The use of these layers makes it possible, in particular, to change the permeability of the tunneling barrier by continuously varying its width within the same sample. This opportunity to vary continuously technologically specified parameters (such as the thickness of the layers) makes it possible to obtain experimental data that can in a number of cases provide new information about the physical phenomenon under investigation. In this study, we use the spectral-correlative method and PL spectroscopy to gain insight into the PL of two tunneling-coupled QWs in a laterally nonuniform system formed consecutively from a GaAs barrier, an $In_yGa_{1-y}As$ QW, a GaAs tunneling barrier, an $In_yGa_{1-y}As$ QW, and a GaAs barrier.

2. EXPERIMENTAL

The spectral-correlative method we use implies a study of multilayer semiconductor structures that include a combination of laterally uniform and correlated laterally nonuniform layers. It is important that the sample should contain not only the structure under investigation but also an auxiliary structure that provides information about the built-in nonuniformity. In order to analyze experimentally these structures, spectroscopic methods are used that make it possible to observe the special spectral features related to the auxiliary structure and characterize the variable parameter in each locally studied region of inhomogeneous sample, as well as observe simultaneously the features related to the structure under investigation. Subsequent analysis of correlative relations between spectral parameters makes it possible to study the behavior of parameters of the structure under investigation in a field of built-in inhomogeneity in the sample.

The sample under investigation was grown by molecular-beam epitaxy on a semi-insulating GaAs substrate 76 mm in diameter, a layer-by-layer cross section of which is shown schematically in Fig. 1. Two $In_yGa_{1-y}As$ QWs (QW_E and QW_F) had a different width, were separated by a GaAs tunneling barrier, and were grown on a GaAs buffer layer. An auxiliary structure consisting of two isolated GaAs QWs (QW_B and QW_C) with $Al_xGa_{1-x}As$ barrier layers was also formed on the upper GaAs barrier layer; a thin undoped GaAs layer and then a thin doped GaAs layer were grown on top of this structure. The sample grown in this way was a combination of laterally uniform and correlated later-

GaAs:Si, 15 nm	
GaAs, 20 nm	
$Al_xGa_{1-x}As$, 100 nm $x^* = 0.22$	
GaAs, 1.8 nm	QW_B
$AlxGa_{1-x}As$, 60 nm $x^* = 0.22$	
GaAs, 5 nm	QW_C
$Al_xGa_{1-x}As$, 100 nm $x^* = 0.22$	
GaAs, 60 nm	
$In_yGa_{1-y}As$, 7 nm $y^* = 0.2$	QW_E
GaAs, 8.5 nm	Tunneling barrier
$In_yGa_{1-y}As$, 12 nm $y^* = 0.2$	QW_F
GaAs, 800 nm	Buffer layer
GaAs	Substrate

Fig. 1. Schematic representation of the multilayer structure under study. Estimated values of the layer thickness and composition of the ternary compounds are given for the central region of the sample. The laterally nonuniform layers are marked by thick solid lines.

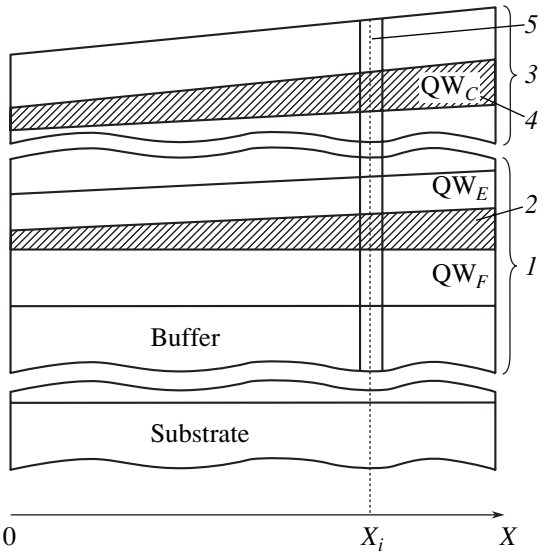

Fig. 2. Schematic representation of a simplified sample for studying tunneling-coupled QWs using the spectral-correlative method. (*1*) A system of tunneling-coupled quantum wells QW_E and QW_F that contains a laterally nonuniform layer of the tunneling barrier (*2*), (*3*) an auxiliary structure containing a laterally nonuniform layer (*4*, the quantum well QW_C), and (*5*) the region of local spectroscopic investigation.

ally nonuniform layers. The GaAs tunneling barrier between the $In_yGa_{1-y}As$ QWs in the structure under investigation and also both GaAs QWs in the auxiliary structure were laterally nonuniform. The nonuniformity of these layers was attained by growing them epitaxially on nonrotating substrates. The nonuniformity of the GaAs layers was caused by the spatially nonuniform distribution of the flux of Ga atoms in the plane of the growth surface of the sample. In order to attain identical patterns of planar distribution of the thus formed nonuniformity in different layers, the latter were grown at the same fixed spatial position of the substrate, which specified the correlation between thicknesses of these layers. All the other layers were grown on a rotating substrate, which ensured a high degree of lateral uniformity of these layers. The estimated values of thickness for nonuniform layers are given in Fig. 1; these estimates were obtained on the basis of the duration of the layers' growth and corresponded to the central (close to the rotation axis) region of the sample.

The PL spectra of the sample were measured at liquid-nitrogen temperature in the wavelength range 650–1000 nm. In order to excite the PL, we used an Ar^+ laser with a wavelength of 488 nm and a radiation intensity as high as 200 W/cm^2 within a focused radiation spot of about 50 μm in diameter on the sample. The excitation radiation was incident at an angle of 45° on the surface of the sample. The PL emission was analyzed using an automated system of spectrum detection based on an MDR-23 monochromator and a cooled FÉU-62 photomultiplier used in the photon-counting mode.

The scheme shown in Fig. 2 illustrates the essence of the spectral-correlative method using a simplified sample that contains two laterally nonuniform layers as an example. The structure under investigation *1* includes the quantum wells QW_E and QW_F and also the laterally nonuniform tunneling-barrier layer *2* that separates these QWs. The auxiliary structure *3* contains a laterally nonuniform narrow-gap layer *4* that represents the QW_C quantum well. We emphasize that, in the case under consideration, the structure under investigation and the auxiliary structure are physically different. Indeed, the laterally nonuniform layer is a barrier in the former structure and a QW layer in the latter structure. Nonuniformity of the layers in the simplified sample in the cross section shown in Fig. 2 manifests itself in the dependence of their thickness on coordinate X, whereas the correlation between these layers manifests itself in the specified constant value of the ratio of their thicknesses for any coordinate X. Let us assume that the aim of the study consists in determining the dependence of a spectral parameter S_1 which is related to layer *2* and characterizes the structure of tunneling-coupled QWs under investigation on the thickness of this layer

W_1 ($S_1 = f_1(W_1)$). A spectroscopic study of local regions of the sample makes it possible to obtain a set of values of the parameter S_{1i} under investigation for various coordinates X_i in the region under investigation. The values of the layer thickness W_{1i} corresponding to each X_i remain unknown. In order to determine these values, auxiliary layer *4* was introduced into the structure; the observed spectral parameter S_2 of this layer is related to the layer thickness W_2 by the known relation $S_2 = f_2(W_2)$. In the case under consideration, this layer is a QW, since the dependences of energies of the quantum states on the main QW parameters (in particular, the QW width) have been adequately studied [3, 4]. The use of PL spectroscopy in this case allows one to determine the parameters S_1 and S_2 in various spectral regions, which makes it possible to analyze these parameters independently. The set of resulting spectral parameters can be used to obtain the correlation dependence $S_{1i} = f_k(S_{2i})$, where S_{2i} are the values of the parameter S_2 at points X_i. This dependence represents a relation of the parameter S_1 to the thickness W_1, since the dependence $S_2 = f_2(W_2)$ and the ratio of the layer thicknesses W_1/W_2 are known. Here, S_2 can be treated as a generalized thickness parameter; the experimental form of the desired dependence $S_{1i} = f_1(W_{1i})$ can be recovered taking into account the aforementioned known relations.

In the sample studied by us, the auxiliary structure consisted of two laterally nonuniform isolated QWs based on the $Al_xGa_{1-x}As$–GaAs–$Al_xGa_{1-x}As$ system (a narrow QW_B and a wider QW_C). The PL data were used to determine the parameters of this structure in a local region of the nonuniform sample under investigation and, ultimately, to determine the thickness of the tunneling barrier in this region. In order to use most efficiently the range of variations in the tunneling-barrier thickness and simultaneously minimize the effect of possible radial nonuniformity of the layers in which the inhomogeneity was not intentionally formed (for example, the $Al_xGa_{1-x}As$ barrier layers), the PL spectra were measured over a semicircle near the edge of the wafer from the region with the smallest thickness of laterally nonuniform layers to the region with the largest thickness of these layers. We then studied the dependences of local values of PL parameters for tunneling-coupled QWs on the determined values of the tunneling-barrier width.

A comparison of experimental data with the results of calculations and determination of the parameters of the semiconductor structure were carried out using a numerical solution to the Schrödinger equation in the context of the method of envelope wave functions. We calculated the energies of optical transitions and the squared overlap integrals for the wave functions of electrons and holes in a QW. These calculations require knowledge of the parameters of the energy-band structure of semiconductors, in particular, the charge-carrier effective masses and the dependences of these parameters on the composition of the layers. At present, there is some dispute in the published data concerning the values of these parameters for an $In_yGa_{1-y}As$–GaAs system. For example, the data on the ratio between the conduction-band offsets at the $In_yGa_{1-y}As$–GaAs heterointerface $\Delta E_c/\Delta E_g$ (ΔE_c is the difference in energies between the conduction-band bottoms in GaAs and $In_yGa_{1-y}As$ and ΔE_g is the difference between the corresponding band gaps) differ from publication to publication: 0.52 [5], 0.6 [6], 0.7 [7, 8], and 0.83 [9]. A similar situation exists in respect to the data on the effective mass of heavy holes in GaAs: $0.62m_0$ [6], $0.52m_0$ [8], $0.51m_0$ [10], and $0.36m_0$ [9] (m_0 is the mass of a free electron). Contradictory data also exist on the dependence $E_g(y)$ of the band gap of strained $In_yGa_{1-y}As$ layers in a GaAs–$In_yGa_{1-y}As$–GaAs system on the mole fraction of In [6, 11, 12].

When calculating the QW energy spectrum in a GaAs–$In_yGa_{1-y}As$ system, we used the generally accepted average value of the ratio $\Delta E_c/\Delta E_g = 0.7$ and linear approximations of dependences of the effective masses of electrons and holes in $In_yGa_{1-y}As$ on the mole fraction of In $m_e^*(y) = (0.067 - 0.042y)m_0$ and $m_{hh}^*(y) = (0.52 + 0.25y)m_0$, which coincide with the data reported in [8] for $y = 0.21$.

When approximating the dependences $E_g(y)$, we selected the coefficients of the second-degree polynomial in such a way that the dependences of the energies of optical transitions on the QW width were consistent with the relevant experimental data reported in [11].

When calculating the energy spectrum of an $Al_xGa_{1-x}As$–GaAs–$Al_xGa_{1-x}As$ QW, we used a value of the band gap of the $Al_xGa_{1-x}As$ barrier layers equal to 1.833 eV; we determined this value experimentally from the observed edge PL emission from these layers. The ratio of the band offsets at the $Al_xGa_{1-x}As$–GaAs interface $\Delta E_c/\Delta E_g$ was taken to be equal to 0.6; the effective masses of electrons and heavy holes were determined from the expressions $m_e^*(x) = (0.0665 + 0.0835x)m_0$ and $m_{hh}^*(x) = (0.51 + 0.2x)m_0$, respectively [10]. We also used the dependence of exciton binding energy on the QW width [4].

3. RESULTS AND DISCUSSION

A typical PL spectrum of the sample under investigation is shown in Fig. 3. The spectrum includes a low-intensity line *A* in the vicinity of 1.83 eV (677.5 nm) (this line is related to the edge emission of the $Al_xGa_{1-x}As$ barrier layers) and a number of lines with a higher intensity. The latter include the lines *B* and *C*, which correspond to the emission from the narrow and wide $Al_xGa_{1-x}As$–GaAs–$Al_xGa_{1-x}As$ QWs, respectively (QW_B and QW_C); the lines *E* and *F*, which correspond to the emission from two tunneling-coupled QWs in the structure that consists of a GaAs layer, an $In_yGa_{1-y}As$ quantum well (QW_E), a GaAs layer, an $In_yGa_{1-y}As$

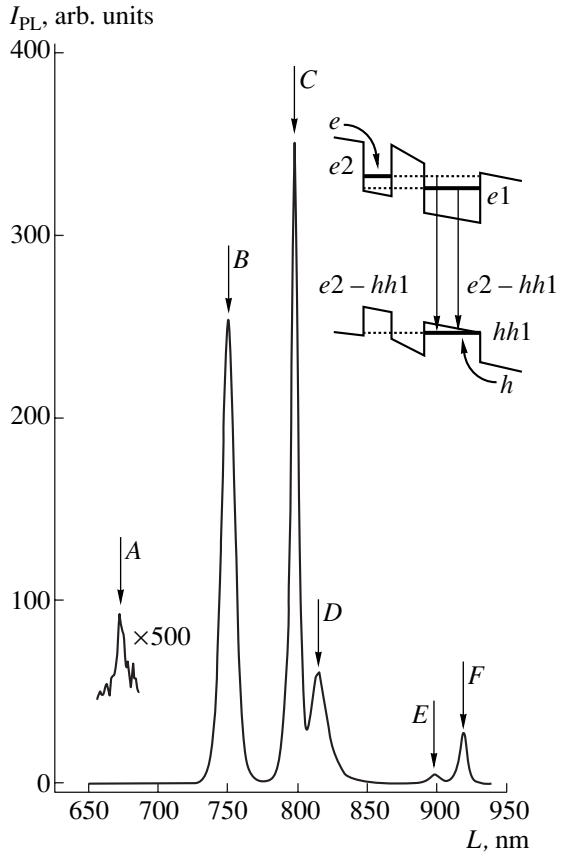

Fig. 3. A typical photoluminescence spectrum of the sample. Arrows indicate spectral lines *A*, *B*, *C*, *D*, *E*, and *F*. An energy-band diagram for a system of tunneling-coupled QWs is shown in the inset.

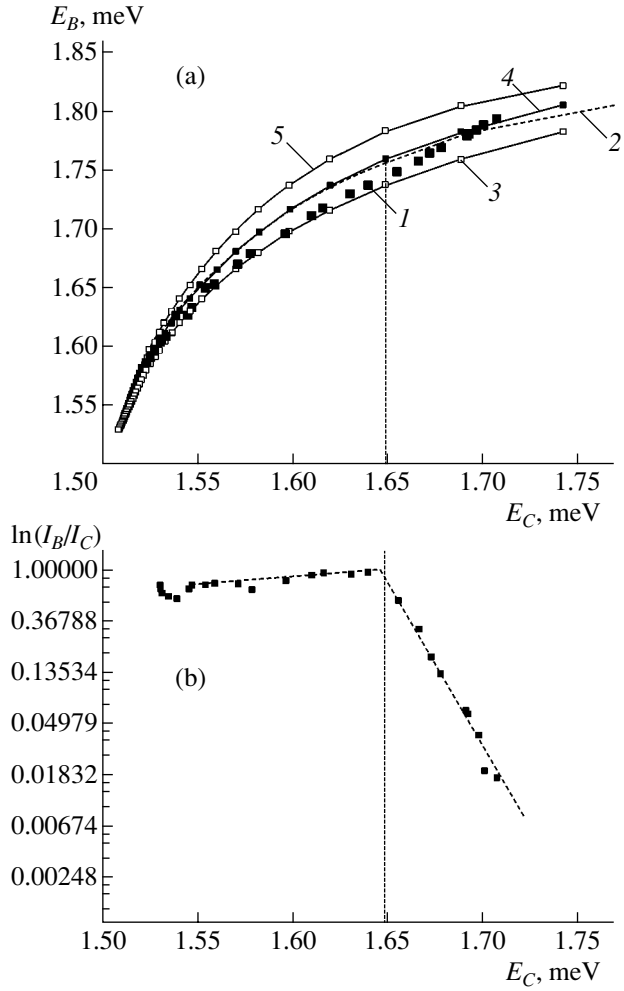

Fig. 4. Experimental and theoretical dependences of the photoluminescence parameters for the quantum well QW_B on the energy E_C in a laterally nonuniform system. (a) Experimental dependence of E_B on E_C; (*2*–*5*) dependences of calculated energies of optical transitions *e*1–*hh*1 for a rectangular QW with the width W_1 (QW_B) on similar values for a QW with the width W_2 (QW_C): (*2*) $W_1 = W_B$, $W_2 = W_C$, and $W_B/W_C = 0.36$; (*3*) $W_1 = W_B + 2m$, $W_2 = W_C + 2m$, and $W_B/W_C = 0.36$; (*4*) $W_1 = W_B + m$, $W_2 = W_C + 2m$, and $W_B/W_C = 0.36$; and (*5*) $W_1 = W_B$, $W_2 = W_C + 2m$, and $W_B/W_C = 0.36$. (b) Experimental dependence of relative intensity of line *B* on the energy E_C.

quantum well (QW_F), and a GaAs layer; and the line *D*, which is related to the PL of the top doped GaAs layer (this line disappeared after the top GaAs layer had been etched off).

When the focused laser spot was shifted over the surface of the sample, the energy positions of the lines *B* and *C* varied appreciably, which was caused by the dependence of the energy positions of the quantum-confinement levels in QWs on the QW width. The intensities of the lines *B*, *C*, *E*, and *F* and the spectral position of the line *E* varied simultaneously. The special features of these variations are illustrated in Figs. 4–6.

3.1. Photoluminescence of Isolated AlGaAS–GaAs–AlGaAs Quantum Wells

In this subsection, we report the results of spectroscopic studies of the auxiliary structure formed in the sample—a combination of two isolated, laterally nonuniform GaAs QWs in a system that consisted of an $Al_xGa_{1-x}As$ layer, a GaAs quantum well (QW_B), an $Al_xGa_{1-x}As$ layer, a GaAs quantum well (QW_C), and an $Al_xGa_{1-x}As$ layer.

We determined the energy positions of the peaks of the lines *B* (E_B) and *C* (E_C) from the PL spectra at various points on the surface of the sample. The dependence of E_B on E_C based on the above measurements is shown in Fig. 4a (curve *1*). The experimental points of this dependence are generally located somewhat below theoretical curve *2*, which is calculated for the energy of optical transitions $\Delta E_{e1-hh1} = E_{e1} - E_{hh1}$ between the lower electronic level E_{e1} in the conduction band and the first level of heavy holes in the valence band E_{hh1} (the transition *e*1–*hh*1). The calculation was performed in the context of a model of rectangular QWs with finite barriers taking into account the binding energy of exci-

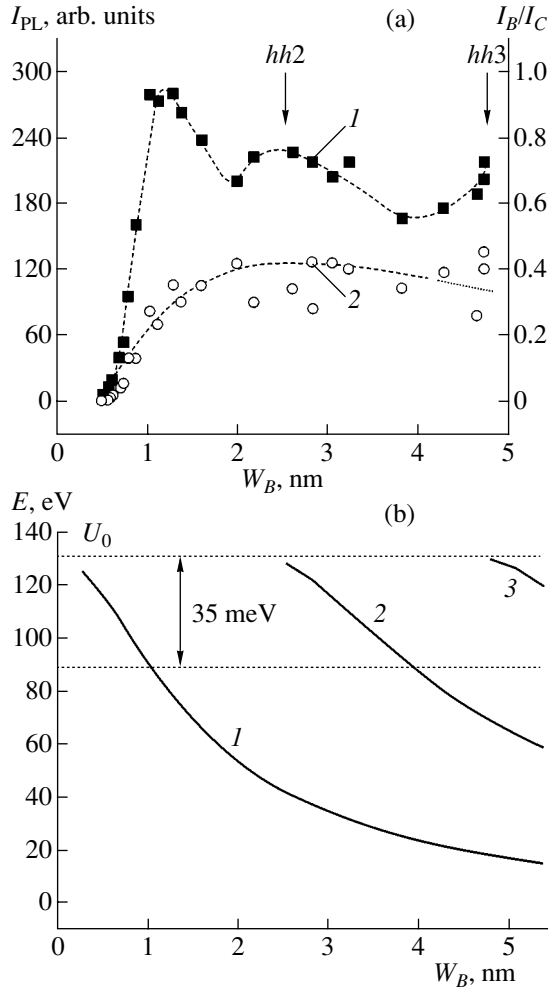

Fig. 5. (a) Dependences of experimental values of (*1*) relative and (*2*) absolute intensities of line *B* on the average width of the quantum well QW_B. Arrows indicate the calculated values of the width of the quantum well QW_B that correspond to the appearance of new heavy-hole energy subbands in this QW. (b) Calculated dependences of the dimensional-quantization levels for heavy holes in the quantum well QW_B (curves *1*, *2*, and *3* correspond to subbands *1*, *2*, and *3*); the energy is reckoned from the bottom of the valence band in the narrow-gap QW layer and is within the valence band.

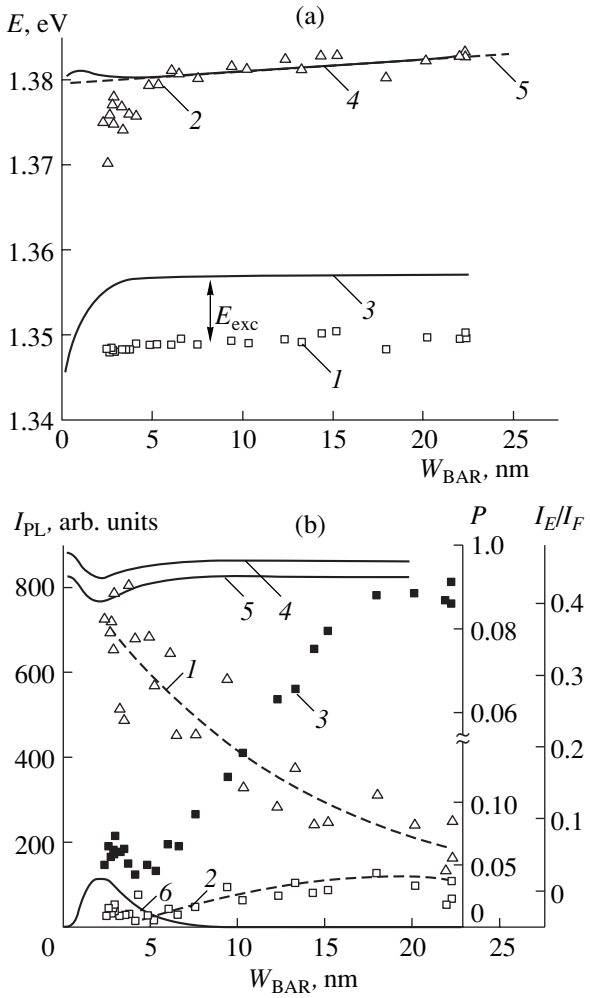

Fig. 6. Dependences of experimental and calculated PL parameters for a system of tunneling-coupled QWs on the width of the tunneling barrier. (a) Dependences of experimental values of the energy corresponding to the peak of lines (*1*) *E* and (*2*) *F* and theoretical dependences of the energy of optical transitions (*3*) *e*1–*hh*1 and (*4*) *e*2–*hh*1 on the tunneling-barrier width W_{BAR}; (*5*) direct regression of experimental values of the energy corresponding to the peak of line *E*. (b) Dependences of experimental values of absolute intensities of lines (*1*) *F* and (*2*) *E* and of (*3*) relative intensity of line *E* on the tunneling-barrier width; theoretical dependences of squared overlap integrals (*P*) for the wave functions of a system of tunneling-coupled QWs on the tunneling-barrier width are also shown: curves *4*, *5*, and *6* correspond to the transitions *e*1–*hh*1, *e*2–*hh*2, and *e*2–*hh*1, respectively.

tons. The ratio between the width of the thin QW (W_B) and that of the wide QW (W_C) is equal to the ratio between the growth rates of GaAs layers and is estimated at $W_B/W_C = 0.36$. Previously [2], a deviation of experimental data from the results of calculations was observed for another sample; however, this deviation had the opposite sign. Such behavior of PL spectra was related [2] to a small-scale profile in the QW interface; this profile was averaged owing to the excitonic state. The deviations observed in this study can also be related to the structure of the QW interfaces. However, the trends in the deviations (the PL lines are shifted to lower energies relative to the calculated values) suggest that the cause of the observed behavior of emission lines may be related to the profile in the QW interfaces when the characteristic size of steps in the interface plane is larger than the exciton size. In this case, the predominant contribution to the emission is made by optical transitions from wider QW regions, which gives rise to a shift of PL QW-related lines to longer wavelengths [13].

Assuming that there can exist a deviation by the width of a monolayer *m* for each heterointerface (the

spacing between neighboring crystallographic planes of Ga in GaAs) on both sides of the average position, we obtained curve *3*, calculated for optical transitions within the widest QW regions with a width of $W_B + 2m$ and $W_C + 2m$ for quantum wells QW_B and QW_C, respectively. In this case, the quantities W_B and W_C have the significance of average values of the QW width; their ratio remains equal to the ratio of the growth times of the layers ($W_B/W_C = 0.36$). Figure 4a also shows curves *4* and *5*, calculated for the quantum-well QW_B width equal to $W_B + m$ and W_B, respectively; the QW_C width remained equal to $W_C + 2m$.

The theoretical curves in Fig. 4a were calculated for values of the width of the narrow QW that were specified with a step equal to a monolayer. Therefore, points in these curves make it possible to estimate the average QW_B width for corresponding experimental energy positions of PL lines.

The experimental points in Fig. 4a are in good agreement with calculated curve *3* for large values of the QW width; however, curve *3* runs appreciably below the experimental values in the region of small thickness of the layers ($W_B < 3m$). As the QW width decreases (as E_C increases), the experimental dependence crosses curve *4* and approaches curve *5*.

The observed pattern is quite consistent with the assumed structure of heterointerfaces. At large values of the layers' thickness, both QWs are fairly wide and contain portions with deviations of the width from the average value by two monolayers due to variations in the position of both heterointerfaces; these portions with an increased width make the major contribution to the emission. As the layer thickness decreases for the narrow quantum well (QW_B), the correlating effect of the profile of the lower heterointerface on the character of nonuniformity of the upper heterointerface becomes important, which is typical of the layer-by-layer growth of such structures. Simultaneously, the total area of the QW regions where the deviations of two heterointerfaces are out-of-phase decreases. For an ultimately narrow QW, the profile of the upper heterointerface reproduces in general the profile of the lower interface. In this situation, the fraction of QW regions with increased width decreases drastically, since an increasingly larger fraction of emission is formed in the narrow QW regions. The width of relevant QW (QW_C) remains fairly large, and the emission from this QW corresponds to the regions with the width $W_C + 2m$.

In Fig. 4b, we show the dependence of relative intensity of the line *B* (the ratio between the intensities of lines *B* and *C* at their peaks) on E_C, the energy position of the line *C*. The onset of a drastic (nearly exponential) decrease in the intensity of emission from the narrow QW (QW_B) is in good agreement with an estimate of average width of this QW (three monolayers; see calculated curves in Fig. 4a). In the context of the model of a shift of heterointerfaces by a monolayer, the above reasoning shows that, for the QW width under consideration, there remains a single GaAs monolayer that is unaffected by displacement of the interface positions. A further decrease in the QW width leads to the fact that steps in the interfaces disrupt the continuity of the GaAs layer more and more; ultimately, this layer decomposes into separate islands. Apparently, in this case, QWs with a width of two monolayers still exist, and the conditions for recombination of the formed excitons seem to be satisfied. We believe that the exponential falloff of the *B*-line intensity observed under these conditions is related to a disruption of the last unperturbed QW monolayer, which hampers the motion of charge carriers in the QW and, as a result, the formation of excitonic pairs. In this situation, radiative recombination is hindered by the fact that a large fraction of electrons and holes remains spatially separated in the QW plane.

The suggested model and the analysis of experimental data based on this model make it possible to determine local values of the thickness of nonuniform layers taking into account the structure of QW interfaces. These values were obtained on the basis of experimental data on the energy positions of the *C*-line peak (E_{Ci}), the relation $E_{Ci} = \Delta E_{e1-hh1}(W_{Ci} + 2m)$, and the known ratio between the growth times of the layers. Here, $E_{Ci} = \Delta E_{e1-hh1}(W_{Ci} + 2m)$ is the calculated energy of the $e1$–$hh1$ transition for a QW with the width $W_{Ci} + 2m$, and the subscript i represents the number of the measurement point at the sample surface.

As is well known, the PL intensities that correspond to QW_B and QW_C and are measured at different points on the surface of the sample may be affected by factors that are not directly related to the PL emission. These factors may include different conditions for reflection of light in various areas of the sample surface, spatial fluctuations of the fraction of nonradiative recombination at the surface and in the bulk of the structure, a number of factors related to instrumentation, and so on. All these factors give rise to background oscillations in the level of absolute PL intensity, which hamper analysis of the dependences obtained. Therefore, it is preferable in a number of cases to study the dependence of the relative PL intensity for two similar objects (for example, QW_B and QW_C) on certain parameters in order to minimize the effect of background factors. In this case, it can be expected that the dependence of relative PL intensity for QW_B and QW_C on the QW width will be affected to a much lesser extent by factors of background origin and will be mainly sensitive to special features of radiative process in the QW_B–QW_C system.

In Fig. 5a, we show the dependences of relative (curve *1*) and absolute (curve *2*) intensities of the line *B* on the average width W_B of the quantum well QW_B. As can be seen from Fig. 5a, dependence *1* clearly features maxima and minima. At the same time, the spread of experimental points in curve *2* gives no way of drawing a similar conclusion.

It can be seen from Fig. 5a that the dependence of relative PL intensity for the line B on W_B is oscillatory. We believe that such behavior of this intensity is related to processes that lead to redistribution of the charge-carrier recombination fluxes between QWs. By comparing the experimental dependence with calculated dependences of dimensional-quantization levels for heavy holes in a rectangular QW on W_B (Fig. 5b), we observe that the peaks in the experimental curve correspond to the values of W_B at which the energy position of the dimensional-quantization level for holes is either close to the energy of the potential barrier for holes (U_0) at the QW boundaries or is spaced from U_0 by the energy on the order of the energy of a longitudinal optical phonon. For example, the first peak in curve *1* (Fig. 5a) is located at values of W_B that correspond to the situation where the bottom of the lower dimensional subband of heavy holes is lower than U_0 by approximately 35 meV. A similar situation also applies to electrons with respect to the same peak in curve *1*. Further peaks correspond to situations where the bottoms of the second or third hole subbands have energies on the order of U_0; i.e., they correspond to the values of W_B at which the next hole subband appears in the QW. In this case, oscillations of the relative PL intensity in relation to the QW width can be apparently related to nonmonotonic variation in the efficiency of trapping of photoexcited holes by QW. This variation is caused by changes in the energy positions of quantum-mechanical subbands in the QW as the QW width varies. It should be noted that the quantity U_0 plays the role of the energy origin, which in our opinion indicates that the QW is filled with holes from the barrier layers; these holes have preliminarily relaxed to the bottom of the valence band in the barriers.

3.2. Photoluminescence of Tunneling-Coupled GaAs–InGaAs–GaAs Quantum Wells

The PL spectrum of a structure composed of two tunneling-coupled QW_E and QW_F quantum wells consists of an intense line F and a much less intense line E; the latter appears as the high-energy wing of the line F if the tunneling barrier is thin. When analyzing the spectrum, we approximated the aforementioned lines using two Lorentzian components. The parameters of this approximation, i.e., the energy positions of peaks of the lines and areas under the curves, were used in the analysis of energies of optical transitions and integrated PL intensities, respectively. In Fig. 6, we show the dependences of the above parameters on the tunneling-barrier width W_{BAR}. The value of W_{BAR} was determined from the previously found average width W_B of the quantum well QW_B taking into account the ratio between the growth times for the layers of the QW_B quantum well and the tunneling barrier (see Fig. 1).

Let us discuss first the behavior of dependences of energy positions of the lines F and E on the tunneling-barrier width W_{BAR}. We now assume that the line F is related to the $e1$–$hh1$ interband transitions and the line E is related to the $e2$–$hh1$ transitions, i.e., to transitions to the common subband of heavy holes from the first (the first transition) and second (the second transition) common electron subbands of two tunneling-coupled QWs, respectively. As a result, we should note that the first transition is virtually "direct" in the "energy–coordinate" diagram for two tunneling-coupled QWs, since the densities of electrons and holes at the levels $e1$ and $hh1$ are mainly concentrated in a single quantum well QW_F. In contrast, the second transition is "indirect" in the coordinate space, since the electron and hole densities are mainly located in QW_E and QW_F, respectively. It is evident that the energy positions of both lines should remain virtually unchanged with increasing W_{BAR} when the barrier width becomes so large that tunneling between QWs is negligible. Indeed, we found that the energy position of line F remains virtually unchanged in the entire range of variations in the tunneling-barrier width (experimental dependence *1*, Fig. 6a). However, the experimental dependence of the energy position for the line E on W_{BAR} is described by a steadily ascending curve as W_{BAR} increases; this dependence is linear at $W_{BAR} > 5$ nm. This observation is confirmed by the results of statistical processing of experimental data by plotting a direct regression that minimizes the mean-square deviation of experimental values (Fig. 6a, dashed straight line *5*). We assume that this linear dependence may be related to the presence of a built-in transverse electric field in the region of QWs. Indeed, an electric field in such a situation, as follows from the energy-band diagram shown in the inset in Fig. 3, has virtually no effect on the energy of the direct band-to-band transition $e1$–$hh1$ in the QW_F as W_{BAR} increases, whereas the energy of the indirect transition $e2$–$hh1$ should increase linearly with increasing barrier width. We calculated the energies of the interband $e1$–$hh1$ and $e2$–$hh1$ transitions in the presence of a constant transverse electric field and obtained good agreement between the results of calculations and experimental data for an electric-field strength of 5×10^3 V/cm. Figure 6a illustrates the agreement between the calculated energies of the $e2$–$hh1$ transitions (curve *4*) and experimental values for the line E at $W_{BAR} > 5$ nm.

This result corresponds to recombination without formation of an indirect exciton, which is reasonable to expect for a tunneling barrier with a fairly large width.

The parameters of the layers in the QW_E and QW_F quantum wells (the thickness and the In content) were determined from experimental data taking into account possible radial inhomogeneity of the layers; these parameters were used in the calculations. The aforementioned layers were formed during growth with averaged spatial distribution of molecular fluxes as a result of the substrate rotation. Consequently, the procedure for determining the parameters of the layers under consideration also included averaging of the found values of the barrier-layer thickness over the studied semicircle of the sample with subsequent con-

sideration of both the ratio of the growth time of this layer to that of the $In_yGa_{1-y}As$ layers and possible values of the parameter y. The true value of the parameter y was identified with the value that ensured agreement between calculated energies of the $e1$–$hh1$ transition and experimental values of the energy position of the line F taking into account the exciton binding energies. It was also presumed in calculations that the positions of QW interfaces could be varied within two monolayers. Thus, we determined the following QW parameters: the average width of the quantum well QW_E W_E = 6 nm, the average width of the quantum well QW_F W_F = 10.3 nm, and y = 0.18. Smaller values of both the In content in the QW and the layer thickness with respect to the expected values (see Fig. 1) are probably related to the processes of segregation and evaporation of In during epitaxial growth of these layers [11] and to the possible radial inhomogeneity of the layers that manifests itself in the vicinity of the wafer edge. In Fig. 6a, we show the experimental dependences of the energy E_F for the line F on the barrier width W_{BAR} (curve *1*) and the calculated energies of transitions $e1$–$hh1$ in relation to W_{BAR} (curve *3*). The exciton binding energy E_{exc} for the QW_E quantum well was taken to be equal to 7 meV according to the dependence of E_{exc} on the QW width (see [14]).

We also studied the dependences of intensities of lines E and F on the tunneling-barrier width W_{BAR} (henceforth, by intensity we mean an estimate of the integrated radiance of a spectral component). We observed an almost exponential falloff of integrated intensity of the line F with increasing W_{BAR} and a simultaneous increase in the integrated intensity of line E (see Fig. 6b, dependences *2* and *1*, respectively). First of all, it is noteworthy that the intensity of line E is relatively low and there are no other spectral features that can be associated with direct $e2$–$hh2$ transitions, despite the fact that these transitions are highly probable theoretically in the entire range of W_{BAR} under consideration (Fig. 6b, curve *5*). The calculated probability of the $e1$–$hh1$ transitions is close to unity and is independent of the tunneling-barrier width for fairly large values of W_{BAR} (Fig. 6b, curve *4*), whereas the experimental dependence of the F-line intensity on W_{BAR} features an exponential falloff (Fig. 6b, dependence *1*). In contrast, the intensity of the line E increases with increasing W_{BAR}, whereas the calculated probability of the $e2$–$hh1$ transition at $W_{BAR} > 3$ nm decreases exponentially (Fig. 5b, curve *6*). In general, the pattern of PL in the tunneling-coupled QWs studied by us cannot be explained if only the calculated dependences of the squared overlap integrals for the wave functions on W_{BAR} are taken into account. We believe that the observed behavior of the radiative-recombination intensity in the structure under investigation is governed predominantly by asymmetrical occupation of the energy subbands with photoexcited charge carriers whose nonuniform (but steady-state) spatial distribution varies as the tunneling-barrier width changes. Specifically, the absence of an intense component related to the direct $e2$–$hh2$ transitions in the narrow quantum well QW_E in the PL spectrum can apparently be related to the low concentration of holes in this QW. At the same time, the high intensity of line F indicates that there is a fairly high concentration of holes in the wide quantum well QW_F. Such special features of occupancy of the tunneling-coupled QWs under consideration with charge carriers may be caused by the asymmetry of the carrier-trapping processes. For example, the strong effect of an increase in the barrier width W_{BAR} on the intensity of line F (a decrease in this intensity) may be indicative of the important role of nonequilibrium photoexcited electrons in the occupation of the wide quantum well QW_F with charge carriers. The photoexcited electrons can either tunnel to the aforementioned QW from the narrow quantum well QW_E or come to the quantum well QW_F from the region above the barrier (the above-barrier electrons).

A higher concentration of holes in the quantum well QW_F is similarly governed by predominant occupation of this QW with holes from the lower-barrier GaAs layer and by the low permeability of the barrier that separates the QWs for these charge carriers.

A special feature of the observed PL pattern consists in the rather rapid decrease in the total intensity of lines E and F as W_{BAR} increases; it is noteworthy that the drastic decrease in the intensity of line F is accompanied by a slight increase in the intensity of line E. In turn, this observation indicates that the barrier separating the QWs not only affects the redistribution of charge carriers between the QWs but also reduces the efficiency of the charge-carrier recombination in the structure under consideration.

We believe that the observed pattern can be accounted for by the existence of an internal electric field in the structure, which introduces an appreciable asymmetry into the system. The presence of this field with a strength of about 5×10^3 V/cm makes it possible to explain the dependence of the energy position of line E on W_{BAR}. This field also controls to a great extent the occupation of QWs with drift flows of relaxed photoexcited charge carriers, i.e., electrons from the upper GaAs barrier layer that borders the narrow QW and holes from the lower GaAs layer that borders the wide QW. Apparently, the role of the above flows in the course of filling the tunneling-coupled QWs with charge is determinative in the structure under consideration. It is evident that the tunneling barrier is conducive to separation of electrons and holes trapped by different QWs and, thus, retards the charge-carrier recombination; the thicker the barrier, the larger its effect. Thus, a relatively high nonequilibrium concentration of holes in the quantum well QW_F allows for the intense direct recombination of electrons trapped in this QW and also enhances the intensity of indirect transitions of electrons from QW_E. In this case, an increase in the intensity of line E, which accompanies a decrease in the intensity of line F, can be related to a decrease in the

tunneling outflow of electrons from the QW_E quantum well, i.e., to an increase in the steady-state nonequilibrium concentration of electrons in this QW as the barrier permeability for tunneling decreases, which ultimately leads to an increase in the rate of the radiative-recombination emission from the QW_E quantum well. As W_{BAR} increases further, the intensity of line *E* tends to decrease with increasing W_{BAR} (Fig. 6b, curve *2*), as might be expected for the process of recombination of charge carriers separated by a potential barrier.

A rapid decrease in the intensity of line *F* with increasing W_{BAR} is not compensated by an increase in the intensity of line *E* and is indicative of a change in the recombination properties of the entire system of tunneling-coupled QWs. Apparently, the observed variation in the intensity is caused not only by the tunneling component of the electron flow to the QW_F quantum well from the QW_E quantum well but also by a variation in the dynamics of trapping the electrons from the GaAs conduction band by the QW_F quantum well. Indeed, an increase in W_{BAR} in the presence of an electric field leads to an increase in the potential difference between QWs, i.e., to an increase in the velocity of the above-barrier electrons. This effect in turn can lower the probability of trapping of electrons in the QW_F quantum well. In this case, there is a decrease in the flow of electrons arriving at the QW_F quantum well without accumulation of these electrons in the QW_E quantum well and, consequently, without an increase in the electric-field strength in the barrier. This behavior is consistent with the dependence of the energy of observed optical transitions from QW_E on W_{BAR}; this dependence is linear for $W_{BAR} > 5$ nm (Fig. 6a, curve *5*).

As in the case of isolated QWs considered above, the dependence of relative intensity of line *F* (the ratio between the intensity of line *E* and that of line *F*) on the barrier width W_{BAR} features a small spread of experimental points, which makes it possible to reveal more clearly the special features in this dependence in the region of small values of the barrier width (Fig. 6b, curve *3*). For example, as W_{BAR} decreases to values smaller than 5 nm, the observed decrease in the relative PL intensity slows down and is replaced by a local increase in this intensity. In the same range of values of W_{BAR}, we observe a decrease in the energy that corresponds to the peak of line *E* (Fig. 6a, curve *2*) and a deviation of this energy from the calculated curve *4* (Fig. 6a) obtained for transitions without the involvement of excitons.

We believe that the special features under consideration may be related to a gradual change in the character of indirect optical transitions from the QW_E quantum well to the QW_F quantum well; i.e., the excitonless transitions for large values of W_{BAR} are replaced by exciton-involved transitions in the region under consideration. In this case, the contribution of the excitonic component becomes more significant as W_{BAR} decreases. Simultaneously, we can expect an increase in the binding energy of indirect excitons and a change in the kinetics of the recombination process, which can manifest itself in a variation in the PL intensity.

The special features in the curve showing a variation in the energy of direct transitions from the QW_F quantum well are also related to the small tunneling-barrier width. The dependence *1* in Fig. 6a shows that, at small values of W_{BAR}, the energy position of the spectral emission peak related to the first electron subband is only slightly affected by the proximity of the narrow quantum well QW_E. However, the calculation predicts a decrease in the energy of the direct transitions $e1$–$hh1$ as W_{BAR} decreases. The absence of this tendency in experimental curve *1* indicates that the observed intensity of line *F* is not directly controlled by the transition $e1$–$hh1$. The excitonic origin of this line implies that excitons recombine with the involvement of charge carriers localized in the wide QW if the barrier width is fairly large. The effect of the narrow QW_E quantum well manifests itself in an increase in the effective width of the wide QW due to the tunneling escape of electrons from level $e1$ to the narrow QW. This effect changes the conditions for the existence of the excitonic state and may manifest itself in a decrease in the exciton binding energy or may cause the exciton to disappear. It is likely that the contribution of the corresponding optical transitions in the case of compensating variation in the exciton binding energy can result in the fact that the energy corresponding to the PL spectral line peak remains virtually unchanged.

4. CONCLUSION

The spectral-correlative method for studying nanostructures was applied to an analysis of photoluminescence of tunneling-coupled and isolated quantum wells (QWs) in structures with laterally nonuniform layers. This method made it possible to study in the same sample the dependences of the intensity of photoluminescence (PL) lines and their energy positions on the tunneling-barrier width in a system of tunneling-coupled GaAs–InGaAs–GaAs QWs and on the QW width for a system of isolated AlGaAs–GaAs–AlGaAs QWs.

The precision (on the scale of several monolayers) variation in the width of the narrow QW in a system of two isolated AlGaAs–GaAs–AlGaAs QWs showed that the dependences obtained were sensitive to the profile of the QW interfaces. In turn, this circumstance made it possible to determine the local values of the average QW width taking into account the profile of heterointerfaces and ascertain the important role of the motion of charge carriers in the QW plane in the process of radiative recombination in the QW. We observed an oscillatory behavior of the dependence of the relative PL intensity for two QWs on the QW width; this behavior is related to a periodic variation in the efficiency of trapping photoexcited charge carriers by a QW.

The agreement between experimental and calculated dependences for the energies of optical transitions in a structure of two tunneling-coupled QWs GaAs–InGaAs–GaAs–InGaAs–GaAs made it possible to identify the observed direct and indirect (in the coordinate space) optical transitions and relate the PL parameters of this structure to an internal constant transverse electric field.

We analyzed the pattern of variations in the intensities of PL lines and concluded that the electric field affected the process of filling the QWs with photoexcited charge carriers. The presence of an electric field leads to asymmetrical nonequilibrium occupancy of quantum subbands in the system as a result of the appreciable role played by the drift of charge carriers as they fill the QWs. These concepts can be used to qualitatively describe the pattern of observed PL in tunneling-coupled QWs in the entire range of variations in the tunneling-barrier width. Specifically, we managed to interpret special features in the observed dependences in the region of small values of the barrier width; these features may be related to the recombination of excitonic states in tunneling-coupled QWs.

The mechanism of filling QWs by drift flows of relaxed photoexcited charge carriers is consistent with the experimental PL pattern for both QW systems under consideration.

ACKNOWLEDGMENTS

We thank A.V. Guk for his help in preparing the sample. V.A. Petrov thanks the Russian Foundation for Basic Research (project no. 01-02-17450) for partial support of this study.

REFERENCES

1. Yu. V. Khabarov, RF Patent No. 2,168,238 (2001).
2. Yu. V. Khabarov, Fiz. Tekh. Poluprovodn. (St. Petersburg) **37**, 339 (2003) [Semiconductors **37**, 322 (2003)].
3. M. A. Herman, D. Bimberg, and J. Christen, J. Appl. Phys. **70**, R1 (1991).
4. G. Bastard, C. Delalande, Y. Guldner, and P. Voison, in *Advances in Electronics and Electron Physics*, Ed. by Peter W. Hawkes (Academic, Boston, 1988), Vol. 72.
5. I. A. Avrutskiĭ, V. A. Sychugov, and B. A. Usievich, Fiz. Tekh. Poluprovodn. (Leningrad) **25**, 1787 (1991) [Sov. Phys. Semicond. **25**, 1074 (1991)].
6. I. V. Bradley, W. P. Gillin, K. P. Homewood, and R. P. Webb, J. Appl. Phys. **73**, 1686 (1993).
7. G. Ji, D. Huang, U. K. Reddy, *et al.*, J. Appl. Phys. **62**, 3366 (1987).
8. M. Wojtowiez, D. Pascua, A.-C. Han, *et al.*, J. Cryst. Growth **175–176**, 930 (1997).
9. T. G. Anderson, Z. G. Chen, V. D. Kulakovskii, *et al.*, Phys. Rev. B **37**, 4032 (1988).
10. L. Pavesi and M. Guzzi, J. Appl. Phys. **75**, 4779 (1984).
11. P. O. Vaccaro, M. Takahashi, K. Fujita, and T. Watanabe, J. Appl. Phys. **76**, 8037 (1994).
12. A. S. Ignat'ev, M. V. Karachevtseva, V. G. Mokerov, *et al.*, Fiz. Tekh. Poluprovodn. (St. Petersburg) **28**, 125 (1994) [Semiconductors **28**, 75 (1994)].
13. Er-Xuan Ping and V. Dalal, J. Appl. Phys. **74**, 5349 (1993).
14. M. J. L. S. Haines, N. Ahmed, S. J. A. Adams, *et al.*, Phys. Rev. B **43**, 11944 (1991).

Translated by A. Spitsyn

Semiconductors, Vol. 38, No. 4, 2004, pp. 447–450. Translated from Fizika i Tekhnika Poluprovodnikov, Vol. 38, No. 4, 2004, pp. 465–468.

LOW-DIMENSIONAL SYSTEMS

A Model of Photoinduced Annealing of Intrinsic Defects in Hexagonal CdS_xSe_{1-x} Quantum Dots

V. P. Kunets*, N. R. Kulish, M. P. Lisitsa, and V. P. Bryksa

Lashkarev Institute of Semiconductor Physics, National Academy of Sciences of Ukraine, Kiev, 03028 Ukraine

**e-mail: vl_kunets@yahoo.com*

Submitted August 21, 2003; accepted for publication September 18, 2003

Abstract—A possible mechanism of photoinduced annealing of intrinsic defects in quantum dots with a hexagonal crystal structure is justified on the basis of the studies of the kinetics of photoinduced decay of luminescence of CdS_xSe_{1-x} quantum dots synthesized in a glass matrix and *ab initio* calculations of chemical bond energies at the interface in the *n*(CdSe)–SiO_x-type cluster. The model proposed implies that photoinduced Se–O bond breaking at the anionic face results in an increase in electric field inside the quantum dot; this field stimulates cadmium vacancy diffusion to the surface. This model accounts for the degradation of luminescence and of the parameters of nonlinear optical devices observed during photoinduced annealing. © *2004 MAIK "Nauka/Interperiodica".*

The experimentally observed photodarkening effect [1–10] in structures with CdS_xSe_{1-x} quantum dots (QDs) is accompanied (under continuous illumination with an intensity exceeding 0.1–1.0 W/cm^2) by photoluminescence (PL) decay; a change in the refractive index ($\Delta n \approx 8 \times 10^{-7}$ [8]); an increase in the absorption coefficient ($\Delta K \approx 0.05$–0.1 cm^{-1}) in the region of transparency [8]; and a decrease in the nonlinear Kerr susceptibility, the time of the nonlinear response of system, and the lifetime of nonequilibrium charge carriers [3].

The mechanism of PL degradation has not been established. It was assumed that it is related to photochemical reactions [1], QD photoionization [11], and (or) the increase in the number of surface nonradiative recombination centers [4]. The interest in the study of the effect is motivated by the necessity of clarifying the causes of PL degradation and the change in the parameters of II–VI QDs and nonlinear QD optical devices. The aim of this study is to justify a possible model of the effect of PL degradation of CdS_xSe_{1-x} QDs whose average radius $\bar{r}$ is comparable to the exciton Bohr radius.

The PL spectra for QDs with $\bar{r}$ = 2.9 nm were recorded in the conventional "reflection geometry." Excitation and photoinduced annealing were carried out using continuous argon laser radiation (λ = 514.5 nm). The spectra were recorded at light intensities 0.05–0.5 W/cm^2; the light intensity for photoinduced annealing and for the measurements of the kinetics of PL decay was varied in the range $I_t < I_0 < 10^3$ W/cm^2. Depending on the light intensity during photoinduced annealing I_0, characteristic PL decay times varied from several seconds to several tens of minutes.

At low excitation levels (about 0.05 W/cm^2), there are three bands in the spectra of original (unannealed) samples (Fig. 1). Two of these bands (at 1.34 and 1.99 eV) correspond to transitions of free electrons from quantum confinement levels to the deep (0.56–0.60 eV) and shallow (0.24–0.26 eV) acceptor levels generated by the cationic vacancies V_{Cd} and complexes of the type A-M_i, respectively; here, A is V_{Cd} and the M_i are Cd interstitial atoms [12]. The nature of the band at 1.57 eV has not been reliably established. The band of direct electron–hole recombination (2.21 eV) is clearly seen in the spectra for excitation levels $I_0 > 0.1$ W/cm^2. After photoinduced annealing, the intensity of the

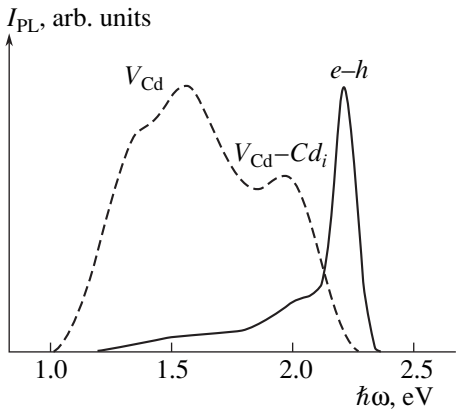

Fig. 1. Photoluminescence spectra of $CdS_{0.32}Se_{0.68}$ quantum dots with $\bar{r}$ = 2.90 nm measured at excitation intensity 0.05 W/cm^2 and temperature 77 K before (dashed curve) and after (solid curve) photoinduced annealing for 0.5 h at illumination intensity I_0 = 60 W/cm^2.

1063-7826/04/3804-0447$26.00 © 2004 MAIK "Nauka/Interperiodica"

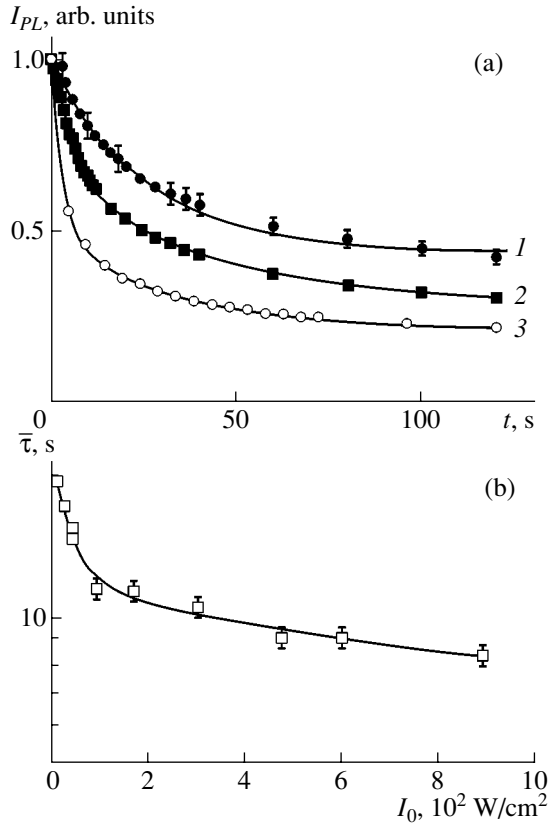

Fig. 2. (a) Typical kinetics of photoluminescence decay for $CdS_{0.32}Se_{0.68}$ quantum dots ($\bar{r}$ = 2.90 nm) at excitation intensities I_0 (*1*) 7.3, (*2*) 20.9, and (*3*) 166.6 W/cm^2. (b) Effective photoinduced-annealing time as a function of the excitation intensity I_0.

acceptor bands decreased by 90–95% and the intensity of the band of direct electron–hole recombination decreased by 10–15%; as a result, the latter band is predominant in the spectrum (Fig. 1).

The kinetics of the PL decay $I_{PL}(t)$ has a complicated character (Fig. 2a). In most cases, it can be described by the exponential law

$$I_{PL}(t) \propto A + B\exp(-t/t_1) + C\exp(-t/t_2)$$

with two characteristic decay constants t_1 and t_2; here A, B, and C are constants depending on the sample type and on the excitation conditions. In some cases, the dependence $I_{PL}(t)$ has a more complicated character and such decomposition appears to be unsatisfactory. Therefore, for the analysis of the dependence of photoinduced annealing efficiency on the illumination intensity, it is convenient to introduce the parameter $\bar{\tau}$ defined by

$$\bar{\tau} = \frac{1}{I_{PL}^{max}}\int_0^\infty I_{PL}(t)dt, \qquad (1)$$

where I_{PL}^{max} is the initial PL signal before photoinduced annealing. The upper integration limit is practically determined by the time at which the degradation levels off. The parameter $\bar{\tau}$ introduced in this way characterizes the time of the nonequilibrium process and is determined by the area under the curve $I_{PL}(t)$ bounded by the residual PL signal. The quantity $\bar{\tau}$ is a measure of the photoinduced-annealing efficiency.

A characteristic feature of the $\bar{\tau}(I_0)$ dependence obtained by analyzing the set of kinetic curves $I_{PL}(t)$ measured at different excitation levels I_0 is the presence of two clearly pronounced exponential regions (Fig. 2b). In the first region corresponding to the excitation levels $0 < I_0 < 10^2$ W/cm^2, where the degradation is slow, $\bar{\tau}$ sharply decreases with increasing I_0. In the second region, where $I_0 > 10^2$ W/cm^2, the degradation is more effective and $\bar{\tau}$ weakly depends on I_0. We note that the value of $\bar{\tau}$ decreases with the average QD radius. Such behavior of $\bar{\tau}$ shows that the PL degradation mechanism is related to a process which slows down with increasing light intensity. In our model of the effect, it is assumed that the aforementioned process consists in breaking the Se–O and S–O chemical bonds at the anionic face of the QD; the number of such bonds is limited. We assume that QDs are synthesized like hexagonal prisms; this assumption is corroborated by the reflection electron microscopy (SEM) data. The anionic face of the prism is charged negatively and the cationic side, positively. Since synthesis is performed in glass containing 60–70% SiO_2, the majority of anions and cations are chemically bonded with oxygen and silicon atoms; i.e., the most probable bonds are Cd–O, Se(S)–O, Cd–Si, and Se(S)–Si. Among the possible binary compounds that have such bonds, cadmium silicides are the only ones that do not occur in nature [13].

In order to simulate the charge state of anionic and cationic faces of the quantum dot and calculate the energies of the cited bonds, we considered a CdSe cluster of hexagonal structure interacting with a SiO_x fragment (Fig. 3). Ab initio calculations of the bond energies, e.g., of Se–O and Se–Si bonds (Fig. 4), and of the lines of electric potential in the cluster by the semiempirical PM3 method within the framework of the self-consistent Hartree–Fock scheme in the NDDO (Neglect of Diatomic Differential Overlap) approximation have shown that the highest energies correspond to the Se–O (109.9 kcal/mol) and Cd–O (123.5 kcal/mol) bonds with equilibrium interatomic distances of 1.6 and 2.0 Å, respectively. The magnitudes of the induced charge at the anionic and cationic faces of the cluster increase with the approach of an oxygen atom; i.e., the positive charge of the cationic face increases and the negative charge of the anionic face decreases (Fig. 5). Our data show that, at the interface between a CdSSe QD and glass, the bonds of Cd and Se (S) atoms with

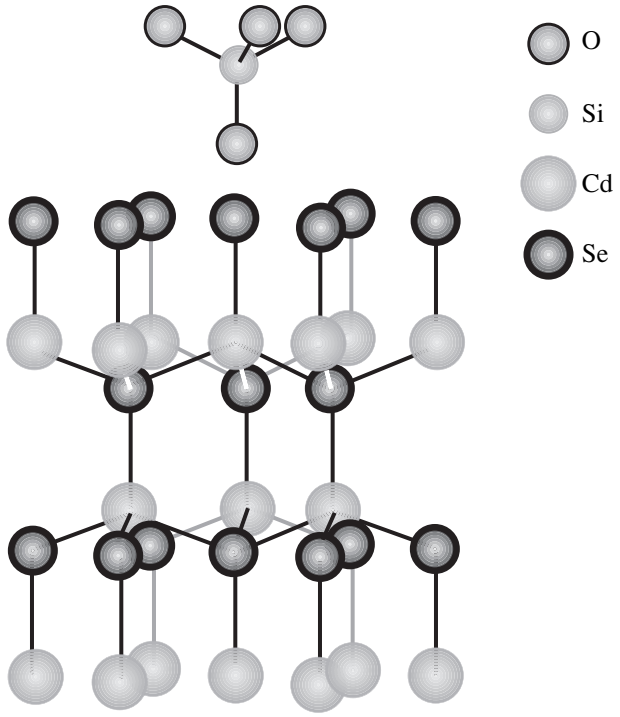

Fig. 3. Hexagonal *N*(CdSe) cluster with lattice parameters $a = 4.2$ Å and $c = 7.01$ Å and the SiO_x fragment.

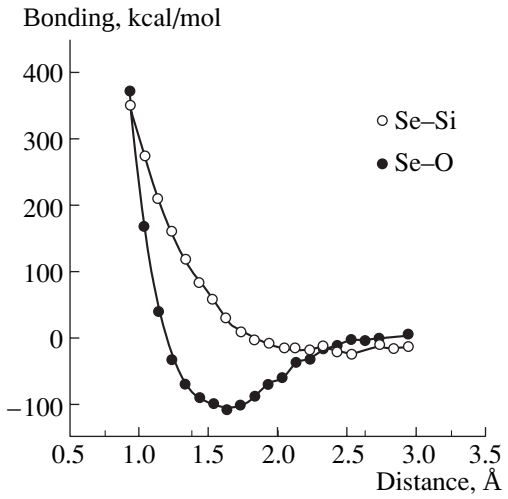

Fig. 4. The energies of Se–O and Se–Si bonds as functions of the interatomic distance.

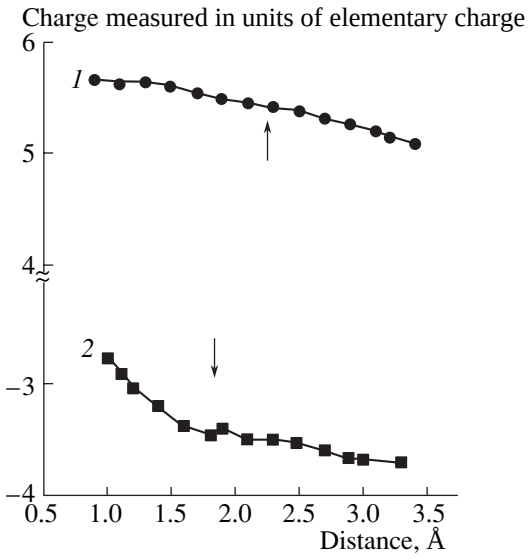

Fig. 5. The magnitude of the induced charge at the faces (*1*) Cd and (*2*) Se of a CdS_xSe_{1-x} quantum dot as functions of the distance from the oxygen atom (Cd–O or Se–O). The arrows indicate the equilibrium distances.

oxygen are most probable, and their formation or breaking changes the charge of anionic and cationic faces and the potential difference between them.

The main assumptions of the model suggested are (a) a QD with hexagonal crystalline structure and with a partially ionic type of chemical bonding has an internal electric-dipole moment directed along the hexagonal axis and created by alternating planes of ions of opposite charge; (b) the energy of excitons generated by light in the QD is spent on breaking chemical bonds at one of its faces, predominantly at the anionic face.

The mechanism of such a process is the following. Calculations of the excited state of a cluster simulated by replacing the bonding wave function in the cluster by an antibonding one show that the energies of Se–O and Cd–O bonds in the excited state decrease by 50 and 30 kcal/mol, respectively. In actual structures, an electron and a hole can tunnel outside the QD to the glass matrix. A nonequilibrium electron of the *e–h* pair generated by light can be captured by an E_1 center in the matrix, if the temperature is sufficiently low [14], or by a surface trap. A nonequilibrium hole can be captured by an H_1 center in the glass matrix [14] or it can pass to the negatively charged anionic face of the QD, which is equivalent to the chemical bond breaking at this face. Ab initio calculations show that such bond breaking increases the negative potential of the anionic face and the potential difference between the cationic and anionic faces of the QD. The field created in this way inside the QD induces the diffusion of singly charged cadmium vacancies to the surface; as a result of this, acceptor states in the bulk of the QD disappear and the corresponding PL bands are quenched. We note that the transfer of vacancies from the bulk to the surface results in the ordering of the QD crystalline structure and in an increase in the number of dangling bonds at the interface. The photostimulated nature of this process is evidence of such mechanism. Photoluminescence decay is fast at liquid helium temperature as well, even if the excitation intensity is not sufficient for heating the QDs [15]. Annealing the structure for several hours at temperatures of 300–500°C can restore the PL signal. During such annealing, new cadmium vacancies are formed in the bulk of the QDs.

The reliability of our model can be confirmed by experimental verification of the conclusions of the model. Specifically, the increase in the refractive index of the structures [8], the decrease in the nonlinear Kerr susceptibility [3] and in the lifetime of nonequilibrium charge carriers, and the appearance of photoinduced absorption attributed [8] to surface states indicate that the number of dangling bonds at the interface between the phases increases. The degradation and recovery of acceptor PL bands confirm that photoinduced annealing of acceptor states takes place and that it is possible to recover them by subsequent heat treatment of the structures. The decrease in the effective annealing time $\bar{\tau}$ with decreasing average QD radius is accounted for by the faster cadmium vacancy transport to the surface.

REFERENCES

1. P. Roussignol, D. Ricard, J. Lukasik, and C. Flytzanis, J. Opt. Soc. Am. B **4**, 5 (1987).
2. J. P. Zheng, L. Shi, F. S. Choa, *et al.*, Appl. Phys. Lett. **53**, 643 (1988).
3. M. Mitsunaga, H. Shinojima, and Ken-ichi Kubodera, J. Opt. Soc. Am. B **5**, 1448 (1988).
4. M. Kull, J. L. Coutaz, G. Manneberg, and V. Griviskas, Appl. Phys. Lett. **54**, 1830 (1989).
5. J. P. Zheng and H. S. Kwok, Appl. Phys. Lett. **54**, 1 (1989).
6. Chunming Jin, Jiaqi Yu, Weiping Qin, *et al.*, J. Lumin. **53**, 483 (1992).
7. P. Maly, F. Trojanek, and A. Svoboda, J. Opt. Soc. Am. B **10**, 1890 (1993).
8. A. Vanhaudenarde, M. Trespidi, and R. Frey, J. Opt. Soc. Am. B **11**, 1474 (1994).
9. P. Nemec, F. Trojanek, and P. Maly, Phys. Rev. B **52**, R8605 (1995).
10. Q. Shen, K. Ab. Shgigenari, and T. Toyoda, J. Lumin. **87–89**, 444 (2000).
11. V. Ya. Grabovskis, Ya. Ya. Dzenis, A. I. Ekimov, *et al.*, Fiz. Tverd. Tela (Leningrad) **31**, 272 (1989) [Sov. Phys. Solid State **31**, 149 (1989)].
12. M. Ya. Valakh, N. R. Kulish, V. P. Kunets, *et al.*, Ukr. Fiz. Zh. **38**, 1667 (1993).
13. G. V. Samsonov, L. A. Dvorina, and B. M. Rud', *Silicides* (Metallurgiya, Moscow, 1979).
14. A. N. Trukhin, M. N. Tolstoj, L. B. Glebov, and V. L. Savelev, Phys. Status Solidi B **99**, 155 (1980).
15. M. Ya. Valakh, V. P. Kunets, N. R. Kulish, and M. P. Lisitsa, Zh. Prikl. Spektrosk. **65**, 252 (1998).

Translated by I. Zvyagin

Semiconductors, Vol. 38, No. 4, 2004, pp. 451–454. Translated from Fizika i Tekhnika Poluprovodnikov, Vol. 38, No. 4, 2004, pp. 469–472.

LOW-DIMENSIONAL SYSTEMS

Carrier Density Profile in Weakly Coupled GaAs/AlGaAs Superlattices

P. N. Brunkov*^, S. O. Usov, Yu. G. Musikhin*, A. E. Zhukov*, G. E. Cirlin***, V. M. Ustinov*, S. G. Konnikov*, and G. K. Rasulova******

**Ioffe Physicotechnical Institute, Russian Academy of Sciences, St. Petersburg, 194021 Russia*
^e-mail: brunkov@mail.ioffe.ru
***St. Petersburg State Polytechnical University, St. Petersburg, 195251 Russia*
****Institute for Analytical Instrumentation, Russian Academy of Sciences, St. Petersburg, 190103 Russia*
*****Lebedev Physical Institute, Russian Academy of Sciences, Moscow, 119991 Russia*
Submitted September 17, 2003; accepted for publication September 18, 2003

Abstract—The effect of doping level on the current–voltage characteristics of semiconductor heterostructures with GaAs/AlGaAs superlattices was studied by the electrochemical capacitance–voltage profiling method. It was shown that a high density of free electrons in the GaAs/AlGaAs superlattice screens the external electric field and inhibits the formation of a domain with a high electric field that is responsible for resonant tunneling in weakly coupled superlatticest. © *2004 MAIK "Nauka/Interperiodica".*

Carrier transport in semiconductor superlattices is currently being widely studied with the aim of designing high-frequency (up to several GHz) generators operating on the effect of negative differential resistance (NDR) [1–4]. We present the results of studying structures based on weakly coupled GaAs/AlGaAs semiconductor superlattices with wide wells and barriers in which the width of the miniband of the quantum-well levels does not exceed 1 meV owing to weak overlapping of the electron wave functions between the neighboring quantum wells (QW). As follows from theoretical calculations [5, 6], in these structures a high-electric-field domain is formed, which makes possible the tunneling from the ground state of a QW to excited states of a neighboring QW. In a structure with wide wells, there are several quantum-well levels for which the miniband width increases as the energy of the level increases. The tunneling time defines the domain motion velocity and, therefore, the generation frequency, which increases as the number of the QW subband into which the tunneling occurs increases. Different miniband levels are involved in the resonant tunneling, depending on the static bias applied to the structure, which allows one to control the generation frequency [3, 4].

As shown in [5, 6], the condition for the formation of a stable domain depends on the doping level in the superlattice. This generated a need to derive a method for monitoring this doping level. The presence of heavily doped ($\sim 5 \times 10^{18}$ cm^{-3}) contact layers renders inapplicable the standard method of concentration profiling by the capacitance–voltage (*C–V*) technique using the Schottky barrier, where the minimum thickness of layers under study is limited by the width of the space-charge region (SCR) at the breakdown voltage for the sample. To get over this limitation, we chose the electrochemical *C–V* profiling (ECV) method [7–9], which consists in alternating electrochemical etching and *C–V* measurements across the Schottky barrier at the electrolyte/semiconductor interface. The electrochemical etching technique was optimized to obtain higher spatial resolution (on the order of several nanometers).

Two types of samples based on GaAs/AlGaAs compounds, F237 and 4-995, were studied. The structures were grown in different MBE machines on n^+-GaAs substrates. They were superlattices comprising 30 periods of weakly coupled (30 nm) GaAs QWs separated by 10-nm-thick $Al_{0.3}Ga_{0.7}As$ barriers. The superlattice region was uniformly doped with Si to 5×10^{16} cm^{-3} and confined on both sides with $Al_{0.3}Ga_{0.7}As$ (5 nm) barriers. Heavily doped n^+-GaAs contact layers were grown below and on the top of the superlattice (doping level 2×10^{18} cm^{-3}, thickness 0.5 and 1 μm, respectively).

ECV measurements were done using a Polaron Equipment Ltd. PN4200 setup, which allows simultaneous measurement of the capacitance (*C*) and its derivative with respect to voltage (*dC/dV*). The electrolyte was a 10% solution of tiron in deionized water. The electrolyte serves two functions: to etch and to form the electrical contact for studies of current–voltage (*I–V*) and *C–V* characteristics.

Bringing an *n*-GaAs epitaxial layer into contact with the electrolyte causes the redistribution of charges in the system. In the system under study, the work function of the semiconductor is smaller than that of the electrolyte; thus, electrons pass from the semiconductor to the electrolyte. The carrier density in the used electrolyte exceeds 10^{22} cm^{-3}. Therefore, the depth of

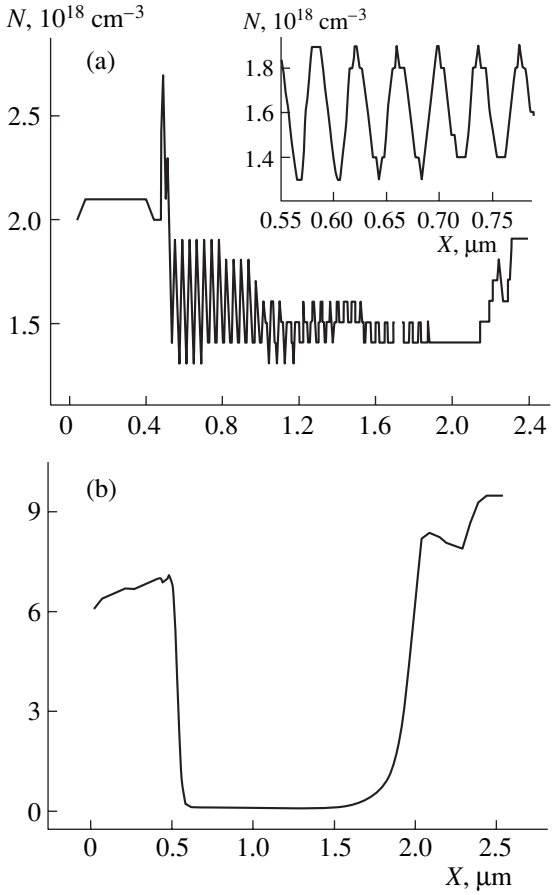

Fig. 1. Carrier density profiles for samples (a) F237 and (b) 4-995. The inset in Fig. 1a shows the carrier density profile for sample F237 in the range 0.55–0.80 μm.

the electric field penetration to the electrolyte is negligible, and the electrolyte/semiconductor interface behaves like a Schottky barrier.

The semiconductor material is decomposed in the process of chemical etching. The decomposition results in increasing charge redistribution. Equilibrium is attained due to the reduction of free energy through decomposition, and it is counterbalanced by the increase in the electrostatic energy related to the charge redistribution (Helmholtz electrical double layer) [7]. In the equilibrium, the anodic etching current is counterbalanced by the charge transfer from the electrolyte to the semiconductor. The penetration depth is determined by the Faraday law [7]:

$$X_e = \frac{M}{zFDS}\int_0^t I_e dt, \quad (1)$$

where M is the molecular mass; D, the density of a semiconductor; F, the Faraday constant; z, the number of charge carriers transferred by a solute molecule; I_e, the etching current; and t, the time of etching.

The total depth for which the free carrier density is determined is expressed by

$$X = X_e + X_d, \quad (2)$$

where X_d is the SCR thickness at the semiconductor/electrolyte Schottky barrier:

$$X_d = \frac{S\varepsilon_0\varepsilon_r}{C(V)}, \quad (3)$$

where C is the capacitance; V, the voltage; S, the contact area; ε_r, the dielectric constant of a semiconductor; and ε_0, the permittivity of free space.

The carrier density distribution profile across the structure thickness can be calculated in terms of the depletion layer approximation [7]:

$$N(X) = \frac{2}{q\varepsilon_r\varepsilon_0 S^2}\left[\frac{d(C^{-2})}{dV}\right]^{-1}, \quad (4)$$

where q is the elementary charge.

Alternating a $C(V)$ measurement for the determination of carrier density and etching with simultaneous measurement of the etching current I_e, we can determine the carrier density profile $N(X)$ to a considerable depth, which is limited by the inhomogeneity of the etching over the semiconductor/electrolyte interface.

Figure 1a shows an ECV profile of the carrier density distribution $N(X)$ obtained on structure F237 with an etching step of X_e = 2 nm. For n-semiconductor materials, the etching rate is defined by the intensity of illumination in the fundamental absorption range and by the reverse bias [7]. It was found that the optimal planarity of the etch-pit bottom is obtained at the etching current density I_e = 1 mA/cm^2, with the corresponding etching rate of 1.5 nm/s.

ECV measurements on structure F237 have shown that the top contact n^+-GaAs layer was about 0.4 μm in thickness and was doped with Si to 2×10^{18} cm^{-3} (Fig. 1a). In the superlattice region, the ECV profile $N(X)$ exhibits 30 peaks caused by the accumulation of carriers in GaAs QWs [10]. The average peak-to-peak distance is 40 nm (see inset in Fig. 1a), which coincides with the period of the GaAs/AlGaAs superlattice. These data are in good agreement with the data of transmission electron microscopy (TEM) shown in Fig. 2, where the GaAs(12 nm)/AlGaAs(27 nm) superlattice with a period of 39 nm is clearly visible.

The total thickness of the superlattice determined from ECV profile $N(X)$ is 1.4 μm. It is worth noting also that peaks in the $N(X)$ dependence are well resolved to a depth of 1.85 μm (Fig. 1a). As the depth of etching increases, the amplitude of the density modulation $N(X)$ decreases, which is related to the increased depth nonuniformity of the pit floor etching [8, 9].

An analysis of the ECV profile $N(X)$ of structure F237 by numerically solving the self-consistent Schrödinger and Poisson equations [10] has shown that the doping level of wide-gap $Al_{0.3}Ga_{0.7}As$ layers in the

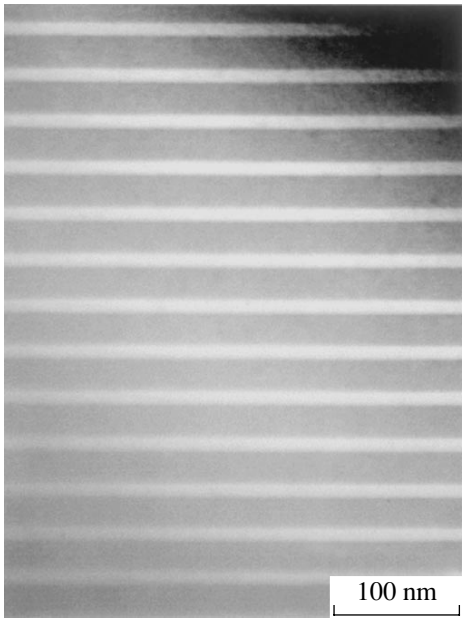

Fig. 2. Dark-field (g = 200) cross-sectional TEM image of structure F237.

superlattice is about 10^{18} cm^{-3}. This exceeds the level prescribed by the growth technology, which may be caused by the presence of an uncontrolled impurity in the Al source of the MBE machine.

Analysis of the ECV profile $N(X)$ of structure 4-995 led to the conclusion that the carrier density in the superlattice layer is 2×10^{17} cm^{-3}, and no modulation related to the redistribution of carriers between the barriers and QWs is observed (Fig. 1b), whereas the TEM demonstrates parameters similar to those in structure F237. Model calculations of the carrier density profile show that this situation occurs when the doping level in $Al_{0.3}Ga_{0.7}As$ barriers in the superlattice does not exceed 2×10^{17} cm^{-3}. The lack of the carrier density modulation in the superlattice layer is due to the fact that its doping level is significantly lower than that in n^+-GaAs contact layers (Fig. 1b). Therefore, a slight penetration of the SCR into heavily doped side walls of the etch pit makes a greater contribution to the capacitance measured by ECV than the superlattice layer.

Figure 3a shows an I–V chracteristic of structure 4-995 measured at temperature T = 4.2 K. This characteristic clearly demonstrates portions related to the formation of a high-electric-field domain, in which the tunneling occurs from the ground state in QW (E_0) to excited states of the neighboring QW (E_1, E_2, E_3, etc.) [1]. The I–V characteristic of structure 4-995 contains a great number of NDR portions. Figure 4 shows an example of current oscillations with a frequency of about 3.6 MHz in structure 4-995 at T = 4.2 K and a bias of 4.42 V. In contrast to structure 4-995, the I–V characteristic of structure F237 exhibits no evident portions related to the formation of a high-electric-field domain

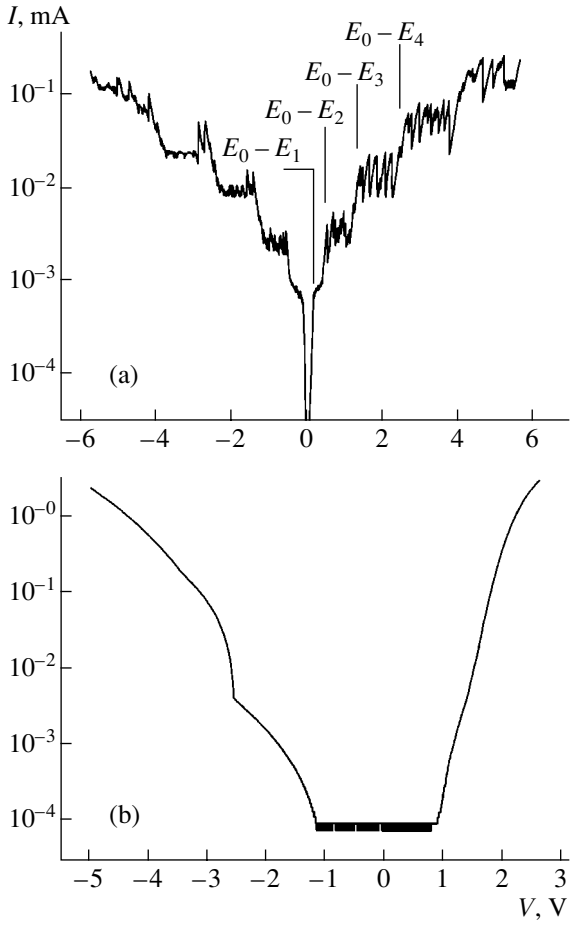

Fig. 3. I–V characteristics of structures (a) F237 and (b) 4-995 recorded at T = 4.2 K. Arrows in Fig. 3a mark the voltages of the formation of a high-electric-field domain related to tunneling from the QW ground state E_0 to excited states of the neighboring QW (E_1, E_2, E_3, etc.).

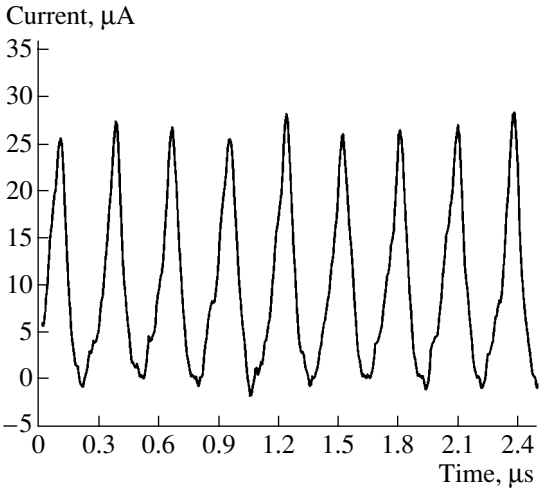

Fig. 4. Current oscillations of 3.6 MHz frequency in structure 4-995; temperature T = 4.2 K, the bias 4.42 V.

(Fig. 3b). This may be caused by the high density of free carriers in QWs of structure F237, which screens the electric field of the external bias and inhibits the formation of a high-electric-field domain.

Thus, the effect of the doping level on the *I–V* characteristics of semiconductor heterostructures with GaAs/AlGaAs superlattices was studied by electrochemical *C–V* profiling. It was shown that a high concentration of free electrons in a GaAs/AlGaAs superlattice inhibits the formation of a domain with a high electric field that is responsible for resonant tunneling in weakly coupled superlattices. One should note the high spatial resolution (to 10 nm) of the ECV profiling method, which provides detailed information on the carrier distribution in semiconductor heterostructures with quantum-well layers. This is especially important in the design of LEDs, lasers, and photodetectors.

ACKNOWLEDGMENTS

This study was supported by the Russian Foundation for Basic Research (project no. 01-02-17957).

REFERENCES

1. H. T. Grahn, H. Schneider, and K. von Klitzing, Phys. Rev. B **41**, 2890 (1990).
2. J. Kastrup, R. Klann, H. T. Grahn, *et al.*, Phys. Rev. B **52**, 13761 (1995).
3. J. Kastrup, R. Hey, K. H. Ploog, *et al.*, Phys. Rev. B **55**, 2476 (1997).
4. X. R. Wang, J. N. Wang, B. Q. Sun, and D. S. Jiang, Phys. Rev. B **61**, 7261 (2000).
5. L. L. Bonilla, J. Galan, J. A. Cuesta, *et al.*, Phys. Rev. B **50**, 8644 (1994).
6. A. Wacker, M. Moscoso, M. Kindelan, and L. L. Bonilla, Phys. Rev. B **55**, 2466 (1997).
7. P. Blood, Semicond. Sci. Technol. **1**, 7 (1986).
8. I. V. Irin and A. V. Murel', Prib. Tekh. Éksp., No. 6, 151 (1993).
9. V. I. Shashkin, R. I. Karetnikova, A. V. Murel', *et al.*, Fiz. Tekh. Poluprovodn. (St. Petersburg) **31**, 926 (1997) [Semiconductors **31**, 789 (1997)].
10. P. N. Brounkov, T. Benyattou, and G. Guillot, J. Appl. Phys. **80**, 864 (1996).

Translated by D. Mashovets

Semiconductors, Vol. 38, No. 4, 2004, pp. 455–460. Translated from Fizika i Tekhnika Poluprovodnikov, Vol. 38, No. 4, 2004, pp. 473–478.

AMORPHOUS, VITREOUS, AND POROUS SEMICONDUCTORS

Electrical Properties of Fine-Grained Polycrystalline CdTe

S. A. Kolosov, Yu. V. Klevkov, and A. F. Plotnikov

Lebedev Physical Institute, Russian Academy of Sciences, Moscow, 119991 Russia

Submitted July 7, 2003; accepted for publication July 14, 2003

Abstract—The temperature dependence of conductivity, the photoconductivity, and the hole mobility in fine-grained polycrystalline CdTe have been studied. The results obtained agree well with the concept of charged grain boundaries. The potential barriers at grain boundaries and the way in which these barriers affect the free carrier mobilities have been determined. © *2004 MAIK "Nauka/Interperiodica".*

1. INTRODUCTION

The promising development of semiconductor devices for solar power engineering requires that a low-cost material for solar cells be created. One of the most promising materials that are suitable for this purpose is polycrystalline CdTe. As CdTe is a direct-gap semiconductor and has a band gap of $E_g \approx 1.5$ eV at room temperature, it is the optimal material for detection of solar light. The theoretical limit to conversion efficiency for polycrystalline CdTe is 29%. However, this parameter does not exceed 12% in practical devices, which is primarily due to difficulties in controlling the transport characteristics of the polycrystals [1].

The second promising area in which CdTe polycrystals can be used is the development of detectors for hard X and γ rays. The large atomic numbers of the constituents of the material, $Z = 48$ (Cd) and $Z = 52$ (Te), provide higher quantum efficiency compared with silicon-based detectors. The wide band gap allows CdTe detectors to operate at room temperature. However, the considerable loss of radiation-induced charge in its transport between the electrodes of a detector leads to a significant decrease in energy resolution. For example, with 300 V applied to a 2-mm-thick detector, only 16% of the carriers generated by radiation are detected by the device at mobility–lifetime product for holes $\mu\tau = \mu_p\tau_p = 2 \times 10^{-5}$ cm^2/V, compared with nearly complete collection of the carriers at $\mu_p\tau_p \sim 10^{-3}$ cm^2/V. This fact is due to the low mobility and short lifetime of the holes [2].

These problems are already widely understood, and therefore it is not surprising that only the transport phenomena were examined in the majority of studies concerned with the electrical properties of polycrystals [3–5].

The physics of polycrystalline semiconductors is primarily the physics of grain boundaries. A polycrystalline material is an aggregate of relatively small crystallites separated by grain boundaries. Within any particular crystallite, atoms are arranged in a strictly periodic way. The grain boundaries are complex structures that are commonly composed of several layers of spatially disordered atoms. They can be regarded as transition regions between differently oriented crystallites.

Depending on the size of the crystallite, the extent to which the grain boundaries are charged, and the type of interaction of these boundaries with background impurities and dopants, the properties of polycrystalline semiconductors may vary extremely widely.

Our preceding study [6] was concerned with transport phenomena in coarse-grained *p*-CdTe polycrystals (grain size ~100 μm). In [6], we established that the hole mobility in polycrystals of this kind is determined by scattering on acoustic phonons at room temperature and on charged grain boundaries at lower temperatures. In addition, it was found that the hole mobility can be controlled by exposure of a sample to white light.

This paper reports the results obtained in studying the transport phenomena in fine-grained CdTe polycrystals.

2. CARRIER TRANSPORT IN FINE-GRAINED POLYCRYSTALS

The model we use to explain the experimental data presented below was first suggested by J. Seto [4] and later improved by G. Baccarani and B. Ricco [5]. The model is based on the assumption that the electrical properties of polycrystals are determined by capture of carriers by dangling bonds of atoms at grain boundaries, which leads, first, to a decrease in the number of free carriers involved in conduction and, second, to a considerable drop in their mobility because of the scattering on potential barriers at the boundaries.

In real polycrystals, the crystallites have different sizes and surface areas. It is virtually impossible to take this circumstance into account in theoretical calculations. Therefore, the model assumes that all crystallites are identical, have size L (cm), and contain a single type of impurity with concentration N (cm^{-3}).

It is further assumed that the interfacial region is considerably narrower than L and contains Q_t [cm^{-2}] traps, which are partly or completely charged through

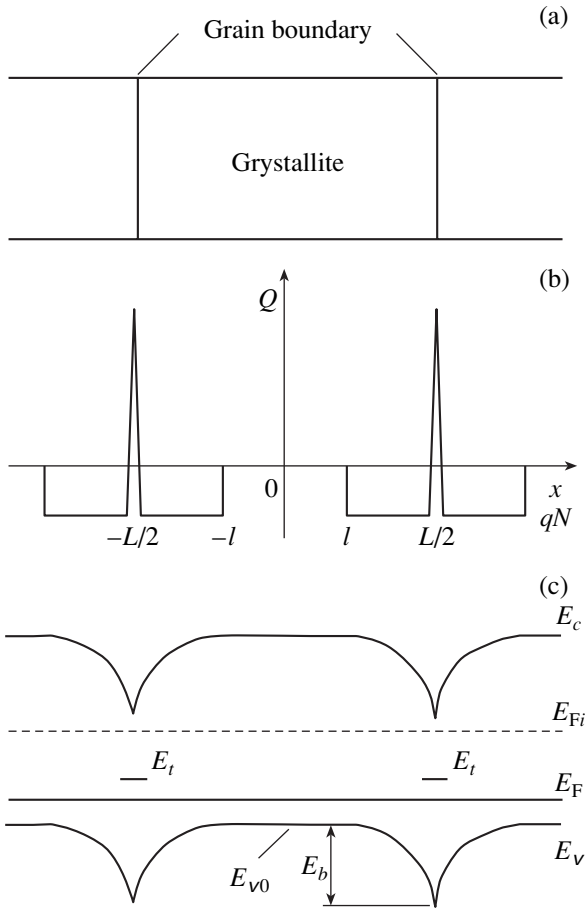

Fig. 1. Model of the grain boundary in *p*-type polycrystals: (a) structure of a polycrystal, (b) distribution of charge Q within the grain and at the grain boundary, and (c) band diagram. E_c, conduction bad edge; E_v, valence band edge; E_t, trap level; E_{Fi}, Fermi level in an intrinsic semiconductor; E_b, energy barrier height; and $E_{v0} = qV_{v0}$.

capture of free carriers. The model is illustrated by Fig. 1. It is assumed that all the free carriers from the region $L/2 - l$ at the interface are captured by traps at grain boundaries to form a depletion region, and the contribution from free carriers in this region is disregarded. A real polycrystal is a three-dimensional (3D) structure; however, it suffices to consider a 1D model to reveal all the characteristic features of the transport properties of the polycrystal.

Under these assumptions, solving the Poisson equation

$$\frac{d^2V}{dx^2} = \frac{qN}{\varepsilon}, \quad l < |x| < L/2 \tag{1}$$

(ε is the dielectric constant of the polycrystal) makes it possible to find the potential distribution:

$$V(x) = \frac{qN}{2\varepsilon}(x-l)^2 + V_{v0}, \quad l < |x| < L/2, \tag{2}$$

where V_{v0} is the potential of the valence band edge at the center of the crystallite, and q is the elementary charge. In these calculations, the Fermi-level energy in the intrinsic material is taken to be zero and the energy is positive in the direction toward the valence band.

At a given size of the crystallites, two cases are possible, depending on the doping level: (a) $LN < Q_t$ and (b) $LN > Q_t$.

The first case ($LN < Q_t$) corresponds to conditions in which a crystallite is totally depleted and the traps are only partly filled. Under these conditions, the potential barrier height V_b is given by

$$V_b = \frac{qL^2N}{8\varepsilon}. \tag{3}$$

From formula (3) follows that the barrier height grows linearly as the concentration N increases. In this case, the Fermi level is given by

$$E_F = E_t - kT\ln\left[\frac{1}{2}\left(\frac{Q_t}{LN} - 1\right)\right], \tag{4}$$

where T is temperature and k is the Boltzmann constant.

In the second case ($LN > Q_t$), only part of the crystallite is depleted, and the potential barrier height is

$$V_b = \frac{qQ_t^2}{8\varepsilon N}. \tag{5}$$

The total current through the polycrystal is determined both by the conductivity of the grains and by the mechanism of carrier transfer from one grain into another, i.e., by the conductivity of grain boundaries. As a rule, the conductivity of the crystallites substantially exceeds that of the boundaries, and, therefore, the latter should be primarily considered when studying the transport properties of polycrystals.

The two most important processes that determine the current across the boundaries are considered in the literature: tunneling (field emission) and thermionic emission. The tunneling currents are important in the case of very narrow barriers, e.g., in heavily doped silicon polycrystals with a grain size of ~1 μm. In moderately doped polycrystals ($N \sim 10^{16}$–10^{17} cm^{-3}), the tunneling currents are negligible compared to thermionic emission currents [4].

With a voltage $U_a < kT/q$ applied to the barrier, the current density of thermionic emission is given by

$$j = \frac{q^2 p_a}{\sqrt{2\pi m^* kT}}\exp\left(-\frac{qV_b}{kT}\right)U_a, \tag{6}$$

where p_a is the averaged density of holes in a partly depleted crystallite and m^* is their effective mass.

From formula (6) it follows that the conductivity of a polycrystal with a crystallite size L is

$$\sigma = \frac{Lq^2 p_a}{\sqrt{2\pi m^* kT}} \exp\left(-\frac{qV_b}{kT}\right). \quad (7)$$

It is assumed that $qV_b = E_b$, and, consequently,

$$\sigma \propto \exp[-(E_g/2 - E_F)/kT] \text{ at } NL < Q_t, \quad (8a)$$

$$\sigma \propto T^{-1/2} \exp[-E_b/kT] \text{ at } NL > Q_t. \quad (8b)$$

In this case, the effective mobility is given by

$$\mu_{\text{eff}} = \frac{Lq}{\sqrt{2\pi m^* kT}} \exp\left(-\frac{E_b}{kT}\right). \quad (9)$$

3. EXPERIMENTAL

We studied the temperature dependence of conductivity, the photoconductivity, and the hole mobility of high-purity textured *p*-CdTe polycrystals with a resistivity $\rho \sim 10^2$–10^5 Ω cm (room temperature). The samples were cut from polycrystalline ingots synthesized from thoroughly purified components at 600–620°C [7]. The contacts were fabricated after etching the samples in a bromine-methanol solution by depositing gold from a solution of auric chloride. As a rule, contacts of this kind are nearly ohmic.

The temperature dependences of conductivity and the photoconductivity spectra were measured in the temperature range from 290 to 65 K.

The free hole mobilities were found from the results of transient photoconductivity measurements by the method described in [8]. To make the density of mobile carriers higher, the samples were illuminated with a halogen lamp with a filament temperature of ~3000°C (photon flux ~10^{18} cm^2 s^{-1}).

4. RESULTS AND DISCUSSION

4.1. Temperature Dependences of Conductivity

Figure 2 shows the temperature dependence of the resistivity of a *p*-CdTe sample with grain sizes in the range 5–10 μm and a resistivity of 6×10^4 Ω cm at 250 K (curve *a*). The activation energy of conductivity, calculated from the slope of the linear portion, is 0.09 eV. This activation energy cannot be attributed to the trapping of holes at lower temperatures to an acceptor level E_v + 0.09 eV, since all the acceptors of this kind are completely ionized in the temperature range in question [9] and, consequently, cannot contribute to a change in the carrier density.

Hence, it follows that the slope we observed can only be accounted for by a decrease in the mobility of holes at a lower temperature, because of their scattering by the potential barriers at grain boundaries. It is the average height of these barriers that determines the activation energy [see Eq. (9)]. It is noteworthy that we observed a similar phenomenon in coarse-grained polycrystals [6].

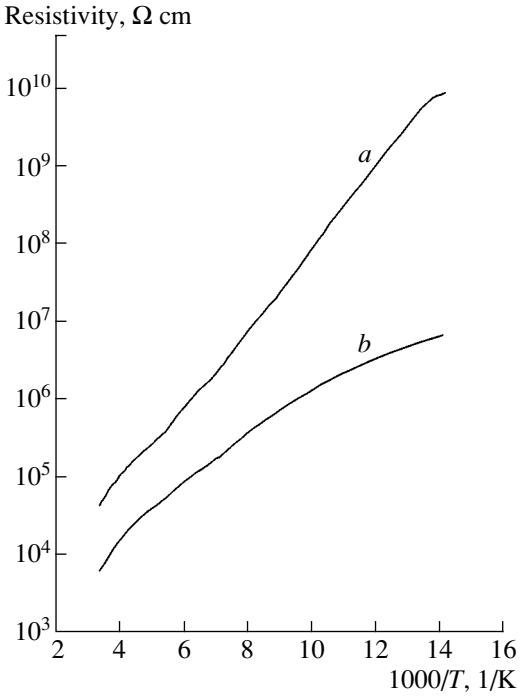

Fig. 2. Temperature dependence of the resistivity of finely crystalline *p*-CdTe (*a*) without illumination and (*b*) under exposure to white light.

If the potential barrier height is known, the density of charged traps at the interface and the effective mobility of holes can be evaluated by formulas (5) and (9) (evaluated, rather than calculated exactly, since an oversimplified model is used for lack of a better one). In the case in question, $Q_t \approx 7 \times 10^{10}$ cm^{-2} and $\mu_{\text{eff}} \approx 1$ cm^2/(V s).

Having evaluated these quantities and assuming that holes are excited to the valence band from these same centers with energy level E_v + 0.24 eV, which we repeatedly observed previously in polycrystals of this kind [6, 10, 11], we can state the following. In the given sample, the acceptor dopant concentration is $N_a \approx 2 \times 10^{15}$ cm^{-3} and the product $LN_a > (1\text{–}2) \times 10^{12}$ cm$^{-2} > Q_t$, which confirms the validity of formula (8b) for interpretation of the results we obtained.

The intensity of carrier scattering by grain-boundary potentials can be varied by raising or lowering the extent to which the grain boundary is charged. This conclusion is confirmed by curve *b* in Fig. 2, which represents the temperature dependence of the resistivity of this same sample, measured under illumination.

In polycrystalline CdTe, the $\mu\tau$ product for electrons always exceeds that for holes, $\mu_e\tau_e \gg \mu_p\tau_p$ and, therefore, white light mainly generates mobile electrons. These electrons rapidly fall into the potential well at the

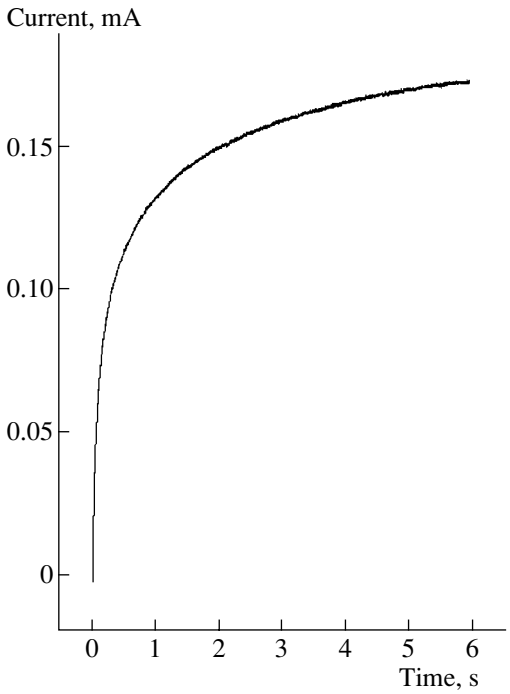

Fig. 3. Time dependence of the photocurrent through a *p*-CdTe sample exposed to a steplike pulse of light.

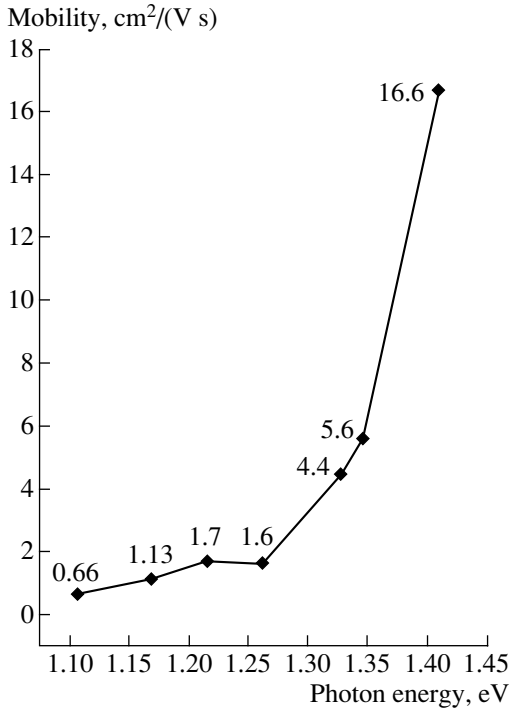

Fig. 4. Carrier mobility in finely crystalline *p*-CdTe vs. the photon energy of the exciting radiation. The mobilities are given at the points [in $cm^2/(V\ s)$].

interface and recombine with holes captured in this region, which makes the charge of the grain boundary smaller and thereby lowers the potential barrier.

The potential barrier height calculated from the average slope of the temperature dependence of resistivity (Fig. 2, curve *b*) is 0.06 eV. A decrease in the barrier height by 0.03 eV leads to an increase in the hole mobility at ~80 K by several orders of magnitude.

4.2. Hole Mobility in Fine-Grained CdTe Polycrystals

In this study, we determined the free carrier mobility by measuring the transient photoconductivity.

A sample cut in the form of a parallelepiped with a cross-section *S* and a length *L* was placed in a beam of monochromatic light incident perpendicularly to the electric field applied to the sample. The samples were exposed to steplike light pulses with a photon energy lower than the band gap width.

The power of radiation absorbed in a sample, which goes to carrier excitation, can be found from the expression

$$I = \frac{h\nu SL}{\beta}\frac{dp}{dt}, \tag{10}$$

where $h\nu$ is the energy of an absorbed photon; β, the quantum efficiency (assumed to be unity); and dp/dt, the rate of carrier generation in the linear region of the time dependence of the photocurrent. In the case in question, sample illumination leads to the generation of holes, since the light used has a photon energy lower than the band gap width.

The rate of current variation in the sample can be written as

$$\frac{di}{dt} = \frac{e\mu US}{L}\frac{dp}{dt}, \tag{11}$$

where *U* is the voltage applied to the sample. Eliminating the generation rate from Eqs. (10) and (11), we obtain the following expression for mobility:

$$\mu = \frac{h\nu L^2(di/dp)}{IeU}. \tag{12}$$

The measurements were carried out at 300 K and different photon energies of incident light. A typical time dependence of the photocurrent is shown in Fig. 3. As follows from the figure, the time constant of the photocurrent is rather long, ~0.5 s, which indicates that the carrier mobility is low. In the initial stage, the rise in the current through the sample is virtually linear, and it is this fact that allows expression (12) to be used to determine the mobility.

The results of calculation for various wavelengths are shown in Fig. 4. It should be noted that the mobility strongly depends on the photon energy and, what is more important, increases sharply as the photon energy approaches the band gap width. This result can be accounted for in terms of the previously suggested model of surface charge neutralization at grain boundaries [6]. As already mentioned in [6], the density of

surface states at the boundary is continuously distributed over energy in the band gap and is higher at its edges. Under equilibrium conditions, the interfacial states with energies higher than the Fermi energy are filled with captured holes (Fig. 5). When a sample is illuminated, electrons are captured into these surface states and neutralize the charge of the holes. This mechanism reduces the potential barrier height and, consequently, leads to an increase in hole mobility. As the photon energy increases, the barrier height decreases to a greater extent, since the density of states at band edges is considerably higher, and, consequently, the number of holes neutralized is greater.

4.3. Photoconductivity

Studying the photoconductivity spectra is one of the most informative methods for revealing the influence exerted by various imperfections of a semiconductor on its electrical properties. We have already used this method to study properties of CdTe polycrystals [11]. It was shown that the relaxation times of holes excited from "grain-boundary" traps are rather long, and, therefore, reasonable evidence about the traps can be obtained only from dc photoconductivity measurements (without light beam modulation). This is also indicated by the data in Fig. 3.

Figure 6 shows a dc photoconductivity spectrum for one of the *p*-CdTe samples we studied. The result obtained is consistent with the model of grain-boundary traps.

In equilibrium, those traps whose energy levels lie above the Fermi level are occupied by holes (Fig. 5). The density of these states is the highest at the conduction band bottom and decreases rather sharply into the band gap [12]. When a sample is exposed to light with photon energies lower than the band gap width, transitions of electrons from the valence band to trap levels occupied by holes are possible, which gives rise to photoconductivity. The photoelectric threshold should coincide with the position of the Fermi level; however, the photoconductivity is weak because of the low density of states in this region. As the photon energy becomes higher, the photoconductivity signal grows to reach a maximum at $h\nu = E_g - E_b$. Later, the signal should fall sharply. However, no abrupt fall would be expected in practice because of the presence of density-of-states tails in the band gap of disordered semiconductors.

The model we suggested makes it possible to estimate rather accurately the heights of potential barriers at grain boundaries, without making any additional assumptions or performing cumbersome calculations.

Specifically, the barrier height E_b found for the sample studied from photoconductivity measurements is 0.085 eV, which agrees well with the value of ~0.1 eV previously obtained from the temperature dependence of resistivity [6].

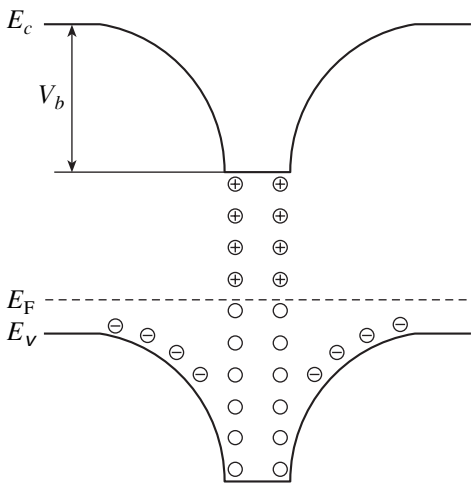

Fig. 5. Energy diagram of the grain boundary in *p*-type polycrystals.

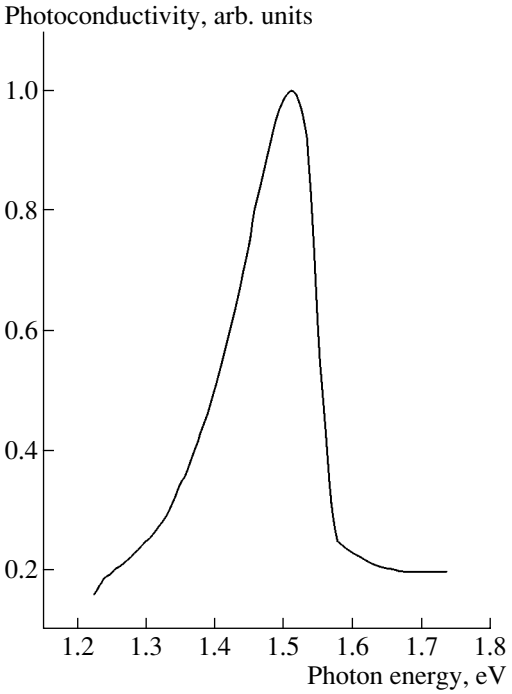

Fig. 6. Photoconductivity spectrum of a *p*-CdTe polycrystal at 70 K.

5. CONCLUSION

The results obtained in studying the temperature dependence of conductivity, the free carrier mobility, and the photoconductivity in CdTe polycrystals indicate that the barrier model allows a rather good interpretation of experimental results.

Two main models are currently in use for explaining the transport properties of polycrystals: the segregation model [12] and the "trap" model (which assumes carrier trapping at interfaces) [13]. Hall measurements in

polycrystalline phosphorus-doped silicon films show that the concentration of electrically active impurities in grains is significantly lower than the total concentration of implanted phosphorus ions. This fact, on the one hand, confirms the hypothesis that there is a pronounced segregation of impurities at grain boundaries. On the other hand, the temperature dependences of conductivity of polycrystalline films can only be accounted for in terms of the "trap" model. Reasonable analysis of experimental results in terms of a particular theory requires knowledge of the grain sizes and the energy distribution of electronic states related to grain-boundary traps. The grain size can be easily determined experimentally (by X-ray measurements), whereas the energy distribution of electronic states of traps is a matter of speculation. There are two opinions: (i) all the grain-boundary traps have the same energy level, which lies close to the midgap, and (ii) the electronic states of the traps are continuously distributed within the band gap, and the density of states increases toward band edges.

The results obtained in this study are most adequately accounted for in terms of the "trap" model and a continuous distribution of trap energies within the band gap.

ACKNOWLEDGMENTS

The authors are deeply grateful to Prof. V.S. Bagaev for valuable advice.

This study was supported by the Russian Foundation for Basic Research (grant nos. 02-02-17324 and 00-02-16500).

REFERENCES

1. A. Balciogln, R. K. Ahrenkiel, and F. Hasoon, J. Appl. Phys. **88**, 7175 (2000).
2. Tadayuki Takahashi and Shin Watanabe, IEEE Trans. Nucl. Sci. **48**, 950 (2001).
3. A. Zumbiehl, M. Hage-Ali, M. Agoub, *et al.*, IEEE Trans. Nucl. Sci. **49**, 1254 (2002).
4. J. Y. W. Seto, J. Appl. Phys. **46**, 5247 (1975).
5. G. Baccarani and B. Ricco, J. Appl. Phys. **49**, 5565 (1978).
6. S. A. Kolosov, Yu. V. Klevkov, and A. F. Plotnikov, Fiz. Tekh. Poluprovodn. (St. Petersburg) **38**, 473 (2004) [Semiconductors **38**, 455 (2004)].
7. S. A. Medvedev and Yu. V. Klevkov, RF Patent No. 243014 (20 December 1999).
8. L. Gildart and A. W. Ewald, Phys. Rev. **83**, 359 (1951).
9. K. Seeger, *Semiconductor Physics* (Springer, Wien, 1973; Mir, Moscow, 1977).
10. Yu. V. Klevkov, S. A. Kolosov, S. A. Medvedev, and A. F. Plotnikov, Fiz. Tekh. Poluprovodn. (St. Petersburg) **35**, 1192 (2001) [Semiconductors **35**, 1139 (2001)].
11. S. A. Medvedev, Yu. V. Klevkov, S. A. Kolosov, *et al.*, Fiz. Tekh. Poluprovodn. (St. Petersburg) **36**, 937 (2002) [Semiconductors **36**, 874 (2002)].
12. A. L. Fripp, J. Appl. Phys. **46**, 1240 (1975).
13. Y. W. Seto, J. Electrochem. Soc. **122**, 701 (1975).

Translated by M. Tagirdzhanov

Semiconductors, Vol. 38, No. 4, 2004, pp. 461–467. Translated from Fizika i Tekhnika Poluprovodnikov, Vol. 38, No. 4, 2004, pp. 479–485.

AMORPHOUS, VITREOUS, AND POROUS SEMICONDUCTORS

Exciton Photoluminescence in Doped Quasi-1D Structures Based on Silicon

A. V. Sachenko*, D. V. Korbutyak*, Yu. V. Kryuchenko*, and O. M. Sreseli**

**Lashkarev Institute of Semiconductor Physics, National Academy of Sciences of Ukraine, Kiev, 03028 Ukraine*

***Ioffe Physicotechnical Institute, Russian Academy of Sciences, St. Petersburg, 194021 Russia*

e-mail: Olga.Sreseli@mail.ioffe.ru

Submitted October 10, 2003; accepted for publication October 17, 2003

Abstract—The dependence of carrier density in silicon quantum wires sheathed with SiO_2 on the wire diameter and the position of impurity atoms in respect to the wire center is analyzed theoretically. It is shown that, as the diameter of wires and nanocrystals decreases, the ionization energy of a dopant increases; therefore, the free carrier density decreases, and the screening of the Coulomb attraction becomes ineffective. As a result, the photoluminescence is defined by the radiative recombination of excitons even in the case of heavily doped Si. These conclusions are supported by the data of experimental study of spectral, excitation-power, and temperature dependences of photoluminescence in porous silicon structures fabricated on lightly and heavily doped Si substrates. © *2004 MAIK "Nauka/Interperiodica".*

1. INTRODUCTION

In the 3D case, the screening of the Coulomb interaction between electrons and holes in semiconductors leads, at a high enough carrier density, to an excitonic Mott transition. For example, in Si at $T = 300$K, the carrier density at which the excitonic Mott transition occurs is 8.3×10^{17} cm^{-3} [1]. The question now arises, what happens when the dimensionality of a semiconductor decreases? In this case, not only the character of screening is changed, but also the ionization energy of impurity considerably increases. An especially strong increase is expected in the quantum limit in the case of a simultaneous occurrence of so-called "dielectric enhancement," when the dielectric constant of the dielectric sheath is significantly lower than that of the semiconductor (see, e.g., [2]).

As shown in [3, 4], in GaAs/AlGaAs quantum wells (QW) the excitonic Mott transition is observed at a low doping level (about 5×10^9 cm^{-2}). According to [4], this occurs with a fairly large width of QWs (~20–30 nm). At these QW dimensions, the character of screening of the Coulomb potential is mixed; it changes from purely 2D at large distances in the plane of QW to 3D at small distances. A similar situation was observed in [5], where photoluminescence (PL) was studied at room temperature in a standard nanoporous Si and in mesoporous Si produced from a material with a hole density of 4×10^{18} cm^{-3}. The average wire diameter in these samples was 6–8 nm. The PL peak was blue-shifted with respect to the absorption edge of bulk Si, and the dependence of the PL intensity on the illumination intensity was quadratic, which is typical of band-to-band radiative recombination. We believe that these results are indicative of an excitonic Mott transition. It seems that in this case the screening of the Coulomb interaction between electrons and holes had a quasi-3D character, because the wire diameter significantly exceeded the Debye screening length r_D (in Si, r_D is about 1.5 nm for this hole density at room temperature). The ionization energy for acceptors in the studied porous silicon (*por*-Si) did not change significantly compared to the bulk material. Even though quantum confinement took place, the broadening of the band gap was relatively small (several tens of meV), and several quantum-confinement subbands were involved in the screening. As a result, the *por*-Si studied was found to be similar in its properties to ordinary bulk silicon.

In this study we analyzed the possibility of an excitonic Mott transition in quantum wires of smaller diameter (less than the Bohr radius of exciton in Si, $a_B \approx 4$ nm), in particular, in nanoporous Si. It was shown that an excitonic Mott transition does not occur up to the highest doping level of the starting Si material. This is related primarily to the significant rise in the energy of impurity ionization and, consequently, to a considerable decrease in the free carrier density.

2. THEORY

First, we analyze the relation between the Bohr radius of exciton, a_B, and the average distance between the screening electrons in semiconductors of varied dimensionality at fixed concentration of donor centers, taking into account that the energy depth of shallow impurity levels (as well as the exciton binding energy) increases as the dimensionality decreases. Our examination of quantum wells and quantum wires is restricted to the case of the quantum limit, when only

the lowest quantized subbands are filled with electrons and holes.

The density of electrons is $N_i = N_{ci}\exp[(E_f - E_c)/kT]$, so their number in a unit volume of a semiconductor in the 3D-case ($i = 3$), or their number per unit area of a quantum well ($i = 2$), or per unit length of a quantum wire ($i = 1$) is determined, as usual, from the neutrality condition

$$\frac{N_{di}}{1 + \exp[(E_f - E_d)/kT]} = N_i, \qquad (1)$$

where E_c, E_d, and E_f are the energies of the conduction band edge (taking into account the quantization in quantum-confined structures), the donor level, and the Fermi level, respectively; $N_{d3} = N_d$, $N_{d2} = dN_d$, and $N_{d1} = (\pi d^2/4)N_d$, where d is the thickness of a quantum structure; $N_{c3} = N_c$, where N_c is the effective density of states in the conduction band in the 3D-case; and $N_{c2} = N_c^{2/3}$, $N_{c1} = N_c^{1/3}$.

The average distances (R_i) between electrons in Si in the case when $N_d = 10^{18}$ cm^{-3}, $E_d - E_c = -0.01$ eV, and $T = 300$ K are $R_3 \approx 10$ nm, $R_2 \approx N_{d2}^{-1/2} \approx 20$ nm, and $R_1 \approx N_{d1}^{-1} \approx 150$ nm for $d = 3$ nm. If $E_d - E_c = -0.2$ eV, which is typical of *por*-Si for the diameter of the quantum wire used, then $R_1 \approx 1000$ nm.

These estimates show that, for the same volume concentration of donors, the average distance between electrons increases as the dimensionality of a semiconductor is lowered. This can be related, on the one hand, to the decrease in the effective density of states in the lowest conduction band, and, on the other, to the increase in the donor ionization energy. In order that the excitonic Mott transition occur, it is necessary that the size of the exciton in the direction of its free motion ($\approx 2a_B$) be comparable with R_i. Taking into account that $a_B \approx 4$ nm in Si, this condition is fulfilled only for 3D and 2D semiconductors with the set of parameters listed above. For quantum wires, R_1 exceeds $2a_B$ by more than an order of magnitude even for $N_d = 10^{20}$ cm^{-3}. As temperature decreases, R_1 increases further, so that the ratio $R_1/2a_B$ becomes much more than unity.

Thus, excitons should exist in nanocrystalline *por*-Si up to the heaviest doping level; this circumstance is related to small Coulomb energy $q^2/\varepsilon_0\varepsilon_{eff}R_1$ compared to the exciton binding energy E_x. A majorized estimate of $q^2/\varepsilon_0\varepsilon_{eff}R_1$ for *por*-Si can be obtained assuming that the effective dielectric constant $q^2/\varepsilon_0\varepsilon_{eff}R_1$ equals that of SiO_2. Then, even if the rise in the donor ionization energy is disregarded, we obtain at $R_1 = 150$ nm a Coulomb energy of about 0.03 eV, which is one order of magnitude smaller than the exciton binding energy E_x in a Si quantum wire 3 nm in diameter sheathed with SiO_2 [6]; i.e., the criterion above is well satisfied.

Naturally, all the above is valid for the case when free carriers are holes, i.e., for *por*-Si samples produced from *p*-type Si. Since our *por*-Si samples were produced by electrochemical etching of precisely *p*-Si, this factor is taken into account in all the calculations presented below.

The energy levels of carriers interacting with a charged Coulomb center in a cylindrical quantum wire embedded in a dielectric matrix are determined from the solution of the Schrödinger equation:

$$\left[-\frac{\hbar^2}{2\mu}\left(\Delta_\rho + \frac{d^2}{dz^2} + \frac{1}{\rho^2}\frac{d^2}{d\varphi^2}\right) + U_s(\rho) + U_b(\rho) + U_I(\mathbf{r}, \mathbf{r}_i)\right]\Psi(\mathbf{r}) = E\Psi(\mathbf{r}), \qquad (2)$$

where $\mathbf{r} = \{\rho, z, \varphi\}$ are the coordinates of a carrier in cylindrical coordinates; $\mathbf{r}_i = \{\rho_i, 0, 0\}$, the coordinates of an impurity center; $\Delta_\rho = d^2/d\rho^2 + (1/\rho)d/d\rho$; and μ, the effective mass of a carrier, which depends on its position ($\mu = m_2$ in the region $\rho < R$ within the quantum wire, and $\mu = m_1$ in the external region $\rho > R$; R is the wire radius). The potential energy $U_s(\rho)$ describes the self-action of carriers due to the polarization of the cylindrical heterointerface (the so-called potential energy of image forces); the summand $U_b(\rho)$ accounts for the band offset at the heterointerface (conduction band, δU_c, or valence, δU_v, depending on the conduction type); and $U_b(\rho) = 0$ within the wire and $U_b(\rho) = \delta U_{c(v)}$ in the coating dielectric material. The summand $U_I(\mathbf{r}, \mathbf{r}_i)$ is the potential energy of a carrier in the field of a charged impurity center. It is the sum of the potential energy of the direct Coulomb interaction between the carrier and the impurity and the potential energy of the carrier in the field of image forces of this center. Analytical expressions for the potential energies $U_s(\rho)$ and $U_I(z, \rho, \rho_i)$ can be obtained using the standard Green's function method [7] from the solution of a standard Poisson equation with point charges of the carrier and impurity, as was done in [8]:

$$U_s(\rho) = -\frac{e^2}{\pi}\frac{\varepsilon_2 - \varepsilon_1}{\varepsilon_1}\sum_{m=0}^{\infty}(2 - \delta_{m,0}) \times \int_0^\infty \frac{I_m(\eta R)I'_m(\eta R)\eta R}{\varepsilon_1 + (\varepsilon_2 - \varepsilon_1)K_m(\eta R)I'_m(\eta R)\eta R}K_m^2(\eta\rho)d\eta, \qquad (3)$$

if $\rho > R$, and

$$U_s(\rho) = -\frac{e^2}{\pi}\frac{\varepsilon_2 - \varepsilon_1}{\varepsilon_2}\sum_{m=0}^{\infty}(2 - \delta_{m,0}) \times \int_0^\infty \frac{K_m(\eta R)K'_m(\eta R)\eta R}{\varepsilon_1 + (\varepsilon_2 - \varepsilon_1)K_m(\eta R)I'_m(\eta R)\eta R}I_m^2(\eta\rho)d\eta, \qquad (4)$$

if $\rho < R$. Here, K_m and I_m are modified Bessel functions; ε_1, the dielectric constant of the barrier material around the quantum wire (for SiO_2, $\varepsilon_1 = 2.1$); and ε_2, the dielectric constant of the quantum wire material (for Si wire, $\varepsilon_2 = 11.7$). The shift of the band edges (valence or conduction band) in the center of the wire, which results from such a polarization self-action, is

$$U_s(0) = -\frac{e^2}{\pi}\frac{\varepsilon_2 - \varepsilon_1}{\varepsilon_2} \times \int_0^\infty \frac{K_0(\eta R)K_0'(\eta R)\eta R}{\varepsilon_1 + (\varepsilon_2 - \varepsilon_1)K_0(\eta R)I_0'(\eta R)\eta R} d\eta. \quad (5)$$

In the case when a carrier and impurity are in the barrier material outside the quantum wire (i.e., when both ρ and $\rho_i > R$), the potential energy of the carrier in the field of an oppositely charged impurity in this quantum system can be presented as

$$U_I(\mathbf{r}, \mathbf{r}_i) = -\frac{e^2}{\varepsilon_1|\mathbf{r} - \mathbf{r}_i|} + \frac{2e^2}{\pi}\frac{\varepsilon_2 - \varepsilon_1}{\varepsilon_1}\sum_{m=0}^{\infty}(2 - \delta_{m,0}) \times \exp(im\varphi)\int_0^\infty \frac{I_m(\eta R)I_m'(\eta R)\eta R\cos(\eta z)}{\varepsilon_1 + (\varepsilon_2 - \varepsilon_1)K_m(\eta R)I_m'(\eta R)\eta R} \times K_m(\eta\rho)K_m(\eta\rho_i)d\eta. \quad (6)$$

When a carrier is within the quantum wire and the impurity is in the surrounding barrier material, or vice versa, we have

$$U_I(\mathbf{r}, \mathbf{r}_i) = -\frac{e^2}{\varepsilon|\mathbf{r} - \mathbf{r}_i|} + \frac{2e^2}{\pi}\frac{\varepsilon_2 - \varepsilon_1}{\varepsilon}\sum_{m=0}^{\infty}(2 - \delta_{m,0}) \times \exp(im\varphi)\int_0^\infty \frac{[K_m(\eta R)I_m'(\eta R)\eta R - 0.5]\cos(\eta z)}{\varepsilon_1 + (\varepsilon_2 - \varepsilon_1)K_m(\eta R)I_m'(\eta R)\eta R} \times I_m(\eta\rho_<)K_m(\eta\rho_>)d\eta, \quad (7)$$

where $\varepsilon = (\varepsilon_1 + \varepsilon_2)/2$. In the last relation, $\rho_< = \rho$ and $\rho_> = \rho_i$ at $\rho < \rho_i$; on the contrary, $\rho_< = \rho_i$ and $\rho_> = \rho$ at $\rho_i < \rho$. Finally, when both the carrier and the impurity are within the quantum wire (i.e., when both ρ and $\rho_i < R$),

$$U_I(\mathbf{r}, \mathbf{r}_i) = -\frac{e^2}{\varepsilon_2|\mathbf{r} - \mathbf{r}_i|} + \frac{2e^2}{\pi}\frac{\varepsilon_2 - \varepsilon_1}{\varepsilon_2}\sum_{m=0}^{\infty}(2 - \delta_{m,0}) \times \exp(im\varphi)\int_0^\infty \frac{K_m(\eta R)K_m'(\eta R)\eta R\cos(\eta z)}{\varepsilon_1 + (\varepsilon_2 - \varepsilon_1)K_m(\eta R)I_m'(\eta R)\eta R} \times I_m(\eta\rho)I_m(\eta\rho_i)d\eta. \quad (8)$$

The first terms on the right side of Eqs. (6)–(8) describe the direct Coulomb interaction between a carrier and impurity; the indirect interaction related to the polarization of the heterointerface by a charged impurity center is described by the second terms.

The energy spectrum of a carrier in a quasi-1D quantum well in the field of a charged impurity was calculated in terms of the perturbation theory. The wave functions were sought in the form of expansion

$$\Psi(\mathbf{r}) = 1/\sqrt{2\pi}\sum_{mnj} C_{mnj}F_j(z)\chi_{mn}(\rho)\exp(im\varphi) \quad (9)$$

in terms of eigenstates of the model Hamiltonian which, on the one hand, served as a good approximation to the real Hamiltonian in Eq. (2) and, on the other, allowed the separation of variables related to the transverse (radial) and longitudinal (along the wire) motion of a charge. In Eq. (9), C_{mnj} are the expansion coefficients; m, the azimuthal quantum numbers; n, the radial quantum numbers corresponding to quantum-well levels E_{mn}; j, the quantum numbers of states of a carrier bound on a quasi-1D Coulomb center with the binding energy E_j. The precision of this method is limited by the number of terms taken into account in (9). For the ground state, only the summands with $m = 0$ are of significance; the others may be disregarded.

The wave functions $\chi_{mn}(\rho)$ of the transverse motion of carriers in a square cylindrical potential well with renormalized height of the external potential barrier $\delta\tilde{U} = \delta U_{c(v)} - U_s(0)$, along with the corresponding energies E_{mn}, are easily found in the standard way by solving the Schrödinger equations

$$-\frac{\hbar^2}{2m_2}\left(\Delta - \frac{m^2}{\rho^2}\right)\chi_{2,mn}(\rho) = E_{mn}\chi_{2,mn}(\rho) \quad (10)$$

for the internal ($\rho < R$) and

$$\left[-\frac{\hbar^2}{2m_1}\left(\Delta - \frac{m^2}{\rho^2}\right) + \delta\tilde{U}\right]\chi_{1,mn}(\rho) = E_{mn}\chi_{1,mn}(\rho) \quad (11)$$

for the external ($\rho > R$) regions, and matching the functions and their fluxes at the heterointerface. Within the quantum wire, wave functions of the transverse motion $\chi_{mn}(\rho)$ are Bessel functions $J_m(k_{2,mn}\rho)$, correct to a normalization factor, and in the barrier region they are modified Bessel functions $K_m(k_{1,mn}\rho)$, in which the quantum wave numbers $k_{1,mn}$ and $k_{2,mn}$ and fundamental energies E_{mn} are found from the condition of nontrivial solvability of the system of boundary conditions. The normalization factors were determined from the normalization condition $\int_0^\infty \chi_{mn}^2(\rho)\rho d\rho = 1$. We have chosen this model system with the renormalized depth of the potential well, because here the shift $U_s(0)$ makes the major contribution and is easily taken into account in the final result. The remaining part of the potential energy of the polarization self-action makes a significantly smaller contribution to the energy shifts of levels, owing to the strong mutual compensation of the contributions from the internal and external regions of

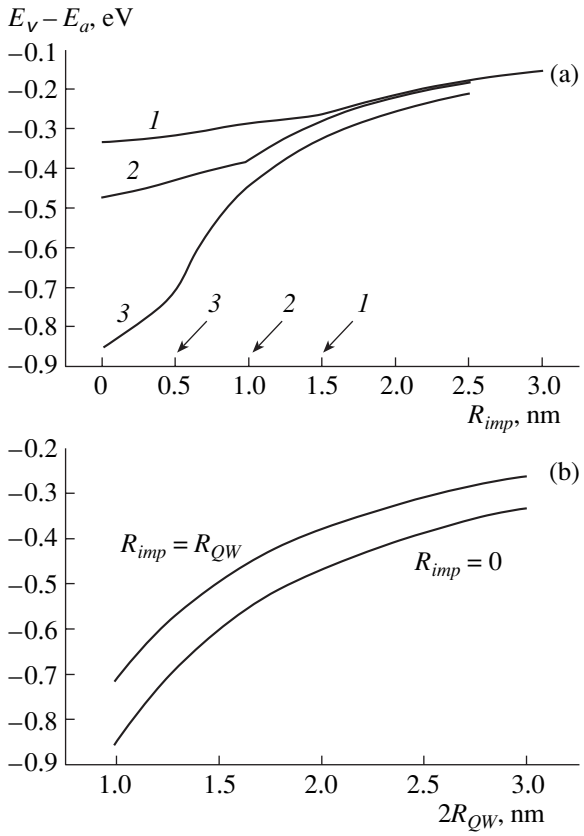

Fig. 1. The ionization energy of acceptors, $E_v - E_a$, vs. (a) the distance between the impurity center and the axis of a Si quantum wire in a SiO_2 sheath, R_{imp}, and (b) the wire diameter $2R_{QW}$. Wire diameter in Fig. 1a: (*1*) 3, (*2*) 2, and (*3*) 1 nm. Arrows indicate the wire radius.

a wire (we used a linear approximation of the total single-particle potential in the vicinity of the heterointerface, as was done in [6]).

As wave functions of the longitudinal motion $F_j(z)$, we used the eigenstates of the model 1D Schrödinger equation:

$$\left[-\frac{\hbar^2}{2m_2}\frac{d^2}{dz^2} + \tilde{W}_C(z)\right]F_j(z) = E_jF_j(z), \qquad (12)$$

where the second term in brackets $\tilde{W}_C = -e^2/\varepsilon^2(|z| + a)$ approximates the direct Coulomb interaction $W_C = -e^2/\varepsilon^2|\mathbf{r} - \mathbf{r}_i|$ between a carrier and impurity in the wire. A nonzero positive parameter a in $\tilde{W}_C$ makes it possible to use a complete system of states of the 1D longitudinal motion of a carrier in a quantum wire in the field of a charged impurity center, including the ground state [9]. If $a \longrightarrow 0$, the binding energy of this ground state tends to infinity, and the corresponding wave function transforms into a δ-function. For this reason, the approximation of a real Coulomb interaction in a quantum wire by a 1D Coulomb interaction $\tilde{W}_1^C(z) = -e^2/(\varepsilon_2|z|)$ results in the loss of the lowest state and the expansion (9) is incomplete. Naturally, the final result should not depend on a specific value of a. However, there is good reason to use an optimized value of a to provide rapid convergence of series (9). If the subject of interest is the lowest state of a carrier in a quantum wire in the presence of an impurity center, a must be calculated from the requirement of the best convergence just for this state. This is equivalent to the requirement of the best approximation of the real Coulomb interaction, averaged over the transverse motion of carriers in a quantum wire in the ground state, with a 1D potential $\tilde{W}_C(z)$. In a simplified version, it is sufficient to demand that, in the point $z = 0$, the values of $\tilde{W}_C$ should be equal to the real Coulomb interaction averaged over the transverse motion.

As is well known, the solutions of Eq. (12) for bound states of a carrier in the field of a charged impurity center can be expressed in terms of the Whittaker functions [9], $F_j(z) = C_jW_{\beta_j}, 1/2(\tilde{z})[z/|z|]^p$, where C_j is the normalizing constant; p, the parity ($p = 1$ for odd and $p = 2$ for even states); and $\beta_j = (-E_j/\mathrm{Ry})^{-1/2}$, $\mathrm{Ry} = m_2e^4/(2\hbar^2\varepsilon_2^2)$, $\tilde{z} = 2(|z| + a)/(\beta_j r_B)$, and $r_B = \hbar^2\varepsilon_2/(e^2m_2)$. The continuity condition for the wave function F and its flux at $z = 0$ are used to obtain the dispersion equations $W'_{\beta, 1/2}(2a/(r_B\beta)) = 0$ for even and $W_{\beta, 1/2}(2a/(r_B\beta)) = 0$ for odd states; from here the quantum numbers β_j and corresponding energy eigenvalues E_j are determined.

When the system of basis functions is chosen, the algebraic equations for the expansion coefficients C_{mnj} take the following standard form:

$$(E - E_{mn} - E_j)C_{mnj} - \sum_{m'n'j'} T(m, m'; n, n'; j, j')C_{m'n', j'} = 0, \qquad (13)$$

where $T(m, m'; n, n'; j, j')$ are the matrix elements of the difference of the Hamiltonians (the initial, with the real Coulomb 3D interaction, and the model one) in the basis of the wave functions of the model Hamiltonian. The energy spectrum of bound states E_N ($N = 1, 2, 3, \ldots$) of a carrier in the quantum well in the field of a charged impurity is determined from the condition of the nontrivial solution of this system of algebraic equations (i.e., from the secular equation for this system).

Figure 1a shows calculated dependences of the acceptor ionization energy, $E_v - E_a$, on the radial position of the impurity atom in respect to the wire axis, for a nanostructure formed by a Si quantum wire in a SiO_2 sheath. The parameter of the theoretical curves is the wire diameter. As can be seen in the figure, impurity atoms located at the wire axis have the maximum ionization energy (reckoned from the bottom of the first quantum subband in the valence band). As the distance from the wire axis increases, the acceptor ionization

energy decreases, though it remains rather high as far as the heterointerface. E_a falls to zero when the impurity atom is located outside the wire, i.e., in SiO_2.

Figure 1b shows calculated dependences of $(E_v - E_a)$ on the diameter of a Si quantum wire for two positions of an acceptor: in the wire center ($R_{imp} = 0$), and on the interface with SiO_2 ($R_{imp} = R$).

Since the acceptor positions along the wire are distributed with a certain probability (e.g., are equiprobable), it is evident that the density of holes p will fluctuate along the wire. Figure 2 shows the dependences of the hole density in a Si wire on the wire diameter at $N_a = 10^{19}$ cm^{-3} and $T = 300$ K for two limiting cases: all the acceptors are located (i) at the wire axis (lower curve) or (ii) on the periphery (upper curve). Evidently, if the contribution of acceptors located in SiO_2 is disregarded, the local density of holes in the wires will vary between these limiting values. Two factors allow us to disregard the contribution of acceptors in SiO_2: the first is that the SiO_2 layer, which can emit holes to the Si wire, is thin (~1 nm); the second is that the acceptor concentration in SiO_2 is smaller than in Si by a factor of 2.7, because the volume of silicon oxide increases in respect to unoxidized silicon. As can be seen in Fig. 2, even in the case when all the acceptors are located on the wire periphery, the hole density in a wire 3 nm in diameter at room temperature is two orders of magnitude lower than the acceptor concentration. This concentration, calculated per unit wire length, is $N_{1a} \approx 7 \times 10^5$ cm^{-1}. This means that no more than 1% of acceptors are ionized, and the remaining 99% are un-ionized; i.e., they are in the neutral state. This result coincides with the data of [10], where it was shown that as the porosity of *por*-Si increases, i.e., the wire size decreases, the boron concentration in the layer remains constant, whereas the ratio between the number of neutral boron atoms and the number of the remaining Si atoms increases.

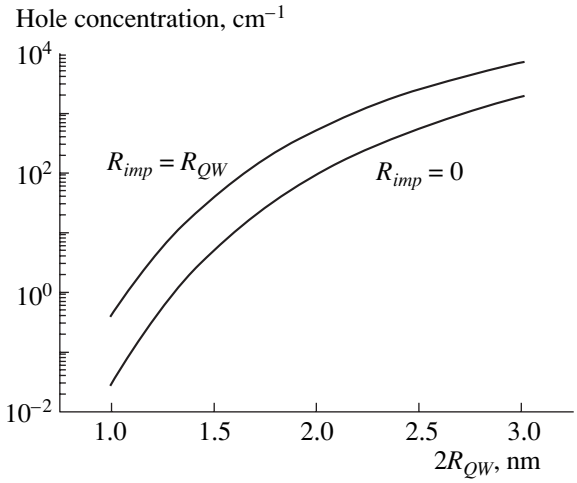

Fig. 2. Hole density in a Si–SiO_2 quantum wire vs. its diameter. $N_a = 10^{19}$ cm^{-3}, $T = 300$ K.

3. EXPERIMENTAL RESULTS AND DISCUSSION

For experimental verification of the assumptions based on our numerical calculations, we studied photoluminescence (PL) of a nanocrystalline *por*-Si produced by electrochemical etching of *p*-Si with an acceptor concentration of 4×10^{18}–10^{19} cm^{-3}. The data obtained were compared with similar data for other samples of nanoporous Si produced from a weakly doped *p*-type material.

Single-crystal *p*-Si was used for the substrates: weakly doped, with $\rho = 12$ Ω cm resistivity ($p = 10^{15}$ cm^{-3}), and heavily doped, with $\rho = 10$–20 mΩ cm ($p = 4 \times 10^{18}$–10^{19} cm^{-3}).

Layers of *por*-Si were produced using the technique of anodic etching in ethanol solutions of hydrofluoric acid. The standard HF : ethanol (1 : 1) solution was used for weakly doped samples, and, in accordance with the recommendations in [11], an electrolyte that contained a smaller amount of acid and a small amount of water, HF : alcohol : H_2O = (1 : 2 : 1), for heavily doped samples.

The etching conditions were as follows: for weakly doped samples, the current density was $j = 20$ mA/cm^2 and etching time $t = 5$ min; for heavily doped samples, $j = 25$ mA/cm^2 and $t = 15$ min.

A computerized spectrometer based on an MDR-2 monochromator and an FEU-79 photomultiplier was used for PL studies with excitation by light of a pulsed laser ($\lambda = 337$ nm, 10 ns duration) or a CW LG-106 laser with a selected wavelength ($\lambda = 514.5$ nm). Three modes of PL measurement were employed: stationary, quasi-stationary (with a large delay between the exciting laser pulse and the instant of the PL pulse recording), and time-resolved. Temperature dependences were studied in a cryostat with sapphire windows for the radiation input/output.

The maximum power of the laser beam exciting PL was 20 mW/cm^2 for the CW laser ($\lambda = 0.5145$ μm) and 100 mW/cm^2 (peak value) for the pulsed laser ($\lambda = 0.337$ μm).

Figure 3 shows the PL intensity spectra of nanoporous Si samples produced from heavily doped material (curve *1*) and from the material with a low doping level (curves *2*, *3*). The average diameter of wires in the nanoporous Si produced from heavily doped material was 2.7 nm (the estimate is obtained from Fig. 3 of [12]). Figure 4 shows the PL intensity as a function of the excitation level for nanoporous Si samples: points *1* and *2*, respectively, correspond to samples produced of weakly and heavily doped material. Figure 5 shows temperature dependences of the PL intensity, with the same notations for samples.

As can be seen from Figs. 3–5, the PL intensity for *por*-Si samples produced from heavily doped material is comparable with that for nanocrystalline *por*-Si produced

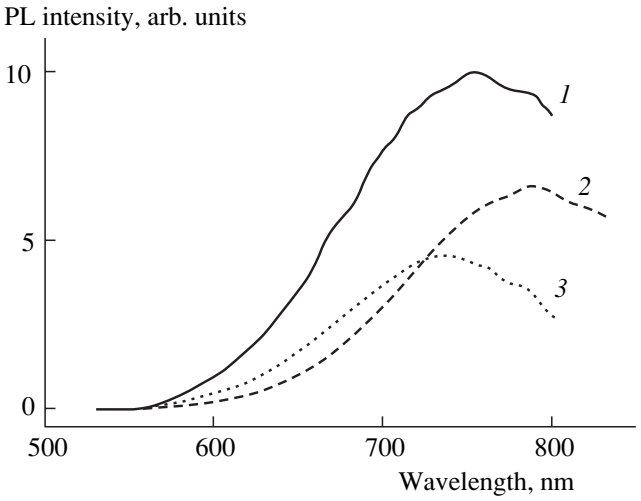

Fig. 3. PL spectra of nanoporous Si samples produced from (*1*) heavily and (*2*, *3*) weakly doped material. T = 300 K.

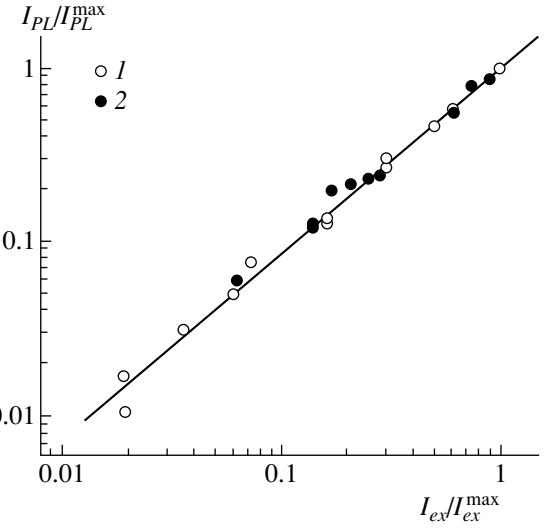

Fig. 4. PL intensity of nanoporous Si samples, I_{PL}, vs. the excitation level, I_{ex}: (*1*) weakly doped and (*2*) heavily doped material. T = 300 K.

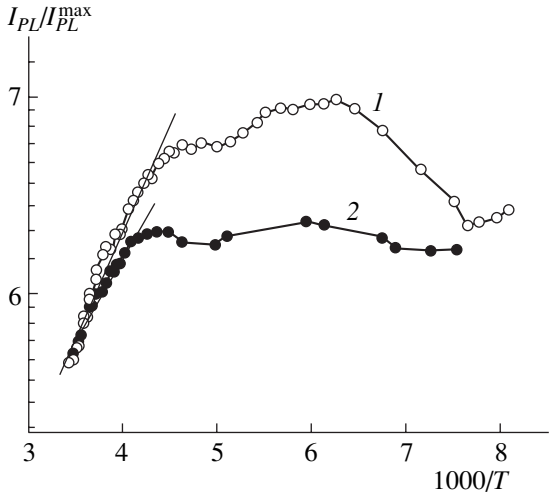

Fig. 5. Temperature dependences of the PL intensity of nanoporous Si samples: (*1*) weakly doped and (*2*) heavily doped material.

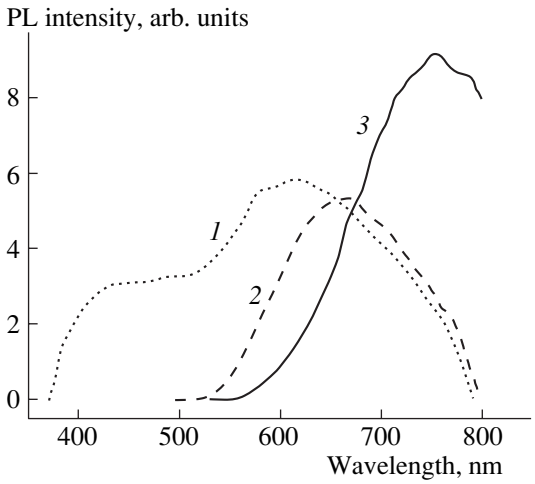

Fig. 6. PL spectra of nanoporous Si samples produced from heavily doped material. The spectra were recorded with different delays between the exciting laser pulse and the instant of the PL pulse recording: (*1*) 80 and (*2*) 480 ns; (*3*) the stationary spectrum. T = 300 K.

from the material with a resistivity of about 10 Ω cm. For both types of samples, the PL intensity dependences on the excitation level are linear, which is indicative of the exciton mechanism of PL. Finally, the temperature dependences of the PL intensity are also similar: as temperature decreases from room temperature, an exponential increase in the intensity is observed; then the dependence levels off or in some cases decreases.

Thus, the experimental data obtained confirm our conclusion that there is no excitonic Mott transition in nanocrystalline *por*-Si produced from a material with a very high doping level. One should note the decisive role of dielectric enhancement, which leads to a significant additional increase in the energy of impurity ionization in Si quantum wires sheathed with SiO_2. The presence of a considerable amount of SiO_2 in *por*-Si samples is confirmed by the time-resolved PL spectra of these samples (Fig. 6), which exhibit a well-resolved band of "fast" PL. As is well known (see, e.g., [13]), an intense short-wavelength band with a small relaxation time is typical of oxidized *por*-Si layers.

Furthermore, the results of our theoretical calculation offer an explanation for the very strong increase in the resistivity of nanoporous Si compared with the ini-

tial material, without invoking the artificial hypothesis that the impurity atoms are "washed out" in the electrochemical process of *por*-Si production.

ACKNOWLEDGMENTS

This study was supported in part by the Ministry of Education and Science of Ukraine (project no. 1F of the interstate Russian–Ukrainian program "Nanophysics and Nanoelectronics" and project no. 02.07/00129 of the State Foundation for Basic Research) and INTAS Call2001 NANO-0444.

O.M. Sreseli acknowledges the support of the "Physics of Solid-State Nanostructures" and "Low-Dimensional Quantum Structures" programs of the Presidium of the Russian Academy of Sciences.

REFERENCES

1. A. V. Sachenko and Ju. V. Kryuchenko, Semicond. Phys. Quantum Electron. Optoelectron. **3**, 150 (2000).
2. A. Shik, J. Appl. Phys. **74**, 2951 (1993).
3. S. I. Gubarev, I. V. Kukushkin, S. V. Tovstonog, *et al.*, Pis'ma Zh. Éksp. Teor. Fiz. **72**, 469 (2000) [JETP Lett. **72**, 324 (2000)].
4. D. V. Kulakovskiĭ, S. I. Gubarev, and Yu. E. Lozovik, Pis'ma Zh. Éksp. Teor. Fiz. **74**, 123 (2001) [JETP Lett. **74**, 118 (2001)].
5. M. G. Lisachenko, E. A. Konstantinova, V. Yu. Timoshenko, and P. K. Kashkarov, Fiz. Tekh. Poluprovodn. (St. Petersburg) **36**, 344 (2002) [Semiconductors **36**, 325 (2002)].
6. Yu. V. Kryuchenko and A. V. Sachenko, Physica E (Amsterdam) **14**, 299 (2002).
7. J. D. Jackson, *Classical Electrodynamics* (Wiley, New York, 1962; Inostrannaya Literatura, Moscow, 1965).
8. E. A. Mulyarov and S. G. Tikhodeev, Zh. Éksp. Teor. Fiz. **111**, 274 (1997) [JETP **84**, 151 (1997)].
9. R. Loudon, Am. J. Phys. **27**, 649 (1959).
10. G. Polisski, G. Dollinger, A. Bergmeier, *et al.*, Phys. Status Solidi A **168**, R1 (1998).
11. G. Polisski, H. Heckler, D. Kovalev, *et al.*, Appl. Phys. Lett. **73**, 1107 (1998).
12. C. Delerue, G. Allan, and M. Lannoo, J. Lumin. **80**, 65 (1998).
13. D. N. Goryachev, G. Polisskiĭ, and O. M. Sreseli, Fiz. Tekh. Poluprovodn. (St. Petersburg) **32**, 1016 (1998) [Semiconductors **32**, 910 (1998)]; L. V. Belyakov, T. L. Makarova, V. I. Sakharov, *et al.*, Fiz. Tekh. Poluprovodn. (St. Petersburg) **32**, 1122 (1998) [Semiconductors **32**, 1003 (1998)].

Translated by D. Mashovets

Semiconductors, Vol. 38, No. 4, 2004, pp. 468–471. From Fizika i Tekhnika Poluprovodnikov, Vol. 38, No. 4, 2004, pp. 486–489.

AMORPHOUS, VITREOUS, AND POROUS SEMICONDUCTORS

A Small-Molecule Organic Semiconductor[1]

F. Yakuphanoglu*, M. Aydin, N. Arsu**, and M. Sekerci*****

**Firat University, Faculty of Arts and Sciences, Department of Physics, 23119 Elazig, Turkey*

***Yildiz Technical University, Faculty of Arts and Sciences, Department of Chemistry, 34210 Davutpaşa–Istanbul, Turkey*

****Firat University, Faculty of Arts and Sciences, Department of Chemistry, 23119 Elazig, Turkey*

Submitted August 7, 2003; accepted for publication September 16, 2003

Abstract—The electrical conductivity and optical properties of *bis*-diethylaminokumarin have been investigated. The electrical conductivity of the compound exhibited three-dimensional hopping conduction in the temperature range 295–321 K. The compound shows a typical semiconductor property, and its semiconducting property results from delocalization of the π-electrons in the structure. To determine the optical band gap of the compound, an optical absorption study was made in the wavelength range 250–600 nm. The optical study revealed that the optical transition is the allowed indirect one. The electronic parameters, such as the electrical conductivity at room temperature σ_{25}, activation energy E, and optical band gap E_g of the compound are 1.46×10^{-5} S/cm, 0.42 eV, and 2.46 eV, respectively. These values are in agreement with electronic parameters of organic semiconductors. © *2004 MAIK "Nauka/Interperiodica".*

1. INTRODUCTION

Organic semiconducting materials are grouped as polymer, monomer, and organic compounds. The current revival of interest in their electronic properties is reflected by the considerable increase in the number of investigations dealing with the measurement of electrical conductivity, and they are of great interest in electronic devices and have multiple advantages because of the variety of structures. Their electrical transport properties are of current interest, and they give different aspects of the conduction mechanism, the nature of charge carriers, and their properties [1]. In the literature, the electrical properties of many semiconducting organic compounds are reported [1]. Intensive research activities on organic semiconducting materials have led to insights into their chemical and physical properties. The potential usefulness of semiconducting materials has been explored in many fields such as electronic switches, batteries, light emitting diodes, and Schottky diodes [2, 3]. They have attracted considerable attention, since the investigation of these systems has generated entirely new scientific conceptions and a potential for its future application in molecular electronics. They contain an extended π-electron system, and this system can be changed from a semiconducting state to a conducting state [4].

Organic semiconductors are used extensively in the fabrication of active and passive solid-state devices. In this connection, we synthesized *bis*-diethylaminokumarin to create a semiconductor material and investigate its electrical and optical properties.

2. EXPERIMENTAL

Bis-diethylaminokumarin was synthesized according to the literature [5]. The chemical structure of the investigated compound is given in Fig. 1. The powders were compacted at pressures on the order of 10^4 kg/cm^2. Figure 2 shows the diagram of the electrical conduction measurement system. The conductivity measurements were performed on compacted powders [5, 6] using a Keithley 2000 $6^{1/2}$ digital multimeter. To determine the optical properties of the compound, the UV spectra were recorded at room temperature with a Philips PU 8700 UV-Vis spectrophotometer.

3. RESULTS AND DISCUSSION

3.1. DC Conductivity

The temperature dependence of the conductivity is shown in Fig. 3. With temperature, the conductivity of the compound substantially increases up to 321 K (region I) and, afterwards, the conductivity is decreased (region II). The linear portion of the graph (region I) is fitted to an Arrhenius-type equation [6],

$$\sigma = \sigma_0 \exp(-E/kT), \quad (1)$$

where σ_0 is a constant and E is the activation energy. The electronic parameters σ_0 and E were calculated and are given in Table 1. In region I, the conductivity increases with increasing temperature due to delocalized π-electrons.

The exponential band tail in the compound, as observed by us from UV absorption spectra of the com-

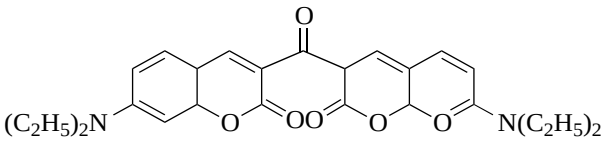

Fig. 1. The chemical structure of the compound.

[1]This article was submitted by the authors in English.

pound, indicated that there are localized states, which lead to variable hopping conduction (VRH). Thus, the conduction mechanism for the first region can be expressed by the following equations [7]:

$$\sigma(T) = \sigma_1 \exp\left[-\left(\frac{T_0}{T}\right)^{1/4}\right]. \quad (2)$$

This behavior is referred to as variable-range hopping conduction by Mott. We have applied the VRH model to investigate the conduction mechanism of this compound. For this purpose, we fitted our conductivity data to Eq. (2) using a least-squares fit procedure, so that the best fit values of electronic parameters may be obtained. The $\ln\sigma$ vs. $T^{1/4}$ was plotted and is shown in Fig. 4. In Eq. (2), T_0 can be expressed by the following relation [7]:

$$T_0 = \frac{16}{N(E_F)kL_{loc}^3} \quad (3)$$

and

$$R = \left[\frac{9L_{loc}}{8\pi kTN(E_T)}\right]^{1/4}, \quad (4)$$

where L_{loc} is the localization length, $N(E_F)$ is the density of states at the Fermi level, and R is the hopping distance. Assuming $L_{loc} = 10^{-7}$ cm [7], we calculated the electronic parameters of the compound using these relations and data given in Table 2. It is found that this compound exhibits three-dimensional hopping conduction in the temperature range 295–321 K. In this conduction mechanism, when the temperature is low enough, so that carriers cannot be excited into one of the allowed bands, the dominant conduction takes place via hopping conduction of the charge carriers in the localized states near the Fermi level [7].

As seen in Fig. 3, in region II, a deviation from the Arrhenius equation (1) appears within the temperature range $T > 321$ K; the conductivity decreases with temperature. The thermal variation of $\sigma(T)$ can be attributed to the saturation of the electronic concentration growth, which is typical for semiconductors when all carriers are released from the localization centers to the conduction band. A subsequent decrease of the conductivity, again similarly to semiconductor behavior, can result from the decrease of the carrier mobility caused by the scattering on the lattice vibrations.

This discussion shows that the compound is a semiconductor and has semiconducting properties in the temperature region under consideration. This type of conduction agrees with those of the usual organic compounds.

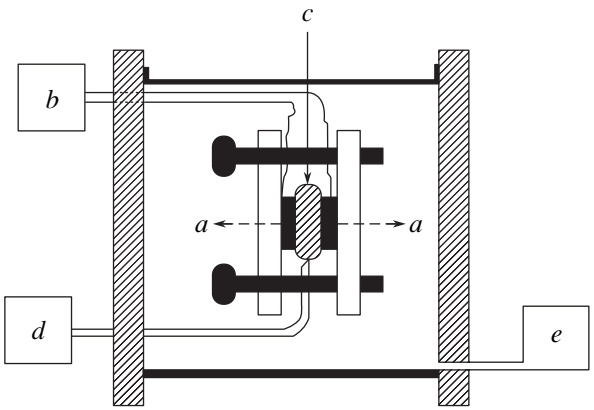

a: electrodes
b: digital multimeter
c: sample
d: thermocouple controller
e: heating and cooling system

Fig. 2. The experimental setup for electrical conductivity measurements.

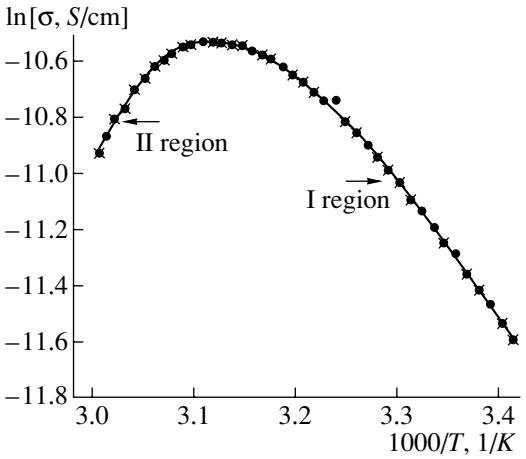

Fig. 3. The electrical conductivity of the compound.

The conductivity of the compound could be attributed to thermal excitations of the carbon–oxygen bonds in the structure. The lone pair of electrons on the oxygen atom with the σ-bond in the structure makes the delocalization of the π-electrons possible, as shown in Fig. 5.

It is well known that the electronic transport properties of organic semiconductors depend on their chemi-

Table 1. The electronic parameters of the compound

E (eV)	σ_{25} (S/cm)	σ_0 (S/cm)	λ_{max} (nm)	E_g (eV)	E_0 (eV)	Concentration n, mol/l	Molar absorption coefficient ε, l/(mol cm)
0.42	1.46×10^{-5}	145.77	459	2.46	46.4	1.2755×10^{-5}	860001

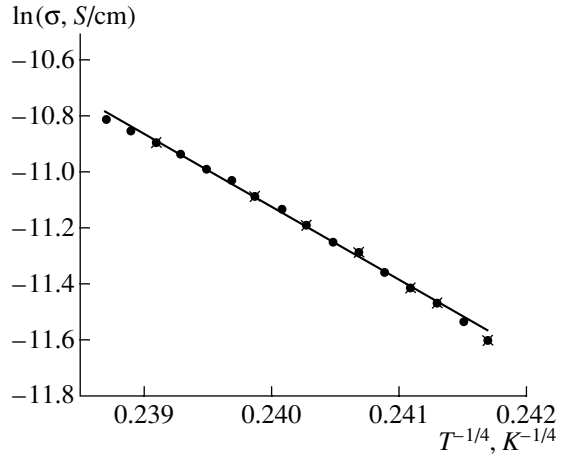

Fig. 4. The three-dimensional hopping conduction of the compound.

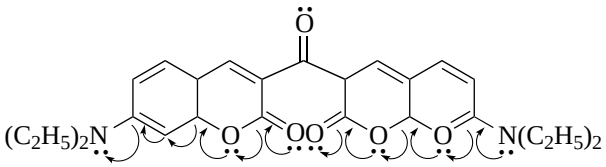

Fig. 5. The possible delocalization of π-electrons in the structure of the compound.

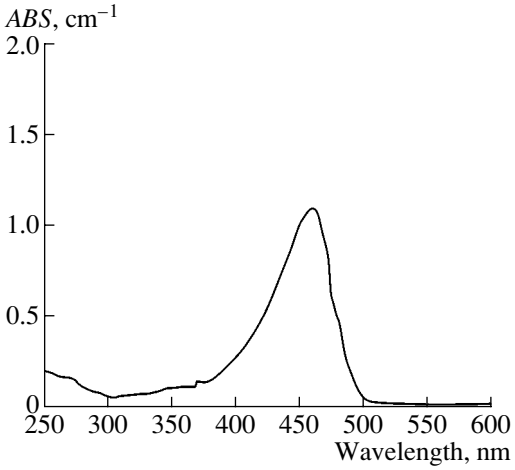

Fig. 6. UV spectrum of *bis*-diethylaminokumarin.

cal structure [4]. It is seen from the chemical structure of the compound that there are many π-electrons in the structure due to the aromatic groups. In such a structure, large numbers of electrons cause a decrease of the excitation energy of the π-electrons. The π-electrons also create a decrease in the system's internal energy and apparently allow electrons to participate in conduction. The increase of the conductivity in region I at $T <$ 321 K (see Fig. 4) can be associated with the number of π-electrons in the compound.

Table 2. The hopping conduction parameters of the compound

T_0 (K)	$N(E_F)$ (m^{-3} eV^{-1})	R (m)
4.74×10^9	4.66×10^{22}	2.33×10^{-8}

As a result, the conduction may be explained according to the chemical structure of the compound: it is seen from Fig. 1 that, in the structure, benzene rings are available which have many π-electrons. The π-electrons are mobile in the structure, and, thus, conduction results from the transfer of π-electrons. The electronic excitation of the benzene rings followed by transfer of an electron to another molecule is considered to be an important step of the conduction process. The studied compound possesses π-electrons extending along the structure; its electron states are delocalized, allowing the electronic transport to be described in terms of hopping conduction.

3.2. Optical Properties

The UV spectrum of the *bis*-diethylaminokumarin was recorded in the wavelength range of 250–600 nm and is given in Fig. 6. Some parameters related to the spectrum are given in Table 1. The nature of the optically induced transitions can be determined from the UV spectrum. The relation between the absorption coefficient α and optical band gap E_g is given by the following relation [8]:

$$\alpha h\nu = B(h\nu - E_g^{\text{opt}})^2, \quad (5)$$

where B is an energy-independent constant and E_g is the indirect optical band gap. The optical band gap of the compound was calculated by extrapolating the straight line portions of the $(\alpha h\nu)^{1/2}$ vs. $h\nu$ curve (Fig. 7) and is given in Table 1. The indirect forbidden gap determined by the optical method is larger than $2E$ obtained from the electrical conductivity measurements. Thus, it is evaluated that the electronic activation energy, ΔE, may correspond to any electronic level in the band gap of the compound.

The optical absorption coefficient near the fundamental absorption edge is found to be exponentially dependent on the incident photon energy and obeys the empirical Urbach rule [9]

$$\alpha = \alpha_0 \exp\left(\frac{h\nu}{E_0}\right), \quad (6)$$

where E_0 is the Urbach energy, and it can be evaluated as the width of the localized states [6]. The variation of $\ln\alpha$ vs. photon energy is given in Fig. 8. The value of E_0 was calculated from Fig. 8 and is given in Table 1. The exponential dependence of α on photon energy for the compound indicates that it obeys Urbach's energy equation. An electronic transition between localized states in the band edge tails is valid in this compound.

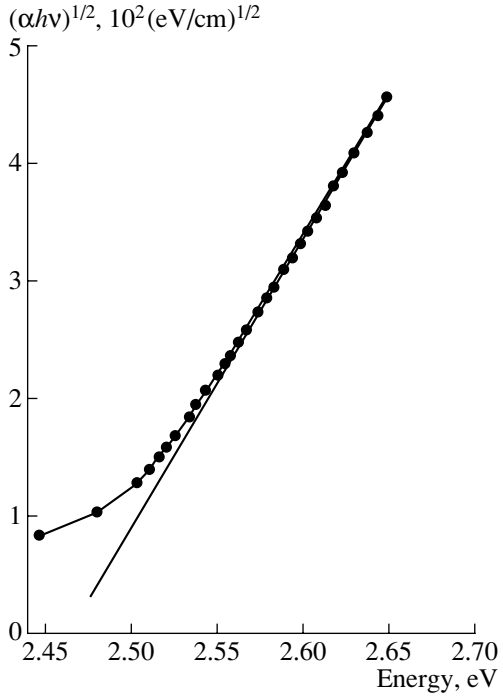

Fig. 7. Extrapolation to zero of the curve representing the function $(\alpha h\nu)^{1/2} = f(h\nu)$.

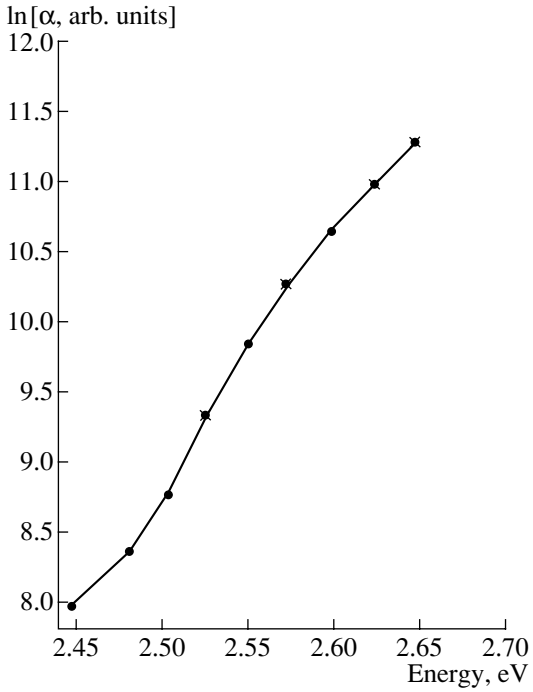

Fig. 8. Plot of $\ln\alpha$ vs. $h\nu$ of the compound.

The exponential dependence of the optical absorption coefficient with photon energy may arise from the electronic transitions between the localized states, which tail off in the band gap [10].

4. CONCLUSION

The electrical conductivity and optical properties of the *bis*-diethylaminokumarin have been investigated. It is found that the compound is a typical organic semiconductor with calculated electronic parameters.

REFERENCES

1. R. V. Rao, M. H. Shridhar, S. Ganesh, and K. C. Prashanth, Chem. Phys. Lett. **341**, 306 (2001).
2. G. D. Sharma, D. Saxena, and M. S. Roy, Synth. Met. **123**, 189 (2001).
3. *Extended Linear Chain Compounds*, Ed. by J. S. Miller (Plenum, New York, 1983), Vols. 1–3.
4. J. P. Farges, *Organic Conductors* (Marcel Dekker, New York, 1994).
5. D. P. Specht, P. A. Martic, and S. Farid, Tetrahedron **38**, 1203 (1982).
6. F. Yakuphanoglu, PhD Thesis (Firat Univ., Elazig, Turkey, 2002).
7. B. I. Shklovskiĭ and A. L. Éfros, *Electronic Properties of Doped Semiconductors* (Nauka, Moscow, 1979; Springer, Berlin, 1984).
8. H. Hasegawa, S. Yazaki, and T. Shimizu, Solid State Commun. **26**, 4070 (1978).
9. F. Urbach, Phys. Rev. **92**, 627 (1966).
10. E. Abd El-Wahabb, M. M. El-Samandouy, and M. Fadel, Appl. Surf. Sci. **174**, 106 (2001).

Semiconductors, Vol. 38, No. 4, 2004, pp. 472–479. Translated from Fizika i Tekhnika Poluprovodnikov, Vol. 38, No. 4, 2004, pp. 490–497.

PHYSICS OF SEMICONDUCTOR DEVICES

Characteristics of Nuclear Radiation Detectors Based on Semi-Insulating Gallium Arsenide

E. M. Verbitskaya*, V. K. Eremin*, A. M. Ivanov*, N. B. Strokan*, V. I. Vasil'ev*, V. N. Gavrin, E. P. Veretenkin**, Yu. P. Kozlova**, V. B. Kulikov***, A. V. Markov****, and A. Ya. Polyakov******

**Ioffe Physicotechnical Institute, Russian Academy of Sciences, ul. Politekhnicheskaya 26, St. Petersburg, 194021 Russia*
***Institute for Nuclear Research, Russian Academy of Sciences, pr. Shestidesyatiletiya Oktyabrya 7a, Moscow, 117312 Russia*
****State Unitary Enterprise NPP Pulsar, Okruzhnoĭ proezd 27, Moscow, 105187 Russia*
***** Institute for Chemical Problems in Microelectronics, B. Tolmachevskiĭ per. 5, Moscow, 109017 Russia*
Submitted July 21, 2003; accepted for publication July 22, 2003

Abstract—The characteristics of detectors based on bulk semi-insulating GaAs (*SI*-GaAs) have been studied by α particle detection and spectrometry. A distinctive feature of these detectors is the dependence of the width of the space charge region *W* on reverse bias voltage *U*. The rate of increase in *W*(*U*) is ~1 μm/V, which permits formation of a sensitive region a few millimeters thick. The main obstacle to applying kilovolt-range bias voltages *U* is the reverse current noise. The characteristics of diode structures in which a rectifying barrier to *SI*-GaAs was formed by metal deposition (Schottky diodes) and by growing heterostructures with heavily doped AlGaAs or GaAsSb epitaxial layers were compared. Nonequilibrium carrier transport in epitaxial structures capable of sustaining bias voltages above 1 kV was investigated in both weak (below 1 kV/cm) and strong (10–30 kV/cm) electric fields. In both cases, the carrier lifetimes were found to be about a few nanoseconds. Such low values are due to the high concentration of trapping centers (*EL*2-type native defects), which limits the carrier transport. An analysis of the spectral line shape revealed that the lifetime is almost constant throughout the detector volume. The charge introduced by a particle was found to be enhanced in fields of ~30 kV/cm. This effect can be qualitatively explained by focusing the electric field lines at the vertex of the α-particle track, which leads to an increase in the local field strength to ~10^{-5} V/cm and impact ionization by nonequilibrium electrons.

1. INTRODUCTION

GaAs detectors are traditionally employed in medicine (for X-ray and γ-radiation detection) and high-energy physics. In both cases, the signals to be detected are weak. Thus, the major problem is to attain the maximum possible sensitive volume while preserving a low noise. Recently, the possibility of using GaAs detectors in a new area—the measurement of solar neutrinos—was discussed [1]. The fact that interactions between neutrinos and Ga atoms are fairly rare make the problem of increasing the sensitive volume of the detector and, hence, the bias voltage applied to the latter even more acute.

As for the noise, its level is determined by the capacitance of the detector and its reverse current. These quantities should be made as little as possible by properly optimizing the parameters of the starting material and the technique employed in the fabrication of the detector structure (formation of the rectifying and back contact regions and optimization of the overall design of the structure).

The single crystals of semi-insulating gallium arsenide (*SI*-GaAs) used in this study had resistivity ρ ~ 10^8 Ω cm. The high resistivity is due to the high concentrations of *EL*2 native lattice defects (As_{Ga}) ($N_t \gtrsim 10^{15}$–10^{16} cm^{-3}) and residual impurities (primarily carbon). *EL*2 defects create deep double donor levels with energy E_c – 0.78 eV. The carbon impurity gives rise to shallow acceptor levels. Compensation brings the Fermi level of the material close to the midgap position.

Application of a reverse bias voltage to the detector may lead to an additional compensation of $EL2^+$ centers as a result of the sharp increase in the cross section of their capture of electrons in electric fields $F \gtrsim$ 10 kV/cm. The study of this mechanism [2] revealed a characteristic linear dependence of the width of the space charge region *W* on reverse voltage *U*, and the rate of its increase $\gamma \approx 1$ μm/V. The existence of a certain initial value $W_0 \approx 24$ μm was pointed out in [3]. Thus,

$$W = W_0 + \gamma U, \quad (1)$$

so that, for $W > W_0$, the electric field *F* is constant: $F = \gamma^{-1} \approx 10^4$ V/cm. At bias voltages $U \sim 1$ kV, the sensitive detector region should be about $W \sim 1$ mm thick, an acceptable value for testing the detectors in the above problems.

We compared here various types of detector structures, based on either Schottky barriers or epitaxial het-

erostructures, in order to find the optimum design for stationary and pulsed operation modes. Our studies included, along with the measurements of the *I–V* curves, the techniques based on pulsed excitation of nonequilibrium carriers by either a semiconductor laser operating at a wavelength of 840 nm, with subsequent observation of the transient current (with a time resolution of ~1 ns), or 5.79-MeV α particles, followed by pulse-height analysis of the resultant charge *Q*.

2. TYPES OF STRUCTURES BASED ON BULK *SI*-GAAS

The conventional detectors are Schottky diodes, with both the rectifying and back contacts formed by metal deposition. In a modified version, the back ohmic contact is formed by ion implantation. A comparatively new approach is based on the fabrication of a rectifying barrier (which impedes the arrival of carriers from the external circuit) by epitaxial growth [1].

2.1. Schottky Barriers

To reduce the surface leakage currents, a guard ring was etched around the central electrode in the Schottky barriers. The area of the structures was 4×4 mm^2. The ring width and the gap between the ring and the central electrode were varied. To ensure transparency of the back contact in the measurements of nonequilibrium carrier transport from the back side of the detector, the contact was made in the form of a metal grid. In essence, the Schottky barrier is a heterostructure. However, there are surface states at the metal–GaAs interface that are involved in carrier tunneling and excess recombination. Heterostructures with heavily doped epitaxial layers appear to be more promising for attaining low currents.

2.2. Heterostructures

In the detectors based on heterostructures, the latter contained heavily doped epitaxial layers of III–V ternary compounds (see inset in Fig. 1). Fabrication of the first-type detectors, p^+-GaAs–p^+-$Al_xGa_{1-x}As$–*SI*-GaAs–n^+-$Al_xGa_{1-x}As$–n^+-GaAs, was started by growing heavily doped layers of the $Al_xGa_{1-x}As$ alloy ($x \geq 0.3$) on both sides of an *SI*-GaAs substrate. The band gap width of the $Al_xGa_{1-x}As$ layers ($x \gtrsim 0.3$) was such that they were transparent for the laser radiation used in the measurements (840 nm). Next, heavily doped GaAs layers were formed to provide reliable ohmic contacts. The layers were grown by liquid epitaxy with an initial growth temperature of 650–750°C. The p^+-GaAs layer on the front side of the detector was etched away down to the p^+-$Al_xGa_{1-x}As$ layer, while the strip onto which metal was deposited was preserved. The entrance window area was 7.8 mm^2.

The other type of the heterostructures under study was as follows: p^+-$GaAs_xSb_{1-x}As$–*SI*-GaAs–n^+-GaAs

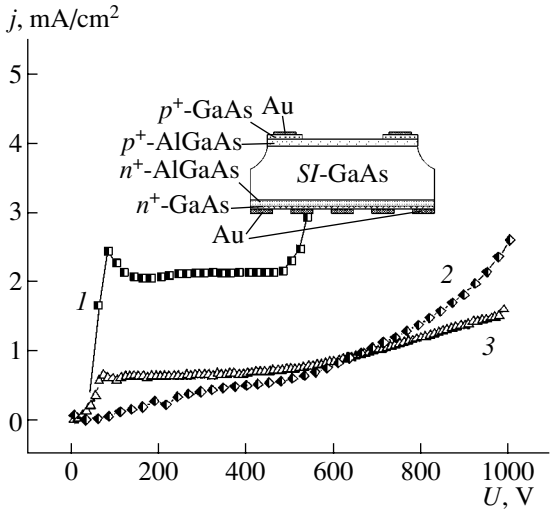

Fig. 1. Reverse *I–V* characteristic for three types of the structure studied: (*1*) Schottky barrier (specimen 553-1a1) and heterostructures with epitaxial (*2*) GaAsSb (Nu13-3d) and (*3*) AlGaAs (553-b4) layers; a schematic of the AlGaAs heterostructure is shown in the inset.

with $x \leq 0.03$. Two factors play a positive role here. The initial growth temperature decreases to 600–630°C, and the melt wets the substrate surface better. The latter circumstance is due to the absence of aluminum in the flux (it is well known that aluminum readily oxidizes, making the melt inhomogeneous, up to the formation of breaks in the layer). Only small-size structures of this type (~0.07 mm^2) can be fabricated presently.

A mesa was fabricated by properly etching the entire wafer with the grown epitaxial layers, which made it possible to prevent the formation of regions with high electric field strengths. The metal deposited on the back side of the structure likewise formed grids. The thickness of the *SI*-GaAs wafer was in both cases 400 μm; the thicknesses of the epitaxial layers were in the range 1.0–1.5 μm.

3. *I–V* CURVES

Figure 1 shows the dependences of the current density on reverse bias voltage, $j(U)$, for the structures under study. As can be seen from Fig. 1, the current through the Schottky barriers increases at $U \leqslant 100$ V to reach a plateau, after which the current rises steeply. The voltage at which the current begins to rise rapidly is about 500 V.

For the heterostructures, the voltages at which the current begins to rise rapidly lie in the range $U = 0.8$–1.0 kV, so that the detectors based on such structures operate at high voltages. Some specimens show a dependence $j(U)$ similar to those typical of Schottky barriers, with an increase in the current up to $U = 100$ V, followed by a plateau. In detectors of another type, the current increases without the aforementioned jump. However, in both cases, the current increases rather

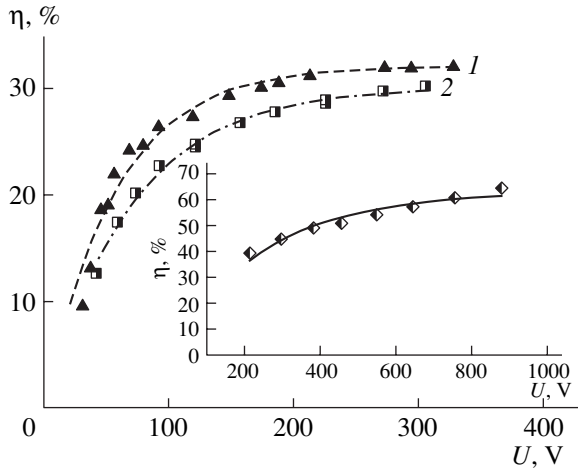

Fig. 2. Average signal in the pulse-height spectrum of α particles, normalized to the absorbed energy E_α = 5.70 MeV, as a function of reverse bias voltage. (*1*) Schottky barrier (specimen 553-1a1), (*2*) heterostructure with epitaxial AlGaAs layers (512-1b3). Inset: heterostructure with epitaxial GaAsSb layers (Nu13-3d). Symbols represent the experimental data and the lines show the results of calculation by Eq. (2) with P_1 and P_2 as fitting parameters (see text).

smoothly. Note also that, at $U < 500$ V, the current densities for the heterostructures turn out to be about four times lower than those for the Schottky barriers.

Another important factor is the high reproducibility of the current density in the heterostructures. Indeed, the value of j averaged over 11 specimens from two wafers with epitaxial AlGaAs layers was found to be (1.17 ± 0.33) μA/cm^2. In the case of structures with GaSbAs layers, the current density averaged over 26 specimens is $j = (1.69 \pm 0.28)$ μA/cm^2.

4. CHARACTERISTICS OF NONEQUILIBRIUM CARRIER TRANSPORT

Nonequilibrium carrier transport in detectors was studied by pulse-height analysis (α-particle spectrometry) and measurement of the transient current induced by pulsed laser radiation. The range of 5.79-MeV α particles in GaAs is 20 μm; according to the Bragg ionization curve, carriers are generated primarily at the end of the range. In contrast, the laser radiation is absorbed in a surface layer 2–3 μm thick. Application of the transient current technique to determination of the carrier transport characteristics was described in detail in [1] and is not considered here. We should only note that the parameters measured by this technique did not differ markedly from those obtained by the α-particle spectrometry.

When α particles are used to excite nonequilibrium carriers, reverse voltage (a few hundred volts) is commonly applied and a detector is irradiated from the p^+ contact side. Under these conditions, the electron transport in strong electric fields ($F \sim 10^4$ V/cm) is studied.

Because of the high resistivity of *SI*-GaAs, forward bias voltage (a few tens of volts) can be applied to the detector structures as well. With the detector connected in this way and the p^+ contact irradiated, the signal observed is due to the hole transport. Accordingly, when α particles bombard the back n^+ contact, it is electrons that drift through the specimen. In contrast to the case of reverse bias, nonequilibrium carriers drift in a weak field ($F \leqslant 10^3$ V/cm), distributed uniformly over the detector thickness.

4.1. Reverse Bias

When a reverse bias voltage is applied to a detector, the voltage dependence of the signal has the form [1, 4]

$$\eta = Q/Q_0 = (\mu F\tau/d)[1 - \exp(-\gamma^2 U/\mu\tau)] = (\mu F\tau/d)[1 - \exp(-W/\mu F\tau)]. \quad (2)$$

Here, Q_0 is the charge introduced by an α particle, d is the detector thickness, and μ and τ are, respectively, the mobility and lifetime of nonequilibrium carriers before their localization at trapping centers.

Equation (2) was derived on the assumption that nonequilibrium carriers can be lost only due to their capture by centers during the drift. Thus, possible recombination of the nonequilibrium carriers in the stage of "track plasma" is disregarded. The linear track dimensions, which are small in comparison with the detector thickness, are also disregarded; in other words, the generation is assumed to occur only in the immediate vicinity of the detector.

When an α particle penetrates the detector, the nonequilibrium electrons drift initially in the space charge region for a short time $W/\mu F$. However, when electrons enter the high-resistivity base, they slow down considerably on their way to the back electrode, because the base recovers its charge neutrality with the time of Maxwell relaxation. This time exceeds several tens of times the time required to process the signal. Therefore, according to Ramo's theorem [5], a charge ~W/d will appear at the detector electrodes in the absence of capture. Hence, Eq. (2) contains two factors, namely, the distance passed by a charge during the carrier lifetime, reduced to the detector thickness, and the probability for a charge to drift through the W region without being trapped.

Introducing two quantities, $P_1 = \mu F\tau/d$ and $P_2 = \gamma^2/\mu\tau$, as fitting parameters, one can properly approximate the experimental relations $\eta = Q/Q_0$ as a function of U (Fig. 2, electron transport). In this way, one determines the main detector characteristics: the lifetimes of nonequilibrium carriers before trapping, which govern the charge-collection efficiency, and γ, the propagation velocity of the field F (see the table). Unfortunately, in the case under consideration, the electron lifetimes were not sufficiently long ($\tau_r^e \sim 1$ns) to provide complete charge collection. The maximum values of η were

0.35. The only exception was specimen Nu13-3d (see the inset in Fig. 2), for which η was 0.65; this detector also exhibited some specific features in signal behavior at $F > 10^4$ V/cm (see below). The value of γ for all the specimens studied was found to be close to 1 μm/V, which is in agreement with the model [2].

Equation (2) also makes it possible to analyze the shape of the pulse-height spectrum and the detector energy resolution. The latter quantity characterizes the spectral-line spread and is defined as the full width at half maximum (FWHM) reduced to the average height (at the center of gravity of the spectral band). The pulse height spread originates physically from the spatial inhomogeneity of the carrier trapping time. As a result, the carrier drift gives rise to a spectrum of the values of τ. Its most likely shape is a Gaussian curve [1, 4], and, therefore, one can introduce an inhomogeneity factor R_τ as the ratio of the FWHM of the spectrum τ to the average value τ_{av}: $R_\tau = (\mathrm{FWHM}_\tau)/\tau_{av}$ (similar to the resolution in a pulse-height spectrum).

Interestingly, an increase in the detector bias voltage and the growth of the average signal amplitude leads to a broadening of the spectrum as well (Fig. 3, specimen 512-1c3). This finding is not consistent with the line narrowing as the charge losses decrease (a feature characteristic of spectrometric detectors). The increase in FWHM with the bias U is associated with the specific role of τ in the dependence of the signal amplitude on voltage, $Q(U)$. According to formula (2), as the volume of the drift region of nonequilibrium carriers, $W(U)$, increases, an ever increasing interval of values of Q falls within a fixed interval of τ. The spectrum width stabilizes as depletion is attained in the structure.

Characteristics of *SI*-GaAs and nonequilibrium-carrier transport in *SI*-GaAs-based detectors

Sample no.	ρ, MΩ cm	γ, μm/V	τ_r^e, ns	τ_f^e, ns	τ_f^h, ns
512-1b3	–	1.87	1.3	–	–
554-1c1	–	1.2	0.80	–	–
554-34c1	140	1.1	0.80	1.15	6.5
553-1a1	60	1.7	1.3	1.45	7.0
554-34a1	78	1.3	0.81	1.0	–
554-1e3	72	1.2	0.81	1.07	4.0

The calculated curve FWHM = $f(U)$ (Fig. 3) was plotted with the parameters $P_1 = 0.302$ and $P_2 = 0.014$ taken from Fig. 2. A satisfactory agreement with experiment was reached for $R_\tau = 0.2$. Thus, the value of the charge given by formula (2) allows one to determine the main characteristics of detectors: the values of η and carrier lifetime before trapping τ; the propagation velocity of electric field in the structure γ; and the nonuniformity factor of carrier transport through the detector volume R_τ.

4.2. Forward-Bias Mode

When a detector is forward-biased, the contacts do not limit the current, and all the voltage drops across the high-resistivity *SI*-GaAs layer of the structure. The signal amplitude depends linearly on the forward bias U_f (Fig. 4) as

$$Q/Q_0 = \mu F \tau / d. \quad (3)$$

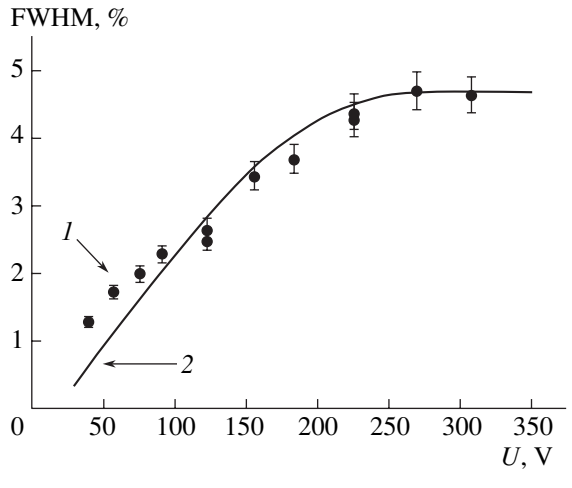

Fig. 3. Spectral width FWHM normalized to the average amplitude of the spectrum as a function of reverse bias voltage. Specimen with epitaxial AlGaAs layers (512-1b3). Points represent the experimental data and the line shows the results of calculation for the nonuniformity factor R_τ of the electron lifetime equal to 0.2.

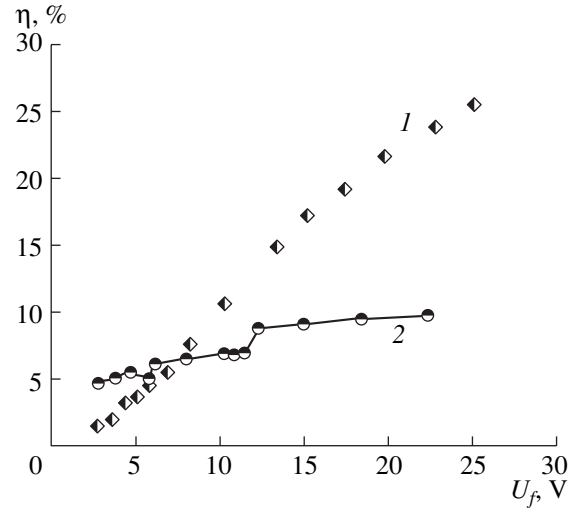

Fig. 4. Average signal in the pulse-height spectrum of α particles, normalized to the absorbed energy $E_\alpha = 5.70$ MeV, as a function of the forward bias voltage U_f. Specimen with a Schottky barrier (553-1a1). Transport of (*1*) electrons and (*2*) holes.

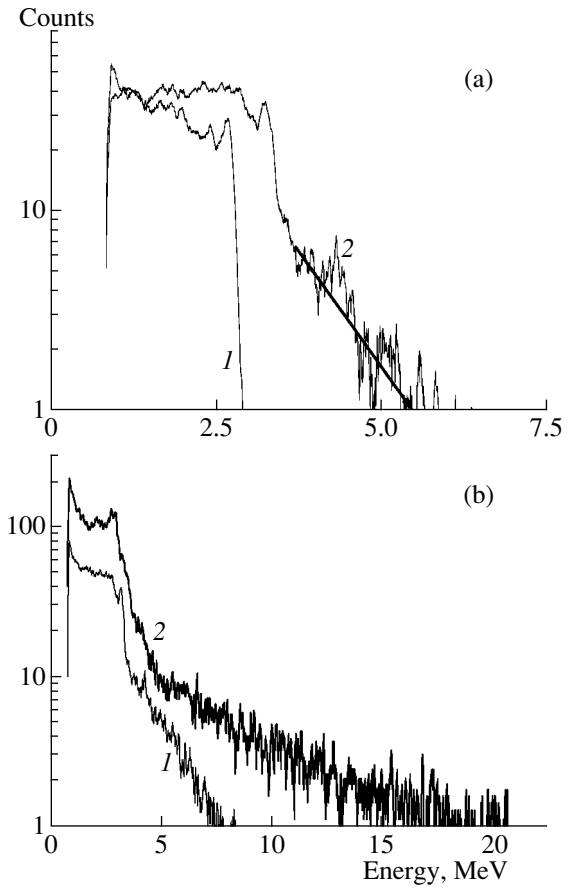

Fig. 5. Pulse-height spectra of a heterostructure-based detector with epitaxial GaAsSb layers (Nu13-3d) measured with variation of bias voltage in the range 0.5–1.25 kV. (a) α-particle energy is 4.4 MeV, U = (*1*) 0.5 and (*2*) 1.0 keV. (b) Spectrum of α particles with an energy of 4.4 MeV also contains a weak line at 5.8 MeV; U = (*1*) 1.0 and (*2*) 1.2 keV.

As already mentioned, $F \leqslant 1$ kV/cm in practice. Assuming the electron and hole mobilities in weak fields to be 7000 and 400 cm^2/V, respectively, we obtained the values of the lifetimes of electrons, τ_f^e, and holes, τ_f^h (see table). For electrons, these values are 20–30% higher than those measured under reverse bias, which should apparently be attributed to the difference in the filling of nonequilibrium-carrier-trapping centers. For the holes, the lifetimes were found to be slightly longer (4–7 ns), which is due to the dominant role of $EL2^+$ electron traps.

5. EFFECT OF A STRONG ELECTRIC FIELD ($F > 10^4$ V/cm)

The fields F used in the above α-particle detection measurements did not exceed 10 kV/cm. However, it is of interest to study the carrier transport in higher fields by making use of the advantage inherent in the α-particle detection technique, specifically, the introduction of a precisely calibrated charge into a detector.

Nonequilibrium-carrier transport in fields $F >$ 10 kV/cm was studied for the second-type heterostructures p^+-GaAs$_x$Sb$_{1-x}$–*SI*-GaAs–n^+-GaAs because, as was mentioned above, p^+-GaAsSb layers are more homogeneous, while the diodes based of these heterostructures are smaller in size. The latter circumstance allows one to reduce the detector noise.

Indeed, the structures used to record the spectra of α particles could withstand voltages of up to U = 1.25 kV (which corresponded to F = 30 kV/cm) without the appearance of excess noise. The pulse-height spectra of ^{244}Cm α particles were measured for two energies: E_α = 5.79 and 4.40 MeV. The first value is the decay energy. The second one was obtained by slowing α particles in air. Note that the exposure times in spectral measurements were chosen to be equal.

The use of small-area mesas allows one to obtain high fields F (which is actually our target goal). At the same time, the small area of mesas complicates isolation of the lines with the above energies in the spectrum. The reason is that the conditions of transport of the nonequilibrium charge produced by α particles striking different areas of the structure surface are substantially different. As a result, instead of a characteristic single line, a set of amplitudes with a distribution close to equiprobable was observed in the spectrum of detector signals (Fig. 5), which is in qualitative agreement with the geometrical layout used.

The spectrum in Fig. 5a exhibits a transformation with increasing U, with three main effects pronounced. First, the right-hand (sharp) edge shifts to higher energies, which indicates an improvement in the carrier transport conditions. However, the carrier transport through the sensitive volume remains incomplete within the voltage range employed ($U \leqslant 1.0$ kV), so that the limiting position of the right-hand edge of the spectrum at 3.3 MeV does not attain the energy introduced by α particles into the detector (4.4 MeV). As can be seen from the inset in Fig. 2, η remains equal to 0.75. Second, in addition to the reasonable behavior of the sharp edge of the spectra, the total number of counts increases (at a fixed exposure time). Finally, starting from U = 0.7 kV, counts arise with energies exceeding that introduced by α particles. This part of the spectrum represents an exponentially decaying extended tail (see Fig. 5a, spectrum *2*).

To study this group of counts, we smoothed the corresponding spectral region and extrapolated the number of counts N in a channel to N = 1. For U = 1 kV, this procedure yields the value of boundary energy E_b = 5.48 MeV, which exceeds the energy absorbed in the detector, E_α = 4.40 MeV, by a factor of 5.48/4.40 = 1.24.

It is significant that this tail is more pronounced for higher α-particle energies. For instance, the addition of the weak 5.79-MeV α line to spectrum *2* in Fig. 5a (for the same U = 1 kV) had almost no effect on the shape of the main part of the spectrum but, at the same time,

increased significantly the number of counts to the right of the sharp drop (see Fig. 5b, spectrum *1*). The boundary energy is now 7.8 MeV, which exceeds the α-particle energy 5.79 MeV by a factor of 1.35.

An increase in the bias voltage to 1.25 kV shifts E_b to 17.5 MeV (see Fig. 5b, spectrum *2*), with the average energy in the triangular tail of the spectrum becoming 5.85 MeV, which is nearly the same as the α-particle energy 5.79 MeV. This observation suggests signal amplification, and the question naturally arises as to the mechanism of this effect.

It appears important to establish whether the effect under study is a manifestation of nonequilibrium carrier generation. Recall that, in the case of α particles, the generation is intermittent, and the initial carrier density in the track is about 10^{16} cm^{-3}. The geometry of the track, whose spread is due to nonequilibrium-carrier drift and diffusion, can be represented at the initial moment as a hemi-ellipsoid and, then, as a hemisphere ~20 μm in radius. Diametrically opposite conditions can be realized by steady-state exposure to light that is strongly absorbed by the material. In this case, carriers will be generated with equal probability over the surface of the specimen.

To study the role of the conditions of nonequilibrium-carrier generation, the structure was illuminated by a In:GaN light-emitting diode. Most of the photons had a wavelength of 0.46 μm, so that carriers were generated primarily in a surface region thinner than 1 μm. The photocurrents were a few tens of nA, i.e., substantially in excess of the dark current, which was less than 2 nA at the maximum bias U = 1.25 kV. Figure 6 shows the dependence of the photocurrent I_{ph} on reverse bias voltage U. One can clearly see two linear regions. The rate of current rise within the second region (at higher U) is higher by a factor of 1.5 compared to the first region. It is worth noting that the transition from the first to the second region occurs at $U \approx 0.7$ kV—the value at which amplitudes $E_b > E_\alpha$ appear in the α-particle spectra.

Within the interval U = 1.0–1.25 kV, the current increases by 32%. This rise, despite the differences in the conditions of carrier generation mentioned above, is similar to the increase in the average energy (27%) for the triangular tail in the spectrum in Fig. 5b. However, the boundary energy of the spectrum E_b increases much faster (by 54%).

This fact suggests that some α tracks are characterized by conditions that are particularly favorable for signal amplification. In other words, the specific features of the locality of carrier generation manifest themselves in this case. Note also that, in the bias-voltage range 1.0–1.25-kV, the photocurrent does not exhibit a superlinear rise—a feature characteristic, for instance, of the effect of carrier multiplication by "uniform" impact ionization.

The attendant noise is more sensitive to the manifestation of impact ionization. The noise was studied by the technique developed in [6, 7]. This technique consists essentially in analyzing the behavior of the diode noise as a function of a photocurrent at several fixed values of U. The pulse-height analyzers were used as before, and the magnitude of the noise was found from the broadening of the line of the precision-amplitude generator. According to the analysis performed in [7], the linear dependence $(\mathrm{FWHM}_g)^2 = f(I)$, where FWHM_g is the width of the line of a precision-amplitude generator at half maximum, indicates the shot noise. The appearance of nonlinearity in this dependence is indicative of the occurrence of flicker noise.

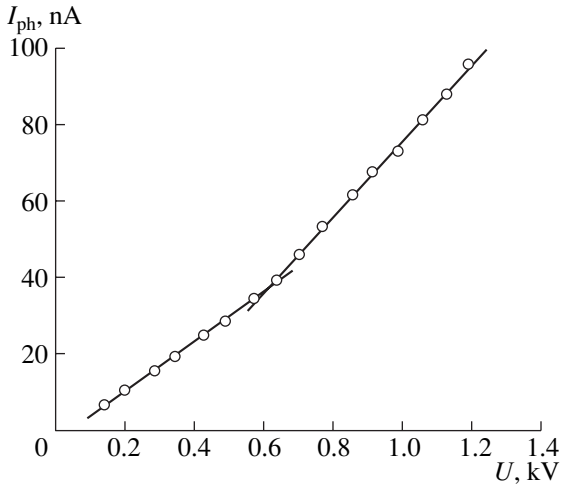

Fig. 6. Photocurrent as a function of the reverse bias under illumination with a In:GaN light-emitting diode. The voltage $U \approx 0.7$ kV, at which current begins to rise faster, correlates with the appearance of anomalously high energies in the α-particle spectra.

Figure 7 shows the dependence of the noise on the total current $I = I_d + I_{ph}$ (I_d and I_{ph} are the dark current and photocurrent, respectively), obtained for bias voltages in the range U = 0.55–1.20 kV. A linear dependence $(\mathrm{FWHM}_g)^2 = f(I)$ is observed only at the initial bias U = 0.55 kV (Fig. 7, curve *1*). Starting from U = 0.75 kV, the dependences exhibit pronounced nonlinearity (curves *2*–*4*). It is significant that, at higher voltages, the dependences of the noise on current coincided; i.e., the noise saturated with a further increase in U (Fig. 7, curves *3*, *4*, inset). This circumstance suggests that no noise characteristic of impact ionization was observed in the illumination mode. The observed increase in the noise in the interval U = 0.75–1.20 kV, compared to that at U = 0.55 kV, is most likely associated with the appearance of flicker noise due to the propagation of the electric field to the side area of the mesa.

As was mentioned above, the results discussed in this section refer to the effect of steady-state carrier excitation with equal probability over the surface area. Therefore, in the case of α particles, the appearance of signals corresponding to energies higher than E_α (see Fig. 5) should be attributed to the specific features of carrier generation by short-range ions. It was noted pre-

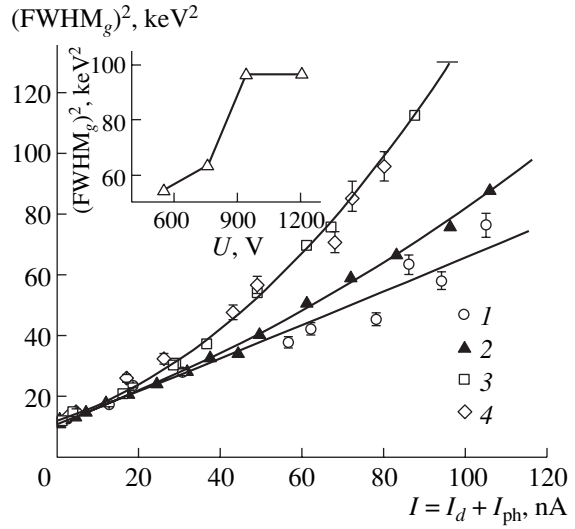

Fig. 7. Noise as a function of current measured with variation in the bias voltage on a detector: U = (*1*) 0.55, (*2*) 0.76, (*3*) 0.94, and (*4*) 1.2 keV. Inset shows the dependence of noise on bias voltage for a current of 80 nA.

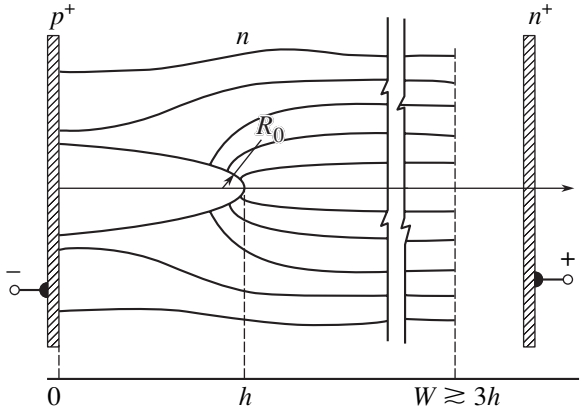

Fig. 8. Electric field configuration in a *p*–*n* junction in the presence of a high-density track of electron–hole pairs produced by a short-range ion (cf. [8], Fig. 1). W is the boundary of the space-charge region and R_0 and h are the parameters of an ellipsoid modeling the track geometry.

viously [8] that the introduction of a dense track of electron–hole pairs into a region of strong electric field leads to characteristic changes in the field configuration. The field lines become focused at the vertex of the track and, accordingly, the field strength near the vertex increases (see Fig. 8).

The focusing effect is dynamic in nature and weakens as the track spreads due to the diffusion and drift. However, in the initial stage of the carrier spread from the track, the increase in F is significant. Indeed, the calculations in [8] show that the average value of F within the 1-μm-wide region around the track vertex exceeds the steady-state value fivefold. In the case under consideration, this corresponds to F = 150 kV/cm.

Note that a spectrometric detector was used in [8], which made it possible to observe directly the single line at E_α and peaks with larger amplitudes in the spectra. Even under the conditions when peaks with $E > E_\alpha$ were distinctly seen against the E_α line, we could obtain only qualitative agreement of the results of calculations with experiment. This may be explained by the fact that the calculations did not take into account the additional field screening by the charge of the electrons emerging from the track region. This screening results in an increase in the effective track radius R_{eff}. For instance, in field-emission microscopes, this effect increases the value of R_{eff} to $7R_0$ (R_0 is the cathode-tip radius) [9]. In the case under consideration (nonspectrometric structure, incomplete charge collection in the detector), any attempt to quantitatively interpret the data on the increase in the measurable energy would be all the more incorrect. Nevertheless, the above comparative observations of the response of the structure to a steady-state weak excitation by light revealed important qualitative features: the absence of nonlinearity in the dependence of the signal amplitude on bias voltage and the saturation of excess noise. The latter phenomenon suggests that the nature of signals at energies in excess of the starting energy can be interpreted in terms of the mechanism of local impact ionization in fields amplified by dynamic focusing at the vertex of the track of an ionizing particle.

6. CONCLUSION

We studied the characteristics of the detectors of short-range strongly ionizing particles, based on semi-insulating GaAs, using the detection and spectrometry of α particles as an example. The diode structures of the detectors were fabricated with contacts in the form of Schottky barriers or heterostructures with epitaxially grown heavily doped layers.

In the case of Schottky barriers, operating bias voltages up to $U \approx 0.5$ kV were attained with electric fields $F \approx 10$ kV/cm. Mesa heterostructures retain a low noise level up to $U \approx 1.25$ kV ($F \approx 30$ kV/cm).

Transport of nonequilibrium carriers in strong ($F \approx$ 10 kV/cm) and weak ($F \approx 1$ kV/cm) fields was studied. The electron lifetimes were measured to be ~1.0 and 1.2 ns for the Schottky diodes and heterostructures, respectively. The difference in the electron lifetimes can be explained by the differences in the filling of trapping centers. The comparatively short lifetimes are due to the high concentration of impurities and lattice defects (of the *EL*2 type) in GaAs.

It was found that, in high fields ($F \approx 30$ kV/cm), the charge introduced by a particle is amplified. The amplification is related to the specific features in the geometry of the α-particle track, when the field lines are dynamically focused at the track vertex. A local increase in the field strength up to $F \approx 10^5$ V/cm initiates impact ionization of nonequilibrium carriers.

ACKNOWLEDGMENTS

This study was supported by the basic research program of the Russian Academy of Sciences "Neutrino Physics," the Russian Foundation for Basic Research (project no. 03-02-16837), and in part by the program of the President of the Russian Federation on the Support of Leading Scientific Schools (project NSh-2223.2003.02).

REFERENCES

1. E. Verbitskaya, V. Eremin, A. Ivanov, *et al.*, Nucl. Instrum. Methods Phys. Res. A **439**, 634 (2000).
2. D. S. McGregor, R. A. Rojeski, G. F. Knoll, *et al.*, Nucl. Instrum. Methods Phys. Res. A **343**, 527 (1994).
3. A. Castaldini, A. Cavallini, L. Polenta, *et al.*, Nucl. Instrum. Methods Phys. Res. A **410**, 79 (1998).
4. N. B. Strokan, Zh. Tekh. Fiz. **69** (5), 139 (1999) [Tech. Phys. **44**, 606 (1999)].
5. S. Ramo, Proc. IRE **27**, 584 (1939).
6. A. M. Ivanov and N. B. Strokan, Zh. Tekh. Fiz. **70** (2), 139 (2000) [Tech. Phys. **45**, 281 (2000)].
7. M. E. Boĭko, V. K. Eremin, A. M. Ivanov, *et al.*, Prib. Tekh. Éksp., No. 2, 1 (2000).
8. E. M. Verbitskaya, V. K. Eremin, Kh. Kh. Ismailov, *et al.*, Fiz. Tekh. Poluprovodn. (Leningrad) **21**, 1388 (1987) [Sov. Phys. Semicond. **21**, 845 (1987)].
9. L. Brodie and J. Muray, *The Physics of Microfabrication* (Plenum, New York, 1982; Mir, Moscow, 1985).

Translated by G. Skrebtsov

Semiconductors, Vol. 38, No. 4, 2004, pp. 480–485. Translated from Fizika i Tekhnika Poluprovodnikov, Vol. 38, No. 4, 2004, pp. 498–503.

PHYSICS OF SEMICONDUCTOR DEVICES

Investigation of Characteristics of InSb-Based Photodiode Linear Arrays

P. V. Biryulin*^, V. I. Turinov*, and E. B. Yakimov**

**NPO Istok, Fryazino, 141190 Russia*

^e-mail: birulin@sl.ru

***Institute of Microelectronic Technology and High-Purity Materials, Russian Academy of Sciences, Chernogolovka, Moscow oblast, 142432 Russia*

e-mail: yakimov@ipmt-hpm.ac.ru

Submitted March 18, 2003; accepted for publication August 20, 2003

Abstract—Electrical characteristics of eight-element InSb-based photodiode arrays were investigated at T = 78–145 K. The mutual-coupling coefficients of neighboring *p–n* junctions were no larger than 4.3%. The surface of Zn-implanted *p–n* junctions was investigated using a scanning microscope in a secondary-electron mode and by the electron-beam induced current method. The defects of the surface under the ZnS film, as well as local inhomogeneities of the current through the *p–n* junctions, were revealed. © *2004 MAIK "Nauka/Interperiodica".*

The nature of currents in experimental InSb-based *p–n* junctions obtained by various methods has been investigated in many studies [1, 2]. Therefore, here we consider only the interpretation of measurements of current–voltage (*I–V*) characteristics of *p–n* junctions in a photodiode array with the aim of determining the magnitude of the minimal mutual electrical coupling coefficient of neighboring *p–n* junctions with the preservation of their high sensitivity.

The electrical characteristics of InSb-based photodiode arrays with eight elements 80 × 100 μm in area, which were designed for operation at temperatures above 77 K, were investigated in a specially developed microcryostat for a specific application. For some *p–n* junctions, we observed the anomalies of the differential resistance R_d in a form of an additional peak in the *I–V* characteristic (Fig. 1) at T = 78 K and low bias voltages $U \approx 0 \pm k_0T/q$. Here, k_0 is the Boltzmann constant; q is the elementary charge; and T is the temperature in K. This observation also motivated us to carry out a more detailed investigation of the characteristics of linear arrays and technology processes of their fabrication; the results are reported in this paper.

The starting *n*-InSb of the brand ISÉ-1V had a carrier concentration of n(78 K) = (1–3) × 10^{14} cm^{-3} and a Hall mobility of μ_H(78 K) = (4–9) × 10^5 $cm^2/(V\ s)$. The linear arrays with *p–n* junctions were fabricated by the implantation of 120-keV Zn^{++} ions and a dose of 20 μC/cm^2. A ZnS film ~0.5 μm thick was used as a mask and to passivate the surface. We also experimented with doping ISÉ-1V wafers with 60-keV B^+ ions through a passivating ZnS film ~0.05 μm thick to slow down the ions, i.e., to reduce the degree of surface damage by ions. For such ion energies, according to the data in [3], the mean ion range in InSb with an unprotected surface, for example, for Zn ions, is $L_i \approx 220$ Å for E = 40 keV. The thickness of doped layers d_0 considerably exceeds L_i and depends on the doping level of the starting material and on the temperature of the subsequent annealing T_a. For example, annealing of Zn^+-doped *p*-InSb with $p = 10^{14}$ cm^{-3} at T_a = 400°C for 15 min yields d_0 = 0.7–12 μm [4]. However, the technology of doping with B^+ through a ZnS film turns out to be less reliable with respect to the recovery of the specific differential resistance of the *p–n* junction R_0A for U = 0 V (A is the area of the *p–n* junction) and the uniformity of photoelectric parameters of linear arrays. Therefore, the implantation of Zn^{++} was used to fabricate these arrays. The investigations of the Zn^{++} doping in relation to the ion dose in the range from 3×10^{12} to 6.2×10^{14} cm^{-2} showed that no *p–n* junctions were formed for a dose lower than 3×10^{12} cm^{-2}. For doses higher than 6.2×10^{14} cm^{-2}, the surface was severely damaged by ions up to its amorphization, which confirmed the data of Korshunov [5]. The damaged surface layer traps the dopant [1] and prevents its spreading during heat treatment; as a result, the doping profile remains unchanged and corresponds to the ion range. Precision etching removed both the ion-damaged layer and the dopant itself, and it was impossible to restore R_0A. For the doses mentioned, the doping level affected R_0A only slightly; therefore, a dose of 9×10^{12} cm^{-2} (30 μC/cm^2), which exceeded the lower limit of doping by a factor of 3, was used in the technology. No effect of the ion energy in the range E = 60–120 keV on R_0A

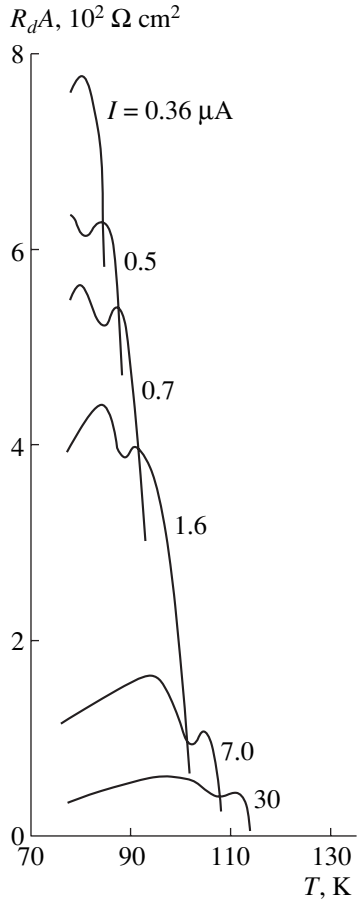

Fig. 1. Temperature dependence of R_dA for an InSb-based p–n junction with an anomaly in R_dA at $U = \pm k_0T/q$ for various reverse currents.

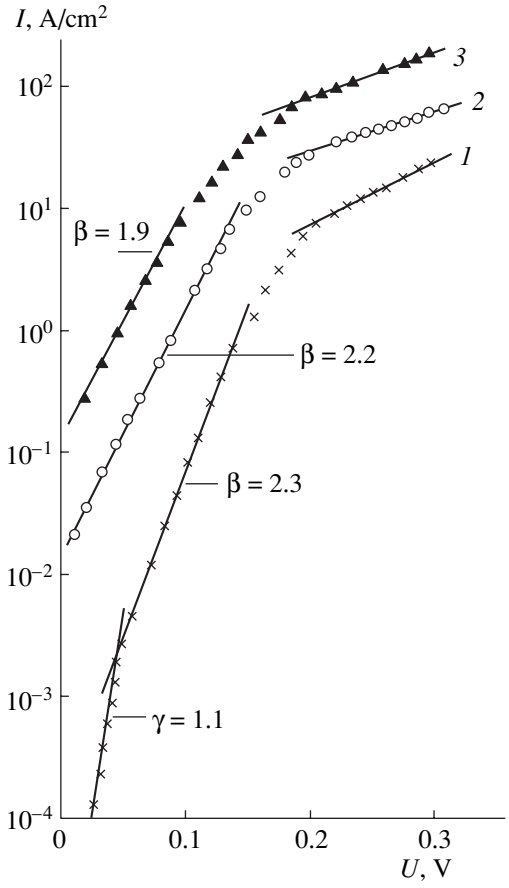

Fig. 2. Current–voltage characteristics of InSb-based p–n junctions for forward biases at temperatures T = (*1*) 78, (*2*) 115, and (*3*) 145 K. See the text for explanations.

was observed, since the annealing of radiation defects and subsequent precision etching masked the effect of the initial distribution profile of the dopant on the parameters of photodiodes in our technology.

During annealing of the damage in the range $T \approx$ 360–380°C, along with the healing of defects, thermal conversion of n-type to p-type conductivity occurs in starting n-InSb wafers. This process starts at the surface and extends into the semiconductor bulk. As a result, the inversion layer is formed over the entire surface of the semiconductor wafer [1]. This layer operates as the leakage channel, and R_d of the p–n junctions decreases. Therefore, we searched for a precision method of removing a thermal-conversion p-layer. The anodic oxidation of the surface of the n-InSb wafers in a 0.1 N NaOH solution in ethylene glycol was tested. The thermal-conversion p-layer was initially transformed into oxide, which was removed by etching in HCl or HF. We also used chemical etching in the CP-4A + H_2O (1 : 5) solution and, finally, etching in a 1% solution Br + methanol. The latter method yielded the most acceptable and reproducible results with respect to the recovery of R_d.

Figure 2 shows the forward portions of the I–V characteristics of InSb-based photodiode structures measured at three temperatures. Three current mechanisms were observed for the p–n junctions in the range of forward biases investigated at 78 K. For $U < 7k_0T/q$, the I–V characteristic had the form $I = I_d\exp(qU/\gamma k_0T)$, where $\gamma = 1.1$ and $I_d = 4 \times 10^{-7}$ A/cm^2. Such a characteristic is typical of the diffusion current. For $7k_0T/q < U < 20k_0T/q$, the I–V characteristic corresponded to the dependence $I = I_0\exp(qU/\beta k_0T)$, where $\beta = 2.3$ and $I_0 = 1.5 \times 10^{-4}$ A cm^{-2}. Thus, along with the diffusion component of the current, the recombination component was also observed. For $U > 30k_0T/q$, high-level injection set in. The resistance of the space-charge region became comparable with that of the semiconductor bulk, the diffusion process was developed deeper into the base, and the I–V characteristic was described by the dependence $I = I_c\exp(qU/ck_0T)$ [6]. Here, $c = 2[b + \cosh(d/l_d]/(b + 1)$, d is the thickness of the diode base,

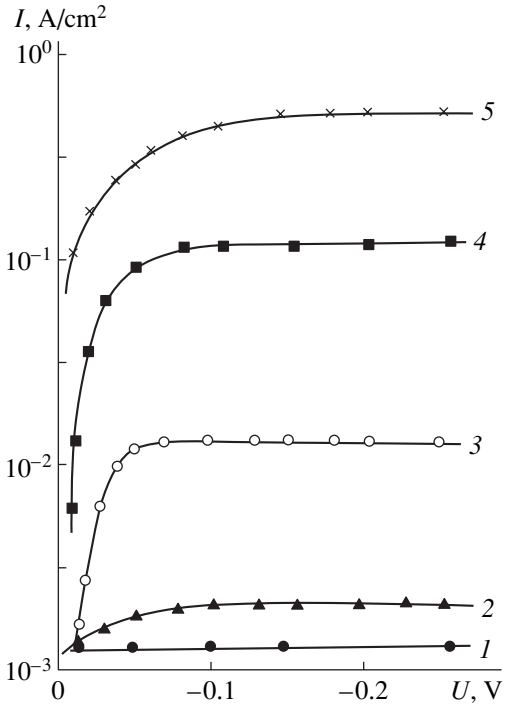

Fig. 3. Current–voltage characteristics of InSb-based *p–n* junctions for reverse biases. Temperature T = (*1*) 78, (*2*) 95, (*3*) 115, (*4*) 130, and (*5*) 145 K.

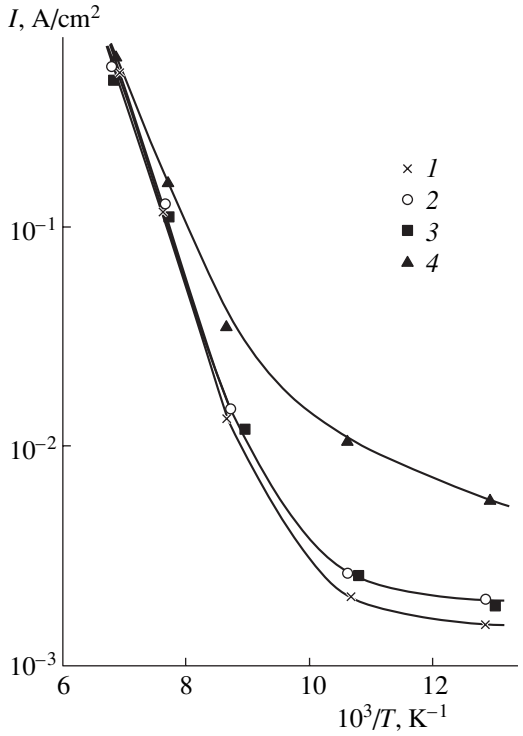

Fig. 4. Temperature dependence of reverse currents of InSb-based photodiodes nos. *1–4* for U = –0.2 V.

$l_d = L[2b/(b + 1)]^{1/2}$, L is the diffusion length, and $b = \mu_n/\mu_p$ is the ratio of carrier mobilities. According to the experimental dependences at d = 350 μm and b = 50, the diffusion length L of carriers in the base was estimated. At T = 78 K, L = 44 μm and slightly increased to 46 μm at T = 145 K. As the temperature increased, the characteristic portion of a purely diffusion mechanism disappeared at T > 110 K, and the value of β decreased from 2.3 at T = 78 K to 1.9 at T = 145 K. Thus, at such temperatures, the current of the InSb-based *p–n* junctions consisted of two components, namely, diffusion and recombination components, over the entire range of forward biases up to the high-level injection mode.

For reverse biases, the *I–V* characteristics of the InSb-based *p–n* junctions were described by the dependences $I = (I_d + I_g)[\exp(qU/ck_0T) - 1] = I_s[\exp(qU/ck_0T) - 1]$, where I_d is the diffusion component of the current. In general, for $n_p = p_n$ (concentrations of minority carriers in the *p*- and *n*-type regions, respectively), I_d consisted of electron and hole components of *p*- and *n*-type regions of the junction. $I_g = qn_iW/2\tau_0$ is the generation current of the space-charge region (SCR) (Fig. 3), where W is the width of the SCR, n_i is the intrinsic-carrier concentration, and τ_0 is the corresponding effective lifetime. Over the entire temperature range investigated, the *I–V* characteristics had the dependence $I = I_s$. However, the current I_s was not saturated, but increased slowly. The nature of the I_s current can be determined from its temperature dependence (Fig. 4). For $U \approx$ –0.2 V and temperatures in the vicinity of 78 K, the current I_s varied slightly as the temperature increased, which corresponded neither to the I_d nor to the I_g temperature dependences. Such behavior of the I_s current can be attributed to the surface leakage [7]. At T > 110 K and $U \approx$ –0.2 V, the I_s current varied with the temperature according to the exponential law. When the nature of this current was clarified, as well as that of the current in the increasing portion of the *I–V* characteristic ($I < I_s$) for the reverse biases, the dependences of R_dA of the *p–n* junctions on U and temperature were investigated (Fig. 5). At T > 110 K and $I < I_s$, the kinks characteristic of the alteration of the current mechanism were observed in the $R_dA = f(U)$ curves. The temperature dependences $R_dA = f(10^3/T)$, which were plotted for three photodiodes for U = –75 mV and U = –250 mV (Fig. 6), gave us an insight into the nature of currents, since the value of $(R_dA)_{diff} \propto 1/I_d$ varied with the temperature as $1/n_i^2$, while $(R_dA)_g \propto 1/I_d \propto 1/n_i$. It follows from Fig. 6 that, at T > 110 K and U > –0.1 V, the current I_d is predominant, whereas, for U < –0.1 V, the current I_g is predominant. As the temperature increases, the region of prevalence of I_g shifts to the larger reverse biases (Fig. 5, dashed curves). This is caused by the need to compensate the decrease in the

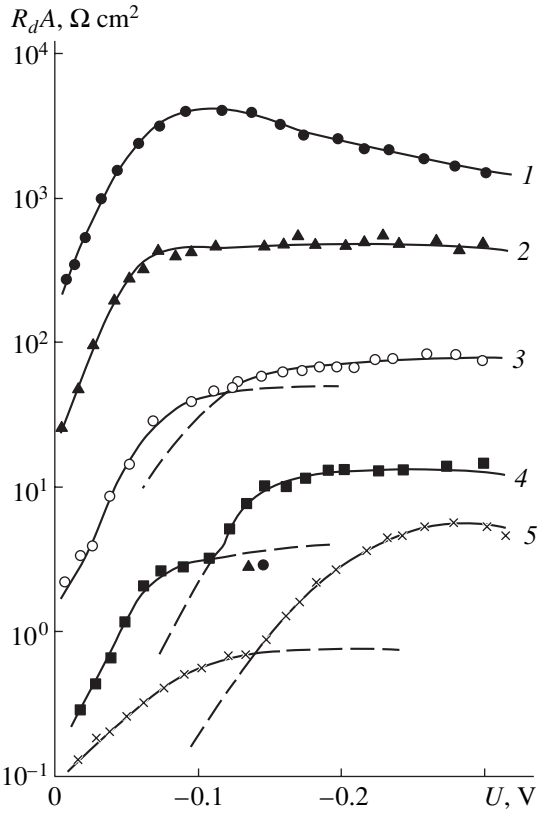

Fig. 5. Reverse-bias dependence of the differential resistance of the current–voltage characteristics for InSb-based *p–n* junctions. Temperature T = (*1*) 78, (*2*) 95, (*3*) 115, (*4*) 130, and (*5*) 145 K.

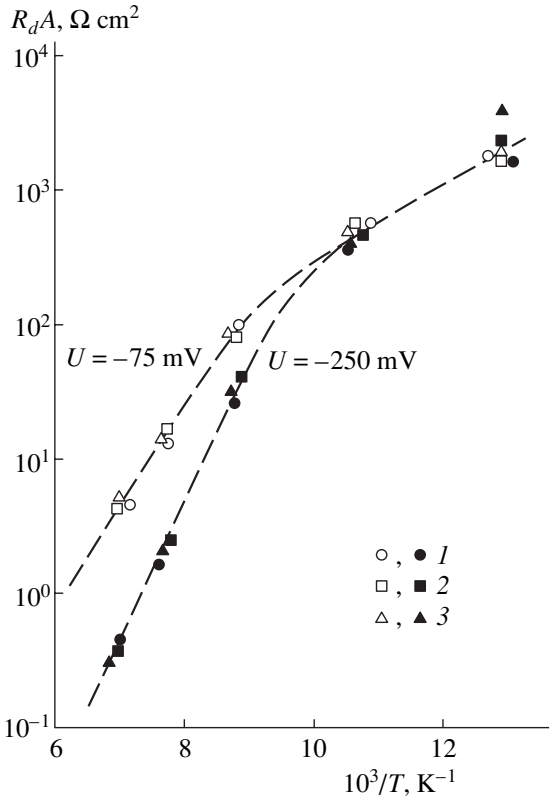

Fig. 6. Temperature dependence of components of the differential resistance for InSb-based photodiode structures nos. *1–3* for two bias voltages.

width W of the SCR in the *p–n* junction by the voltage as the temperature increases.

For the same linear arrays, the *p–n* junctions were investigated using a scanning electron microscope (SEM) in the electron-beam-induced-current (EBIC) mode [8, 9]. This method allows one to reveal the recombination defects, both grown-in defects and those introduced during the treatment, as well as nonuniformities in the distribution of the EBIC over the area of the *p–n* junction. These nonuniformities are associated, for example, with the nonuniform distribution of the diffusion length of minority carriers. The examples of the results obtained are illustrated in Figs. 7b–9b. Figures 7a–9a show the corresponding SEM images of the surface of the samples; the secondary-electron mode was used. Analysis of these images allows us to separate bulk defects in the material itself (in this case, InSb) from defects at the surface, specifically, those at the outer surface of the ZnS film (compare Figs. 7b–9b and 7a–9a). We failed to reveal the individual extended defects in the *p–n* junction shown in Fig. 7. However, the distribution of the EBIC was nonuniform: the current increased in the region near the metal contact. The anomaly of R_dA was observed for this *p–n* junction (Fig. 1). The dependence $I(10^3/T)$ for the same *p–n* junction is shown in Fig. 4 (photodiode *5*). For such photodiodes, the values of the current sensitivity S_i were also relatively small. For the *p–n* junction whose SEM image is shown in Fig. 8, the EBIC is uniformly distributed over the area of the *p–n* junction, and the diffusion length is larger than that for the *p–n* junction shown in Fig. 7. For this junction, we managed to reveal individual extended defects (Fig. 10) with a magnification of ×2000. These defects increase the local rate of recombination; however, they have virtually no effect on the value of S_i for the *p–n* junction. For the *p–n* junction in Fig. 9, the diffusion length was even larger than for the junction shown in Fig. 8, which caused an increase in the coefficient of mutual coupling between the elements of the linear array. With a large magnification (×2400, Fig. 11), the extended defects were also revealed for this *p–n* junction, specifically, a linear defect, which is possibly associated with a bundle of dislocations or with the low-angle boundary. In the SEM images shown in Figs. 7b–9b, the defects in the InSb layer at a depth as great as 3 μm and the defect at the ZnS/InSb interface itself are distinct. In the latter case, these defects exist in the form of voids and inclusions of Zn and S, which emerge in this case at the initial stage of the thermal decomposition of ZnS (compare Figs. 8b and 9b with Fig. 7b, where these defects

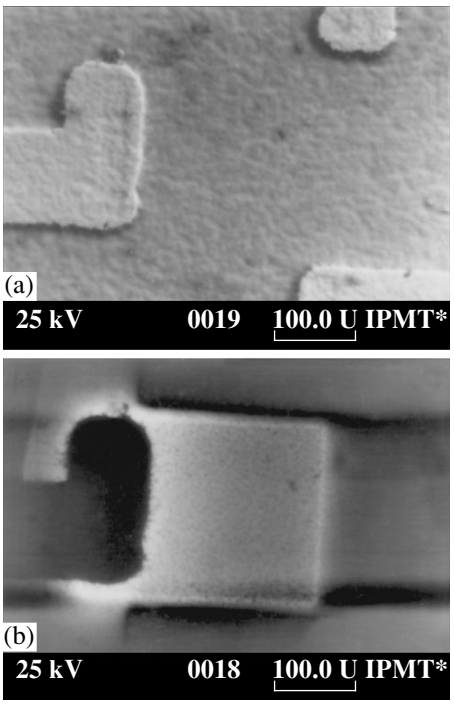

Fig. 7. SEM image of an element of the InSb-based linear array (a) in the secondary-electron mode and (b) in the EBIC mode; magnification ×100.

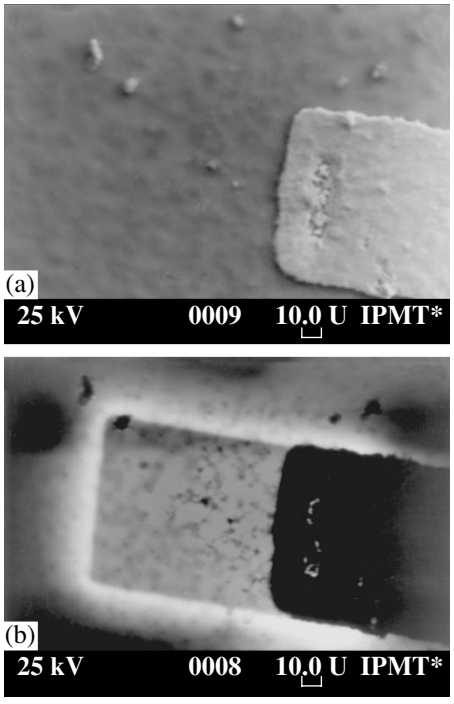

Fig. 8. SEM image of an element of the InSb-based linear array (a) in the secondary-electron mode and (b) in the EBIC mode; magnification ×100.

are virtually absent). Consequently, the resolution of this method is ~3 μm.

The results of investigating the mutual-coupling coefficient for photodiodes of the linear array shown in Fig. 8 are given in the table. It can be seen that the average mutual-coupling coefficient for neighboring photodiodes does not exceed 4.3%. This value is comparable with the value of 3% known from the literature [10]. The average mutual-coupling coefficient for alternate photodiodes did not exceed 0.7%. The voltage sensitivity of photodiodes was in the range of (1.15–1.27) × 10^6 V/W with an average of $S_v = 1.24 \times 10^6$ V/W. Thus, the nonuniformity of S_v did not exceed 9.7% and also differed insignificantly from the value known from the literature (±8%) [11], which was obtained for a large matrix of 128 × 128 elements. The nonuniformity of D^* was considerably higher (51%); i.e., the noise of the photodiode structures made the main contribution to the spread of D^*.

These data and additional research on surface etching during the precision removal of the implantation-damaged layer showed that the anomalies in *I–V* characteristics consisted in the emergence of an "incipient" *S*-like portion near to the zero bias. This portion

Parameters of the InSb-based photodiode linear array

No. of photodiode in the linear array	Mutual coupling coefficient, %						
1	2	3	4	5	6	7	8
1	3.5	0.8					
2	100	4.2	0.5				
3	4.9	100	3.8	0.9			
4	0.7	4.7	100	4.1	0.6		
5		0.6	4.2	100	4.1	0.5	
6			0.8	4.7	100	4.1	0.7
7				0.7	4.3	100	4.2
8					0.9	4.8	100

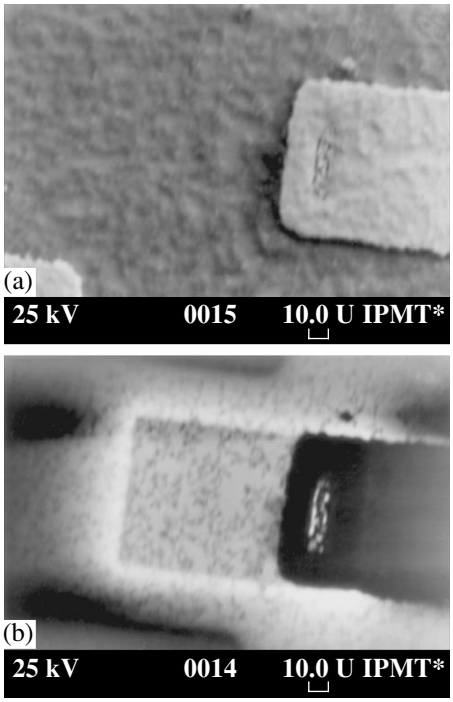

Fig. 9. SEM image of an element of the InSb-based linear array (a) in the secondary-electron mode and (b) in the induced-current mode; magnification ×100.

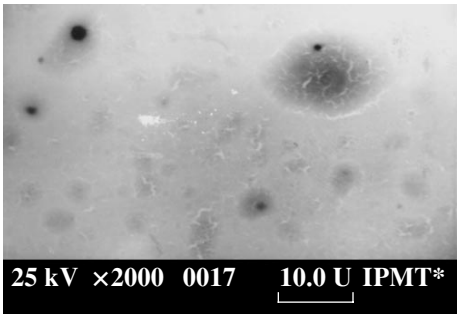

Fig. 10. SEM image of the element shown in photograph 2b with magnification ×2000.

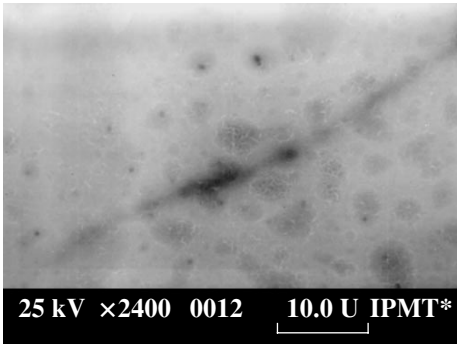

Fig. 11. SEM image of the element shown in photograph 3b with magnification ×2400.

emerged with incomplete etching of the surface, which caused an increased leakage resistance of the *p*-type layer implanted with Zn^{++}. As a result, a portion of the photocarrier current "dropped out" at this *p*-type layer and did contribute to the external current of the photodiode. Such photodiodes usually had low S_v, increased noise, and a drift of parameters during the operation in the vicinity of $U = 0$. The aforementioned anomalies in the *I–V* characteristics, i.e., the emergence of the *S*-like feature, could be observed for some photodiodes using a PNKhT (a device for the observation of transistor characteristics). However, in most cases these anomalies were not revealed by using such a device, and time-consuming measurements of R_d depending on U and temperature were required to discover them. However, excess etching of the surface layer after the annealing of radiation defects (the element in Fig. 3) also had a detrimental effect on the parameters of the linear array due to an increase in the coefficient of mutual coupling between the elements. This was not so important for single photodiodes; however, for *p–n* junctions in the linear array, it was a substantial disadvantage.

REFERENCES

1. C. E. Hurwitz and J. P. Donnelly, Solid-State Electron. **18**, 753 (1975).
2. O. V. Kosogov and L. S. Perevyazkin, Fiz. Tekh. Poluprovodn. (Leningrad) **4**, 1611 (1970) [Sov. Phys. Semicond. **4**, 1387 (1970)].
3. V. A. Bogatyrev, G. A. Kachurin, and L. S. Smirnov, Fiz. Tekh. Poluprovodn. (Leningrad) **12**, 102 (1978) [Sov. Phys. Semicond. **12**, 57 (1978)].
4. V. A. Bogatyrev, G. A. Kachurin, and L. S. Smirnov, Fiz. Tekh. Poluprovodn. (Leningrad) **12**, 878 (1978) [Sov. Phys. Semicond. **12**, 517 (1978)].
5. A. B. Korshunov, Fiz. Tekh. Poluprovodn. (Leningrad) **13**, 1846 (1979) [Sov. Phys. Semicond. **13**, 1074 (1979)].
6. V. I. Stafeev, Zh. Tekh. Fiz. **28**, 1631 (1958) [Sov. Phys. Tech. Phys. **3**, 1502 (1958)].
7. V. I. Turinov, in *Abstracts of 9th Scientific and Technical Conference on Photometry and Its Metrological Equipment* (VNIIOFI, Moscow, 1992), p. 43.
8. G. N. Panin, V. F. Kuleshov, and E. B. Yakimov, in *Abstracts of VII All-Union Symposium on Semiconductors with Narrow Band Gap and Semimetals* (Lvov. Gos. Univ., Lvov, 1986), Part 1, p. 43.
9. E. B. Yakimov, Izv. Ross. Akad. Nauk, Ser. Fiz. **56**, 31 (1992).
10. I. Bloom and Y. Nemirovsky, IEEE Trans. Electron Devices **38**, 1792 (1991).
11. G. C. Bailey, C. A. Niblack, and J. T. Wimmers, Proc. SPIE **686**, 76 (1986).

Translated by N. Korovin

Semiconductors, Vol. 38, No. 4, 2004, pp. 486–493. Translated from Fizika i Tekhnika Poluprovodnikov, Vol. 38, No. 4, 2004, pp. 504–511.

PHYSICS OF SEMICONDUCTOR DEVICES

Thermal Calculation of SiC *p–i–n* Diodes

P. B. Gamuletskaya, A. V. Kirillov**, A. A. Lebedev*, L. P. Romanov**, and V. A. Smirnov****

**Ioffe Physicotechnical Institute, Russian Academy of Sciences, Politekhnicheskaya ul. 26, St. Petersburg, 194021 Russia*

***ZAO Svetlana-Élektronpribor, St. Petersburg, Russia*

Submitted September 3, 2003; accepted for publication September 9, 2003

Abstract—Thermal calculations of various design models of SiC *p–i–n* diodes with a structure capacity of 0.2 pF are carried out for substrate thicknesses of 360, 50, and 2 mm. Comparison with a silicon *p–i–n* structure on an integrated heat sink is performed. © *2004 MAIK "Nauka/Interperiodica".*

1. INTRODUCTION

It is well known that silicon carbide is a promising material for power electronics due to its unique electrical parameters [1]. However, the high density of structural defects in SiC epitaxial structures is a serious obstacle for the commercial production of high-current SiC devices. At the same time, small-size microwave SiC devices exhibit characteristics close to the theoretical ones, which has led to the active development of SiC-based microwave engineering.

In this study, the thermal resistance of the SiC *p–i–n* diode was theoretically studied for the first time in the frequency range ~10 GHz.

2. CALCULATION PROCEDURE

In the calculations, the structure capacitance of reverse-biased *p–i–n* diodes was taken as C_{pn} = 0.2 pF, which is a typical value for the 3-cm wavelength range. The base thickness (n^- region) was h_n = 2 and 6 μm. The thickness H_{n^+} of the n^+-SiC low-resistivity substrate was taken as follows:

(i) 360 μm for a typical SiC substrate (wafer);

(ii) 50 μm for a substrate thinned in order to reduce resistive losses;

(iii) 2 μm for a totally removed substrate with the purpose of minimizing resistive losses (the ideal case); an analog is the silicon *p–i–n* diode structure on an integrated heat sink.

Table 1 lists the main parameters of silicon carbide, silicon, and diamond (for the case of a diamond heat sink). The thermal conductivity of SiC-4*H* was taken from [2]; the other SiC parameters were taken from [3].

The thermal resistance was calculated within the simplified equivalent model for a multilayer wafer heated by a circular source under stationary conditions, using the technique of [4].

A schematic representation of the thermal model used in the calculation is shown in Fig. 1. When a simulated structure had no diamond pedestal, layers *7–9* are absent in the calculation scheme (Fig. 1).

The resistance calculation in terms of the simplified equivalent model for a round heat source consists in consideration of the heat-flow spread over the volume of a layer (body), if the sizes of the latter exceed the sizes of the heat source. A schematic diagram of the heat flow from the heat source to the heat sink is shown in Fig. 2.

Table 1

Parameter and designation	Unit	SiC-4*H*		Silicon		IIa diamond	IIb diamond
		n^--type	n^+-type	n^--type	n^+-type		
High-frequency permittivity ε		6.7		11.8			
Thermal conductivity λ	W/(cm K)						
at T = 300 K		3.8	2.9	1.45	0.8	22	13
at T = 500 K		1.8	1.8	0.8	0.45	10	6
Specific heat C_p	J/(g K)	0.6		0.76		0.63	0.63
Density P	g/cm^3	3.21		2.32		3.5	3.5

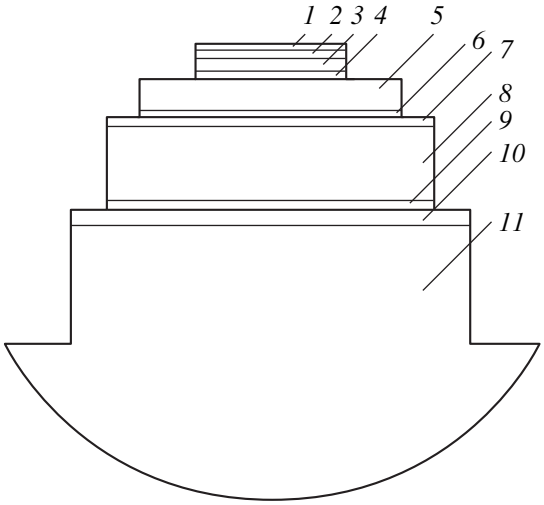

Fig. 1. Thermal model of the SiC *p–i–n* structure on a copper holder: (*1*) ohmic contact to the p^+ region (the thicknesses of the Al, Ti, Pt, Ni, and Au layers are 0.05, 0.1, 0.025, 0.05, and 0.2 μm, respectively [5]); (*2*) p^+ region of the *p–i–n* structure; (*3*) n^- region of the *p–i–n* structure (n^--type epitaxial layer 2 or 6 μm thick); (*4*) n^+ region of the *p–i–n* structures (n^+-SiC substrate 360, 50, or 2 μm thick); (*5*) ohmic contact to the n^+ region (0.2 μm of Ni and 2 μm of Au) [5] or the same contact with an integrated Au heat sink 45 μm thick (galvanic coating); (*6*) AuGe solder layer 5 μm thick; (*7*) galvanic coating of the diamond pedestal (Au layer 2 μm thick); (*8*) diamond pedestal (IIa- or IIb-type diamond $0.6 \times 0.6 \times 0.2$ mm in size); (*9*) galvanic coating of the diamond pedestal (Au layer 2 μm thick); (*10*) galvanic coating of the copper holder (Au layer 5 μm thick); (*11*) copper diode holder (a fragment of the diode case). The height and diameter of the pedestal are 0.3 and 1 mm, respectively.

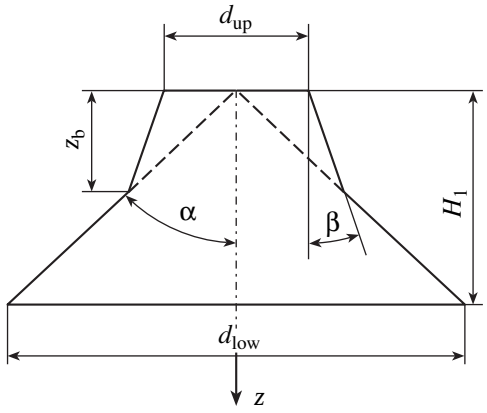

Fig. 2. Schematic diagram of the heat flow through the layer from the heat source to the heat sink.

It can be seen from Fig. 2 that the heat flow entering a layer with uniform electrical and thermal parameters spreads over the layer volume, diverging first at the angle β to the structure axis (*z* axis). At $z = z_b$, the angle of divergence of the heat flow abruptly increases from β to α.

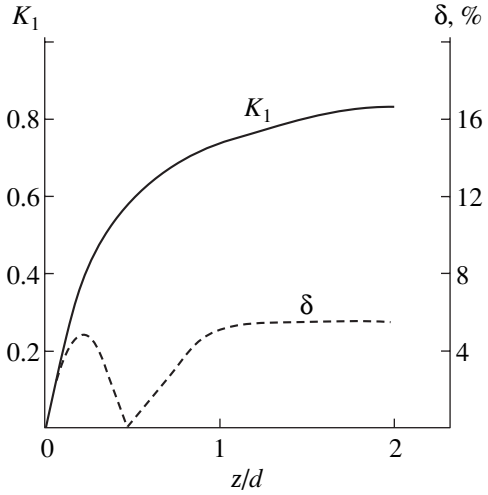

Fig. 3. Dependences of the coefficient K_1 and the relative calculation error δ on the ratio of the layer thickness $z = H_e$ to the diameter *d* of the entering heat flow.

This calculation model is applicable with the following restrictions.

The thickness of a heat-conducting layer $H_1 \le 0.1d_{up}$ (d_{up} is the diameter of the heat flow entering the layer); i.e., the layer is quite thin. In this case, the thermal resistance R_{th} of the layer is calculated using the formula for a cylindrical source,

$$R_{th} = \frac{H_1}{\lambda_1 S} = \frac{4H_1}{\pi d \lambda_1}, \quad (1)$$

where λ_1 is the thermal conductivity and *S* and *d* are the cross-sectional area and the diameter of the heat-conducting cylindrical layer, respectively.

The thickness of the heat-conducting layer $H_1 > 2d_{up}$; i.e., the layer is very thick. Then, the thermal resistance of the layer can be calculated by the formula for the spread in a semi-infinite body,

$$R_{th} = \frac{1}{\pi d_{up} \lambda_1}. \quad (2)$$

If the layer thickness is within $0.1d_{up} < H_1 < 2d_{up}$, R_{th} is calculated taking into account the heat flow spread in the layer by the formula

$$R_{th} = \frac{2K_1}{\pi d_{up} \lambda_1}. \quad (3)$$

Here, K_1 is the coefficient accounting for the heat flow spread; it is determined from the curve [4] shown in Fig. 3.

The diameter d_{low} of the heat flow leaving the layer is calculated as follows. First, the coordinate z_b (Fig. 2) is determined by the formula

$$z_b = \frac{d_{up}}{2(\tan\alpha - \tan\beta)} = 0.622 d_{up}, \quad (4)$$

Table 2. Calculation of R_{th} of the SiC structures with an n^- region 2 μm thick for C_{pn} = 0.2 pF

Layer no. in Fig. 1	Layer material	λ, W/(cm K)		*p–i–n* structure with H_{n^+} = 360 μm					*p–i–n* structure with H_{n^+} = 50 μm				
				thickness, μm	layer diameter, μm		R_{th} of the layer, K/W		thickness, μm	layer diameter, μm		R_{th} of the layer, K/W	
		300 K	500 K		upper	lower	300 K	500 K		upper	lower	300 K	500 K
3	SiC n^- region	3.8	1.8	2	92	96	0.8	1.67	2	92	96	0.8	1.67
4	SiC n^+ region, substrate	2.9	1.8	360	96	600	**20.17**	**26.3***	50	96	176	**10.02**	**17.47***
5	Lower Au contact	3.09	3.0	2	600	600	0.09	0.09**	2	176	179	0.26	0.26**
6	AuGe solder	1.47	~1.42	5	600	608	0.47	0.47**	5	179	187	1.38	1.38**
10	Au coating of the holder	3.09	3.0	5	608	616	0.22	0.22**	5	187	195	0.6	0.6**
11	Cu holder	3.9	3.7	Semi-infinite	616		2.63	2.63**	Semi-infinite	195		8.5	8.5**
Total R_{th}^{tot} at 300 K:							2.38					21.56	
at 500 K:								31.38					29.88

*R_{th} of the layer was calculated taking into account the temperature field gradient inside the layer.
**The values of R_{th} are the same as at 300 K, since the temperature of these layers is low.

Table 3. Calculation of R_{th} of the SiC *p–i–n* structures with an n^- region 6 μm thick for C_{pn} = 0.2 pF

Layer no. in Fig. 1	Layer material	λ, W/(cm K)		*p–i–n* structure with H_{n^+} = 360 μm					*p–i–n* structure with H_{n^+} = 50 μm				
				thickness, μm	layer diameter, μm		R_{th} of the layer, K/W		thickness, μm	layer diameter, μm		R_{th} of the layer, K/W	
		300 K	500 K		upper	lower	300 K	500 K		upper	lower	300 K	500 K
3	SiC n^- region	3.8	1.8	6	160	170	0.79	1.65	6	160	170	0.8	1.67
4	SiC n^+ region, substrate	2.9	1.8	360	170	600	**10.98**	**14.33***	50	170	253	**5.36**	**7.55***
5	Lower Au contact	3.09	3.0	2	600	600	0.09	0.09**	2	253	256	0.13	0.13**
6	AuGe solder	1.47	~1.42	5	600	608	0.47	0.47**	5	256	264	0.66	0.66**
10	Au coating of the holder	3.09	3.0	5	608	616	0.22	0.22**	5	264	272	0.3	0.3**
11	Cu holder	3.9	3.7	Semi-infinite	616		2.63	2.63**	Semi-infinite	272		6.05	6.05**
Total R_{th}^{tot} at 300 K:							15.38					13.29	
at 500 K:								19.39					16.34

Note: The asterisks * and ** indicate the same as in Table 2.

where $\tan\alpha = 1.699$ and $\tan\beta = 0.835$ were determined in [4] for the case of a round heat source. If the layer thickness H_1 does not exceed z_b (i.e., $H_1 < 0.622d_{up}$), the lower diameter d_{low} of the heat flow coming out from the layer is given by

$$d_{low} = d_{up} + 2H_1\tan\beta = d_{up} + 1.67H_1. \quad (5)$$

If the layer thickness $H_1 > 0.622d_{up}$,

$$d_{low} = 2H_1\tan\alpha \approx 3.4H_1. \quad (6)$$

In the latter case, the layer cross size may become limited. For example, if the SiC crystal size is 600 × 600 μm and the thickness H_{n^+} is 360 μm (see Fig. 1 and Table 2, layer *4*), the heat-flow diameter attains a crystal size of

Table 4. Calculation of R_{th} of the SiC *p–i–n* structures with a thin (2 μm) n^+ substrate on a gold integrated heat sink for C_{pn} = 0.2 pF

Layer no. in Fig. 1	Layer material	λ, W/(cm K)		*p–i–n* structure with an n^- region 6 μm thick					*p–i–n* structure with an n^- region 2 μm thick				
				thickness, μm	layer diameter, μm		R_{th} of the layer, K/W		thickness, μm	layer diameter, μm		R_{th} of the layer, K/W	
		300 K	500 K		upper	lower	300 K	500 K		upper	lower	300 K	500 K
3	SiC n^- region	3.8	1.8	6	160	170	0.79	1.65	2	92	96	0.8	1.67
4	SiC n^+ region, substrate	2.9	1.8	2	170	173	0.32	0.51	2	96	99	0.95	1.53
5	Lower Au contact	3.09	3.0	45	173	247	4.67	4.81	45	99	173	**10.61**	**10.94**
6	AuGe solder	1.47	~1.42	5	247	255	0.71	0.71**	5	173	181	1.44	1.44**
10	Au coating of the holder	3.09	3.0	5	255	263	0.32	0.32**	5	181	189	0.63	0.63**
11	Cu holder	3.9	3.7	Semi-infinite	263		**6.23**	**6.23**	Semi-infinite	189		8.6	8.6**
Total R_{th}^{tot} at 300 K:							13.04					23.03	
at 500 K:								14.23					24.81

Note: The asterisk ** indicates the same as in Table 2.

Table 5. Calculation of R_{th} of the SiC *p–i–n* structures with a thin (2 μm) n^+ substrate on a gold integrated heat sink for C_{pn} = 0.2 pF

Layer no. in Fig. 1	Layer material	λ, W/(cm K)		*p–i–n* structure with an n^- region 6 μm thick					*p–i–n* structure with an n^- region 2 μm thick				
				thickness, μm	layer diameter, μm		R_{th} of the layer, K/W		thickness, μm	layer diameter, μm		R_{th} of the layer, K/W	
		300 K	500 K		upper	lower	300 K	500 K		upper	lower	300 K	500 K
3	SiC n^- region	3.8	1.8	6	160	170	0.79	1.65	2	92	96	0.8	1.67
4	SiC n^+ region, substrate	2.9	1.8	2	170	173	0.32	0.51	2	96	99	0.95	1.53
5	Au heat sink	3.09	3.0	45	173	247	**4.67**	**4.81**	45	99	173	**10.61**	**10.94**
6	AuGe solder	1.47	~1.42	5	247	255	0.71	0.71**	5	173	181	1.44	1.44**
7	Au coating of the diamond	3.09	3.0	2	255	258	0.13	0.13**	2	181	184	0.25	0.25**
8	Diamond pedestal:			200	258	600			200	184	600		
	IIa type	22	10				0.73	0.73**				1.09	1.09**
	IIb type	13	6				1.22	1.22**				1.84	1.84**
9	Au coating of the diamond	3.09	3.0	2	600	600	0.09	0.09**	2	600	600	0.09	0.09**
10	Au coating of the holder	3.09	3.0	5	600	608	0.22	0.22**	5	600	608	0.22	0.22**
11	Cu holder	3.9	3.7	Semi-infinite	608		2.63	2.63**	Semi-infinite	608		2.63	2.63**
Total R_{th}^{tot} for IIa-type diamond at 300 K:							10.29					18.08	
at 500 K:								11.48					19.86
for IIb-type diamond at 300 K:							10.78					18.83	
at 500 K:								11.97					20.61

Note: The asterisk ** indicates the same as in Table 2.

Table 6. Calculation of R_{th} of the SiC *p–i–n* structures with a thin (50 μm) n^+ substrate on a diamond pedestal for C_{pn} = 0.2 pF

Layer no. in Fig. 1	Layer material	λ, W/(cm K)$^{-1}$		*p–i–n* structure with an n^- region 6 μm thick					*p–i–n* structure with an n^- region 2 μm thick				
				thickness, μm	layer diameter, μm		R_{th} of the layer, K/W		thickness, μm	layer diameter, μm		R_{th} of the layer, K/W	
		300 K	500 K		upper	lower	300 K	500 K		upper	lower	300 K	500 K
3	SiC n^- region	3.8	1.8	6	160	170	0.79	1.65	2	92	96	0.8	1.67
4	SiC n^+ region, substrate	2.9	1.8	50	170	253	**5.36**	**7.55***	50	96	176	**10.02**	**17.47***
5	Au heat sink	3.09	3.0	2	253	256	0.13	0.13**	2	176	179	0.26	0.26**
6	AuGe solder	1.47	~1.42	5	256	264	0.66	0.66**	5	179	187	1.38	1.38**
7	Au coating of the diamond	3.09	3.0	2	264	268	0.12	0.12**	2	187	191	0.24	0.24**
8	Diamond pedestal:			200	268	600			200	191	600		
	IIa type	22	10				0.78	0.78**				1.05	1.05**
	IIb type	13	6				1.32	1.32**				1.76	1.76**
9	Au coating of the diamond	3.09	3.0	2	600	600	0.09	0.09**	2	600	600	0.09	0.09**
10	Au coating of the holder	3.09	3.0	5	600	608	0.22	0.22**	5	600	608	0.22	0.22**
11	Cu holder	3.9	3.7	Semi-infinite	608		2.63	2.63**	Semi-infinite	608		2.63	2.63**
Total R_{th}^{tot} for IIa-type diamond at 300 K:							10.78					16.69	
at 500 K:								13.85					25.05
for IIb-type diamond at 300 K:							11.32					17.4	
at 500 K:								14.39					25.76

Note: The asterisks * and ** indicate the same as in Table 2.

Table 7. Calculation of R_{th} of the SiC *p–i–n* structures on a gold integrated heat sink for C_{pn} = 0.2 pF

Layer no. in Fig. 1	Layer material	λ, W/(cm K)		Si-*p–i–n* structure with an n^- region 6 μm thick					Si-*p–i–n* structure with an n^- region 2 μm thick				
				thickness, μm	layer diameter, μm		R_{th} of the layer, K/W		thickness, μm	layer diameter, μm		R_{th} of the layer, K/W	
		300 K	500 K		upper	lower	300 K	500 K		upper	lower	300 K	500 K
3	SiC n^- region	1.45	0.8	6	121	131	3.59	6.51	2	70	73	3.6	6.52
4	SiC n^+ region, substrate	0.8	0.45	1	131	133	0.93	1.64	1	73	74	3.98	5.3
5	Lower Au contact	3.09	3.0	45	133	207	6.76	6.97	45	74	148	**15.88**	**16.35**
6	AuGe solder	1.47	~1.42	5	207	215	1.01	1.01	5	148	156	1.97	1.97
10	Au coating of the holder	3.09	3.0	5	215	223	0.44	0.44	5	156	164	0.84	0.84
11	Cu holder	3.9	3.7	Semi-infinite	223		**7.4**	**7.4**	Semi-infinite	164		9.96	9.96
Total R_{th}^{tot} at 300 K:							20.13					35.23	
at 500 K:								23.97					40.94

Table 8

Parameter	Unit	SiC *p–i–n* structure*							
		1	1	3 (IIa)	3 (IIb)	2	4 (IIa)	4 (IIb)	1
Thickness of the n^- region	μm	2	2	2	2	2	2	2	6
Thickness of the n^+ region	μm	360	50	50	50	2	2	2	360
$R_{\text{th } n^-}$ at 500 K	K/W	1.7	1.7	1.7	1.7	1.7	1.7	1.7	1.7
$R_{\text{th } n^+}$ at 500 K	K/W	**26.3**	**17.5**	**17.5**	**17.5**	1.5	1.5	1.5	**14.3**
$R_{\text{th}}^{\text{ihr}}$ at 500 K	K/W	–	–	–	–	**10.9**	**10.9**	**10.9**	–
$R_{\text{th}}^{\text{dia}}$ at 300 K	K/W	–	–	1.0	1.7	–	1.1	1.8	–
$R_{\text{th}}^{\text{holder}}$ at 300 K	K/W	2.63	8.5	2.63	2.63	8.6	2.63	2.63	2.63
$R_{\text{th}}^{\text{tot}}$ at T_{pn} = 300 K	K/W	24.4	21.6	16.7	17.4	23.0	18.1	18.8	15.2
$R_{\text{th}}^{\text{tot}}$ at T_{pn} = 500 K	K/W	31.4	29.9	25.1	25.8	24.8	19.9	20.6	19.4

Parameter	Unit	SiC *p–i–n* structure*						Silicon *p–i–n* structure	
		1	3 (IIa)	3 (IIb)	2	4 (IIa)	4 (IIb)		
Thickness of the n^- region	μm	6	6	6	6	6	6	2	6
Thickness of the n^+ region	μm	50	50	50	2	2	2	1	1
$R_{\text{th } n^-}$ at 500 K	K/W	1.7	1.7	1.7	1.7	1.7	1.7	6.5	6.5
$R_{\text{th } n^+}$ at 500 K	K/W	**7.6**	**7.6**	**7.6**	0.5	0.5	0.5	5.3	1.6
$R_{\text{th}}^{\text{ihr}}$ at 500 K	K/W	–	–	–	4.8	**4.8**	**4.8**	**16.4**	7.0
$R_{\text{th}}^{\text{dia}}$ at 300 K	K/W	–	0.8	1.3	–	0.7	1.2	–	–
$R_{\text{th}}^{\text{holder}}$ at 300 K	K/W	6.1	2.63	2.63	**6.2**	2.63	2.63	10.0	7.4
$R_{\text{th}}^{\text{tot}}$ at T_{pn} = 300 K	K/W	13.3	10.8	11.3	13.0	10.3	10.8	35.2	20.1
$R_{\text{th}}^{\text{tot}}$ at T_{pn} = 500 K	K/W	16.3	13.9	14.4	14.2	11.5	12.0	40.9	24.0

* (1) Typical SiC structure on a copper gold-plated diode heat sink; (2) SiC structure with totally removed substrate on an integrated heat sink consisting of a Au layer 45 μm thick and a copper gold-plated diode heat sink; (3) SiC structure with a thinned substrate on a diamond pedestal installed on a copper gold-plated diode heat sink; (4) SiC structure with totally removed substrate with an Au integrated heat sink 45 μm thick on a diamond pedestal installed on a copper gold-plated diode heat sink; IIa and IIb are the types of the diamond pedestal; $R_{\text{th}}^{\text{ihr}}$ and $R_{\text{th}}^{\text{dia}}$ are the thermal resistances of the integrated Au heat sink and the diamond pedestal; T_{pn} is the temperature of the *p–n* junction.

600 μm even at a distance of 176 μm from the crystal surface (see formula (6)). In this case, the thermal resistance R_{th} of the layer at a distance from the crystal surface below and above 176 μm is determined by formulas (3) and (1), respectively.

The relative error in determining the average thermal resistances of layers by this technique does not exceed 5% [4].

The thermal resistance was calculated layer by layer using the above-mentioned models for layer temperatures of 300 and 500 K, since the thermal conductivity of layer materials (especially semiconductors) may depend heavily on temperature. The results calculated for the *p–i–n* structures with capacitance C_{pn} = 0.2 pF of the depleted *p–n* junction are listed in Tables 2–7.

The resistance R_{th} of multilayer ohmic contacts was calculated for only one layer—the galvanic gold coat-

ing, which is the thickest one and, thus, controls the value of R_{th} of the ohmic contact.

Here we clarify the data in Tables 2–7.

(i) The initial (upper) diameter in the "layer diameter" column is determined by the *p–n* junction area, which, in turn, is derived from the values of capacitance C_{pn} = 0.2 pF and the thickness of the n^--type region (layer *3*): 2 or 6 μm.

(ii) The downward increase in the layer diameter (Fig. 1) is explained by the increase in the area of the heat flow as it moves from the source (*p–n* junction) to the external heat sink. The flow area is restricted only by the size of the structure (600 μm in the case under consideration).

(iii) The data in the column "R_{th} of the layer" (at 500 K) imply that the *p–n* junction is heated to 500 K by the power released in it, while the heat sink is at room temperature.

(iv) The resistance R_{th} for the copper holder was calculated for all types of SiC *p–i–n* structures, as in the case of spread into a semi-infinite body.

(v) The values of the highest layer resistances R_{th} are in boldface.

3. RESULTS AND ANALYSIS

We now consider the calculation of the thermal resistance of a silicon *p–i–n* diode on an integrated heat sink with an n^- region 2 or 6 μm thick and C_{pn} = 0.2 pF.

In order to facilitate the analysis and choose the optimum design (with respect to minimization of the thermal resistance of the SiC *p–i–n* diode), all the basic data are listed in Table 8. For comparison, the data on the silicon *p–i–n* diode on an integrated heat sink are also listed in Table 8.

As follows from the results of calculations, the highest thermal resistance at 500 K is observed in diode structures with a thick n^+-type substrate of thickness H_{n^+} = 360 μm: R_{th}^{tot} = 31.4 K/W (Tables 2, 8) and R_{th}^{tot} = 19.4 K/W (Tables 3, 8) for the structures with a thickness of the n^- region of 2 and 6 μm, respectively. In this case, the major contribution to the thermal resistance is related to the n^+ substrate: R_{thn^+} = 26.3 and 14.3 K/W, respectively. A decrease in the substrate thickness to 50 μm makes it possible to reduce the thermal resistance R_{thn^+} of the n^+ region from 26.3 to 17.5 K/W (by 35%) and from 14.3 to 7.6 K/W (by 47%) for thicknesses of the n^- region of 2 and 6 μm, respectively. The total thermal resistance R_{th}^{tot} decreases only by 5% (from 31.4 to 29.9 K/W) and 16% (from 19.4 to 16.3 K/W) for *n–n*$^+$ structures 2 and 6 μm thick, respectively. This is caused by the increasing role of the thermal spreading resistance R_{th}^{holder} in the copper heat sink (holder) as the heat-flow diameter decreases: R_{th}^{holder} increases from 2.63 to 8.5 K/W and to 6.1 K/W for the above values of structure thickness (2 and 6 μm, respectively). In the ideal case, when the n^+ substrate is almost totally removed (H_{n^+} = 2 μm), the thermal resistance R_{thn^+} decreases to 1.5 and 0.5 K/W for the structure with an n^- region 2 and 6 μm thick, respectively, and is no longer the major component of the thermal resistance of the diode. Introduction of a diamond pedestal (heat sink) provides an additional reduction in R_{th}^{tot} approximately by 20% from 24.8 to 19.9 K/W and from 14.4 to 11.5 K/W for the structures with a base (n^+ region) 2 and 6 μm thick, respectively. As calculations show, diamond pedestals of different modifications (type IIa or IIb) similarly affect the total thermal resistance; the difference is as low as 3%.

For a typical silicon *p–i–n* diode on an integrated heat sink, the value of R_{th}^{tot} exceeds that of a SiC diode on a thick substrate with H_{n^+} = 360 μm by 25–30% and is twice as large as R_{th}^{tot} for a SiC diode on an integrated heat sink with a diamond pedestal. This difference is mainly due to the high permittivity of silicon, ε = 11.8 (for silicon carbide, ε = 6.7), and the rather low thermal conductivity of silicon, λ = 0.45–0.8 K/W at 500 K against 1.8 K/W for silicon carbide.

4. CONCLUSION

We calculated the total thermal resistance R_{th}^{tot} for various designs of SiC *p–i–n* diodes with the junction capacitance C_{pn} = 0.2 pF. The lowest resistance R_{th}^{tot} was obtained for the design that was close to ideal: SiC *p–i–n* structures on a thinned (to 2 μm) substrate with a gold integrated heat sink 45 μm thick on a diamond heat sink (pedestal 0.6 × 0.6 × 0.2 mm in size). The lowest resistances are R_{th}^{tot} = 11.5–12 and 19.9–20.6 K/W for an n^- region 6 and 2 μm thick, respectively. Moreover, this structure should also be characterized by the lowest resistive losses since the resistive losses are negligible in the substrate (n^+ region). However, it is very difficult to implement such structures in practice since SiC membranes 5–10 μm thick have not yet been fabricated, whereas silicon membranes of this thickness can be easily obtained by chemical mechanical etching.

Among the designs of SiC diodes considered above, the *p–i–n* structure with a thin (50 μm) substrate soldered onto a diamond heat sink is of interest; this

design seems to be feasible. Its implementation would make it possible to reduce the diode thermal resistance and resistive losses and, hence, increase the microwave power switched by the diode in comparison with the basic type.

ACKNOWLEDGMENTS

This study was supported by INTAS (grant 01-603) and NATO (grant SfP-978011).

REFERENCES

1. A. A. Lebedev and V. E. Chelnokov, Fiz. Tekh. Poluprovodn. (St. Petersburg) **33**, 1096 (1999) [Semiconductors **33**, 999 (1999)].
2. E. A. Burgemteister, W. von Muench, and E. Pettenpaul, J. Appl. Phys. **50**, 5790 (1979).
3. *Properties of Advanced Semiconductor Materials: GaN, AlN, InN, BN, SiC, SiGe*, Ed. by M. E. Levinshtein, S. L. Rumyantsev, and M. S. Shur (Wiley, New York, 2001), Chap. 5, p. 93.
4. A. L. Zakharov and E. I. Asvadurova, *Calculation of Thermal Parameters of Semiconductor Devices* (Radio i Svyaz', Moscow, 1983).
5. K. V. Vassilevskii, K. Zekentes, A. V. Zorenko, and L. P. Romanov, Mater. Res. Soc. Symp. **622**, T 1.8.1 (2000).

Translated by A. Kazantsev